

R29-92

**Development of Magnetostrictive Active Members
for Control of Space Structures**

FINAL REPORT

July 1992

P. 265

N93-18322

Unclass

G3/18 0143392

Prepared for:
NASA Resident Office-JPL
4800 Oak Grove Drive
Pasadena, CA 91109

Contract No. NAS7-1151

Prepared by:
Bruce G. Johnson, Kevin Avakian, Donald Boudreau, Ralph C. Fenn,
Monique S. Gaffney, Michael Gerver, Timothy Hawkey
SatCon Technology Corporation
12 Emily Street
Cambridge, MA 02139
Tel: 617-661-0540, ext. 207

(NASA-CR-190346) DEVELOPMENT OF
MAGNETOSTRICTIVE ACTIVE MEMBERS FOR
CONTROL OF SPACE STRUCTURES Final
Report, Jun. 1991 - Jul. 1992
(SatCon Technology Corp.) 267 p

SBIR RIGHTS NOTICE (JUN 1987)

These SBIR data are furnished with SBIR rights under Contract No. NAS7-1151. For a period of 2 years, acceptance of all items to be delivered under this contract, the Government agrees to use these data for Government purposes only, and they shall not be disclosed outside the Government (including disclosure for procurement purposes) during such period without permission of the Contractor, except that, subject to the foregoing use and disclosure prohibitions, such data may be disclosed for use by support Contractors. After the aforesaid 2-year period the Government has a royalty-free license to use, and to authorize others use on its behalf, these data for Government purposes, but is relieved of all disclosure prohibitions and assumes no liability for unauthorized use of these data by third parties. This Notice shall be affixed to any reproductions of these data, in whole or in part.

The Contractor, SatCon Technology Corporation, hereby certifies that, to the best of its knowledge and belief, the technical data delivered herewith under Contract No. NAS7-1151 is complete, accurate, and complies with all requirements of the contract.

8/11/92

Richard L. Hockney

Date

Richard L. Hockney, Vice President Engineering

ACKNOWLEDGEMENTS

The authors acknowledge the guidance and support provided by the Jet Propulsion Laboratory (JPL) technical monitor Dr. James Hendrickson. The magnetostrictive active members developed under this project were based on Dr. Gun-Shing Chen's earlier active member development at JPL. We thank him for the use of his design and assistance in modifying it for this program. Angel Garnica and Chris Miller of JPL were instrumental in the active member testing we did at JPL. We thank them for taking time, at short notice, from their busy schedules. A number of JPL staff, including Dr. James Fanson, Dr. Ron Ross, Jeff Umland, Dr. Ben Wada, and Dr. Mark Webster provided us their insights into the active member requirements and state-of-the-art. This research certainly benefitted from their inputs.

As usual, Mel Goodfriend of Edge Technologies was extremely helpful. We particularly thank him for hunting down the elusive cryogenic Terfenol-D data. Dr. Joe Teter of the Naval Surface Weapons Center provided useful advice regarding cryogenic magnetostrictive material selection. We would like to acknowledge the Material Preparation Center of the Ames Laboratory at Iowa State University for their timely production of the Terbium-Dysprosium magnetostrictive crystal.

This research was funded under a Phase II small business innovative research (SBIR) contract, No NAS7-1151, which was issued by the NASA Resident Office at JPL. Under this research program, we have both furthered the development of active members for space structures and furthered the development of SatCon's magnetostrictive design and analysis tools. These improved tools have already proved useful in our efforts to commercialize high-precision magnetostrictive actuators. We gratefully acknowledge the importance of this NASA-JPL funded effort to our future success at SatCon.

Summary

The goal of this Phase II Small Business Innovative Research (SBIR) project was to determine the technical feasibility of developing magnetostrictive active members for use as truss elements in space structures. Active members control elastic vibrations of truss-based space structures and integrate the functions of truss structure element, actively controlled actuator, and sensor. The active members must control structural motion to the sub-micron level, and for many proposed space applications, work at cryogenic temperatures. State-of-the-art active truss members using piezoelectric and electrostrictive materials are capable of producing high accuracy position control actuators but have some disadvantages for space structure applications. They have high voltage requirements of up to 1000 volts and poor performance at cryogenic temperatures.

Recently developed "giant" magnetostrictive materials change shape (strain) in the presence of magnetic fields by up to 2000 μ -strain (ppm) at room temperatures, which is twice the strain available in the best piezoelectric or electrostrictive materials. In magnetostrictive materials, these large strains do not require the use of high voltages. Additionally, in contrast to piezoelectric and electrostrictive materials, magnetostrictive materials perform better at cryogenic temperatures with strain capabilities of over 5000 μ -strain. Hyperconductors or superconductors can be used in the electrical coil at these temperatures and will significantly reduce or eliminate DC power consumption.

Our approach was to design, fabricate and test both room temperature and cryogenic temperature magnetostrictive active members. These mechanical design of active members were based on precision active members previously developed and tested by the Jet Propulsion Laboratory (JPL). The design goal for the magnetostrictive active members was to meet, or exceed when possible, the actuator specifications used in the JPL precision active member design while maintaining geometrical compatibility with their design. The design of the magnetostrictive active member and prediction of its performance required the development of nonlinear dynamic models of the magnetostrictive material, associated drive magnetics, and structural elements, which together constitute a magnetostrictive active member. The dynamic model, was used iteratively to arrive at a magnetostrictive actuator design that maximized the displacement and force capabilities while satisfying the geometrical constraints imposed by the existing design.

A layout of the resulting design is shown in Figure 1 and a photograph in Figure 2. The design features flexures that shunt moments applied to the active member through the outer case, shielding the magnetostrictive actuator from potentially damaging tensile stresses. An adjustable preload system is used to provide a bias compressive stress to the magnetostrictive actuator. The active member incorporates both displacement and flux sensors. A differential-pair of low-noise inductive sensors is used to provide high-resolution displacement measurements. A low-profile Hall-effect sensor is used to provide a measurement of magnetic flux in the actuator. The magnetostrictive actuator uses permanent magnets to provide a bias magnetizing field to the Terfenol-D^{®1} magnetostrictive material. The resulting magnetostrictive active member produces similar stroke and higher clamped force and stiffness than the previously developed electrostrictive and piezoelectric active members at the cost of high mass. A summary of its performance is given in Table 1.

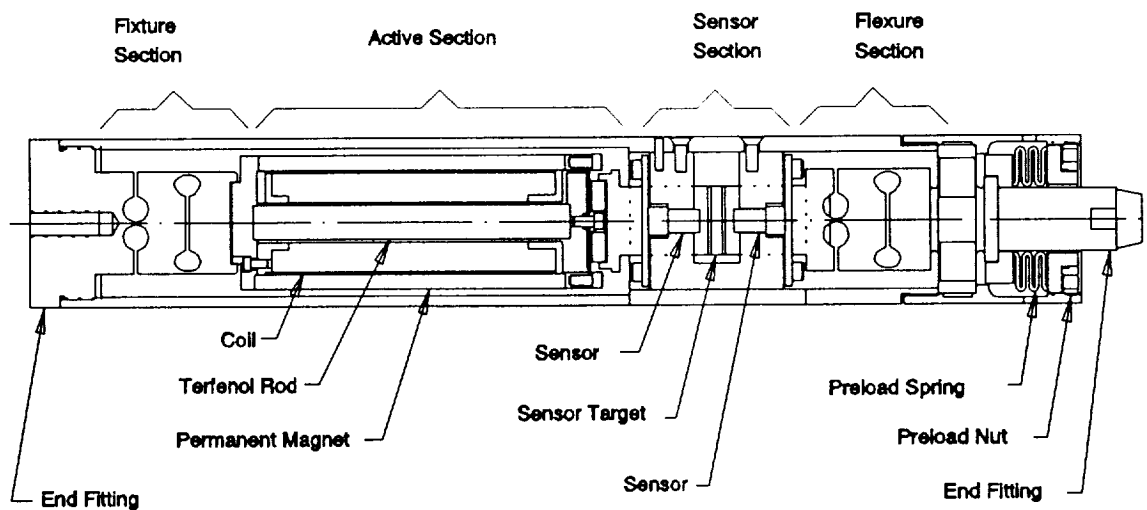


Figure 1. SatCon - NASA JPL magnetostrictive active member.

¹ ETREMA Terfenol-D[®] is commercially produced by Edge Technologies, Inc. under license through Iowa State University and the United States Navy



Figure 2. Room temperature active member.

Table 1. Room temperature Terfenol-D results analysis

	Nominal (± 2 Amps)	Maximum (± 4 Amps)
Free Stroke (microns)	50	65
Free Strain (microstrain)	800	1150
Clamped Force (N)		
Predicted	1000	1500
Extrapolated from "clamped" data	≈ 650	
Clamped Stress (MPa)	17	24
Actuator Stiffness (MN/m)		
Predicted (Material)	28 - 48	
Measured ²	> 10	
Material Modulus (GPa)	23 - 40	
Resistance (Ohms)	2.3	
Inductance (milliHenries)	5 - 10	
Break Frequency (Hz)	55 - 90 Hz	
Coil # of Turns	800	
Power (peak - Watts)	9.2	37

The cryogenic active member used a similar mechanical design to the room temperature design, but slightly modified for cryogenic operation. Two different cryogenic magnetostrictive actuators were fabricated and integrated into the active member. One used cryogenic temperature Terfenol-D, which has a slightly modified chemical composition from the room temperature Terfenol-D. The modified chemical composition provides better performance at the liquid nitrogen temperature used in the

²Not very accurately.

active member than the "room temperature" Terfenol-D composition. As shown in Table 2, the cryogenic temperature active member produced higher strains than the room temperature active member at low power. The other cryogenic temperature active member used a Terbium-Dysprosium crystal as its active element. This material produces exceptionally large strains of up to 0.5 percent with low hysteresis. Its disadvantage is its relatively low compressive strength. A summary of its performance is presented in Table 3. These active members are the first cryogenic active members to be developed and include a specially designed dewar that allows testing of these active members in space structure testbeds.

Table 2 Cryogenic Terfenol-D results analysis.

	Nominal (± 2 Amps)	Maximum (± 4 Amps)
Free Stroke (microns)	42	95
Free Strain (microstrain)	750	1650
Clamped Force (Newtons)	540	770
Clamped Stress (MPa)	17	24
Stiffness (MN/m)	18-42	
Material Modulus (GPa)	33 - 77	
Resistance (Ohms)	1.05	
Inductance (milliHenries)	4 - 5	
Break Frequency (Hz)	35 - 45 Hz	
Coil # of Turns	1200	
Power (peak - Watts)	4.2	17

Table 3. Cryogenic TbDy results analysis.

	Nominal (± 1.5 Amps)	Maximum (± 4 Amps)
Free Stroke (microns)	105	120
Free Strain (microstrain)	3500	4000
Clamped Force ³ (Newtons)	750	750
Clamped Stress (MPa)	25	25
Stiffness (MN/m)	14 - 20	
Material Modulus (GPa)	14 - 20	
Resistance (Ohms)	1.05	
Inductance (milliHenries)	12 - 23	
Break Frequency (Hz)	7.3 - 14	
Coil # of Turns	1200	
Power (peak - Watts)	4.2	17

Besides the hardware development of the magnetostrictive active members, this program also allowed the further development of SatCon magnetostrictive actuator design and analysis tools. In this program, emphasis was placed on developing better models of magnetostrictive material hysteresis in addition to understanding the properties of cryogenic magnetostrictive materials.

The development of actively controlled structures is an enabling technology for numerous planned space missions. Magnetostrictive materials used in active members are a promising means of actively controlling these space structures. At the cryogenic temperatures required of the many proposed infrared optical missions, the performance advantage of magnetostrictive active members is even greater than at room temperature. Additionally, this research has application to magnetostrictive based designs that are being developed for active vibration isolation actuators; for high-performance acoustic, flux, and stress transducers; and for innovative linear motors and positioners.

³Clamped force and stress limited by material strength ≈ 25 MPa.

PHASE II PROPOSAL SUMMARY

The goal of this Phase II SBIR project is to experimentally demonstrate the technical feasibility of using magnetostrictive materials as actuators in actively controlled truss members for space structures. The Phase I research developed a room temperature magnetostrictive design based on the recently developed "giant" magnetostrictive material Terfenol-D. The magnetostrictive design is predicted to produce more free strain and approximately twice the clamped force than existing electrostrictive and piezoelectric designs. In contrast to piezoelectric and electrostrictive materials, magnetostrictive materials do not require high voltages to operate efficiently and perform well at the cryogenic temperatures required of many proposed space applications.

The first objective of the proposed Phase II research is to construct and test the room temperature magnetostrictive design for the JPL precision active member. This will provide direct experimental comparison of a magnetostrictive active member with existing piezoelectric and electrostrictive designs and will further validate the analytical models developed under Phase I. The second objective is to investigate the design options and demonstrate the use of magnetostrictive materials as actively controlled actuators at cryogenic temperatures. A cryogenic temperature magnetostrictive actuator and testbed will be designed and constructed that will allow full characterization of its force and displacement performance as well as its magnetic and thermal characteristics.

POTENTIAL COMMERCIAL APPLICATION OF THE RESEARCH

This research has application to magnetostrictive based designs that are being developed for active vibration isolation actuators, as high-performance acoustic, flux, and stress transducers, and as innovative linear motors and positioners.

TABLE OF CONTENTS

SUMMARY	iii
1. INTRODUCTION	1-1
1.1 Project Objectives	1-1
1.2 Report Outline	1-1
1.3 Introduction to Magnetostrictive Actuators	1-3
1.4 Overview of JPL's Piezoelectric and Electrostrictive Active Members ..	1-8
1.5 Phase I Active Member Design	1-9
2. PHYSICS OF MAGNETOSTRICTIVE MATERIALS	2-1
2.1 General Theory of Magnetostriction	2-1
2.2 Development of Practical "Giant" Strain Magnetostrictive Materials ..	2-4
2.3 Magnetostriction at Cryogenic Temperatures	2-5
2.4 Hysteresis in Magnetostrictive Materials	2-8
3. MODELLING MAGNETOSTRICTIVE ACTUATORS	3-1
3.1 Magnetic Circuit Model	3-1
3.2 Anhysteretic B(H) and Hysteresis	3-5
3.3 Room Temperature Terfenol-D	3-15
3.4 Cryogenic Terfenol-D	3-16
3.5 Terbium-Dysprosium	3-17
3.6 Operation at Zero Stress	3-18
3.7 Linear High Frequency Model	3-19
3.8 Power Dissipation	3-25
3.9. Passive Damper	3-27
4. ROOM TEMPERATURE ACTIVE MEMBER	4-1
4.1 Room Temperature Active Member Design	4-1
4.2 Assembly of Room Temperature Active Member	4-15
4.3 Test Results	4-22
4.4 Room Temperature Active Member Results Analysis	4-63

5. CRYOGENIC TEMPERATURE ACTIVE MEMBER	5-1
5.1 Cryogenic Temperature Active Member Design	5-2
5.2 Assembly of the Cryogenic Temperature Active Member	5-17
5.3 Cryogenic Temperature Test Results	5-18
5.4 Cryogenic Temperature Results Analysis	5-53
6. CONCLUSIONS AND RECOMMENDATIONS	6-1
6.1 Summary of Results	6-1
6.2 Recommendations for Future Research	6-8
APPENDIX A - Room Temperature Active Member Drawing Package	A-1
APPENDIX B - Cryogenic Active Member Drawing Package	B-1
APPENDIX C - Room Temperature Active Member Operating Instructions	C-1

LIST OF TABLES

Table 1. Room temperature Terfenol-D results analysis	vi
Table 2. Cryogenic Terfenol-D results analysis	vii
Table 3. Cryogenic TbDy results analysis	viii
Table 1-1. Summary of Active Member Design Requirements.	1-12
Table 2-1. Temperature dependence of Ratio parameter (x).	2-6
Table 4-1 Dependence of maximum strain and maximum clamped force on radius of TbDy	4-6
Table 4-2 Preload Forces and Stresses	4-30
Table 4-3. Predicted and observed dependence of strain on current and stress, for room temperature actuator	4-64
Table 5-1 Dependence of maximum strain and maximum clamped force on radius of TbDy	5-9
Table 5-2. Cryogenic Terfenol-D preload forces and stresses	5-19
Table 5-3 TbDy preload forces and stresses	5-37
Table 5-4. Predicted and observed dependence of strain on current for the cryogenic Terfenol-D actuator.	5-55
Table 5-5. Comparison of predicted strain at 13.2 MPa with measured strain at nominal stress of 20 MPa, with and without a spacer.	5-60
Table 5-6. Comparison of predicted strain at 7.4 MPa with measured strain at nominal stress of 12.5 MPa, with a spacer.	5-61
Table 6-1 Room temperature Terfenol-D performance	6-3
Table 6-2 Cryogenic Terfenol-D performance	6-4
Table 6-3 Cryogenic TbDy performance	6-5
Table 6-4 Comparison of active members	6-6

LIST OF FIGURES

Figure 1. SatCon - NASA JPL magnetostrictive active member	iv
Figure 2. Room temperature active member	v
Figure 1-1. Terfenol magnetostriction.	1-5
Figure 1-2. Typical permanent magnet biased Terfenol actuator configuration.	1-6
Figure 1-3. Magnetic field lines: performance magnet bias flux only.	1-7
Figure 1-4. Magnetic field lines: permanent magnet and control coil flux.	1-8
Figure 1-5. Drawing of the JPL active member.	1-10
Figure 1-6. JPL actuator motor interface drawing.	1-11
Figure 2-1. Anisotropy as a function of temperature for Tb_xDy_{1-x}	2-7
Figure 2-2. Orientation of easy [111] axes with respect to the rod axis, in grain-aligned Terfenol-D.	2-9
Figure 3-1. Magnetic circuit for magnetostrictive actuator.	3-1
Figure 3-2. Magnetostrictive strain ϵ as a function of B for standard composition Terfenol-D at room temperature, for cryogenic composition Terfenol-D at 77° K, and for TbDy at 77° K.	3-5
Figure 3-3. Hysteresis loops for λ vs. H at various values of constant σ , for standard composition Terfenol-D at room temperature, from Fig. 3 in Moffett et al., J. Acoust. Soc. Am. 89, 1448-1455 (1991).	3-10
Figure 3-4. Anhysteretic stress σ vs. strain λ at various values of H, for standard composition Terfenol-D at room temperature, based on the data given in Fig. 4 of Ref. 3.	3-11
Figure 3-5. Magnetostrictive strain λ vs. H for various values of stress, for TbDy at 77° K, from Fig. 2 of Spano et al., IEEE Trans. MAG <u>26</u> , 1751 (1990).	3-13
Figure 3-6. Stress vs. strain at various values of H for TbDy at 77° K.	3-14
Figure 3-7. Anhysteretic stress vs. strain at various values of H for cryogenic Terfenol-D at 77° K.	3-15
Figure 4-1 Room temperature design tradeoffs; clamped force and maximum strain vs. Terfenol-D radius.	4-3
Figure 4-2. Magnetic finite element mesh.	4-9

Figure 4-3. Magnetic equipotential lines with no excitation current.	4-9
Figure 4-4. Magnetic equipotential lines with no permanent magnet, coil excited. . .	4-10
Figure 4-5. Magnetic equipotential lines with permanent magnet and coil induced field	4-10
Figure 4-6. Final assembly drawing of the room temperature active strut.	4-11
Figure 4-7. KDM-2700D sensor specification.	4-14
Figure 4-8 Drawing of sensor 15N-004 for use with the KDM-7200D systems.	4-15
Figure 4-9. Photograph of unassembled room temperature active member.	4-16
Figure 4-10. Photograph of room temperature magnetostrictive actuator being assembled.	4-18
Figure 4-11. Photograph of room temperature magnetostrictive actuator assembled.	4-19
Figure 4-12. Photograph of room temperature active member assembled.	4-21
Figure 4-13. Laser interferometer test results.	4-23
Figure 4-14. Exponential fit to displacement data.	4-25
Figure 4-15. Displacement versus time at constant excitation.	4-26
Figure 4-16. Active member testbed layout.	4-28
Figure 4-17. Time history of current (12.5 MPa preload free end conditions).	4-32
Figure 4-18. Time history of flux field (12.5 MPa preload, free end conditions). . .	4-32
Figure 4-19. Time history of flux field before assembly (12.5 MPa preload, free end conditions).	4-33
Figure 4-20. Time history of displacement (12.5 MPa preload, free end conditions).	4-33
Figure 4-21. Time history of voltage (12.5 MPa preload, free end conditions).	4-34
Figure 4-22. Displacement vs. current (12.5 MPa preload, free end conditions). . .	4-34
Figure 4-23. Displacement vs. current (12.5 MPa preload, free end conditions). . .	4-35
Figure 4-24. Displacement vs. current (12.5 MPa preload, raw data).	4-36
Figure 4-25. Displacement vs. current (12.5 MPa preload, cleaned data).	4-36
Figure 4-26. Free strain vs. current (12.5 MPa preload, cleaned data).	4-37
Figure 4-27. Displacement vs. current (2 amps, raw data).	4-38
Figure 4-28. Displacement vs. current (2 amps, cleaned data).	4-38
Figure 4-29. Free strain vs. current (2 amps, cleaned data).	4-39
Figure 4-30. Current to displacement frequency response for 1 amp RMS excitation (12.5 MPa preload).	4-40

Figure 4-31. Comparison of the current to displacement frequency response for 0.1, 0.5, and 1.0 amps RMS excitation (12.5 MPa preload).	4-41
Figure 4-32. Comparison of the displacement versus current slopes for random and sinusoidal time history data.	4-42
Figure 4-33. Current to displacement frequency response for swept-sine excitation.	4-43
Figure 4-34. Comparison of random and swept-sine excitation (1 amp rms).	4-44
Figure 4-35. Current to displacement frequency response for 1 amp RMS excitation (12.5 MPa preload).	4-46
Figure 4-36. Voltage to current frequency response for random excitation (12.5 MPa preload, 0 A current bias).	4-47
Figure 4-37. Actuator displacement for free and partially clamped boundary conditions.	4-49
Figure 4-38. Testbed stiffness.	4-49
Figure 4-39. Time history of current (12.5 MPa preload; partially clamped end conditions).	4-50
Figure 4-40. Time history of displacement (12.5 MPa preload, partially clamped end conditions).	4-51
Figure 4-41. Time history of force (12.5 MPa preload, partially clamped end conditions).	4-51
Figure 4-42. Force vs. current (12.5 MPa preload, partially clamped end conditions).	4-52
Figure 4-43. Displacement vs. current (12.5 MPa preload, partially clamped end conditions).	4-53
Figure 4-44. Force vs. current (12.5 MPa preload, raw data).	4-54
Figure 4-45. Displacement vs. current (12.5 MPa preload, raw data).	4-54
Figure 4-46. Force vs. current (2 amps, raw data).	4-55
Figure 4-47. Displacement vs. current (2 amps, raw data).	4-56
Figure 4-48. Displacement vs. current (2 amps, cleaned data).	4-56
Figure 4-49. Frequency response from drive current to force (10 to 500 Hz).	4-58
Figure 4-50. Frequency response from drive current to force (10 to 5000 Hz).	4-59
Figure 4-51. Frequency response from drive current to actuator displacement (5 to 500 Hz).	4-61
Figure 4-52. Frequency response from drive current to actuator displacement (10 to 5000 Hz).	4-62

Figure 5-1. Assembly drawing of the cryogenic temperature active strut.	5-11
Figure 5-2. Drawing showing the adapters for the smaller terbium-dysprosium rod.	5-12
Figure 5-3. Fabricated cryostat with active member installed.	5-15
Figure 5-4. Time history of current (cryogenic Terfenol-D, 20.6 MPa)	5-20
Figure 5-5. Time history of flux field (cryogenic Terfenol-D, 20.6 MPa)	5-21
Figure 5-6. Time history of displacement (cryogenic Terfenol-D, 20.6 MPa)	5-21
Figure 5-7. Time history of voltage (cryogenic Terfenol-D, 20.6 MPa)	5-22
Figure 5-8. Strain vs. current (cryogenic Terfenol-D, 20.6 MPa)	5-23
Figure 5-9. Strain vs. current (cryogenic Terfenol-D, 13.7 MPa)	5-23
Figure 5-10. Displacement vs. current (cryogenic Terfenol-D, 20.6 MPa)	5-24
Figure 5-11. Displacement vs. current (cryogenic Terfenol-D, 13.7 MPa)	5-25
Figure 5-12. Strain vs. current (cryogenic Terfenol-D, 20.6 MPa)	5-25
Figure 5-13. Strain vs. current (cryogenic Terfenol-D, 13.7 MPa)	5-26
Figure 5-14. Flux sensor output vs. current (cryogenic Terfenol-D, 20.6 MPa) . . .	5-26
Figure 5-15. Strain vs. flux sensor output (cryogenic Terfenol-D, 20.6 MPa)	5-27
Figure 5-16. Displacement vs. current (cryogenic Terfenol-D, 2 amps, raw data) .	5-28
Figure 5-17. Displacement vs. current (cryogenic Terfenol-D, 2 amps, cleaned data)	5-29
Figure 5-18. Strain vs. current (cryogenic Terfenol-D, 2 amps, cleaned data)	5-29
Figure 5-19. Voltage to current frequency response for 0.1 amp peak excitation (20.6 MPa)	5-30
Figure 5-20. Comparison of the voltage to current frequency response at 1 amp P excitation, for 0 and 2 amp bias (20.6 MPa)	5-31
Figure 5-21. Comparison of the voltage to current frequency response at 1 amp P excitation, for the various preloads (cryogenic Terfenol-D, 0 bias)	5-32
Figure 5-22. Current to displacement frequency response for 0.1 amp P and 1.0 amp P excitation at 0 amp bias (cryogenic Terfenol-D, 20.6 MPa)	5-33
Figure 5-23. Current to flux sensor output frequency response for 0.1 amp P and 1.0 amp P excitation at 0 amp bias (cryogenic Terfenol-D, 20.6 MPa)	5-35
Figure 5-24. Flux sensor output to displacement frequency response for 0.1 amp P and 1.0 amp P excitation at 0 amp bias (cryogenic Terfenol-D, 20.6 MPa) .	5-36
Figure 5-25. Time history of current (TbDy, 20 MPa, no spacer)	5-38
Figure 5-26. Time history of flux sensor output (TbDy, 20 MPa, 110 spacer)	5-39
Figure 5-27. Time history of displacement (TbDy, 20 MPa, no spacer)	5-39

Figure 5-28. Displacement vs. current (TbDy, 20 MPa, no spacer)	5-40
Figure 5-29. Strain vs. displacement (TbDy, 20 MPa, no spacer)	5-41
Figure 5-30. Strain vs. current (TbDy, 20 MPa, 1 spacer)	5-42
Figure 5-31. Strain vs. current (TbDy, 20 MPa, spacer)	5-42
Figure 5-32. Strain vs current (TbDy, 20 MPa, no spacer)	5-43
Figure 5-33. Flux sensor output vs. current (TbDy, 20 MPa, no spacer)	5-44
Figure 5-34. Strain vs. flux sensor output (TbDy, 20 MPa, no spacer)	5-44
Figure 5-35. Voltage to current frequency response for 1 Amp P excitation, comparing various bias levels (TbDy, 20 MPa, no spacer)	5-45
Figure 5-36. Voltage to current frequency response for 100 mAmp P excitation for various preloads at -2 Amp bias (TbDy)	5-46
Figure 5-37. Current to displacement frequency response for 100 mAmp P excitation with 0 bias (TbDy, 20 MPa, no spacer)	5-48
Figure 5-38. Current to flux sensor output frequency response for 100 mAmp P excitation with 0 bias (TbDy, 20 MPa, no spacer)	5-50
Figure 5-39. Flux sensor output to displacement frequency response for 100 mAmp P excitation with 0 bias (TbDy, 20 MPa, no spacer)	5-52

1. INTRODUCTION

1.1 Project Objectives

The goal of this Small Business Innovation Research (SBIR) project was to determine the technical feasibility of developing magnetostrictive active members for space structures applications. The previously completed Phase I research had three major goals. The first was to understand the physics of magnetostrictive materials and to identify those magnetostrictive materials properties that are drivers in the design of active truss members. The second was to design a magnetostrictive active member, similar to the existing Jet Propulsion Laboratory (JPL) piezoelectric and electrostrictive active members, and to compare the analytical prediction of its performance with the measured performance of the two existing JPL active members. The final objective was to analytically investigate the feasibility of using magnetostrictive materials for control actuation at cryogenic temperatures.

The goals of this Phase II research were similar to the Phase I goals, but with a hardware emphasis. The technical feasibility of developing active members using room temperature magnetostrictive actuators was to be demonstrated with by fabricating and testing the JPL PSR active member with a magnetostrictive actuator. Another goal proposed for the Phase II research was to demonstrate the use of magnetostrictive materials at cryogenic temperatures. During the Phase II program this goal was broadened to include the fabrication and test of a cryogenic magnetostrictive active member. During the program, two different cryogenic active members were tested. In addition to these hardware development goals, the Phase II research was also directed at improving our magnetostrictive actuator design tools, by extending them to new, cryogenic magnetostrictive materials, by investigating the use of magnetostrictive actuators in a passive damping configuration, and by incorporating better hysteresis models.

1.2 Report Outline

This report has six Chapters. Chapter 1 is the introduction, in which the scope of the project is defined and background material presented. The next section provides an overview of magnetostriction and presents a typical actuator design. An overview of the JPL precision active member design is then presented. The performance of these active members form the baseline performance goal for the magnetostrictive actuator. The last section of this chapter summarizes the active member design developed during Phase I.

Chapter 2 discusses the physics of magnetostriction, which yields models of material behavior. Additionally, this chapter provides insights into choosing magnetostrictive materials for specific actuator applications such as the JPL active member. The first section starts with a general presentation of magnetostriction and then focusses on the rare earth or giant magnetostrictive materials. Section 2.2 summarizes the historical development of Terfenol-D to help understand its physics. The issues associated with giant magnetostrictive materials used at cryogenic temperatures are then presented in Section 2.3. The important issue of hysteresis is discussed in Section 2.4.

In Chapter 3 electromechanical design tools for axial-stroke magnetostrictive actuators are developed. These start with the magnetic circuit model development in Section 3.1, and the anhysteretic and hysteretic magnetic material models in Section 3.2. The electromechanical behavior of the three magnetostrictive materials used in this program, Terfenol-D, cryogenic temperature Terfenol-D and Terbium-Dysprosium are modelled in Sections 3.3 through 3.5. Discussion of operation under special conditions are presented, at low stress in Section 3.6 and at high frequency in Section 3.7. Section 3.8 presents models of power dissipation. The chapter finishes with a section that analytically investigates the use of magnetostrictive actuators in a "passive damper" configuration. In this configuration, only passive electronic elements are connected to the active member. Because it does not require active electronics, this passive configuration maybe advantageous in many space structural control applications, at both room and cryogenic temperatures.

Chapter 4 presents the design, fabrication and test of the room temperature magnetostrictive active member. Mechanically, this design is based closely on the JPL PSR active member. This required some significant changes to the magnetostrictive actuator design, as compared to the design developed under the Phase I project. Section 4.1 discusses the design of the room temperature active member with the magnetostrictive actuator design presented in Section 4.1.1, the mechanical design presented in Section 4.1.2, and the sensor selection in Section 4.1.3. Section 4.2 discusses assembly of the actuator. Section 4.3 presents highlights of the test results from the room temperature active member. These results are analyzed, in particular compared with the predicted performance, in Section 4.4.

Chapter 5 presents the design, fabrication, and test of the cryogenic temperature actuators. Two cryogenic actuators were fabricated and tested, one with cryogenic temperature Terfenol-D and the other with TbDy. Sections 5.1.1 presents the

electromagnetic design of both cryogenic actuators. Section 5.1.2 discusses the mechanical design, primarily the differences in the room temperature design that were required for cryogenic operation. Section 5.1.3 discusses the cryogenic sensors and Section 5.1.4 presents the design of the active member dewar. Section 5.2 presents the assembly of these two actuators. The test results and analysis of the cryogenic active members are presented in Section 5.3 and 5.4 respectively.

Chapter 6 contains the conclusion and proposes directions for future development.

Appendices A and B contain the room temperature and cryogenic temperature drawing packages respectively. Appendix C contains one page operation instructions for the room temperature strut.

1.3 Introduction to Magnetostrictive Actuators

Magnetostriction describes the property of materials that causes them to change shape (strain) when in the presence of a magnetic field. The magnetostrictive effect was first discovered in nickel by James Joule in 1840. These strains are limited to approximately 50 parts per million (ppm) or a strain of 50 μm in a one meter rod. Cobalt, iron and alloys were later found to exhibit the same low levels of magnetostriction.¹

Scientists at the Ames Laboratory discovered that the rare earth element² terbium exhibited much larger magnetostrictive strains, greater than 1000 ppm. This element exhibits these "giant" magnetostrictive strains, however, only at cryogenic temperatures and requires very large magnetizing fields. Dr. Clark and fellow researchers at the Naval Surface Weapons Center combined the highly magnetostrictive lanthanides terbium and dysprosium with magnetic transition metals such as nickel, cobalt, and iron. They were able to develop materials such as terbium-iron (TbFe_2) that exhibit these giant magnetostrictive strains at room temperatures. Terbium-iron or Terfenol³, however, still requires a large

¹Butler, J.L.; Application Manual for the Design of ETREMA Terfenol-D™ Magnetostrictive Transducers; Edge Technologies, Inc., Ames, Iowa; 1988.

² The so called "rare" earth materials are not rare in nature. They are part of the fifteen element lanthanide series in the periodic table. As a group, they are more abundant in nature than nickel or copper [Butler 1988].

³ The name Terfenol is formed from the elements of the alloy and the original name of the Navy Laboratory where development was done. The Ter is from terbium, fe from iron, and nol from Naval Ordnance Laboratory (now the Naval Surface Weapons Center).

magnetizing field to produce giant magnetostrictive strains. Further studies conducted in collaboration with Dale McMasters of the Ames Laboratory yielded the alloy family $Tb_xDy_{1-x}Fe_2$ (Terfenol-D)⁴ that produce giant magnetostrictive strains without the requirement of large magnetizing fields⁵.

These "giant" magnetostrictive materials, based on alloys of iron and "rare" earth elements, are currently being investigated for use in a number of transducers, motors, and actuators⁶. These include active vibration isolation⁷ and active control of space structures⁸. The increased level of magnetostrictive actuator research and development is made possible by the commercial availability of room temperature, high performance magnetostrictive materials such as ETREMA Terfenol-D®⁹. ETREMA Terfenol-D® is commercially produced by Edge Technologies, Inc. under license through Iowa State University and the United States Navy. For typical room temperature applications, Terfenol-D actuators use these materials with stoichiometry $Tb_{0.3}Dy_{0.7}Fe_{1.95}$ directionally solidified into a near single crystal by a variety of techniques¹⁰.

The important magnetostrictive properties of Terfenol-D can be seen in Figure 1-1. Shown are curves of magnetostriction, measured in parts per million, versus applied

⁴ The name Terfenol-D is formed from the name Terfenol, as explained earlier, with the -D indicating the addition of dysprosium.

⁵Butler, J.L.; Application Manual for the Design of ETREMA Terfenol-D™ Magnetostrictive Transducers; Edge Technologies, Inc., Ames, Iowa; 1988.

⁶Applications List: Edge Technologies, Inc., Ames, Iowa; 1989.

⁷Hiller, M.W., Bryant, M.D., and Umegaki, J., "Attenuation and Transformation of Vibration through Active Control of Magnetostrictive Terfenol," *Journal of Sound and Vibration*, 133(3), Paper 346/1, 1989.

⁸Anastas, G., Eisenhaure, D., Hockney, R., Johnson, B.; Distributed Magnetic Actuators for Fine Shape Control; SatCon Technology Corporation, Cambridge, MA; R01-88; April 1988.

⁹ ETREMA Terfenol-D is an Edge Technology trademark. ETREMA is the acronym for Edge Technology Rare Earth Magnetostrictive Alloy.

¹⁰McMasters, D.; Manufacturing/Processing, Performance Characteristics, Commercial Availability and Ten Year Price Estimates of Highly Magnetostrictive Transducer Drive Elements; Proceedings of Second International Conference on Giant Magnetostrictive and Amorphous Alloys for Sensors and Actuators, Paper #5, Marbella, Spain; Oct. 12-14, 1988.

magnetizing field H , measured in oersteds, for various compressive stress levels in the material. The magnetostriction in Terfenol-D causes the material to increase in length when the magnetizing field is applied parallel to the material drive axis. As can be seen, strains of over one part in a thousand are possible. Another important property is that magnetostrictive performance improves dramatically if the material is under compressive stress. As can be seen by the symmetry of the curves, the magnetostrictive strain depends only on the magnitude of the applied magnetizing field, not its sign. For actuator applications, such as active space structure members, the material is usually magnetically biased, typically with permanent magnets. This has a number of desirable effects. The first is that the actuator becomes bidirectional about the bias strain. The linearity and gain are also improved.

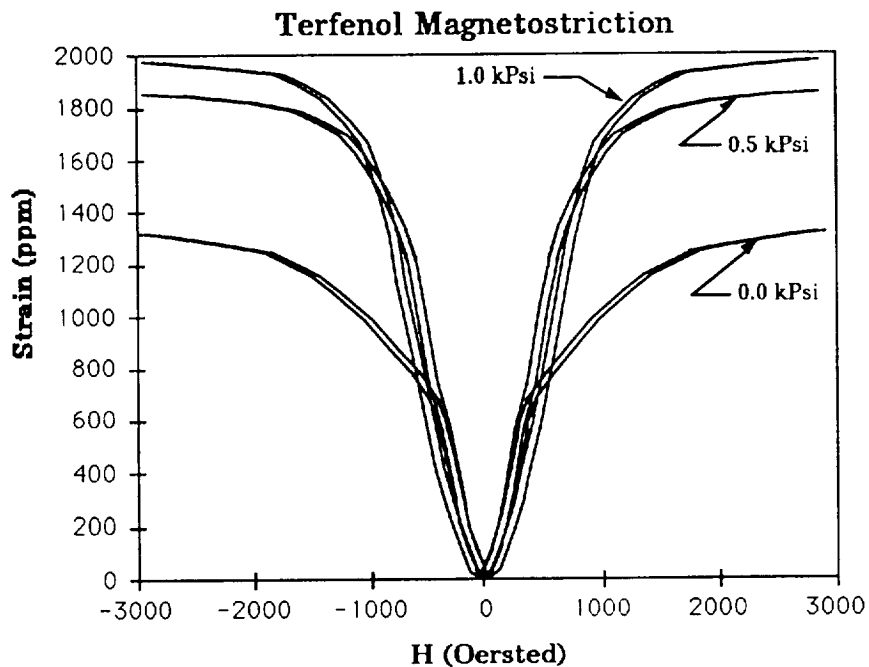


Figure 1-1. Terfenol magnetostriction.

A typical actuator design is shown in Figure 1-2. The axially symmetric design features a Terfenol-D rod running down the center. The bias magnetic field is supplied by the cylindrical permanent magnet, which is axially magnetized. The flux from these permanent magnetics is directed through the Terfenol-D rod by pole pieces made of

magnetic steels. Surrounding the rod is the coil, which provides the magnetizing field used to actively control the magnetostrictive strain. The Terfenol-D rod is normally placed under axially compressive stress by mechanical preloading. The mechanism for this preloading varies for different actuator designs and is not shown in Figure 1-2.

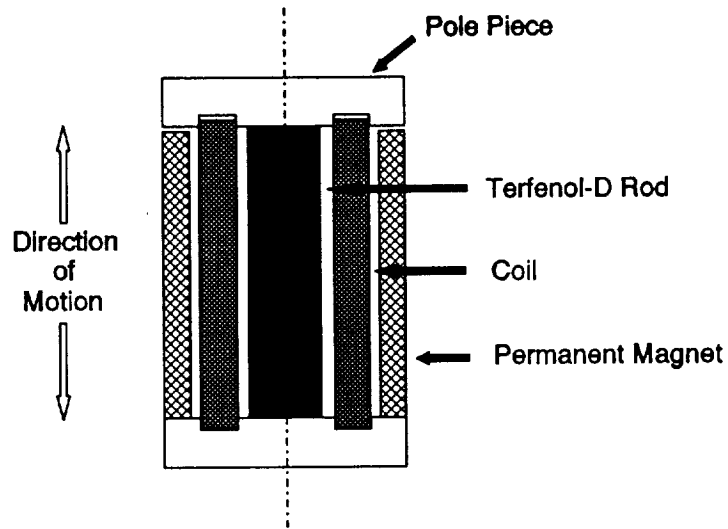


Figure 1-2. Typical permanent magnet biased Terfenol actuator configuration.

The magnetic field lines for this actuator configuration are shown in Figure 1-3, as calculated by a magnetic finite element program. The axial half-plane plot shows lines of constant magnetic potential (magnetic field lines) for the axisymmetric magnetic field. Areas of high flux density are indicated by closely-spaced magnetic field lines. The left side of the plot is the axial centerline of the actuator. Five magnetic components are shown. Working out from the center are the Terfenol-D rod, the cylindrical coil, and the cylindrical permanent magnet. Two steel end caps are used for flux shaping. Figure 1-3 shows the bias magnetic field lines that are produced when the control coil is not excited. Figure 1-4 shows the magnetic field produced when the control current is excited such that its field adds to the bias permanent magnetic field. Note that the magnetic field strength in the Terfenol-D, as indicated by the spacing of the magnetic field lines, is much higher if the coil is activated, causing the Terfenol-D rod to increase in length.

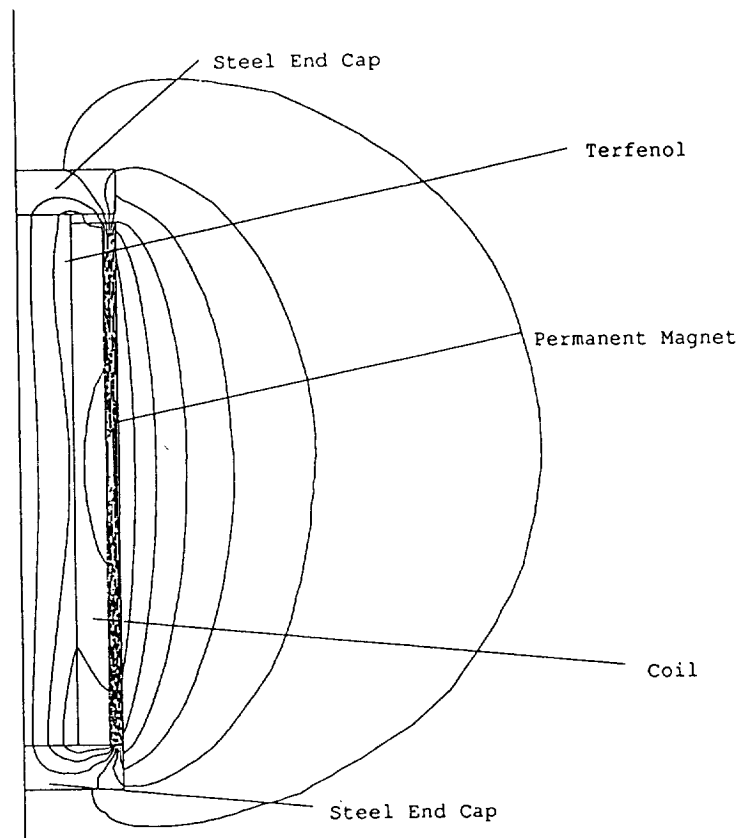


Figure 1-3. Magnetic field lines: performance magnet bias flux only.

This section gave a brief introduction to magnetostrictive materials and how they can be used in actuator designs. As can be seen from this introductory presentation, a number of design issues, including bias magnetic field levels, magnetic field component configuration and geometry, permanent magnet material, mechanical preload level and mechanism, and magnetostrictive material characteristics, must be considered in the design of a magnetostrictive actuator. Chapters 2 and 3 of this report provide more detailed descriptions of the magnetostrictive material physics and electromagnetic modelling of magnetostrictive actuators. The specific designs of the magnetostrictive actuators used in the active members developed under this Phase II program can be found in Chapters 4 and 5 for the room temperature and cryogenic temperature designs respectively.

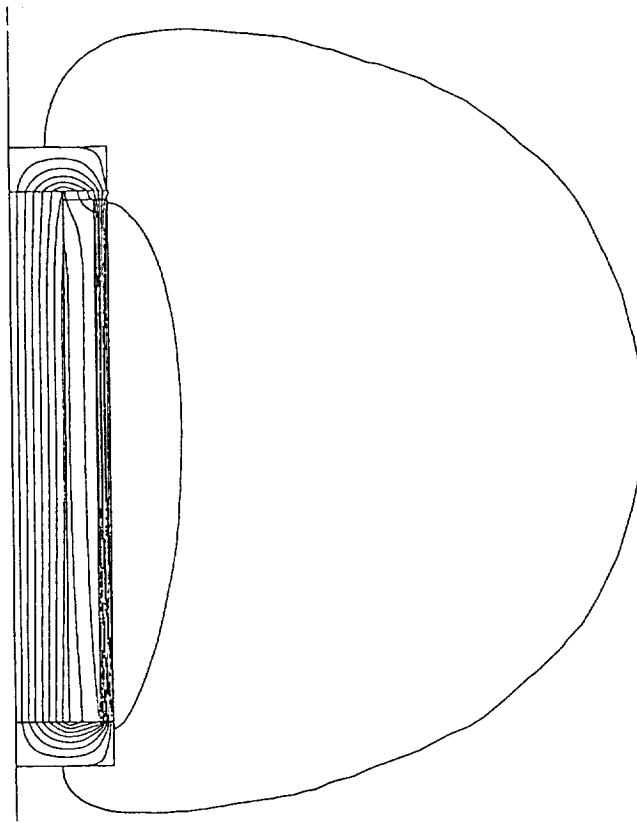


Figure 1-4. Magnetic field lines: permanent magnet and control coil flux.

1.4 Overview of JPL's Piezoelectric and Electrostrictive Active Members

Precision active structure technology is currently being developed by Jet Propulsion Laboratories and other researchers. The aim of the technology development is to produce high performance structures that utilizes a limited number of active members. The active members are needed to control elastic vibrations of space structure to the sub-micron level, as required by many optical and interferometric applications. In order to meet the necessary structural and control requirements of space science missions involving large precision structures, JPL developed a "straw-man" precision active member. This active member was designed as a "zero-stiction ... configuration providing absolute fidelity of commanded and measured motion". The design features interchangeable actuation elements and incorporates a built-in displacement sensor. To date, JPL has tested the active member with both piezoelectric and electrostrictive actuation elements, termed actuator motors by JPL¹¹.

¹¹Anderson, E.H., Moore, D.M., and Fanson, J.L., "Development of an Active Member Using Piezoelectric and Electrostrictive Actuation for Control of Precision Structures," 31st

displacement sensor. To date, JPL has tested the active member with both piezoelectric and electrostrictive actuation elements, termed actuator motors by JPL¹¹.

Given the major design requirements of (a) zero stiction, with absolute fidelity of commanded versus measured motion and (b) operation at typical mission temperatures in high earth orbit (100 K), JPL concluded that electrostrictive actuation shows significant advantages over the more commonly used piezoceramics. Unfortunately, both forms of actuation are severely reduced at the required high earth orbit temperatures (100 K). The study also recommended the testing of magnetostrictive actuators. These are seen as an attractive alternative to piezoelectric or electrostrictive since (a) it is possible to provide the bias field with a permanent magnet, eliminating the need for high voltage bias fields used in piezoelectric and electrostrictive actuators, and (b) magnetostrictive materials exist that have excellent low temperature characteristics.

One of the objectives of this Phase II research was to fabricate and test a magnetostrictive actuator design for the JPL precision active member. The design approach was to meet, or exceed when possible, the "strawman" specifications used in the JPL precision active member design while maintaining geometrical compatibility with their design. The other objective was to fabricate and test the use of magnetostrictive materials for control actuation at cryogenic temperatures, which was achieved by the fabrication and test of two different cryogenic active members. A number of future NASA mission will require actuators that work at cryogenic temperatures. These missions include the Large Deployable Reflector (LDR), the Space Infrared Telescope Facility (SIRTF), the Submillimeter Explorer (SE), and the Submillimeter and Infrared Line Survey (SMILS). As is explained in Chapter 2, the performance of magnetostrictive materials increases significantly at cryogenic temperatures. In addition to increased magnetostrictive material performance, the performance of a magnetostrictive actuator is improved at cryogenic temperatures because of better coil performance. At cryogenic temperatures, the coil resistance can be decreased either through the use of hyperconductors (high purity alloys) or superconductors. Unlike many actuator materials, therefore, magnetostrictive active members will perform better at cryogenic temperatures than room temperatures.

¹¹Anderson, E.H., Moore, D.M., and Fanson, J.L., "Development of an Active Member Using Piezoelectric and Electrostrictive Actuation for Control of Precision Structures," 31st Structural Dynamics and Materials Conference, Long Beach, CA, April 1990.

design is shown in Figure 1-5¹². As an active member, it combines the functions of truss structure, actively controlled actuator, and sensor. Its components, therefore perform a number of functions. The actuator motor produces axial displacement, which may be thought of as the output of the active member, as well as carrying the majority of the axial stress. The mechanical components shield the actuator motor from bending moments, which are carried by the outer shell. The mechanical components also provide mechanical preload to the actuator motor. The sensor subassembly, including the sensor and motion reference rod, provides a precision measurement of the length of the active member.

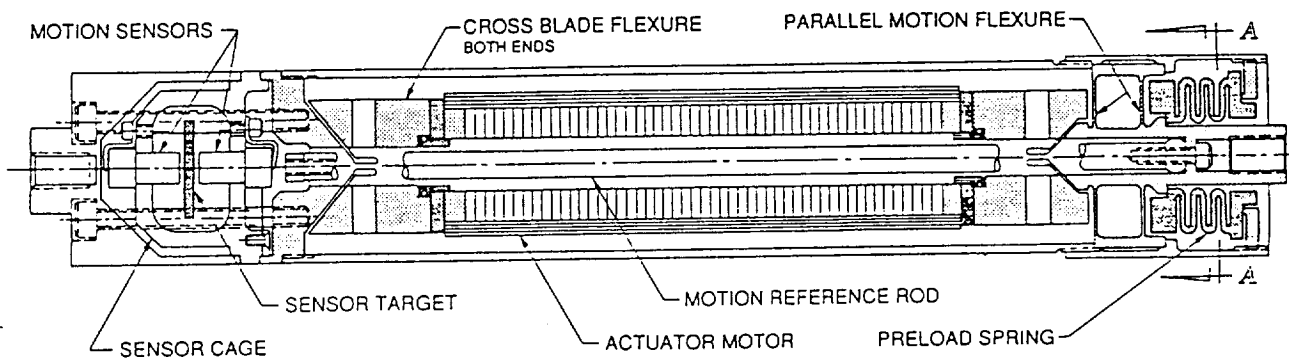


Figure 1-5. Drawing of the JPL active member.

The magnetostrictive design developed under the Phase I portion of this research project used this active member as a baseline. The same mechanical components are used to preload the magnetostrictive material and to shield it from bending moments. The sensor configuration for the magnetostrictive actuator, however, is a more recent JPL design that does not require the motion reference rod running through the center of the actuator motor section. The more recent, PSR design, did not have a cylindrical envelope for the actuator. For our room temperature magnetostrictive active member, which mechanically used the same design as the JPL PSR active member, this non-cylindrical actuator cross-section required the redesign during Phase II of the magnetostrictive actuator, because our Phase I design assumed a cylindrical cross-section was available. This is discussed in more detail in Section 4.1. The cryogenic temperature active member, however, was mechanically redesigned to allow use of the full cylindrical cross-section.

¹²*Ibid.*

Designing a comparable magnetostrictive actuator required the specification of both the allowable geometry of the actuator motor and its performance. The pertinent geometrical constraints on the actuator motor are shown in Figure 1-6, assuming a cylindrical cross-section was available. The cylindrical hole down the center of the actuator motor provides space for the motion reference rod. As mentioned earlier, the magnetostrictive design developed under this program assumed to use of a newer JPL sensor design that does not require the motion reference rod. This small cylindrical volume, therefore, is made available for the magnetostrictive actuator¹³.

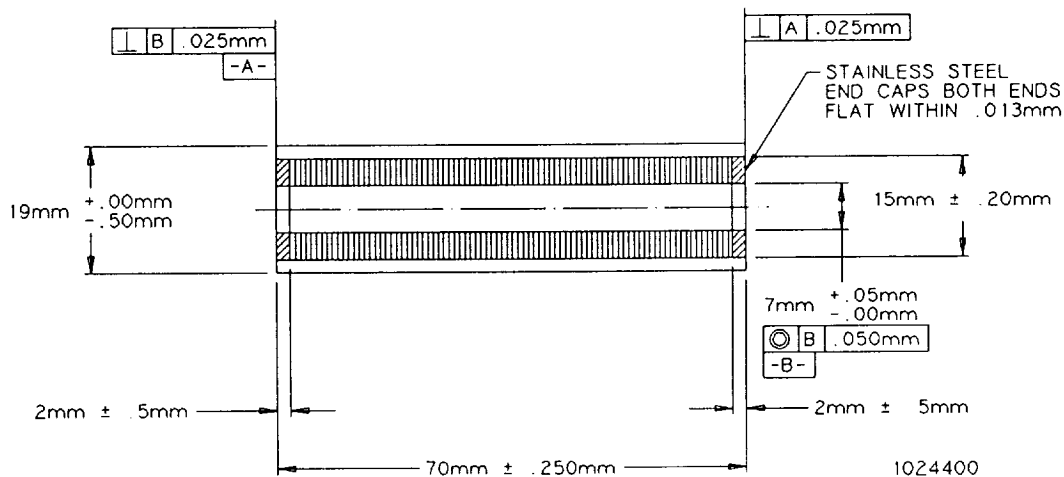


Figure 1-6. JPL actuator motor interface drawing.

The design requirements for the magnetostrictive motor are taken to be the same as the design requirements used in the JPL program. This design approach allows direct comparison of the analytically predicted performance of the magnetostrictive active member with the measured performance of the electrostrictive and piezoelectric active members. From¹⁴ and discussions with JPL personnel, the design requirements, specific to the actuation element, are summarized in Table 1-1.

¹³ The magnetostrictive design could accommodate this motion reference rod by simply using a Terfenol rod with a concentric axial hole, a common configuration for Terfenol. The performance of the magnetostrictive actuator would be slightly reduced due to the reduction in volume available.

¹⁴ Anderson, E.H., Moore, D.M., and Fanson, J.L., "Development of an Active Member Using Piezoelectric and Electrostrictive Actuation for Control of Precision Structures," 31st Structural Dynamics and Materials Conference, Long Beach, CA, April 1990.

Table 1-1. Summary of Active Member Design Requirements.

Requirement	Value
Active Member Length	< 200 mm
Actuation Element Length	< 70 mm
Active Member Nominal Diameter	25 mm
Clamped Force Capability	> 450 N
Unloaded Displacement Capability	> 25 μm
Stiction	Zero

2. PHYSICS OF MAGNETOSTRICTIVE MATERIALS

This chapter discusses the physics of magnetostriction, which yields models of material behavior. Additionally, this chapter provides insights into choosing magnetostrictive materials for specific actuator applications such as the JPL active member. The first section starts with a general presentation of magnetostriction and then focusses on the rare earth or giant magnetostrictive materials. Section 2.2 summarizes the historical development of Terfenol-D to help understand its physics. The issues associated with giant magnetostrictive materials used at cryogenic temperatures are then presented in Section 2.3. The important issue of hysteresis is discussed in Section 2.4.

2.1 General Theory of Magnetostriction

The magnetic exchange energy in ferromagnetic materials, which is lowest when the magnetic moments of all the atoms are in the same direction, is approximately nkT_c (typically 10^{10} ergs/cm³). In this expression for the magnetic exchange energy, n is the density of atoms, k is Boltzmann's constant and T_c is the Curie temperature. A small perturbation on the exchange energy is the magnetic anisotropy energy K , which is the variation in the exchange energy depending on how the magnetic moments of the atoms are oriented to the crystal axes. In the absence of an external magnetic field, the magnetization of a crystal will be aligned in a direction for which the anisotropy energy is at a local minimum; these directions are called easy axes. For crystals of macroscopic size, it is generally energetically favorable for the crystal to be divided into many domains in which the magnetization is in different easy directions because this lowers the demagnetization energy. The anisotropy energy can be as low as a few times 10^2 ergs/cm³ for certain metallic glasses, and as high as 10^8 ergs/cm³ for dysprosium at low cryogenic temperatures. In general, the anisotropy energy varies slightly with strain, ϵ , of the material. This effect is called magnetostriction since it causes the material to change its length when a magnetic field is applied. The physics of magnetostriction is best explained by considering a crystal with only one easy axis of magnetization and with the magnetic field aligned perpendicular to this easy axis. The energy density for a single domain is:

$$U = K\sin^2\theta + \frac{1}{2}E\epsilon^2 - \frac{1}{4\pi}HB_{sat}\sin\theta \quad (2-1)$$

where θ is the angle between the magnetization and the easy axis. B_{sat} is the saturation magnetization, and E is Young's modulus. The anisotropy K is assumed to be a function of the strain ϵ . The direction θ of magnetization which minimizes the energy U for a given applied magnetic force H is given by:

$$\sin\theta = \min\left(\frac{HB_{\text{sat}}}{8\pi K}, 1\right) \quad (2-2)$$

and the strain ϵ which minimizes energy U for a given angle θ is given by $\partial U/\partial \epsilon = 0$, or:

$$\epsilon = -\frac{\partial K}{\partial \epsilon} \frac{\sin^2\theta}{E} \equiv \lambda_s \sin^2\theta \quad (2-3)$$

When $H \geq 8\pi K/B_{\text{sat}}$, so that $\sin\theta = 1$, the strain is λ_s , called the saturation magnetostriction. If a stress σ is applied, then the strain is given by $\partial U/\partial \epsilon = \sigma$, and the internal mechanical energy changes by $\int d\epsilon \sigma$ when the material is compressed. Similarly, the internal magnetic energy changes by $\int dB \cdot H/4\pi$ if the magnetic induction B changes. Because of the dependence of K on ϵ , the mechanical energy can be changed by changing H , and the magnetic energy can be changed by changing σ . The maximum change in internal energy that can be made this way is $\lambda_s^2 E$. This is a figure of merit for magnetostrictive material used in actuators, because it represents the maximum energy density that can be stored by applying a magnetic field and then used to do mechanical work.

Another figure of merit is $\lambda_s^2 E/K$, the magnetomechanical coupling constant, which represents the fraction of mechanical work done on the material that goes into changing the magnetic energy, and vice versa. For most materials with very high λ_s and $\lambda_s^2 E$, such as terbium (Tb), dysprosium (Dy), thulium (Tm) and samarium (Sm) at cryogenic temperatures, and Terfenol (TbFe_2) and Samfenol (SmFe_2) at room temperature, $\lambda_s^2 E/K$ is still very small, as it is for most materials with normal values of λ_s . There are some materials, the iron-based metallic glasses, which have moderate values of λ_s but $\lambda_s^2 E/K$ is close to 1. As we will show, λ_s , $\lambda_s^2 E$, and $\lambda_s^2 E/K$ should all be high in an effective magnetostrictive actuator.

One reason why high λ_s alone is not enough for a magnetostrictive actuator is that it may require an enormous H for the strain to reach λ_s . The required H is related to the permeability μ , but not in a simple way. In Eq. (2-2) we found the relation between

H and the direction of magnetization for a single-domain grain, with a single easy axis aligned perpendicular to H. Imagine a material made up of a collection of such grains, with easy axes all aligned in the same direction, but with the magnetization initially distributed randomly in one or the other of the two easy directions. Then initially, with $H = 0$, the bulk magnetization of the material will be zero, even though each grain has a magnetization of magnitude B_{sat} . As H increases, the magnetization for all grains will have a component $B_{sat}\sin\theta$ in the direction of H, and a component $\pm B_{sat}\cos\theta$ in the direction of the easy axes. The latter will vanish when averaged over many grains, so the bulk magnetization will be $B_{sat}\sin\theta$. The permeability, due to this rotation of the magnetization, is

$$\mu_{rot} = \frac{\partial B}{\partial H} = \mu_0 + B_{sat} \frac{\alpha(\sin\theta)}{\partial H} \quad (2-4)$$

and from Eq. (2-2):

$$\mu_{rot} = \mu_0 + \frac{B_{sat}^2}{8\pi K} \quad (2-5)$$

where $\mu_0 = 4\pi \times 10^{-7}$ is the vacuum permeability. The H needed for saturation of the bulk magnetization (and of the magnetostriction) is:

$$H_s = \frac{B_{sat}}{\mu_{rot} - \mu_0} \quad (2-6)$$

For terbium (Tb) and dysprosium (Dy) at or below liquid nitrogen temperatures, as well as for Terfenol ($TbFe_2$) and Samfenol ($SmFe_2$) at room temperature, H_s is greater than 10^4 Oe. These materials are not very practical to use in actuators. To bring H_s down to a more reasonable level, say 10^3 Oe, K must be reduced by at least a factor of 10. This will bring it down to levels comparable to $\lambda_s^2 E$, which is in the range of 10^5 - 10^6 ergs/cm³ for these materials. If $\lambda_s^2 E/K \approx 1$, then it makes a difference whether the anisotropy energy K is defined at constant strain or at constant stress. If K is defined as the change in energy when the direction of magnetization is rotated, keeping the strain constant, and the permeability is defined as $\partial B/\partial H$ at constant stress, then K in Eq. 2-(5) should be replaced by $K - 2\lambda_s^2 E$:

$$\mu_{rot} = \mu_0 + \frac{B_{sat}^2}{8\pi(K-2\lambda_s^2E)} \quad (2-7)$$

If the grains are not all aligned with easy axis perpendicular to H, or for a material with more than one easy axis, for example a cubic material such as Terfenol (TbFe₂), or a hexagonal material with easy axes in the basal plane, such as terbium (Tb) or dysprosium (Dy), the numerical factor 1/8π in Eq. (2-7) is replaced by a smaller numerical factor, but the dependence on the parameters is the same. In order to make H_s as low as possible, the material used in a magnetostrictive actuator should have K ≈ 2λ_s²E. This also has the advantage of increasing μ, which reduces the amount of flux leakage if the magnetostrictive material is long and thin (as it normally would be in an actuator).

The magnetostrictive strain is always a single valued function of the direction of magnetization, which may be determined by minimizing U with respect to strain, similar to the derivation of Eq. (2-3). The model that we have considered, with a single easy axis perpendicular to H, is unusual, however, in that the magnetostrictive strain and the magnetization are single-valued functions of H, so that there is no hysteresis. This occurs because the magnetization takes place entirely by domain rotation rather than by domain wall motion, and because the θ derivative of the anisotropy energy Ksin²θ increases monotonically as the magnetization moves from the easy directions (corresponding to no bulk magnetization) to the direction of H (corresponding to saturation of the bulk magnetization). In a material without perfect grain alignment, or with more than one easy axis of magnetization, this will not be true, and there will be hysteresis. In a magnetostrictive actuator, hysteresis is undesirable for two reasons: (1) because H can be directly controlled by controlling the current in a coil--but if there is hysteresis, then specifying H does not uniquely specify the strain of the actuator, making the control system more complicated; and (2) hysteresis is undesirable because it is often the dominant power loss, exceeding eddy current dissipation and the resistive power loss in the coil.

2.2 Development of Practical "Giant" Strain Magnetostrictive Materials

For terbium (Tb), dysprosium (Dy), and samarium (Sm), which have large magnetostrictions λ_s at cryogenic temperatures, and for Terfenol (TbFe₂) and Samfenol

(SmFe₂), which have large λ_s at room temperature, K is much greater than $\lambda_s^2 E$, and H_s is too high for these materials to be useful in magnetostrictive actuators. Fortunately, K has opposite signs for Tb and Dy at cryogenic temperatures, as well as for TbFe₂ and DyFe₂ at room temperature. By substituting Dy for Tb (or for Sm) in just the right ratio, it is possible to produce materials with $K \approx 2\lambda_s^2 E$, which have reasonably low H_s and high μ . There is a limit to how low H_s can be and how high μ can be, since by changing the ratio of Tb to Dy in Tb_xDy_{1-x}Fe₂, it is only possible to make the first anisotropy moment K_1 equal to $2\lambda_s^2 E$. There will still be higher order anisotropy moments, principally K_2 , which do not cancel out, and these will limit the permeability at finite H . In the case of Tb_xDy_{1-x}Fe₂ at room temperature, the maximum μ is about $10\mu_0$, with λ_s of 1.6×10^{-3} , and H_s of 1000 Oe. By also including holmium (Ho), it is possible to cancel out both K_1 and K_2 , so higher μ and lower H_s should be possible, but with somewhat lower λ_s and $\lambda_s^2 E$.

As a rule, magnetic anisotropy is quite sensitive to temperature and has a different temperature dependence for different materials. So, if $K \approx 2\lambda_s^2 E$ for a particular temperature, the compensation will only be good in a fairly narrow temperature range. Outside this range, K will be much greater than $\lambda_s^2 E$, and H_s will be too large for a magnetostrictive actuator. The exact ratio of Dy to Tb (or Dy to Sm) that should be used depends on the temperature of operation of the actuator, which will only work in a limited temperature range. For the series Tb_xDy_{1-x}Fe₂ and Sm_xDy_{1-x}Fe₂, if the temperature is too far below the operating range for a given x , or if x is too low, then not only will H_s be very high, but λ_s will be very small as well. The reason for this is that DyFe₂ has easy directions of magnetization along the [100] axes, while TbFe₂ and SmFe₂ have easy directions along the [111] axes, and for all these materials, $\lambda_{100} \ll \lambda_{111}$.

At room temperature, $K \approx 2\lambda_s^2 E$ for Tb_xDy_{1-x}Fe₂ when $x \approx 0.27$. At temperatures below 100 K, the compensation occurs when $x \approx 0.4$, and at higher temperatures it occurs at smaller x (but the resulting compound has smaller λ_s). For Sm_xDy_{1-x}Fe₂, the compensation occurs at $x = 0.15$ at room temperature.

2.3 Magnetostriction at Cryogenic Temperatures

At cryogenic temperatures, higher values of saturation magnetostriction λ_s can be obtained with the series Tb_xDy_{1-x} than are obtained with Terfenol-D, which can work at room temperature. For example, the saturation magnetostriction of Tb₅Dy₅ is 6000 ppm

at liquid nitrogen temperatures¹, compared to 2500 ppm for Terfenol-D. Tb_5Dy_5 also has much lower hysteresis at 77°K than Terfenol-D. $\text{Tb}_x\text{Dy}_{1-x}$ must be used at cryogenic temperatures, below approximately 150 K, to have useful magnetostrictive properties.

$\text{Tb}_x\text{Dy}_{1-x}$ is hexagonal with easy axes in the basal plane. Magnetization out of the basal plane is so difficult that effectively the bulk magnetization is saturated when the magnetization of each grain is oriented as close to H as possible within the basal plane. At lower temperatures, K is extremely sensitive to temperature, increasing several orders of magnitude, and it may not be possible to find a composition which works over more than a very narrow temperature range; this bears investigating. This sensitivity of anisotropy to temperature and composition is shown in Figure 2-1 below, where the magnetic anisotropy is plotted versus absolute temperature². The different curves are for different values of the material ratio x in the material composition $\text{Tb}_x\text{Dy}_{1-x}$. The compensation values x that minimize the magnetic anisotropy are summarized in Table 2-1.

Table 2-1. Temperature dependence of Ratio parameter (x).

Ratio Parameter (x)	Temperature (K)
0.67	60
0.5	100
0.33	120
0.17	135

A major disadvantage of $\text{Tb}_x\text{Dy}_{1-x}$ for some applications is its low yield stress, about 25 MPa for TbDy at 77°K. For applications which require higher stress, the TbDy could be enclosed in a sleeve, but it is possible that this would substantially reduce the maximum strain, and the maximum clamped force, since it would tend to make the stress more isotropic.

¹Spano, M.L., Clark, A.E. and Wun-Fogle, M., "Magnetostriction of TbDy Single Crystals under Compressive Stress," Proceedings of the International Magnetics Conference, Brighton, U.K., April 1990.

²*Ibid.*

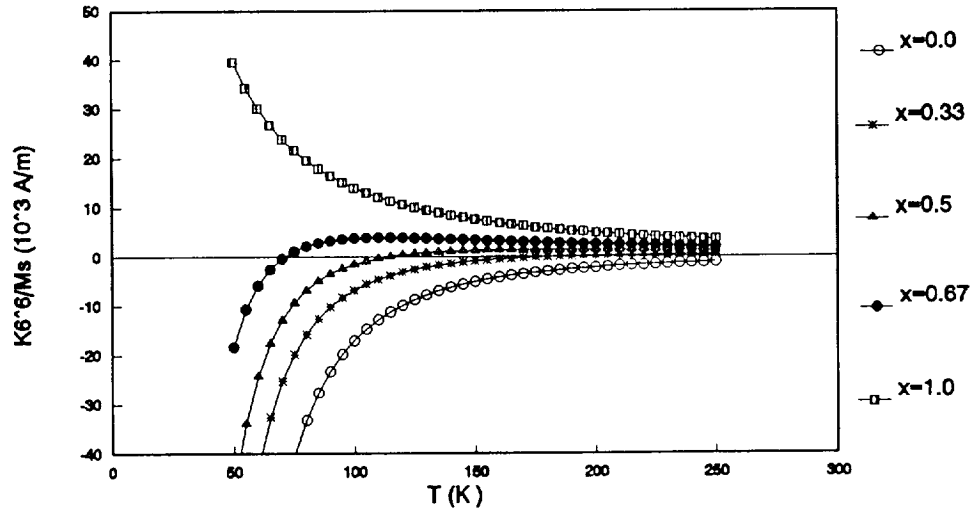


Figure 2-1. Anisotropy as a function of temperature for $\text{Tb}_x\text{Dy}_{1-x}$.

Terfenol-D with composition $\text{Tb}_{.45}\text{Dy}_{.55}\text{Fe}_{1.9}$, the optimum at 77° K, has much higher yield stress than TbDy, and somewhat higher maximum magnetostrictive strain than room temperature Terfenol-D, so may be more suitable for applications which require high stress, but it has much greater hysteresis than either TbDy at 77° K, or Terfenol-D at room temperature, which could be a disadvantage for applications which require precise control of strain over a large range, or which have stringent limits on dissipated power. The reason for this large hysteresis is that the anisotropy increases rapidly with decreasing temperature. The ratio of Tb to Dy is chosen to eliminate the lowest order anisotropy, but higher order components of anisotropy remain, and these result in a much lower μ_{rot} for $\text{Tb}_{.45}\text{Dy}_{.55}\text{Fe}_{1.9}$ at 77° K than for either composition of Terfenol-D at room temperature. At 77° K, the permeability of Terfenol-D is due mostly to domain wall motion, in contrast to room temperature, where domain wall motion and rotation make comparable contributions to the permeability. Since rotation does not have any hysteresis, this is one reason why hysteresis is lower at room temperature. This hysteresis at 77° K is more than a factor of two greater than at room temperature, however, so the domain wall motion itself must exhibit more hysteresis at 77° K. Apparently the higher anisotropy, or some other effect of lower temperature, causes the domain walls to be pinned more strongly.

To the extent that the large hysteresis in cryogenic Terfenol-D is due to large anisotropy, it should be possible to substantially reduce it by adding just the right amount of holmium. This should make it possible to cancel out both the first and second order components of anisotropy, leaving only the third order and higher components, which should be much smaller. This will result in a modest decrease in the maximum magnetostrictive strain, however, because holmium has a somewhat lower λ_s than terbium or dysprosium. Tests of $\text{Tb}_x\text{Dy}_y\text{Ho}_{1-x-y}\text{Fe}_{1.9}$ are currently under way at the Naval Surface Warfare Center, to determine the optimum composition.

2.4 Hysteresis in Magnetostrictive Materials

Hysteresis is undesirable in a magnetostrictive actuator for two reasons. Hysteresis in strain vs. H makes it more difficult to control the strain, since H can generally be controlled directly by changing the current in the coil; having hysteresis between strain and H means that more complicated control algorithms may be needed. Hysteresis in B vs. H gives rise to power dissipation, and can sometimes be the dominant power loss, greater than resistive losses in the coil and eddy current losses. This can be an issue when there are limits on the heat that can be generated by the actuator. In order to provide guidelines for minimizing hysteresis, we describe the processes that cause it.

Hysteresis in strain vs. H in magnetostrictive materials is generally associated with a nonmonotonic θ derivative of anisotropy energy, where θ is the angle between the direction of magnetization and the direction of H . (Hysteresis in B vs. H can occur even if the θ derivative of anisotropy energy is monotonic, as will be discussed later.) For example, in Terfenol-D, a cubic crystal with easy axes in the $[111]$ directions, and H in one of the $[112]$ directions, the anisotropy energy has a θ derivative that has zeroes at 90° and 35.26° , as shown in Fig. 2-2. In TbDy , a hexagonal crystal with easy directions 60° apart in the basal plane, and H also in the basal plane between two easy directions, the θ derivative of the anisotropy energy has zeroes at 90° and 30° .

In an idealized model in which there is no domain wall motion, this can lead to the magnetization taking a sudden jump at a certain value of H . Energy would be dissipated in this jump, which is not reversed at the same value of H . The condition for sudden jumps to occur can be found by starting with a generalization of Eq. (2-1) where the anisotropy term has angular dependence $F(\theta)$ rather than $\sin^2(\theta)$.

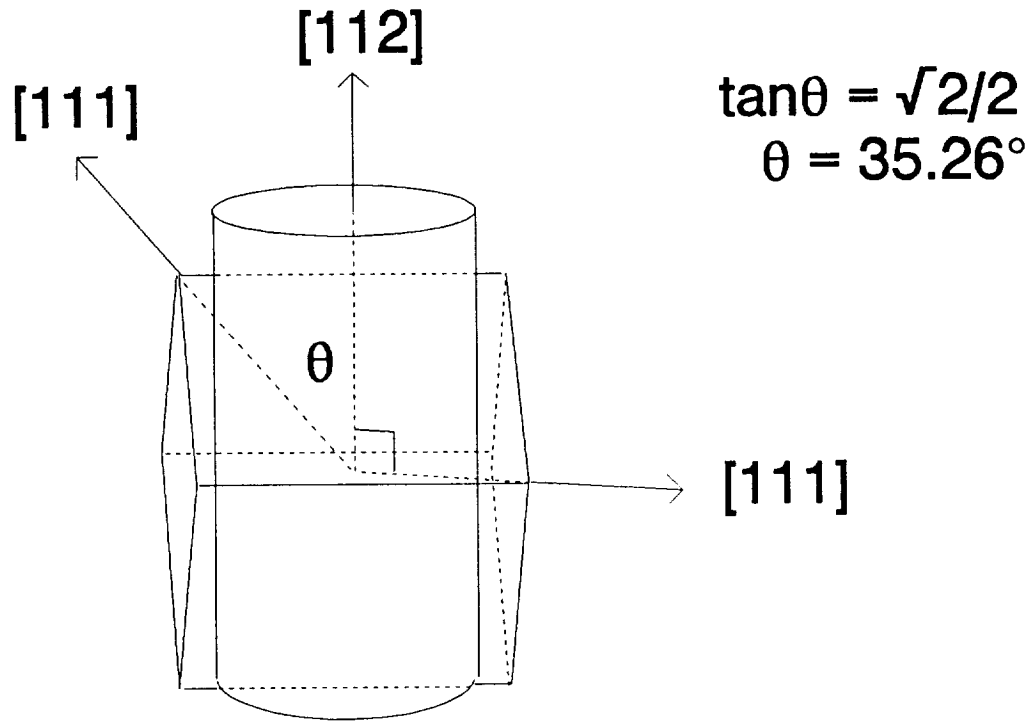


Figure 2-2. Orientation of easy [111] axes with respect to the rod axis, in grain-aligned Terfenol-D.

$$U = KF(\theta) - \frac{HM_s \sin(\theta)}{4\pi} + \frac{\epsilon^2 E}{2} \quad (2-8)$$

At a given H, the material will be in equilibrium if $\partial U / \partial(\sin\theta) = 0$. (If the material is not clamped, but is at zero (or constant) stress, then it is understood that this θ derivative must be taken at constant stress, not at constant strain). Then

$$\frac{\partial F}{\partial(\sin\theta)} = \frac{HM_s}{4\pi K} \quad (2-9)$$

If $\partial F / \partial(\sin\theta)$ is not a monotonic function of $\sin\theta$, then there will be more than one direction of magnetization θ at which the material is in equilibrium for a given H. As H is slowly increased from zero, θ will follow one such branch until it reaches a point at

which $\partial^2 F / \partial (\sin \theta)^2 = 0$, and will then suddenly jump to another branch. If H is decreased again, θ will jump back to the first branch at a different, lower value of H , so there will be hysteresis.

In practice, H does not have to reach the point at which $\partial^2 F / \partial (\sin \theta)^2 = 0$ in order to have the magnetization change to a different branch of equilibrium direction θ . In soft magnetic materials, there are always small domains in which the magnetization is oriented in other directions, in which the anisotropy energy is not minimized. These "seed domains" could be left over from previous magnetization cycles. When H reaches a value for which the anisotropy energy for these seed domains is as low as the anisotropy energy of the domains surrounding them, then the boundaries between the domains begin to move, and the seed domains grow at the expense of the other domains. This does not happen suddenly at the H for which the energies are equal, but over a range of H , since, due to the demagnetization energy, it is energetically favorable to have many domains with magnetization in different directions, even at the expense of somewhat higher anisotropy energy. Eventually the domains that used to be seed domains become dominant, and the other domains shrink to a small size, becoming seed domains themselves until H goes back.

This domain wall motion is subject to hysteresis, because domain walls do not move freely, but become pinned on crystal defects, grain boundaries, and nonmagnetic inclusions. As H is increased past the H at which the domains are in equilibrium, pressure builds up on the domain walls until they become de-pinned, and jump suddenly to a new equilibrium position. These jumps, called Barkhausen events, dissipate energy, and give rise to hysteresis, although this hysteresis has a smaller ΔH than if there were no domain wall motion. This kind of hysteresis will always occur unless there is only a single easy axis of magnetization, or the grains are aligned with all easy axes of magnetization at the same angle to H . These conditions that do not occur in any of the rare earth based giant magnetostrictive materials, which either have cubic crystal structure with easy directions on the [111] axes, in the case of Terfenol-D, or hexagonal crystal structure with easy directions 60° apart in the basal plane, in the case of TbDy. These conditions are approximated, however, in the limit that the magnetic anisotropy due to the crystal structure is relatively small, and there is a uniaxial preload stress parallel to H which dominates the magnetic anisotropy. TbDy has lower anisotropy and hence less hysteresis than Terfenol-D, and Terfenol-D has much lower hysteresis at room temperature than at cryogenic temperatures, because it has much lower anisotropy at

room temperature. (Also, the domain walls are apparently pinned more strongly at cryogenic temperatures.) Reducing the anisotropy of Terfenol-D by adding just the right ratio of holmium should also reduce hysteresis.

In addition to hysteresis associated with a nonmonotonic θ derivative of anisotropy energy, there is also hysteresis associated with 180° domain wall motion, which can occur even if the θ derivative of anisotropy energy is monotonic. Domains with magnetization 180° apart always have the same anisotropy energy, so can always coexist when $H = 0$. As H increases, the domains magnetized in the direction closer to the direction of H grow at the expense of the domains magnetized in the opposite direction. Again, this domain wall motion is irreversible, due to pinning of domain walls, and gives rise to hysteresis. However, this kind of hysteresis only affects B vs. H , not strain vs. H , because domains with magnetization 180° apart always have the same strain. Magnetostrictive actuators are generally designed to avoid having 180° domain walls, because they allow B to change without changing the strain, and thus reduce the maximum magnetostrictive strain. This is done by applying a preload stress which forces the magnetization of the domains to be perpendicular to the rod axis when $H = 0$, and applying H along the rod axis in order to change the strain.

Another source of dissipation is eddy-current losses, which increase quadratically with the frequency at low frequencies. Eddy-current losses are quadratically dependent on the thickness of the material when the material is thin, and these losses can be minimized by lamination of the magnetostrictive material. Eddy currents are more of a problem at low temperatures, where the conductivity is greater than at room temperature, and are worse for TbDy than for Terfenol-D at 77°K , because TbDy has higher permeability. In our room temperature Terfenol-D actuator, eddy currents become important only at a few hundred Hz, while in our cryogenic actuator using TbDy, they are important at a few tens of Hz.

3. MODELLING MAGNETOSTRICTIVE ACTUATORS

3.1 Magnetic Circuit Model

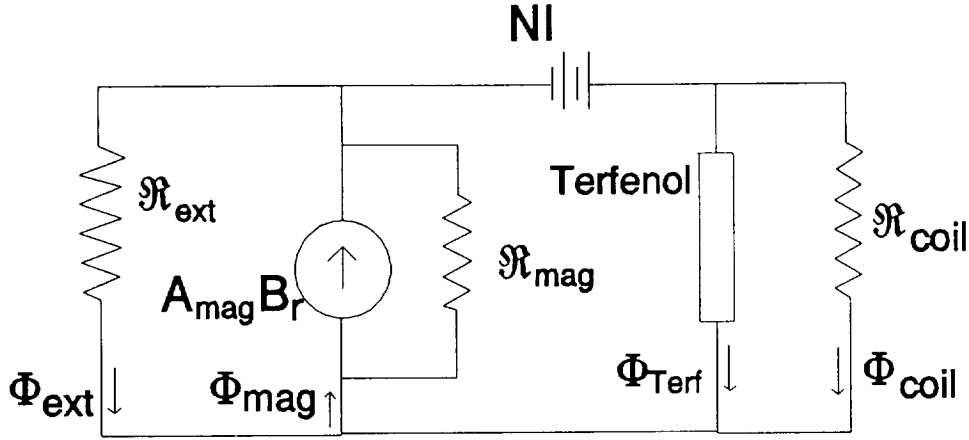


Figure 3-1. Magnetic circuit for magnetostrictive actuator.

The magnetic circuit of a magnetostrictive actuator like the one shown in Fig. 1-2, is shown schematically in Fig. 3-1, drawn like an equivalent electric circuit. The basic circuit consists of a coil, whose NI is analogous to a voltage source, in series with the reluctance of the Terfenol, analogous to a nonlinear resistor, and a permanent magnet, analogous to a source of constant current $B_r A_{\text{mag}}$, where B_r is the retentivity and A_{mag} is the cross-sectional area of the permanent magnet. In parallel with the permanent magnet "current source" are the reluctance of the external space $\mathfrak{R}_{\text{ext}}$ (analogous to a resistor), and the reluctance of the magnet $\mathfrak{R}_{\text{mag}}$ (generally much larger than the reluctance of the external space that it is in parallel with, and hence negligible). In parallel with the reluctance of the Terfenol is the reluctance $\mathfrak{R}_{\text{coil}}$ of flux passing through the coil but missing the Terfenol, due to finite radial thickness of the coil or space between the inner radius of the coil and the Terfenol. Typically we wish to know how H and B in the Terfenol (and hence the strain of the Terfenol) depend on NI and on B_r and A_{mag} , as well as on the Terfenol cross-sectional area A_{Terf} , the Terfenol length ℓ_{Terf} , the magnet length ℓ_{mag} , and the total length of the magnetic circuit (including the steel end caps) ℓ_{tot} , which determines the external reluctance. The properties of the Terfenol give us one equation relating B_{Terf} and H_{Terf} , and we analyze the magnetic circuit to obtain another equation, allowing us to solve for B_{Terf} and H_{Terf} , and to find the strain.

Conversely, by measuring the strain of the Terfenol, and the flux in the Terfenol (or the inductance of the coil), as functions of the bias current in the coil, we can determine the relation between B, H, and strain in the Terfenol.

The equation relating the fluxes in the magnetic circuit (analogous to currents in an electric circuit) is

$$\Phi_{\text{mag}} = \Phi_{\text{Terf}} + \Phi_{\text{ext}} + \Phi_{\text{coil}} \quad (3-1)$$

where Φ_{mag} is the flux through the permanent magnets, Φ_{Terf} is the flux through the Terfenol, Φ_{ext} is the external leakage flux outside the actuator, and Φ_{coil} is the flux passing through the coil (weighted by how much of the coil current it is linking), but not passing through the Terfenol. Here Φ_{Terf} , Φ_{ext} and Φ_{coil} are defined to have the same sign as Φ_{mag} when $NI = 0$, even though B in the Terfenol and the external B are pointing opposite to the direction of B in the magnets in this case. The Terfenol flux is related to B in the Terfenol,

$$\Phi_{\text{Terf}} = B_{\text{Terf}} A_{\text{Terf}} \quad (3-2)$$

and the magnet flux is related to B_r and to H in the magnet by

$$\Phi_{\text{mag}} = (B_r + \mu_0 H_{\text{mag}}) A_{\text{mag}} \quad (3-3)$$

because the reluctance of the magnets, which appears in the equivalent electric circuit as a resistance parallel to the constant current source $B_r A_{\text{mag}}$, is $\mathfrak{R}_{\text{mag}} = \ell_{\text{mag}} / \mu_0 A_{\text{mag}}$. (This is valid for a rare earth magnet, with very high coercivity, and permeability close to the vacuum permeability μ_0 .) Here we have defined H_{mag} to be opposite in sign to Φ_{mag} when $NI = 0$.

There are also three equations relating the magnetomotive potentials, analogous to voltages in the electric circuit,

$$H_{\text{mag}} \ell_{\text{mag}} = -\mathfrak{R}_{\text{ext}} \Phi_{\text{ext}} \quad (3-4a)$$

$$H_{\text{mag}} \ell_{\text{mag}} = NI - H_{\text{Terf}} \ell_{\text{Terf}} \quad (3-4b)$$

$$H_{\text{Terf}} \ell_{\text{Terf}} = \mathfrak{R}_{\text{coil}} \Phi_{\text{coil}} \quad (3-4c)$$

Here NI is defined to have the same sign as Φ_{ext} when the coil increases the magnitude of the flux in the Terfenol induced by the magnets. Equation (3-4b) assumes that the magnets are connected to the Terfenol with infinitely permeable steel end caps, which extend axially to fill in any substantial difference in length between the Terfenol and the magnets, and that the gap between the magnets and the end cap (which must exist to allow for the change in length of the Terfenol) has negligible reluctance. If there is a significant gap between the magnets and end caps, or a significant non-magnetic spacer

between the Terfenol and the end caps, then additional terms must be added to the left hand side, representing the magnetomotive potential across these regions.

To find the coil reluctance \mathfrak{R}_{coil} , we note that the permeance of a thin coil at radius r would be $\mu_0(\pi r^2 - A_{Terf})/\ell_{Terf}$. For a coil of finite thickness, with inner radius r_{ic} and outer radius r_{oc} , the permeance is just the integral of this quantity divided by $(r_{oc} - r_{ic})$, and the reluctance is the inverse the permeance

$$\mathfrak{R}_{coil} = \frac{\ell_{Terf}}{\mu_0} \left[\frac{\pi}{3} (r_{oc}^2 + r_{oc}r_{ic} + r_{ic}^2) - A_{Terf} \right]^{-1} \quad (3-5)$$

For a cylinder whose length ℓ_{tot} is at least twice its diameter, the external reluctance is given to good approximation by

$$\mathfrak{R}_{ext} \approx 4/\pi\mu_0\ell_{tot} \quad (3-6)$$

We have found that using this expression for \mathfrak{R}_{ext} , and the Terfenol properties in the literature, gives results for strain as a function of NI that are in excellent agreement with the test data for the room temperature actuator, provided that ℓ_{tot} is taken to be the total length of the magnetic circuit, including the steel end caps. Combining these six equations and eliminating Φ_{Terf} , Φ_{mag} , Φ_{ext} , \mathfrak{R}_{ext} , and H_{mag} yields the desired equation relating H_{Terf} and B_{Terf} ,

$$H_{Terf} \left(\frac{\pi}{4} \ell_{tot} + \frac{A_{mag}}{\ell_{mag}} + \frac{\pi}{3} \frac{(r_{oc}^2 + r_{oc}r_{ic} + r_{ic}^2)}{\ell_{Terf}} - \frac{A_{Terf}}{\ell_{Terf}} \right) + \frac{A_{Terf}}{\mu_0 \ell_{Terf}} B_{Terf} = \frac{NI}{\ell_{Terf}} \left(\frac{\pi}{4} \ell_{tot} + \frac{A_{mag}}{\ell_{mag}} \right) + \frac{A_{mag} B_r}{\mu_0 \ell_{Terf}} \quad (3-7)$$

The first term in each set of parentheses, $\pi\ell_{tot}/4$, is usually much greater than the other terms in parentheses, which may be neglected. This means that the finite coil reluctance has only a small effect on the equilibrium H_{Terf} and B_{Terf} for a given NI, and it would have no effect if it were not for the external reluctance. However, the finite coil reluctance does have a significant effect on the inductance of the coil, even if there were no external reluctance, and it is for this reason that it has been included in our magnetic circuit analysis. This point will be discussed further in Sec. 5 and Sec. 6, where inductance data is analyzed.

Equation (3-7) is valid for any frequency, but for higher frequencies, at which the skin depth of the Terfenol is comparable to or less than the Terfenol radius, the cross-sectional area A_{Terf} must be replaced by a smaller effective area that takes into account the finite skin depth. Also, if the permanent magnets completely surround the coil with no gaps azimuthally, then azimuthal eddy currents can be induced in the permanent magnets, trapping the flux if the skin depth of the permanent magnets is less than or comparable to their radial thickness, and in this case the external reluctance $\mathfrak{R}_{\text{ext}}$ will be much greater (at that frequency) than the expression given by Eq. (3-6), and Eq. (3-7) and must be appropriately modified. However, arranging the permanent magnets with no azimuthal gap would be a poor design choice for this reason, and would not normally be done. An analysis of skin effects is given in Sec. 3.7, for the case where B_{Terf} is a linear function of H_{Terf} .

To find B_{Terf} and H_{Terf} for a given NI and a given actuator design, Eq. (3-7) must be solved simultaneously with an equation relating B_{Terf} and H_{Terf} which depends on the Terfenol properties and on stress. Once this is done, the strain ϵ of the Terfenol can be calculated, since it is a known function of B_{Terf} . If the actuator has load with finite stiffness, then the stress will depend on ϵ , and both must be found self-consistently. For giant magnetostrictive materials such as Terfenol-D and TbDy, $\epsilon(B)$ exhibits very little hysteresis, is nearly independent of stress, and in fact has only a moderate dependence on composition and temperature, being similar (within a factor of 2 or so) for room temperature Terfenol-D, cryogenic Terfenol-D, and TbDy. Figure 3-2 shows $\epsilon(B)$ for standard composition Terfenol-D at room temperature, from data given by Clark et al.,¹ for TbDy at 77°K, from data given by Spano et al.,² and for cryogenic composition Terfenol-D, at 77°K and at room temperature, inferred from data taken by Clark.³ The data shown is all for 15 MPa, but is nearly the same for other values of stress, as confirmed by our test data discussed in Sec. 5 and Sec. 6. An exception to this occurs

¹A. E. Clark, J. P. Teter, M. Wun-Fogle, M. Moffett, and J. Lindberg, "Magnetomechanical coupling in Bridgman-grown $\text{Tb}_{0.3}\text{Dy}_{0.7}\text{Fe}_{1.9}$ at high drive levels," presented at 34th Conf. on Magnetism and Magnetic Materials, Boston, Nov. 28 - Dec. 1, 1989.

²M. L. Spano, A. E. Clark, and M. Wun-Fogle, "Magnetostriction of TbDy single crystals under compressive stress," IEEE Trans. MAG-26, 1751 (1990).

³Arthur E. Clark, personal communication via Mel J. Goodfriend (1991).

when the stress is very low (typically less than 7 MPa), in which case the magnetization vectors of the domains are not all pointing nearly perpendicular to the axis of the Terfenol at $B = 0$, but a significant fraction of them are pointing in one of the easy directions more closely aligned with the axis. In this case, higher B is needed to obtain a given strain, and the maximum strain, when B is at saturation, is lower than it is at higher stress. Usually the actuator would not be used at such low stress, but would be preloaded with a higher stress so that the full magnetostrictive strain could be obtained.

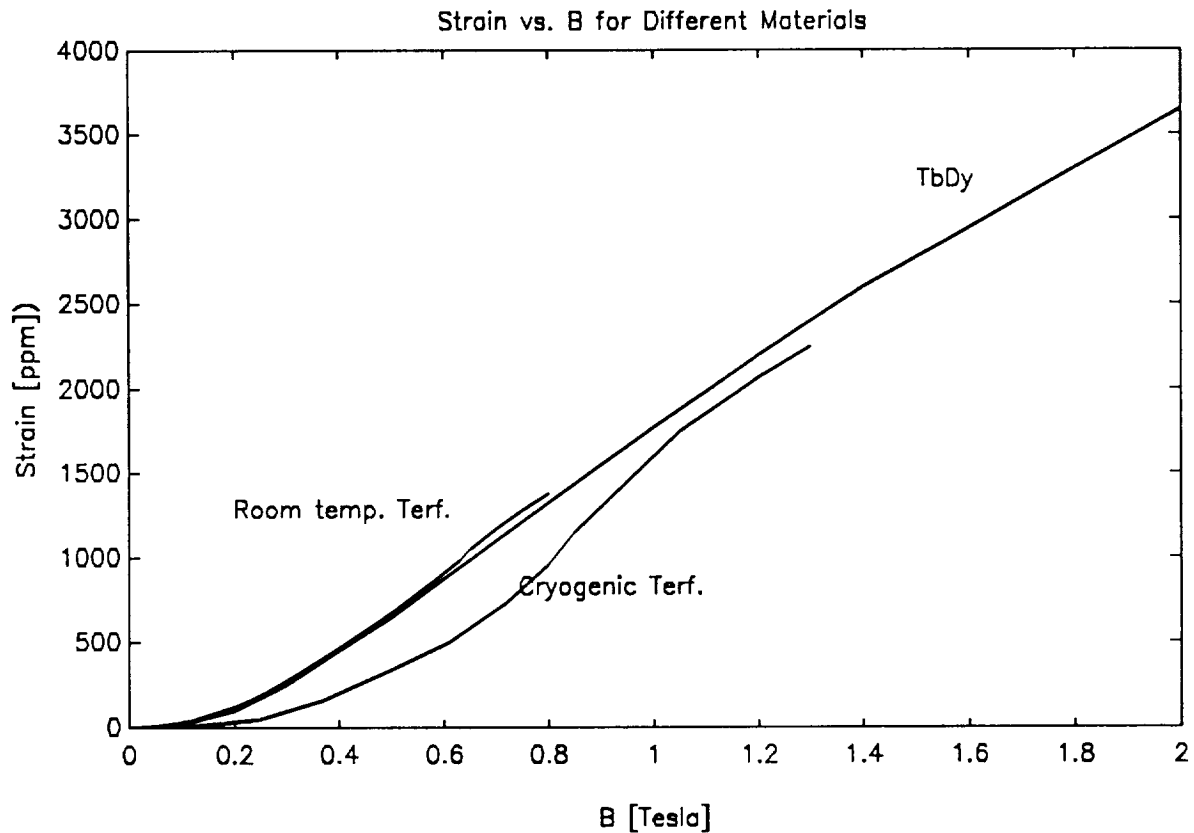


Figure 3-2. Magnetostrictive strain ϵ as a function of B for standard composition Terfenol-D at room temperature, for cryogenic composition Terfenol-D at 77° K, and for TbDy at 77° K.

3.2 Anhyseretic $B(H)$ and Hysteresis

Unlike $\epsilon(B)$, $B(H)$ does depend on stress, and does exhibit hysteresis. To model hysteresis, we first note that for any value of H and stress, there is a unique anhyseretic flux density B_{an} , which does not depend on the past history. This is the B at which the

energy of the Terfenol is minimized, as discussed in Sec. 2. If demagnetization effects are neglected, the minimum energy state would have the magnetization of all domains pointing in a direction at which the anisotropy energy (including its stress dependence) plus the interaction energy $-HB_{\text{sat}}(\cos\theta)/2$ is minimized. (Here θ is the angle between the magnetization vector and H , and B_{sat} is the saturation magnetization.) In Terfenol-D, the crystal structure is cubic, with the anisotropy energy minimized for magnetization in the $[111]$ directions. The Terfenol-D rods used in actuators have crystals with the $[112]$ direction oriented along the axis of the rod, so four of the easy directions are in the plane perpendicular to the rod axis, and four of them are at an angle of $\arctan(\sqrt{2}/2) = 35.26^\circ$ to the rod axis, as shown in Fig. 2-2. In TbDy, the crystal structure is hexagonal, with six easy directions in the plane basal of the crystal. In our actuator the axis of the TbDy rod is in the basal plane between two easy directions, so two easy directions of magnetization are perpendicular to the rod axis, and four easy directions are at an angle of 30° to the rod axis. In both Terfenol-D and TbDy, the rod is given a compressional stress along its axis of at least 7 MPa, which gives the easy directions perpendicular to the axis of the rod somewhat lower energy than the easy directions at angles of 35.26° or 30° to the axis of the rod. Hence at $H = 0$, essentially all of the domains have magnetization perpendicular to the axis of the rod. As the applied H (oriented along the rod axis) increases, the direction of magnetization at which the energy is minimized starts to move toward the rod axis, due to the interaction energy $-HB_{\text{sat}}(\cos\theta)/2$, and B_{an} will be $B_{\text{sat}}\cos\theta$. If the stress is not too great, so the anisotropy energy is only slightly lower for the easy directions perpendicular to the rod axis than for the easy directions at angles of 35.26° or 30° , then, as H increases, the local minimum in energy at θ near 35.26° or 30° will become lower than the local minimum at θ near 90° , before the local minimum near 90° has moved very far from 90° . At this H , the θ at which the energy is minimized will suddenly jump, from a little below 90° to a little below 35.26° or 30° , and $B_{\text{an}}(H)$ will suddenly jump to a higher value. As H increases further, the magnetization will slowly move closer to the axis of the rod, and B_{an} will slowly approach B_{sat} . At higher compressional stress, there will be more difference in anisotropy energy between easy directions perpendicular to the rod axis and those at 35.26° or 30° to the rod axis. The jump in $B_{\text{an}}(H)$ will occur at higher H , and the jump will be smaller; for sufficiently high stress there will be no jump at all.

In practice, $B_{\text{an}}(H)$ will not be discontinuous, because, due to demagnetization energy, it is energetically favorable to have domains with magnetization pointing in

different directions. This is true even in the case of an infinitely long rod, or a rod whose ends are connected to a zero reluctance magnetic circuit, because there is demagnetization energy associated with crystal defects and nonmagnetic inclusions in the Terfenol. So instead of a sudden jump in magnetization direction as H increases, there will be domains present, over a range of H , with magnetization oriented at both values of θ for which the energy is at a local minimum, i.e., a little below 90° and a little below 35.26° or 30° . As H increases, the domain walls will move, increasing the size of the domains with $\theta \approx 35.26^\circ$ or 30° , and decreasing the size of the domains with $\theta \approx 90^\circ$, until the latter disappear almost completely. The anhysteretic permeability will have contributions from the rotation of magnetization, and from domain wall motion,

$$dB_{an}/dH \equiv \mu_{an} = \mu_{rot} + \mu_{wall,an} \quad (3-8)$$

The change in B due to rotation is reversible, but the change in B due to domain wall motion exhibits hysteresis. Domain walls can be pinned by crystal defects and grain boundaries; when H is increased sufficiently, without the wall moving, then the difference in magnetic energy between the two domains exerts a great enough pressure on the wall to de-pin it. The de-pinning process is irreversible, and the pinning energy is dissipated as heat. The difference between $B_{an}(H)$ and B required to de-pin a domain wall depends on the strength of the pinning site, and in any magnetic material there is a variety of pinning sites with different strengths. Initially, starting from the minimum energy state ($B = B_{an}$) with no pressure on the domain walls, if H is increased by a small amount the domain walls will not move at all, since they can be pinned by even the weakest pinning sites, and B will increase only because of rotation. (In high permeability materials like iron, B will also increase initially due to bowing out of domain walls between pinning sites, but this process seems to be unimportant, compared to rotation, in Terfenol-D and TbDy.) As H increases further, and B falls further below $B_{an}(H)$, the pressure on the domain walls will start to increase, and more pinning sites will be released. Finally, when $B_{an} - B = \mu_{an}H_c$, where H_c is the coercivity, the pressure is sufficient to de-pin the walls from even the strongest pinning sites, and dB/dH will be equal to μ_{an} . If H then starts to decrease, dB/dH will again initially be equal to μ_{rot} , and the contribution from domain wall motion will gradually increase, reaching its full anhysteretic value only when $B_{an} - B = -\mu_{an}H_c$.

A simple model of this process is given by Jiles and Atherton⁴, who have dB/dH vary linearly with $B_{an} - B$, from an initial value (μ_{rot} in our case) at $B_{an} - B = -\mu_{an}H_c \text{sgn}(dH/dt)$, to a final value of μ_{an} at $B_{an} - B = +\mu_{an}H_c \text{sgn}(dH/dt)$. They also include the effect of coupling between domains, which is moderately important in materials like iron, but is completely negligible in Terfenol-D and TbDy. Using this model and adjusting the parameters, they compute hysteresis loops which are in excellent agreement with measured hysteresis loops in magnetic steel. This model appears to be valid for hysteresis loops in which H varies by more than H_c , but does not make sense physically for hysteresis loops, centered around $B_{an} = B$, in which H varies by much less than H_c , since such hysteresis loops ought to have dB/dH close to μ_{rot} , and are observed to have dB/dH close to μ_{rot} in our actuator, but according to the model of Jiles and Atherton they would have $dB/dH = (\mu_{rot} + \mu_{an})/2$. To correct this problem, we use a model in which dB/dH always equals μ_{rot} when dH/dt first changes sign, and goes linearly with $B_{an} - B$ until $dB/dt = \mu_{an}$ at $B_{an} - B = \mu_{an}H_c \text{sgn}(dH/dt)$.

$$\frac{dB}{dH} = \frac{(B_{an} - B) \text{sgn}(dH/dt)}{(c+1)H_c} + \frac{c}{c+1} \frac{dB_{an}}{dH} \quad (3-9)$$

where

$$c = \frac{\mu_{rot} + [B^* - B_{an}(H^*)]H_c^{-1} \text{sgn}(dH/dt)}{dB_{an}/dH - \mu_{rot}} \quad (3-10)$$

Here B^* and H^* are the values of B and H when dH/dt last changed sign. These equations have the physically desired properties that (B,H) can never go outside the outer hysteresis loop $B(H) = B_{an} \pm H_c \mu_{an}$, and that with periodic $H(t)$, $B(H)$ will always asymptotically approach a hysteresis loop centered around B_{an} , even if it is not initially centered around B_{an} . In principle H_c should be a function of H and stress, and should become very small in those regimes where domain wall motion is unimportant. In practice, H_c does not fall off so abruptly as $\mu_{wall,an}$ falls off, and in any case one generally wants to operate in the regime where $\mu_{wall,an}$ is not so small, since most of the change in strain occurs in this regime, so it is a pretty good approximation to take H_c as

⁴D. C. Jiles and D. L. Atherton, J. Mag. and Mag. Mater. **61**, 48 (1986).

independent of H and stress. An exception occurs with very low stress, less than 1 ksi. In this case, the contribution of domain wall motion is substantially reduced, because a large fraction of the domains are already magnetized in the easy directions 35.26° or 30° away from the rod axis even at H = 0, so H_c is substantially lower than it is at higher stress; it is still nearly independent of H. It is also possible for H_c to depend on whether the stress is constant in time, or is changing with H because the actuator is completely or partially clamped. This could happen because changes in stress can de-pin domain walls, moving B(H) closer to B_{an} , an effect that has been observed in magnetic steel.⁵ If stress is changing continually with H, this could decrease the effective H_c . But our test data, as well as a comparison of Figs. 3-3 and 3-4 in Moffett et al.,⁶ indicate that this effect is small in Terfenol-D, if it occurs at all.

In Sec. 2, an estimate was made of μ_{rot} , using a simple model in which there were only two easy directions of magnetization, 180° apart, and H was pointing perpendicular to them. We found, for $B \ll B_{sat}$,

$$\mu_{rot} = B_{sat}^2 / 2(K - 2\lambda_s^2 E + \lambda_s \sigma) \quad (3-11)$$

Here K is the anisotropy energy at constant strain, and is defined as the difference in between the energy density when the magnetization is in the easy direction and the energy density when the magnetization is in the hardest direction, i.e., the energy is $K \cos^2 \theta$, where θ is the angle between the magnetization and the hardest direction (which is the direction of H). The anisotropy energy at constant stress is $K - 2\lambda_s^2 E$, where E is Young's modulus, and $\lambda_s \sigma$ is the correction to the anisotropy energy due to stress σ . A similar analysis for a hexagonal material like TbDy, with an anisotropy energy term $K(\cos 6\theta)/2$, yields²

$$\mu_{rot} = B_{sat}^2 / (18K + 2\lambda_s \sigma) \quad (3-12)$$

⁵D. C. Jiles and D. L. Atherton, "Theory of the magnetisation process in ferromagnets and its application to the magnetomechanical effect," J. Phys. D: Appl. Phys. 17, 1265-1281 (1984).

⁶Mark B. Moffett, Arthur E. Clark and Marilyn Wun-Fogle, Jan F. Lindberg, Joseph P. Teter, and Elizabeth A. McLaughlin, "Characterization of Terfenol-D for magnetostrictive transducers," J. Acoust. Soc. Am. 89, 1448-1455 (1991).

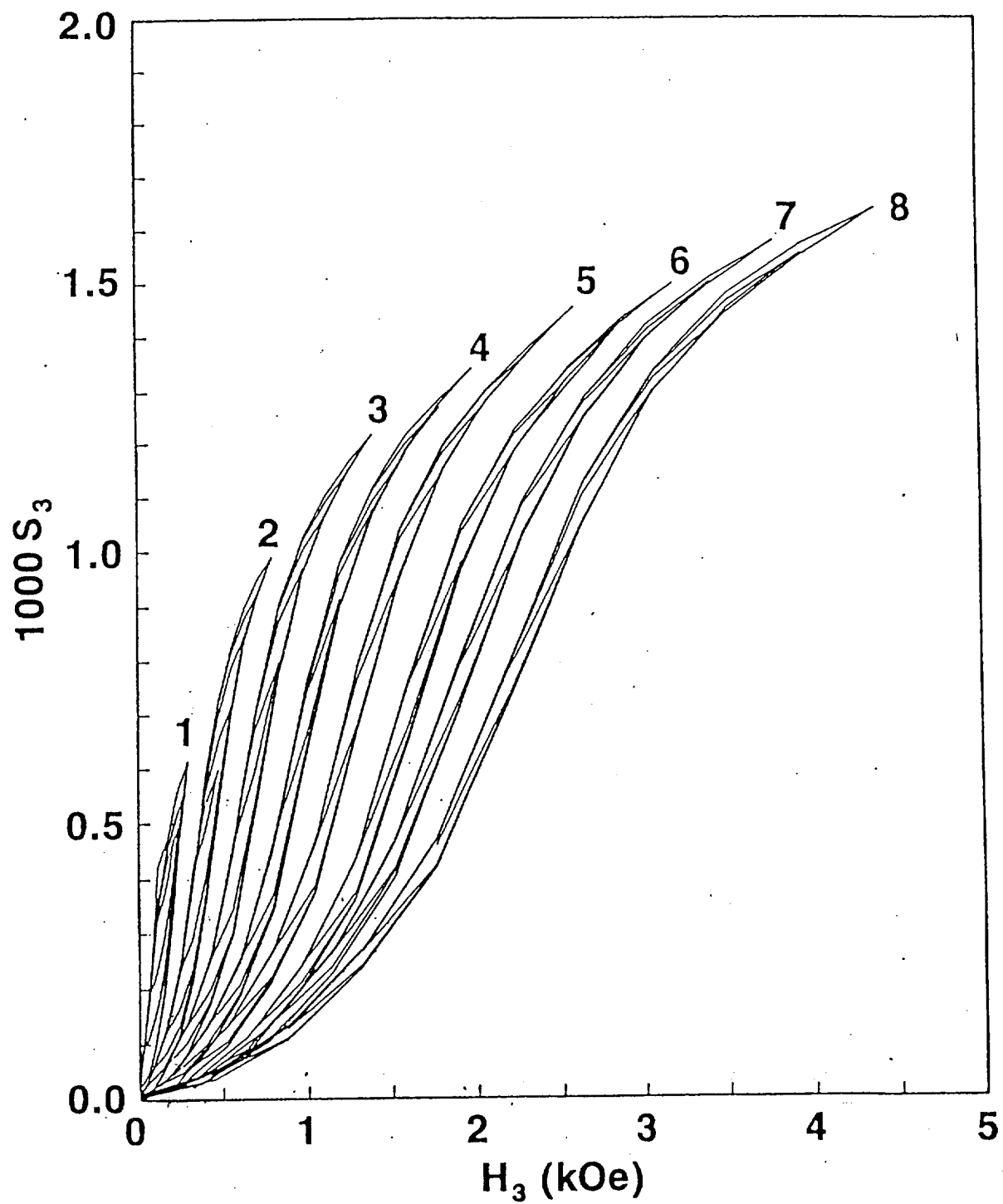


Figure 3-3. Hysteresis loops for λ vs. H at various values of constant σ , for standard composition Terfenol-D at room temperature, from Fig. 3 in Moffett et al., J. Acoust. Soc. Am. 89, 1448-1455 (1991).

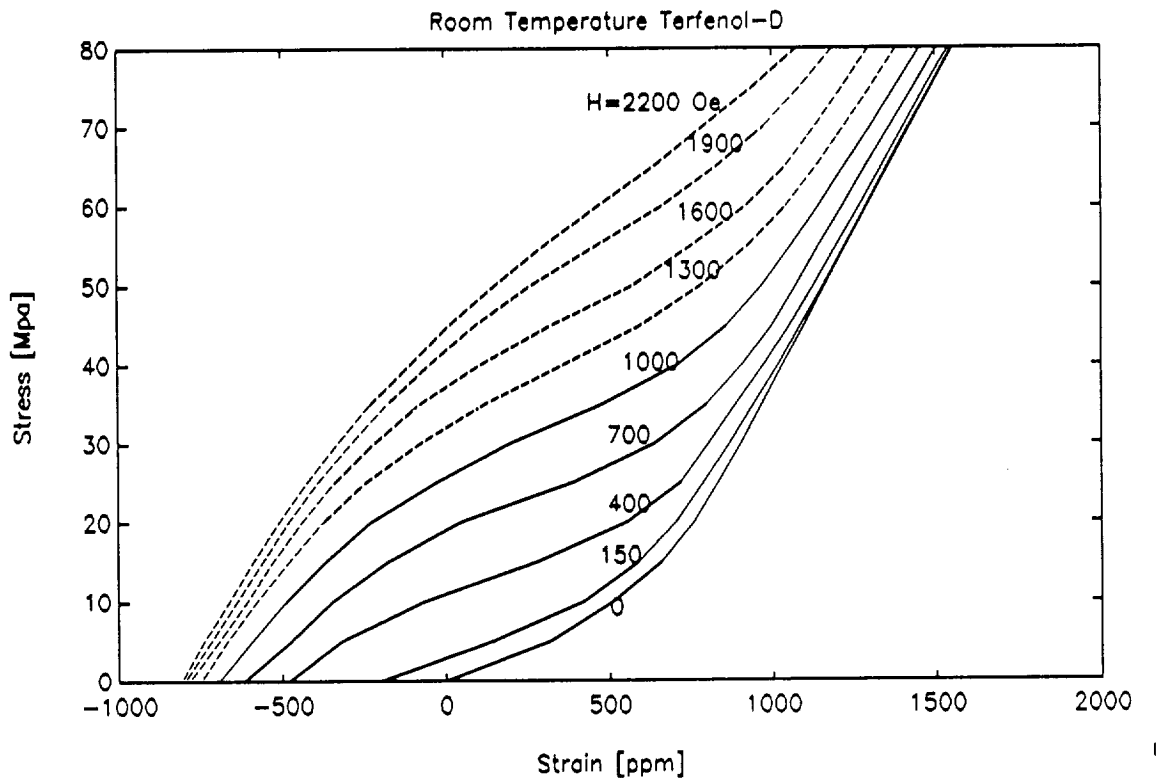


Figure 3-4. Anhyseretic stress σ vs. strain λ at various values of H , for standard composition Terfenol-D at room temperature, based on the data given in Fig. 4 of Ref. 3.

In this hexagonal case, there is no difference (to lowest order) between the anisotropy energy at constant strain and the anisotropy energy at constant stress.⁷ The analysis for a cubic material like Terfenol-D is more complicated, since the easy directions of magnetization (the [111] directions) are not all in the same plane, and furthermore the lowest order anisotropy energy K_1 nearly vanishes at the optimal ratio of terbium to dysprosium, and the higher order anisotropy terms then dominate. The expression for

⁷A. E. Clark, "Magnetostrictive rare earth-Fe₂ compounds," Ch. 7 of *Ferromagnetic Materials*, Vol. 1, E. P. Wohlfarth, ed., North-Holland, 1980; see p. 540.

μ_{rot} should be similar to Eqs. (3-11) and (3-12), with an unknown coefficient in front of the K , with a correction of order $-2\lambda_s^2 E$ as in Eq. (3-11), and with exactly the same stress term $2\lambda_s \sigma$ in the denominator. For purposes of designing magnetostrictive actuators, it is not necessary to be able to predict μ_{rot} and $\mu_{\text{wall,an}}$ from first principles, since $B_{\text{an}}(H, \sigma)$ and $\mu_{\text{rot}}(B, \sigma)$ can be found experimentally. For standard composition Terfenol-D ($\text{Tb}_{0.3}\text{Dy}_{0.7}\text{Fe}_{1.9}$) at room temperature, good data on $\epsilon(H)$ for a range of different stress values, including minor hysteresis loops, is given by Moffett et al.,³ and reproduced here as Fig. 3-3. This data, combined with data on $\epsilon(B)$ shown in Fig. 3-2, can be used to infer major and minor hysteresis loops for $B(H)$ at a range of different stresses. Moffett et al.⁵ also give hysteresis loops for strain versus stress at constant H , which is needed for the design of actuators if they are to be clamped, or to have a stiff load. In Fig. 3-4, we have plotted anhysteretic stress vs. strain curves for constant H , based on the data in Fig. 4 of Moffett et al.,³. A characteristic of these curves for any magnetostrictive material is that the slope (the elastic modulus) approaches a constant value when either H or σ is large; this is the purely mechanical elastic modulus without magnetomechanical coupling, since the magnetostrictive strain is saturated at large H or large σ . Although stress vs. strain curves are often plotted so that they all intersect the origin, they are more useful when plotted as we have done here, so that they approach the same asymptotic limit at large stress. In this way, it is possible to directly read off strain vs. H at constant stress, by taking a horizontal cross-section, or stress vs. H for a clamped actuator (constant strain) by taking a vertical cross-section, or stress and strain vs. H for a load of finite stiffness, by taking a diagonal cross-section of the appropriate slope.

Spano et al.² give data for $\epsilon(H)$ for various values of stress for TbDy at 77°K, reproduced here as Figs. 3-5. They do not explicitly give the strain vs. stress curves at constant H , but they do give the elastic modulus for $H = 0$ over a limited range of stress, and from this and their other data it is possible to find stress vs. strain curves at constant H in this range of stress, plotted in Fig. 3-6. TbDy cannot be used at much higher stress in any case, because it deforms. We are not aware of any published data for cryogenic Terfenol-D ($\text{Tb}_{0.45}\text{Dy}_{0.55}\text{Fe}_{1.9}$), but we have received some unpublished data³ on $\epsilon(H)$ and $B(H)$, taken at 77°K and at room temperature, showing the outer hysteresis loop only, at one value of stress (15.5 MPa). Our own test data for cryogenic Terfenol-D, described in Sec. 5, gives minor hysteresis loops as well, and extends the data to higher values of stress. The data from Clark³ also includes the small amplitude elastic modulus as a function of σ and H for $\text{Tb}_{0.5}\text{Dy}_{0.5}\text{Fe}_{1.95}$, but this is expected to be

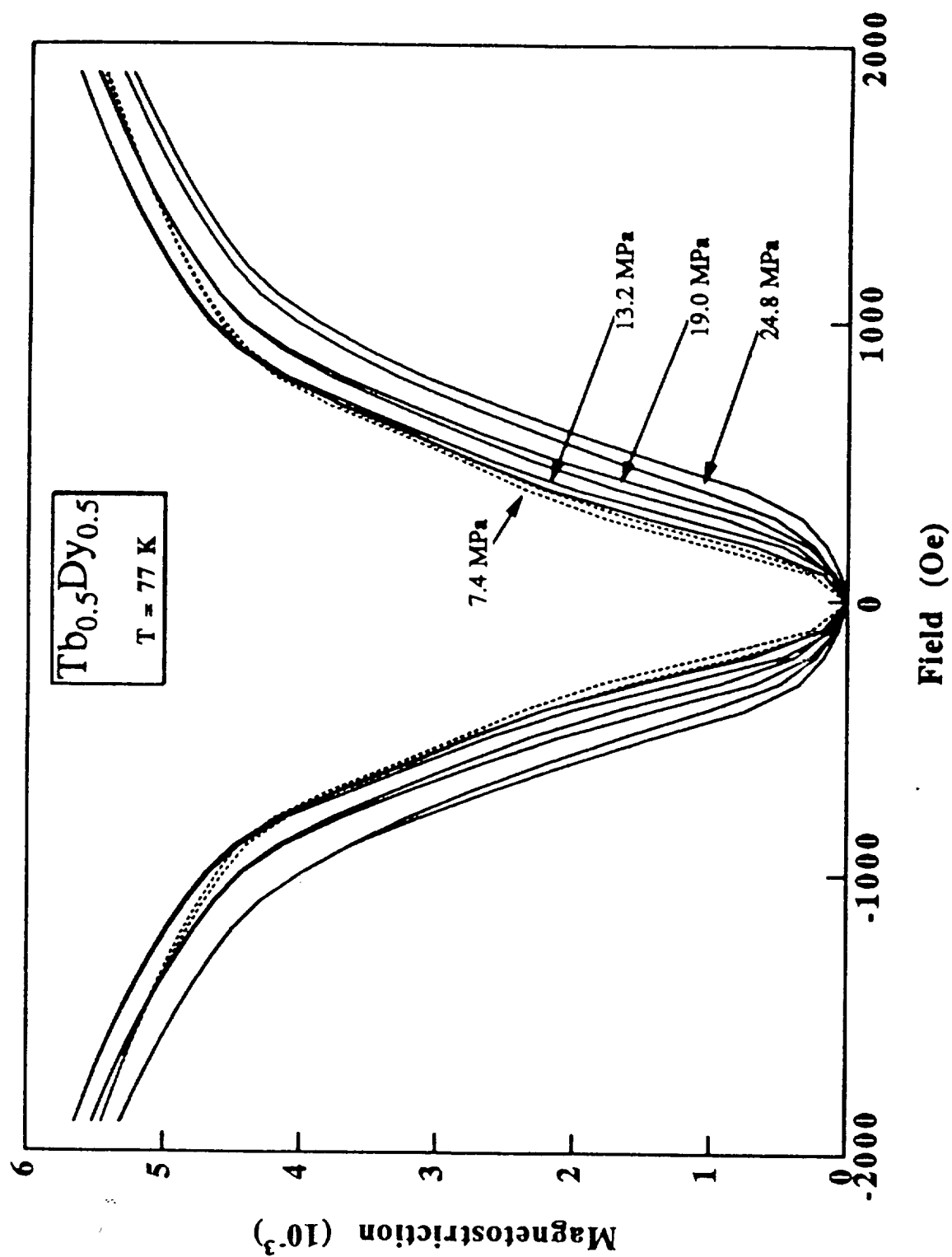


Figure 3-5. Magnetostrictive strain λ vs. H for various values of stress, for TbDy at 77° K, from Fig. 2 of Spano et al., IEEE Trans. MAG 26, 1751 (1990).

substantially greater than the large amplitude (anhysteretic) elastic modulus, and cannot be used directly to infer anhysteretic stress vs. strain curves at constant H . In Fig. 3-7, stress vs. strain curves at constant H are plotted for cryogenic Terfenol-D at 77° K, based on our test data given in Sec. 5, and using Clark's data for the elastic modulus when the Terfenol-D is saturated (in which regime there should be no difference between the large amplitude and small amplitude elastic modulus).

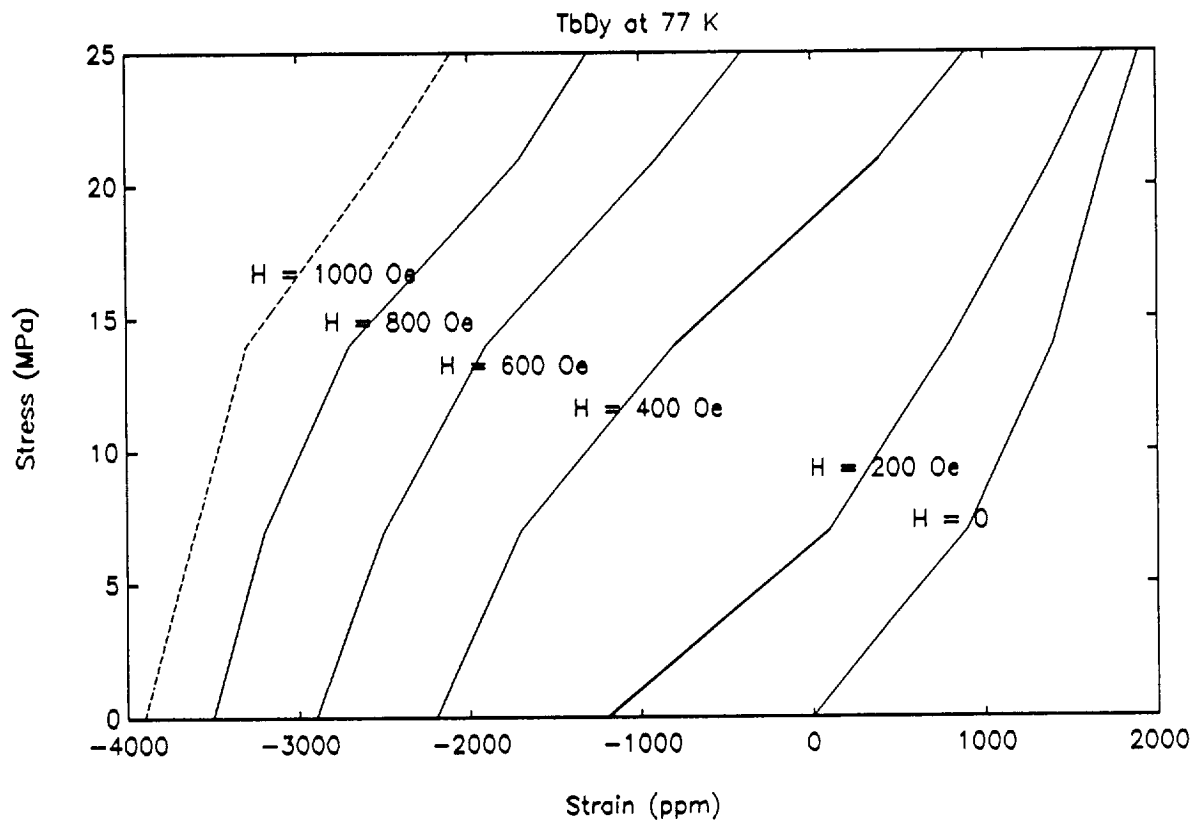


Figure 3-6. Stress vs. strain at various values of H for TbDy at 77° K.

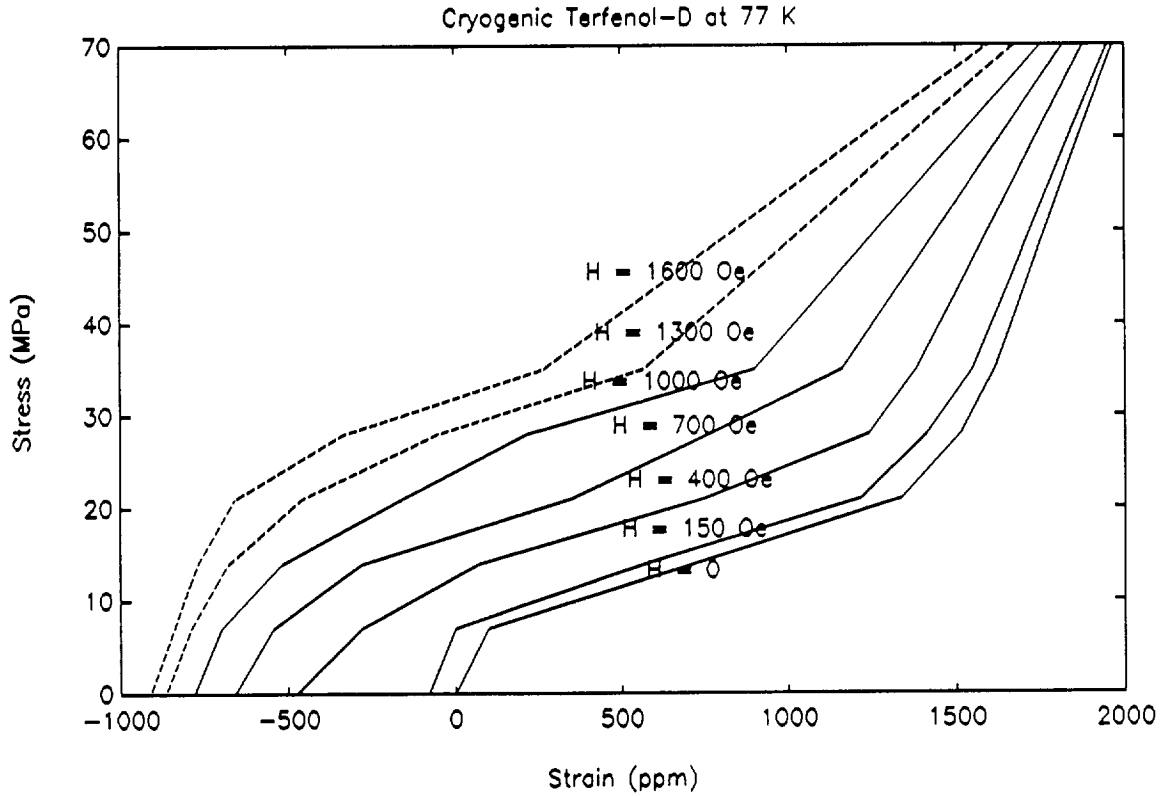


Figure 3-7. Anhyseretic stress vs. strain at various values of H for cryogenic Terfenol-D at 77°K.

3.3 Room Temperature Terfenol-D

From this data, we find that for room temperature Terfenol-D, the initial permeability is given to good approximation (at $B \ll B_{\text{sat}}$) by

$$\mu_{\text{rot}} = B_{\text{sat}}^2 / (1.0 \times 10^5 + 2\lambda_s \sigma) \quad (3-13)$$

in SI units, with $B_{\text{sat}} = 1$ tesla and $\lambda_s = 1.6 \times 10^{-3}$. The term $1.0 \times 10^5 \text{ J/m}^3$ in the denominator is only about one third of the anisotropy of Terfenol-D at constant strain, but the anisotropy at constant stress is substantially lower, due to the large coupling constant, so this expression is reasonable. At $\sigma = 14 \text{ MPa}$, $\mu_{\text{rot}} \approx 6\mu_0$, and falls to about half this value at 40 MPa. As expected, μ_{rot} smoothly decreases as B approaches B_{sat} .

The domain wall contribution $\mu_{\text{wall,an}}$ has its greatest value, about $18\mu_0$, at $\sigma = 6.5 \text{ MPa}$, and rapidly decreases at higher σ , being $10\mu_0$ at 13 MPa, $7\mu_0$ at 19 MPa, and $4\mu_0$ at 25 MPa. (The fact that the initial permeability, given by Eq. (3-13), falls off much more

slowly with increasing stress indicates that the initial permeability is due almost entirely to rotation, with no significant contribution from bowing of domain walls.) These are the maximum values of $\mu_{\text{wall,an}}$, which occur (except for 25 MPa) at low B, and decrease at higher B, becoming very small above 0.6 tesla (at which point almost all of the domains have their magnetization in the easy direction 35.26° from the rod axis). At 25 MPa, $\mu_{\text{wall,an}}$ is smaller at B below 0.2 tesla, is greatest at about 0.4 tesla, and again is very small above 0.6 tesla. The reason for this behavior is that at 25 MPa, the energy is substantially higher for magnetization in the easy direction 35.26° from the rod axis than it is for magnetization in the easy direction perpendicular to the axis, so B increases at first due to rotation, and only at higher H are there enough domains with magnetization in the easy direction 35.26° from the axis to allow domain wall motion to make a substantial contribution. This should be even more true at higher stress.

The coercivity H_c is about 25 oersted at all values of stress and B for which domain wall motion makes an important contribution to the permeability. H_c falls off somewhat at higher B, especially at $B > 0.6$ tesla, but not as rapidly as $\mu_{\text{wall,an}}$ does. At $B = 0.6$ tesla, for example, $\mu_{\text{wall,an}}$ is much smaller than at low B, while H_c has only fallen to about 15 oersted.

3.4 Cryogenic Terfenol-D

For cryogenic Terfenol-D, at 77°K, the magnetic anisotropy is considerably higher, and we find from our test data that the initial permeability is given to good approximation by

$$\mu_{\text{rot}} = B_{\text{sat}}^2 / (5.7 \times 10^5 + 2\lambda_s \sigma) \quad (3-14)$$

where $B_{\text{sat}} = 1.25$ tesla and $\lambda_s = 2.5 \times 10^{-3}$. Comparing this expression to Eqs. (3-12) and (3-13) indicates that the anisotropy at constant stress, $K - 2\lambda_s^2 E$, is 5 or 6 times greater for cryogenic Terfenol-D at 77°K than it is for room temperature Terfenol-D. Although we have not found in the literature any direct data on $K - 2\lambda_s^2 E$ for Terfenol-D as a function of temperature and composition, there is data⁸ showing that K for DyFe_2 increases by a factor of 20 in going from room temperature to 77°K, so it is not surprising that, even with the composition optimized for each temperature, $K - 2\lambda_s^2 E$ for Terfenol-D increases by a factor of 5 or 6.

⁸A. E. Clark, R. Abundi, and W. G. Gillmor, IEEE Trans. Mag. MAG-14, 542 (1978); reproduced in Fig. 22 of Ref. 4.

Eq. (3-14) gives $\mu_{\text{rot}} \approx 2\mu_0$ at σ less than or equal to 14 MPa, and our test data for cryogenic Terfenol-D at 77°K shows $\mu_{\text{wall,an}} \approx 18\mu_0$ for low B at these values of σ , so domain wall motion is much more important than rotation. As in the case of room temperature Terfenol-D, $\mu_{\text{wall,an}}$ gradually decreases at higher B (almost vanishing for B > 1.0 tesla), and at higher stress. At $\sigma = 35$ MPa, $\mu_{\text{wall,an}} \approx 10\mu_0$, while at $\sigma = 70$ MPa, $\mu_{\text{wall,an}} \approx 3\mu_0$. Expressed as a function of the dimensionless stress parameter $\lambda_s \sigma / (K - 2\lambda_s^2 E)$, $\mu_{\text{wall,an}}$ is nearly the same for cryogenic Terfenol-D at 77°K and for room temperature Terfenol-D.

The hysteresis associated with domain wall motion in cryogenic Terfenol-D at 77°K is much greater than in room temperature Terfenol-D, with $H_c \approx 300$ oersted at low B, decreasing to about 150 oersted at B = 0.9 tesla. The hysteresis could probably be substantially reduced if the anisotropy $K - 2\lambda_s^2 E$ were reduced, since that would make domain wall motion less important relative to rotation (which has no hysteresis), and might also directly reduce the hysteresis associated with domain wall motion, if there is some relation between anisotropy and the strength of pinning sites. Theoretically, it should be possible to reduce the anisotropy (at some cost in maximum strain λ_s) by adding holmium to the Terfenol-D, since having three different rare earth elements should make it possible to zero out the second moment of anisotropy as well as the first moment. Efforts are currently underway by Clark to test samples of cryogenic Terfenol-D with various ratios of Tb, Dy, and Ho, supplied by Etrema, to determine the composition with the minimum hysteresis.⁹

3.5 Terbium-Dysprosium

Data on B(H) and e(B) for TbDy at 77°K is given by Spano et al.² at various values of stress. They show that the permeability has a higher value at intermediate values of H, due to 60° domain wall motion, than it does at lower and higher H, where rotation is more important. Hysteresis is negligible at B > 0.6B_{sat} (where B_{sat} = 3 tesla), showing that domain wall motion is negligible in this regime, as expected, but hysteresis falls off only slightly at low H, showing that $\mu_{\text{wall,an}}$, while lower than at intermediate H, is not negligible compared to μ_{rot} . They do not give data for the initial permeability, only for the anhysteretic permeability, so it is not possible to tell from their data what μ_{rot} and $\mu_{\text{wall,an}}$ are at low H, only what their sum is. It is possible to tell what μ_{rot} is at B >

⁹Mel J. Goodfriend, personal communication, 1992.

$0.6B_{\text{sat}}$, where the magnetization is being rotated toward the rod axis from the easy direction 30° away from the rod axis, but in this regime μ_{rot} should have a different dependence on stress and anisotropy than it does at low H , so this data cannot be used to verify Eq.(3-12). A further complication is that they say that their magnetic circuit has a finite reluctance, but do not say what it is, and only give the data in terms of "applied H ", i.e., NI/ℓ , not in terms of the internal H of the TbDy, so the actual permeability ought to be higher than the permeability data they give. Our test data at a stress of 20 MPa, given in Sec. 6, indicates that $\mu_{\text{rot}} \approx \mu_{\text{an,wall}} \approx 14\mu_0$ at intermediate H , and nearly the same at low H .

If we assume that $B_{\text{sat}} = 3$ tesla and $\lambda_s = 6 \times 10^{-3}$, from the data of Spano et al.,⁴ and use the result from our test data that $\mu_{\text{rot}} \approx 14\mu_0$ at a stress of 12.5 MPa or 20 MPa, we find that μ_{rot} is given by Eq. (3-12) with $18K \approx 3.9 \times 10^5$ pascals (intermediate between the anisotropy terms in room temperature and cryogenic Terfenol-D),

$$\mu_{\text{rot}} = \frac{B_{\text{sat}}^2}{3.9 \times 10^5 + 2\lambda_s \sigma} \quad (3-15)$$

It was not possible to verify in our tests that $B_{\text{sat}} = 3$ tesla and $\lambda_s = 6 \times 10^{-3}$ in TbDy, because, for reasons explained in Sec. 5, our TbDy rod had silicon-iron extensions on it which saturated before the TbDy did.

The hysteresis, even at intermediate H where domain wall motion is important, is much lower in TbDy than in cryogenic Terfenol-D, and even somewhat lower than in room temperature Terfenol-D, having $H_c \approx 15$ oersted for $B < 0.6B_{\text{sat}}$, pretty much independent of H and stress, and much lower H_c for $B > 0.6B_{\text{sat}}$.

3.6 Operation at Zero Stress

At zero stress, the hysteresis, in both room temperature and cryogenic Terfenol-D, is much lower than at higher stress, because at zero stress a substantial fraction of the domains have magnetization in the easy direction 35.26° from the rod axis even at $H = 0$. At $H = 0$, of course, there are just as many domains with magnetization pointing in

one direction as in the opposite direction, and there are domain walls which separate domains whose magnetization direction is 180° apart. These 180° domain walls make a large contribution to permeability, because they move more easily than the domain walls that separate domains whose magnetization directions are 70.52° apart, and B rapidly rises to about $0.6B_{\text{sat}}$ at very low H . Beyond this point, most of the domains have magnetization in an easy direction 35.26° from the rod axis, and domain wall motion makes relatively little contribution to the permeability, which is dominated by rotation. Because there is no hysteresis associated with rotation, H_c at this point is about half as great as it is at higher values of stress, 7 MPa and above, where 70.52° domain wall motion is important. The total magnetostrictive strain is substantially less at zero stress than at higher stress, since the change in B due to 180° domain wall motion does not result in any change in strain, and there is very little change in B due to 70.52° domain wall motion, so only the change in B due to rotation (from $B \approx 0.6B_{\text{sat}}$ up to B_{sat}) contributes much to the strain.

3.7 Linear High Frequency Model

If NI is changing sufficiently slowly so that skin effects are unimportant, then Eq. (3-7), combined with Eqs. (3-8) and (3-9), and the appropriate expressions for $\epsilon(B)$, $\mu_{\text{wall,an}}$ and μ_{rot} for the variety of Terfenol being used, can be used to find ϵ , as well as B and H in the Terfenol, as a function of time. At higher frequencies, where skin effects are important, finding $\epsilon(t)$ becomes extremely difficult in the general nonlinear case, requiring the solution of an integral equation in time, but the problem is tractable analytically if we assume that B_{Terf} is a linear function of H_{Terf} . In general there will be a bias H , due to the permanent magnets and perhaps a dc current, and H will vary around this point, so that

$$B_{\text{Terf}} = B_{\text{an}}(H_{\text{bias}}) + (H - H_{\text{bias}})\mu_T \quad (3-16)$$

Equation (3-7), with $B_{\text{Terf}} = B_{\text{an}}(H_{\text{Terf}})$, can be used to find H_{bias} given the permanent magnet parameters and dc current. The ac B and H , including skin effects in the Terfenol and permanent magnet, are then found by solving a second order linear ordinary differential equation in the radial coordinate, derived from Maxwell's equations with constant permeability μ_T in the Terfenol, valid for long thin cylindrical geometry. Physically, this is valid either for small perturbations in H , much less than H_c , in which case μ_T should be set equal to the initial permeability μ_{rot} , or to perturbations much greater than H_c , but still much less than $B_{\text{sat}}/\mu_{\text{an}}$, in which case μ_T should be set equal to

the anhysteretic permeability μ_{an} . In either case, it is possible to treat the hysteresis as a small perturbation and calculate the phase shift and power dissipation due to hysteresis, once the ac B and H are found.

This analysis, which is largely taken from the Phase I final report, also includes the options of having thin planar laminations in the Terfenol, instead of using a solid piece, and of either having a single solid permanent magnet surrounding the coil, or slitting it lengthwise. Laminating the Terfenol, or slitting the permanent magnet, greatly reduces the eddy currents. Although it might seem that choosing either of these options would destroy the cylindrical symmetry assumed in the analysis, making the analysis invalid, we will show that in fact the fields are still nearly cylindrically symmetric outside the Terfenol and the permanent magnets, and that the effects of these options can be treated by making appropriate changes in the boundary conditions. In all of our actuators, the Terfenol was not laminated, but the permanent magnet was slit, consisting of several magnets arranged azimuthally around the coil with gaps between them.

In addition to making some minor corrections in the equations used in the Phase I final report, we also allow the long thin parameter ℓ^2/r_T^2 to be less than μ_T/μ_0 , although it must still be much greater than 1. This means that the effect of finite external reluctance \mathfrak{R}_{ext} on the ac fields is included. (In the Phase I final report, we included the effect of finite external reluctance on the bias field due to the permanent magnet, but implicitly assumed $\ell^2/r_T^2 \gg \mu_T/\mu_0$, neglecting the external reluctance, in calculating the ac fields.)

The analysis starts with the Maxwell equations

$$\nabla \times \underline{H} = \underline{J} = \underline{J}_{ext} + \eta^{-1}\underline{E} \quad (3-17)$$

$$\nabla \times \underline{E} = -\frac{\partial \underline{B}}{\partial t} = j\mu\omega\underline{H} \quad (3-18)$$

where $j = \sqrt{-1}$, \underline{J}_{ext} is the external ac current (present only in the coil), \underline{H} and \underline{E} are the ac magnetic and electric fields induced by the current, η is the resistivity, μ is the permeability, and ω is the frequency of excitation of the coil. The permanent magnet is assumed to be near saturation, so that its μ is close to the vacuum permeability $\mu_0 = 4\pi \times 10^{-7}$. The coil is assumed to be nonmagnetic, of course, so only the Terfenol-D has a permeability, μ_T , that differs appreciably from μ_0 . The term $\eta^{-1}\underline{E}$ represents the eddy current density. The wires in the coil are assumed to be thin enough, much thinner than

a skin depth, so that eddy currents in the coil are negligible, and the $\eta^{-1}\mathbf{E}$ term is not included in the coil. For the Terfenol-D and the permanent magnet, the resistivities are η_T and η_m . The skin depths are

$$\delta_T = (2\eta_T/\mu_T\omega)^{1/2} \text{ for the Terfenol} \quad (3-19)$$

$$\delta_m = (2\eta_m/\mu_0\omega)^{1/2} \text{ for the magnet} \quad (3-20)$$

Eliminating \mathbf{H} from the two Maxwell equations yields

$$\nabla \times \nabla \times \underline{\mathbf{E}} - \frac{2j\underline{\mathbf{E}}}{\delta^2} = j\mu\omega\underline{\mathbf{J}}_{\text{ext}} \quad (3-21)$$

From the symmetry of the problem, \mathbf{E} and \mathbf{J}_{ext} are in the θ direction, \mathbf{H} is in the z direction, and ∇ is in the r direction, so we obtain a second-order ordinary differential equation for E

$$\frac{d}{dr} \frac{1}{r} \frac{d}{dr} rE + \frac{2jE}{\delta^2} = -j\mu\omega J_{\text{ext}} \quad (3-22)$$

with H given by

$$H = \frac{-j}{\mu\omega r} \frac{d}{dr} rE. \quad (3-23)$$

where now E and H are scalar quantities. The equation for E must be solved in five regions, the Terfenol-D, the air gap between the Terfenol-D and coil, the coil, the air gap between the coil and magnet, and the magnet. The current J_{ext} is equal to J_c in the coil and zero everywhere, and the skin depth δ is equal to δ_T in the Terfenol-D, δ_m in the magnet, and infinity everywhere else. The radius of the Terfenol-D is r_T , the inner and outer radii of the coil are r_{ic} and r_{oc} , and the inner and outer radii of the magnet are r_{im} and r_{om} . The coil, Terfenol-D, and magnet all have length ℓ . At the boundaries between the regions, E and H are continuous. If the Terfenol-D is not laminated, we also have the boundary condition

$$E = 0 \quad \text{at } r = 0 \quad (3-24)$$

and if the magnet does not have a slit, and we neglect the external reluctance (valid if $\ell^2/r_T^2 \gg \mu_T/\mu_0$), then we have

$$H = 0 \quad \text{at } r = r_{om} \quad (3-25)$$

If the Terfenol-D is laminated or the magnet does have a slit, or if we include the external reluctance, then they must be treated differently. For the moment, we will express E/H at $r = r_T$ and $r = r_{im}$ as free parameters and find $E(r)$ and $H(r)$ in the coil and air gaps, and hence the inductance L , as a function of these parameters. We will then go back and evaluate the parameters for the cases where the Terfenol-D is or is not laminated, and the magnet does or does not have a slit, including the external reluctance. We define the dimensionless parameters

$$R_m = \frac{-jE(r_{im})}{\mu_0 \omega r_{im} H(r_{im})} \quad (3-26)$$

$$R_T = \frac{-jE(r_T)}{\mu_0 \omega r_T H(r_T)} \quad (3-27)$$

We are not actually interested in finding $E(r)$ for its own sake, but only as a means of finding the inductance L of the coil, and the relation between the ac coil current and the average ac magnetic field $\langle H \rangle_T$ in the Terfenol-D. To do this we only need to know $H(r)$, although of course it will be necessary to solve for $E(r)$ in order to find $H(r)$. Furthermore, we do not need to know $H(r)$ outside the coil, since that does not contribute to L , and we do not need to know the form of $H(r)$ inside the Terfenol-D, only the total flux $\pi r_T^2 \mu_T \langle H \rangle_T$, and this is proportional to $E(r_T)$, and hence to R_T ,

$$\pi r_T^2 \mu_T \langle H \rangle_T = -2j\pi r_T E(r_T)/\omega = 2\pi r_T^2 \mu_0 R_T H(r_T) \quad (3-28)$$

Thus all of the effects of the Terfenol-D and the magnet on L , and on $\langle H \rangle_T$, are described by the parameters R_T and R_m . In the air gaps,

$$\frac{dH}{dr} = 0 \quad (3-29)$$

and in the coil,

$$\frac{dH}{dr} = -J_C \quad (3-30)$$

so $H(r)$ in the coil is

$$H(r) = H(r_T) - (r - r_{ic})J_c \quad (3-31)$$

and the change in H across the coil is

$$\Delta H \equiv H(r_T) - H(r_{im}) = (r_{oc} - r_{ic})J_c = \frac{NI}{\ell} \quad (3-32)$$

where N is the number of turns in the coil, and I is the coil current. The inductance L is the ratio of the current to the flux linking the current, and is given by

$$L = \frac{\pi \mu_0 N^2}{\ell} \left(\frac{H(r_T)}{\Delta H} \left[r_T^2 (2R_T - 1) + \frac{r_{oc}^2 + r_{oc}r_{ic} + r_{ic}^2}{3} \right] - \frac{(r_{oc}^2 - r_{ic}^2)}{6} \right) \quad (3-33)$$

The first term is the flux going through the Terfenol-D, minus the flux that would go through this region if the Terfenol-D were replaced with air. The second term is the total flux through the coil and inside the coil, if there were no Terfenol-D. The third term is a correction due to the fact that the flux through the coil is not linking all of the current, but is passing outside some of the current. The quantity $H(r_T)/\Delta H$ can be calculated only by first solving the differential equation for $E(r)$ in the coil and air gaps. After some straightforward but tedious algebra, we obtain

$$\frac{H(r_T)}{\Delta H} = \frac{\frac{r_{oc}^2 + r_{oc}r_{ic} + r_{ic}^2}{3} + (2R_m - 1)r_{im}^2}{(2R_m - 1)r_{im}^2 - (2R_T - 1)r_T^2} \quad (3-34)$$

We now find R_T and R_m , considering first R_T in the case where the Terfenol-D is not laminated. The differential equation for $E(r)$ is then Bessel's equation with the boundary condition $E(r) = 0$ at $r = 0$, and we find

$$R_T = \frac{(1-j)}{2} \left(\frac{\delta_T \mu_T}{r_T \mu_0} \right) \frac{J_1((1+j)r_T/\delta_T)}{J_0((1+j)r_T/\delta_T)} \quad (3-35)$$

The Bessel functions of complex argument $(1+j)r_T/\delta_T$ may be expressed in terms of Thomson functions ber_0 , bei_0 , ber_1 , and bei_1 with real argument r_T/δ_T . If the Terfenol-D is thinly laminated, so that the laminations can be treated as infinite planes, then

between the laminations $H = H(r_T)$, and within a lamination we can find $H(x)$, where x is the distance across the lamination the short way by solving the differential equation

$$\frac{d^2 H}{dx^2} + \frac{jH}{\delta_T^2} = 0 \quad (3-36)$$

with boundary conditions $H = H(r_T)$ at the surfaces $x = \pm \Delta/2$, where Δ is the width of the laminations. Then the average H in the Terfenol-D is

$$\langle H \rangle_T = (1-j) \left(\frac{\delta_T}{\Delta} \right) H(r_T) \tan \left(\frac{(1+j) \Delta}{2\delta_T} \right) \quad (3-37)$$

and making use of Eq. (3-30), we obtain

$$R_T = \frac{(1-j)}{2} \left(\frac{\delta_T}{\Delta} \right) \left(\frac{\mu_T}{\mu_0} \right) \tan \left(\frac{(1+j) \Delta}{2\delta_T} \right) \quad (3-38)$$

The lack of cylindrical symmetry inside the Terfenol-D has negligible effect on the cylindrical symmetry of the fields at distances much greater than Δ outside the Terfenol-D.

If there is no slit in the permanent magnet, then we solve the differential equation for $E(r)$ in the magnet, which is also in the form of Bessel's equation, subject to the boundary condition

$$H(r_{om}) = 2\pi j r_{om} \mathfrak{R}_{ext} E(r_{om}) / \omega \ell \quad (3-39)$$

where from Eq. (3-6) the external reluctance $\mathfrak{R}_{ext} = 4/\pi\mu_0\ell$. The reason for this boundary condition is that $-2\pi j r_{om} E(r_{om})/\omega$ is the net flux inside r_{om} , so the total flux outside r_{om} is $2\pi j r_{om} E(r_{om})/\omega$, and the magnetic potential $H(r_{om})\ell$ is equal to this flux times the external reluctance. We then obtain

$$R_m = \frac{A_1 J_1(\chi_{im}) - A_2 Y_1(\chi_{im})}{\chi_{im} A_1 J_0(\chi_{im}) - \chi_{im} A_2 Y_0(\chi_{im})} \quad (3-40)$$

where

$$\begin{aligned} A_1 &= 4\delta_m^2 \chi_{om} Y_1(\chi_{om}) - \ell^2 Y_0(\chi_{om}) \\ A_2 &= 4\delta_m^2 \chi_{om} J_1(\chi_{om}) - \ell^2 J_0(\chi_{om}) \end{aligned}$$

$\chi_{im} = (1+j)r_{im}/\delta_m$, and $\chi_{om} = (1+j)r_{om}/\delta_m$. In the limit that the magnet is thin, $r_{om} - r_{im} \ll r_{im}$, this reduces to

$$R_m \approx \frac{\ell^2 \cos(\chi_{om} - \chi_{im}) - 4\delta_m^2 \chi_{om} \sin(\chi_{om} - \chi_{im})}{\chi_{im} [\ell^2 \sin(\chi_{om} - \chi_{im}) - 4\delta_m^2 \chi_{om} \cos(\chi_{om} - \chi_{im})]} \quad (3-41)$$

If $r_{om} - r_{im} > \delta_m$, then eddy currents in the magnet cause much of the flux to be trapped between the coil and the magnet. This can result in substantial power dissipation in the magnet. If there is a slit in the magnet, then eddy currents in the magnet cannot encircle the coil, and flux cannot be trapped between the coil and the magnet. The boundary condition is then like Eq. (3-39) but evaluated at r_{im} instead of r_{om} ,

$$H(r_{im}) = 8jr_{im}E(r_{im})/\mu_0\omega\ell^2 \quad (3-42)$$

so

$$R_m = -\ell^2/8r_{im}^2 \quad (3-43)$$

Eq. (3-40) reduces to Eq. (3-43) in the limit that $\delta_m \gg r_{om} - r_{im}$.

3.8 Power Dissipation

The inductance L given by Eq. (3-33) is in general complex because R_T and $H(r_T)/\Delta H$ have imaginary parts. The imaginary part of ωL is the resistive impedance due to eddy current dissipation in the Terfenol-D and the magnet. The total power dissipated is

$$P = \frac{1}{2}(R + \omega \text{Im}L)I^2 + RI_{\text{bias}}^2 = P_c + P_T + P_m \quad (3-44)$$

where the power dissipated in the Terfenol-D is

$$P_T = \frac{\pi\mu_0 N^2 I^2 \omega r_t^2}{\ell} \text{Re} \left(\frac{H(r_T)}{\Delta H} \right) \text{Im}(R_T), \quad (3-45)$$

the power dissipated in the magnet is

$$P_m = \frac{\pi\mu_0 N^2 I^2 \omega}{2\ell} \text{Im} \left(\frac{H(r_T)}{\Delta H} \right) \left[(2\text{Re}(R_T) - 1)r_T^2 + \frac{1}{3}(r_{oc}^2 + r_{oc}r_{ic} + r_{ic}^2) - (r_{oc}^2 - r_{ic}^2) \right] \quad (3-46)$$

and the power dissipated in the coil is

$$P_c = \frac{I^2 R}{2} + I_{\text{bias}}^2 R \quad (3-47)$$

where R is the coil resistance, I is the peak ac current, and I_{bias} is the dc current. If there is a slit in the magnet, then $\text{Im}\{H(r_T)/\Delta H\} = 0$, so $P_m = 0$ according to Eq. (3-46), which is valid to lowest order in the aspect ratio r/ℓ . But the higher order contributions to P_m may be significant for parameters of interest, so we estimate an upper limit to P_m in that case:

$$P_m < \left(\frac{2\pi}{3} \right) \frac{N^2 I^2 \omega}{\ell^2 \delta_m^2} (r_{om} - r_{im})^3 (r_{om} + r_{im}) r_T |2\mu_T \mu_0 R_T|^{1/2} \quad (3-48)$$

The coil resistance is

$$R = \frac{\pi(r_{oc} + r_{ic})N^2 \eta_c}{(r_{oc} - r_{ic})\ell F_c} \quad (3-49)$$

where η_c is the coil resistivity and F_c is the fill factor.

In addition to resistive dissipation in the coil and eddy current dissipation in the Terfenol-D and permanent magnet, there is also dissipation due to hysteresis in the Terfenol-D. (We neglect hysteresis loss in the magnet, since it is a rare earth magnet close to saturation.) This tends to be the dominant power loss at high frequencies, especially if eddy current losses are reduced by laminating the Terfenol-D and putting a slit in the magnet. This power is

$$P_h = \frac{r_T^2 \ell \omega}{2} \oint H dB \quad (3-50)$$

where the integral is over the hysteresis loop. For $\langle H \rangle_T \gg H_c$, the area of the hysteresis loop is

$$\oint H dB \approx 4\mu_{an}H_c\langle H \rangle_T \quad (3-51)$$

while for $\langle H \rangle_T \ll H_c$, it is

$$\oint H dB \approx 2\mu_{rot}\langle H \rangle_T^3/H_c \quad (3-52)$$

3.9. Passive Damper

If the coil in a magnetostrictive actuator is shorted out, with finite resistance, then it becomes a passive damper, converting mechanical energy into electrical energy which is dissipated in the coil. This occurs because the permanent magnets produce flux Φ in the Terfenol-D even without current, and this flux varies with the externally applied stress σ , because the permeability of the Terfenol-D varies with stress. The change in flux induces an emf in the coil, which drives current.

The time-averaged dissipated mechanical power may be expressed as

$$P_{mech} = \frac{\omega}{2\pi} \ell_{Terf} A_{Terf} \oint d\epsilon \sigma \quad (3-53)$$

where ϵ is the strain, $\ell_{Terf} A_{Terf}$ is the volume of the Terfenol-D, and ω is the frequency at which the stress is being varied. This must be equal to the time-averaged dissipated electric power

$$P_{elec} = \frac{\omega}{2\pi} \int_0^{2\pi} dt I^2 R \quad (3-54)$$

where I is current in the coil, and R is the coil resistance. To show that these two expressions are equal, we note that

$$\oint d\epsilon \sigma = -\oint dB H \quad (3-55)$$

where H and B are the average magnetic field and flux density in the Terfenol-D, because

$$\sigma = -\left(\frac{\partial U}{\partial \epsilon}\right)_B \quad (3-56)$$

$$H = \left(\frac{\partial U}{\partial B}\right)_\epsilon \quad (3-57)$$

where $U(\epsilon, B)$ is the internal energy density of the Terfenol-D. Since $\Phi = A_{\text{Terf}} B$ and $NI = \ell_{\text{Terf}} H + \Phi \mathfrak{R}_{\text{ext}}$, where $\mathfrak{R}_{\text{ext}}$ is the external reluctance (and neglecting the reluctance $\mathfrak{R}_{\text{coil}}$ due to the finite coil thickness), we find

$$\ell_{\text{Terf}} A_{\text{Terf}} \oint d\epsilon \sigma = -\ell_{\text{Terf}} A_{\text{Terf}} \oint dB H = -\oint d\Phi NI = -N \int_0^{2\pi} dt I \frac{d\Phi}{dt} \quad (3-58)$$

where we have used the fact that $\oint d\Phi \mathfrak{R}_{\text{ext}} = 0$ because $\mathfrak{R}_{\text{ext}}$ is constant. Because the total coil voltage is $N d\Phi/dt + IR = 0$, the last expression is just the time integral from 0 to $2\pi/\omega$ of $I^2 R$, and it follows that $P_{\text{mech}} = P_{\text{elec}}$.

To evaluate the dissipated power for a given applied variation in stress, we write H , B , and σ as an equilibrium part and a perturbed part

$$\begin{aligned} \sigma &= \sigma^{(0)} + \sigma^{(1)} e^{-j\omega t} \\ B &= B^{(0)} + B^{(1)} e^{-j\omega t} \\ H &= H^{(0)} + H^{(1)} e^{-j\omega t} \end{aligned}$$

Since there is no equilibrium current in the coil,

$$I = I^{(1)} e^{-j\omega t} \quad (3-59)$$

The equilibrium quantities must satisfy the zero-order equations

$$\begin{aligned} \ell_{\text{Terf}} H^{(0)} &= A_{\text{mag}} B_r \mathfrak{R}_{\text{ext}} - A_{\text{Terf}} \mathfrak{R}_{\text{ext}} B^{(0)} \\ B^{(0)} &= B_{\text{Terf}}(H^{(0)}, \sigma^{(0)}) \end{aligned} \quad (3-60)$$

where $B_{\text{Terf}}(H, \sigma)$ depends on the properties of the Terfenol-D, and may be found from the data in Fig. 3-2 and Fig. 3-4 (for room temperature Terfenol-D), Fig. 3-7 (for cryogenic Terfenol-D), or Fig. 3-6 (for TbDy). We have neglected $\mathfrak{R}_{\text{coil}}$ here. The first order equations are

$$RI^{(1)} = -NA_{Terf} \frac{dB^{(1)}}{dt} = j\omega NA_{Terf} B^{(1)} \quad (3-61)$$

$$H^{(1)} = \sigma^{(1)} \left(\frac{\partial H}{\partial \sigma} \right)_{I=0} + I^{(1)} \left(\frac{\partial H}{\partial I} \right)_\sigma \quad (3-62)$$

$$B^{(1)} = \sigma^{(1)} \left(\frac{\partial B}{\partial \sigma} \right)_{I=0} + I^{(1)} \left(\frac{\partial B}{\partial I} \right)_\sigma \quad (3-63)$$

where

$$\left(\frac{\partial H}{\partial I} \right)_\sigma = \frac{-A_{Terf} \Re_{ext}}{\ell_{Terf}} \left(\frac{\partial B}{\partial I} \right)_\sigma - \frac{N}{\ell_{Terf}} \quad (3-64)$$

$$\left(\frac{\partial B}{\partial I} \right)_\sigma = \left(\frac{\partial B_{Terf}}{\partial H} \right)_\sigma \left(\frac{\partial H}{\partial I} \right)_\sigma \equiv \mu_T \left(\frac{\partial H}{\partial I} \right)_\sigma \quad (3-65)$$

The Terfenol-D permeability at constant stress, μ_T , is either the initial permeability μ_{rot} , if the perturbation is small compared to hysteresis (i.e. $H^{(1)} \ll H_c$), or the anhysteretic permeability μ_{an} if the perturbation is large, $H^{(1)} \gg H_c$. If $H^{(1)}$ is comparable to H_c , then μ_T will be intermediate between these limits, and will have a significant imaginary part, due to hysteresis. It will also have a significant imaginary part if the frequency is high enough for skin effects to be important. Hysteresis and skin effects can both cause damping in addition to the damping caused by the resistance of the coil. We will neglect hysteresis and skin effects in this analysis, but their contribution to damping can be derived from our equations by assigning an appropriate imaginary part to μ_T . The partial derivatives $(\partial H / \partial \sigma)_{I=0}$ and $(\partial B / \partial \sigma)_{I=0}$ can be found from the data in Fig. 3-4, 3-5 or 3-7, together with the data in Fig. 3-2 and Eq. (3-7).

Eliminating $I^{(1)}$ from these equations, we obtain expressions for $H^{(1)}$ and $B^{(1)}$ in terms of $\sigma^{(1)}$,

$$H^{(1)} = \sigma^{(1)} \left[\left(\frac{\partial H}{\partial \sigma} \right)_{I=0} + \left(\frac{\partial B}{\partial \sigma} \right)_{I=0} \frac{j\omega N^2 A_{Terf}}{(\ell_{Terf} + A_{Terf} \Re_{ext} \mu_T) R - j\omega N^2 A_{Terf} \mu_T} \right] \quad (3-66)$$

$$B^{(1)} = \sigma^{(1)} \left(\frac{\partial B}{\partial \sigma} \right)_{I=0} \frac{(\ell_{Terf} + A_{Terf} \Re_{ext} \mu_T) R}{(\ell_{Terf} + A_{Terf} \Re_{ext} \mu_T) R - j\omega N^2 A_{Terf} \mu_T} \quad (3-67)$$

The dissipated power is

$$P = \omega \operatorname{Im}\{H^{(1)*} B^{(1)}\} A_{Terf} \ell_{Terf} \quad (3-68)$$

where the asterisk indicates the complex conjugate. If we assume that μ_T is real (i.e. we neglect damping due to hysteresis and eddy currents), then we find, after some algebraic manipulation,

$$P = \frac{[\sigma^{(1)}]^2 \omega^2 N^2 A_{Terf}^2 \ell_{Terf} R (\ell_{Terf} + A_{Terf} \Re_{ext} \mu_T) \left[\left(\frac{\partial B}{\partial \sigma} \right)_{I=0} - \mu_T \left(\frac{\partial H}{\partial \sigma} \right)_{I=0} \right] \left(\frac{\partial B}{\partial \sigma} \right)_{I=0}}{(\ell_{Terf} + A_{Terf} \Re_{ext} \mu_T)^2 R^2 + \omega^2 N^4 A_{Terf}^2 \mu_T^2} \quad (3-69)$$

This may be more simply expressed as

$$P = \frac{\omega^2 F^2}{(1 + \Re_{ext} / \Re_{Terf})} \operatorname{Re} \left\{ \frac{N^2}{R + j\omega L} \right\} \left[\left(\frac{\partial B}{\partial \sigma} \right)_{I=0} - \mu_T \left(\frac{\partial H}{\partial \sigma} \right)_{I=0} \right] \left(\frac{\partial B}{\partial \sigma} \right)_{I=0} \quad (3-70)$$

where $F = \sigma^{(1)} A_{Terf}$ is the perturbed force, $\Re_{Terf} = \ell_{Terf} / \mu_T A_{Terf}$ is the reluctance of the Terfenol at constant stress, and

$$L = \frac{N^2 A_{Terf} \mu_T}{\ell_{Terf} + A_{Terf} \Re_{ext} \mu_T} \quad (3-71)$$

is the inductance of the coil. Note that the damping is greatest if the coil resistance R is equal to ωL .

To estimate the maximum damping rate, we note that

$$\frac{\partial B}{\partial \sigma} = \mu_T \frac{\partial H}{\partial \sigma} \approx \frac{B_{sat}}{\lambda_s E} \quad (3-72)$$

where E is the elastic modulus of the Terfenol-D, B_{sat} is its saturation magnetization, and λ_s is its saturation magnetostrictive strain. If $R \approx \omega L$, then

$$\text{Im} \left\{ \frac{N^2}{R + j\omega L} \right\} = \frac{N^2}{2\omega L} \approx \frac{\ell_{Terf}}{\omega A_{Terf} \mu_T} \quad (3-73)$$

Assuming $\Re_{ext} < \Re_{Terf}$, we find

$$P \approx \frac{\omega F^2 B_{sat}^2 \ell_{Terf}}{\lambda_s^2 E^2 A_{Terf} \mu_T} \quad (3-74)$$

In terms of the dynamic power (the perturbation energy times ω)

$$P \approx P_{\text{dynam}} B_{sat}^2 / \lambda_s^2 E \mu_T \quad (3-75)$$

The ratio of the dissipated power to the dynamic power is just the magnetomechanical coupling constant, which is of order unity for Terfenol-D and for TbDy. So a large fraction of the energy in the actuator is damped in one oscillation.

The room temperature actuator we designed has $R/2\pi L$ of tens of Hz, but the cryogenic TbDy actuator has $R/2\pi L$ of only about 5 Hz, mostly because of the lower coil resistance, and could effectively damp oscillations at such low frequencies. If the coil were superconducting, or made of hyperconductive aluminum, effective passive damping could be achieved at much lower frequencies, less than 1 Hz.

4. ROOM TEMPERATURE ACTIVE MEMBER

This chapter presents the design, fabrication, assembly, test, and performance analysis of the room temperature magnetostrictive active member. This active member, which has been delivered to JPL, is similar in size to existing JPL electrostrictive and piezoelectric actuators. The goal of this part of the program is to allow a direct comparison between the magnetostrictive, electrostrictive and piezoelectric actuators for use in space structure control applications.

The chapter starts with the design of the magnetostrictive active member, with emphasis on the electromechanical design of the magnetostrictive actuator, which is the heart of the active member. A number of design choices existed for the magnetostrictive actuator, requiring primarily tradeoffs between stiffness, force capability, and displacement capability. These are discussed in Section 4.1.1, electromechanical design. Sections 4.1.2 and 4.1.3 present issues associated with the mechanical design and sensors. Since this active member used the JPL design and displacement sensors, these sections only differences between the JPL and SatCon designs are discussed in any detail. Section 4.2 discusses the assembly procedure for the magnetostrictive actuator and active member.

Section 4.3 presents highlights of the room temperature active member performance testing undertaken both JPL and SatCon. These tests focussed on validating our models of the magnetostrictive actuator performance. Testing the mechanical behavior of the active member was not stressed because this mechanical design has been used previously at JPL. Section 4.4 concludes the chapter by analyzing the test results. The focus of the discussion is on the accuracy of our design models.

4.1 Room Temperature Active Member Design

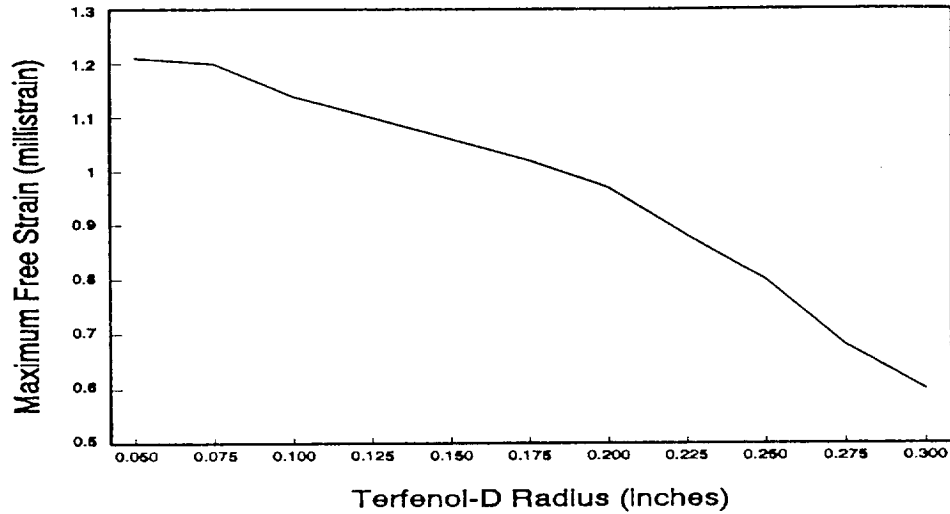
The room temperature active member developed under this program was closely modelled after the previous JPL PSR active member. As is discussed below, one of the results of this program was to formalize the existing PSR active member drawing package, including placing it onto a CAD system. The majority of the design effort, however, was placed on the magnetostrictive actuator, in particular on accurate performance predictions.

4.1.1 Electromechanical Design of the Room Temperature Active Member

The room temperature actuator design was constrained by the requirement that the length and outer diameter match that of the existing JPL actuator. In addition, the permanent magnet cross-sectional area and outer coil radius were fixed by the fact that lugs to which the sensors were attached interfered with the insertion of the magnets and coil, so that the magnets had to fit azimuthally within the spaces between the lugs, and the outer coil radius had to be less than the inner radius of the lugs. (This constraint was removed for the cryogenic actuator, since the sensor lugs were redesigned to avoid this problem.) The Terfenol-D, coil, and permanent magnets were assumed to all have the same length ℓ , fixed by the available space in the existing JPL actuator. Hence the only free parameter was the radius r_T of the Terfenol-D rod. It was assumed that the coil would take up all of the space between the Terfenol-D rod and the inner radius of the permanent magnets, which would correspond to the inner radius of the sensor lugs, and that the permanent magnets take up all of the space between the sensor lugs azimuthally, and extend to the outer radius of the actuator. It would have been possible to use less than all of the area for the permanent magnets, or to use less than the maximum possible B_r for the permanent magnets, if that turned out to be desirable, but as it turned out the flux from the permanent magnets was not as great as desired, so all of the available area was used, and B_r was chosen to be as high as possible. It also would have been possible, if desired, to reduce the outer radius of the coil, and to fill in the space between the coil and the inner radius of the lugs with additional permanent magnet area, which could extend 360° around azimuthally instead of being limited to the space between the lugs. We did look into this, and it turned out not to be desirable to do; even though the optimal permanent magnet area would be slightly greater than the space between the lugs, it would not be that much greater, and the additional permanent magnet area would have to be a very thin annulus, and very fragile. Hence the only free parameter was the Terfenol-D radius r_T .

In order to choose the optimal r_T , we calculated the maximum free strain (i.e. strain at constant preload stress), and the maximum clamped force, as a function of r_T . In general, the maximum strain is greatest when r_T is small, because this allows as much coil cross-section as possible, and hence as much NI as possible, using a reasonable current density. The clamped force, on the other hand, is proportional to the Terfenol-D area $A_{\text{Terf}} = \pi r_T^2$ for small r_T , and hence reaches its maximum value at a larger value of r_T , such that the gain in force from any additional Terfenol-D area would be canceled

Free Strain vs Terfenol-D Radius



Clamped Force vs Terfenol-D Radius

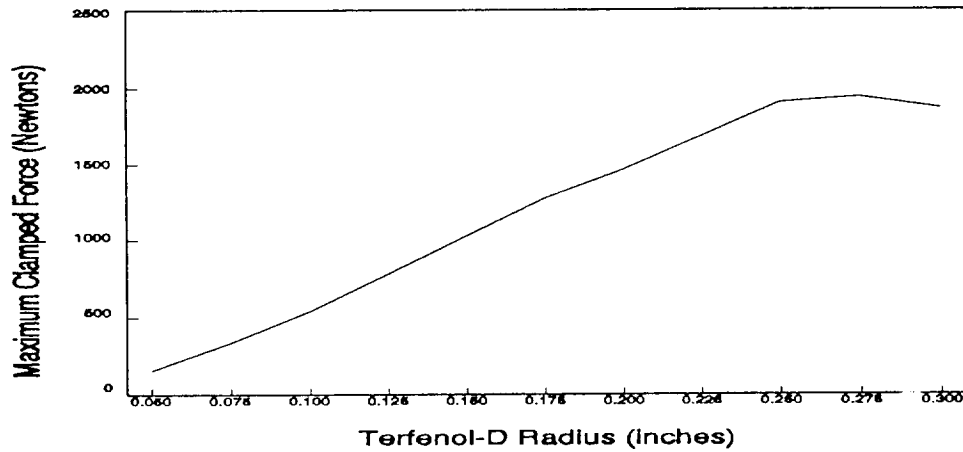


Figure 4-1 Room temperature design tradeoffs; clamped force and maximum strain vs. Terfenol-D radius.

out by the loss in clamped stress due to the decrease in coil area. We looked for an intermediate value of r_T which had maximum strain not too much less than the largest possible value, and still had a reasonably large clamped force.

The maximum strain and maximum clamped force can be calculated as a function of r_T by using Eq. (3-7) relating H_{Terf} , B_{Terf} , and NI , and using

$$NI = (r_{oc} - r_{ic})lJ_{\max} \quad (4-1)$$

where r_{oc} and r_{ic} are the outer and inner radius of the coil, and J_{max} is the maximum current density in the coil, chosen according to some criterion. The relation between H_{Terf} and free strain is given by the lines of constant stress in Fig. 3-4 (or equivalently by Fig. 3-3), while the relation between H_{Terf} and clamped force is given by the lines of constant strain in Fig. 3-4. The relation between H_{Terf} and B_{Terf} can be inferred from Fig. 3-4 and the room temperature Terfenol-D curve in Fig. 3-2.

In fact, we had not yet derived Eq. (3-7) when the actuator was designed, so we used a more approximate method based on the model for the actuator that is described in the Phase I final report. This differs from Eq. (3-7) in that the external reluctance \mathfrak{R}_{ext} and the reluctance associated with the finite coil thickness \mathfrak{R}_{coil} are neglected for purposes of calculating the variation in H_{Terf} due to the coil current, although they are included in calculating the bias H_{Terf} due to the permanent magnets. This approximation causes errors on the order of 20% in calculated the variation in H_{Terf} , and these errors are only mildly dependent on r_T , so they have little effect on the optimal r_T . Another approximation made was that, for purposes of finding the bias H_{Terf} due to the permanent magnets, B_{Terf} was assumed to be $\mu_T H_{Terf}$, rather than using the exact $B_{Terf}(H_{Terf}, \sigma)$, and μ_T was taken to be $9\mu_0$ for purposes of calculating the free strain, and $5\mu_0$ for purposes of calculating the clamped stress. Again, these are fairly good approximations.

The bias field due to the permanent magnet is given approximately by

$$H_{bias} = B_{mag} A_{mag} / (\ell^2 \mu_0 + \pi r_T^2 \mu_T) \quad (4-2)$$

where B_{mag} is the B of the permanent magnet, A_{mag} is the cross-sectional area of the permanent magnet, ℓ is the length of the Terfenol-D, r_T is the radius of the Terfenol-D, μ_T is the permeability of the Terfenol-D, and $\mu_0 = 4\pi \times 10^{-7}$ is the vacuum permeability. This expression is accurate for $\ell \gg r_T$. For our design, based on the existing JPL actuator,

$$\begin{aligned} A_{mag} &\approx 0.175 \text{ in}^2 \\ \ell &= 2.25 \text{ inches} \end{aligned}$$

The permeability of the Terfenol is $\mu_T \approx 9\mu_0$ for zero stress (or any constant stress that is much less than the magnetostriction λ_s times Young's modulus E, which is about 35 MPa), and $\mu_T \approx 5\mu_0$ for zero strain (clamped operation). Then $B_{mag}/\mu_0 H_{bias}$ varies from 29 (for $r_T \rightarrow 0$) up to 51 (for $r_T = 0.375$ inches and $\mu_T/\mu_0 = 9$). Since $B_{mag}/\mu_0 H_{bias}$ is always much greater than 1, B_{mag} is always close to B_r for the permanent magnet, which can be as great as 1.1 or 1.2 tesla for rare earth magnets. Then H_{bias} will range from 400

Oe for small r_T down to about 300 Oe for the largest r_T (0.275 inches) that would be seriously considered.

The field in the Terfenol-D will vary from H_{bias} by $\pm H_{coil}$, induced by the coil, where

$$H_{coil} \approx J_{max}(r_{oc} - r_{ic}) \quad (4-3)$$

Here J_{max} is the maximum current density in the coil, r_{oc} and r_{ic} are the outer and inner coil diameter. This expression is valid for $\ell \gg r_{oc}$. A finite element calculation shows that it is about 10% too high for the ℓ/r_{oc} in our design. To optimize r_{ic} (which is assumed to be equal to r_T), we have used the above expression with $J_{max} = 4 \times 10^6$ A/m², which is equivalent to using the exact result with $J_{max} = 4.4 \times 10^6$ A/m². This refers to the peak (in time) of the current density averaged over the coil cross-section. With a fill factor of η , the coil density in the copper is greater than this by a factor of $1/\eta$, where the greatest possible η is typically about 0.65, and η tends to be lower if $r_{oc} - r_{ic}$ is so small that only a few layers of wire can be wound. On the other hand, for a current with sinusoidal time dependence, the rms current density is lower than this by a factor of $\sqrt{2}/2$, so the rms current density in the copper is about 4 or 5 $\times 10^6$ A/m², a reasonable maximum value.

Using the data in Figs. 3-3 and 3-4 for strain vs. H for various values of stress, and stress vs. strain for various values of H , we found, for several different values of r_T , 1) the maximum range in strain $\Delta\epsilon$ that could be produced at constant stress, and the optimum stress σ and bias field H_{bias} to produce this range of strain; and 2) the maximum range in stress $\Delta\sigma$, and the maximum range in force ΔF , that could be produced at constant strain (i.e. clamped) and the optimum bias stress σ_{bias} and bias field H_{bias} to produce this range of stress. The results are given in Table 4-1 and plotted in Fig. 4-1. The optimal H_{bias} , for both maximum strain at constant stress and maximum stress at constant strain, was equal to the maximum H_{bias} that could be produced by the permanent magnet when r_T was very small, less than 0.1 inches, but was less than the maximum H_{bias} at more reasonable values of r_T . This shows that the magnet cross-sectional area should not be increased at the expense of the coil or Terfenol-D, and that in fact either A_{mag} or B_{mag} should be made somewhat lower than the maximum possible, particularly at larger r_T . The optimal H_{bias} was always (when less than the maximum H_{bias}) only slightly greater than H_{coil} , since the strain as a function of H at constant stress, and the stress as a function of H at constant strain, both reach their maximum slopes at

Table 4-1 Dependence of maximum strain and maximum clamped force on radius of TbDy

r_T (inches)	H_{max} (Oe)	Max. free H_{bias} (Oe)	Max. free $\Delta\epsilon$ $\times 10^{-3}$	σ at max. $\Delta\epsilon$ (kpsi)	H_{bias} at max. $\Delta\epsilon$ (Oe)	Max. clamped H_{bias} (Oe)	Max. clamped $\Delta\sigma$ (kpsi)	σ_{bias} at max. $\Delta\sigma$ (kpsi)	H_{bias} at max. $\Delta\sigma$ (Oe)	Max. clamped ΔF (lbs)	$\Delta F_{\Delta\epsilon\Delta\sigma}$ (inch-lbs)
0.05	416	396	1.21	1.8	396	397	4.5	2.5	397	35	0.095
0.075	384	390	1.20	1.8	390	394	4.3	2.5	394	76	0.205
0.10	352	382	1.14	1.6	380	389	3.9	2.3	360	123	0.315
0.125	320	372	1.10	1.6	360	382	3.6	2.15	330	177	0.438
0.15	288	360	1.06	1.4	328	374	3.3	2.0	298	233	0.556
0.175	256	346	1.02	1.4	296	365	3.0	1.8	266	289	0.663
0.20	224	330	0.97	1.4	284	355	2.65	1.6	234	333	0.727
0.225	192	311	0.88	1.4	252	343	2.4	1.45	202	382	0.756
0.25	160	290	0.80	1.4	240	330	2.2	1.25	170	432	0.777
0.275	128	267	0.68	1.4	208	315	1.85	1.0	138	440	0.673
0.3	96	242	0.60	1.2	165	299	1.5	0.85	106	424	0.572

rather low H as H is increased from zero, and the slope then gradually falls off at higher H .

Another quantity of interest is the maximum work per cycle that can be obtained from the actuator. This quantity was not evaluated precisely, since it is more difficult to read off the σ vs. ϵ vs. H curves, but it should be roughly proportional to the maximum range in force ΔF at constant strain, times the maximum range in strain $\Delta \epsilon$ at constant stress, times ℓ , so that quantity is tabulated in Table 4-1. We see from Table 4-1 and Fig. 4-1 that the maximum range of strain $\Delta \epsilon$ occurs at small r_T , but it falls off slowly up to $r_T \approx 0.2$ inches, corresponding approximately to a 3/8 inch diameter Terfenol-D rod (a size that is commercially available). The maximum range of force ΔF occurs at $r_T = 0.275$ inches, and the maximum product of ΔF and $\Delta \epsilon$ occurs at $r_T = 0.25$ inches. However, the maximum strain is down by 30% from its maximum value when $r_T = 0.25$ inches, and in practice it is likely to be even lower because of the finite number of layers of wire in the coil, and the need to allow some space between the coil and the Terfenol-D. The best overall choice, then, would be a Terfenol-D diameter of 3/8 inches.

With this choice of r_T , interpolating from Table 4-1 we find that the maximum range of clamped stress $\Delta \sigma$ is 2.85 ksi, or 20 MPa, and this requires an NI of about ± 1200 amp-turns, or ± 1.5 amps in our coil which has 800 turns. The clamped force has been calculated for this case without using the approximations that were used in choosing r_T , but instead using Eq. (3-7) and the exact $B_{\text{Terf}}(H_{\text{Terf}}, \sigma)$. When this is done, the clamped stress $\Delta \sigma$ is somewhat lower than 20 MPa with a current of ± 1.5 amps, which is not surprising since the stress starts to saturate at large currents. On the other hand, we found that we could easily exceed the maximum current density conservatively assumed in Table 4-1, without overheating the coil. At a current of ± 2 amps, the clamped stress, starting at the optimal bias value of 12.5 MPa, can vary from 4 MPa up to 21 MPa, or a total range $\Delta \sigma = 17$ MPa, almost as high as predicted in Table 4-1, and with a current of ± 4 amps, the stress can go from 4 MPa up to 28 MPa, a total range $\Delta \sigma = 24$ MPa. (The stress cannot go below 4 MPa, no matter what the current, since this is the stress at which $H_{\text{Terf}} = 0$, if the length is clamped, at a bias stress of 12.5 MPa.)

Another quantity of interest is the stiffness of the actuator, i.e the derivative of force with respect to length, which depends on the elastic modulus of the Terfenol-D, the derivative of stress with respect to strain. This has a different value for small amplitude changes in strain, where the permeability of the Terfenol-D is only the initial permeability μ_{rot} due to domain rotation, and large amplitude changes, where the

permeability of the Terfenol-D is approximately the anhysteretic permeability μ_{an} including domain wall motion. Since μ_{an} is greater than μ_{rot} , there is more magnetomechanical coupling at large amplitude, and the elastic modulus is lower than for small amplitude. For our room temperature actuator design, we find that the large amplitude elastic modulus is 2.3×10^{10} Pa (corresponding to a stiffness of 2.8×10^7 N/m), and the small amplitude elastic modulus is 4×10^{10} Pa (a stiffness of 4.8×10^7 N/m). When the Terfenol-D is saturated, either due to large H or large σ , so that there is no magnetomechanical coupling, then the elastic modulus would be 7.8×10^{10} Pa.

After the design parameters were chosen, the analytical electromagnetic modelling was verified using magnetic finite element software. Two-dimensional cylindrical finite element coordinates were used to model this problem. The permanent magnets, however, do not span the full circumference, which would require a full three dimensional finite element analysis. This effect was modelled using the two dimensional, cylindrical coordinates by appropriately reducing the permanent magnet permeability and remanent magnetism.

The finite element mesh is shown in Figure 4-2. Shown is a cutaway of the actuator. The left hand side of the plot is the axial center line of the actuator. The actuator pieces are labelled in Figure 4-3. The inner most area is the Terfenol-D with the coil and permanent magnets outside of it. The lower, single-piece, magnetic end-cap can be seen below the Terfenol-D, coil and permanent magnet. The two-piece upper end-cap, including the radial air gap is shown above the Terfenol-D, coil and permanent magnet. Figure 4-3 shows the lines of constant magnetic potential when the coil is not excited. This magnetic field is caused only by the permanent magnets. Figure 4-4 shows coil excited magnetic field. In this case the permanent magnets are "turned-off" by setting their remanence to zero. Figure 4-5 shows the equipotential magnetic potential lines when the permanent magnetic and coil flux are combined.

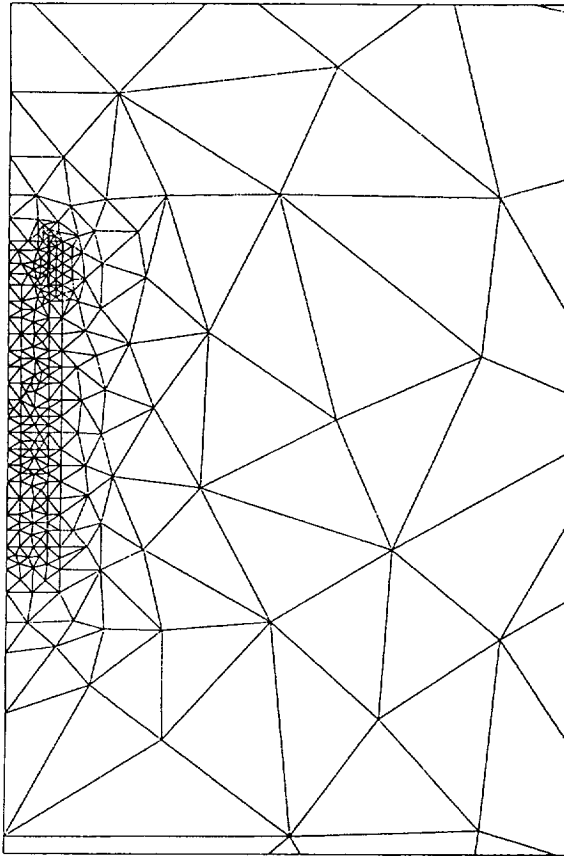


Figure 4-2. Magnetic finite element mesh.

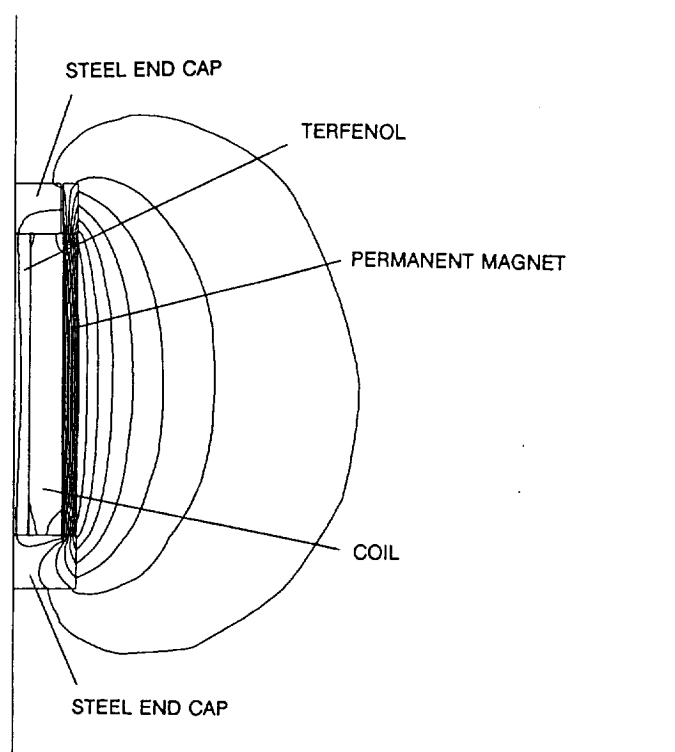


Figure 4-3. Magnetic equipotential lines with no excitation current.



Figure 4-4. Magnetic equipotential lines with no permanent magnet, coil excited.

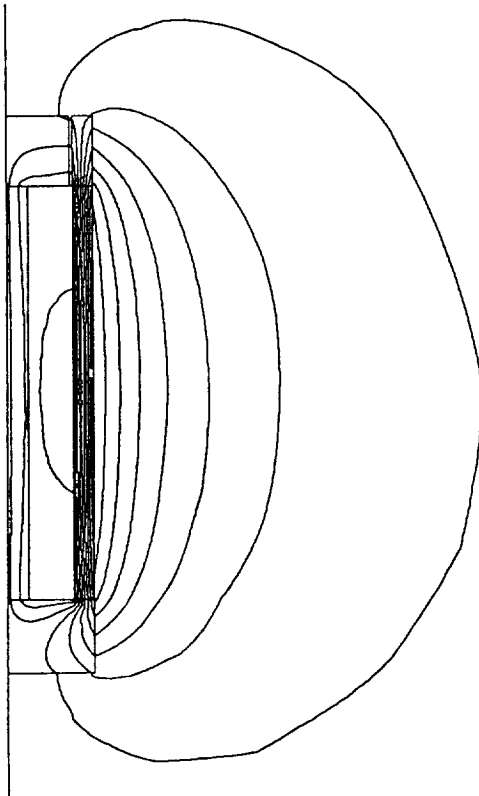


Figure 4-5. Magnetic equipotential lines with permanent magnet and coil induced field

4.1.2 Mechanical Design of the Room Temperature Active Member

One of the goals of this project is to replace the original piezoelectric and electrostrictive strut motors with an "equivalent" magnetostrictive motor. The performance of the magnetostrictive active member could then be compared to other motor types in various areas of interest. One of the guidelines used in the active member design is to essentially have a form, fit, function replacement of the previous motors. To allow the most meaningful comparison, the minimum number of changes were made to the original JPL mechanical design. Any changes in active member characteristics can then be clearly attributed to the motor replacement. The resulting room temperature active member is shown in Figure 4-6. A complete set of mechanical part drawings for the room temperature active member comprises Appendix A.

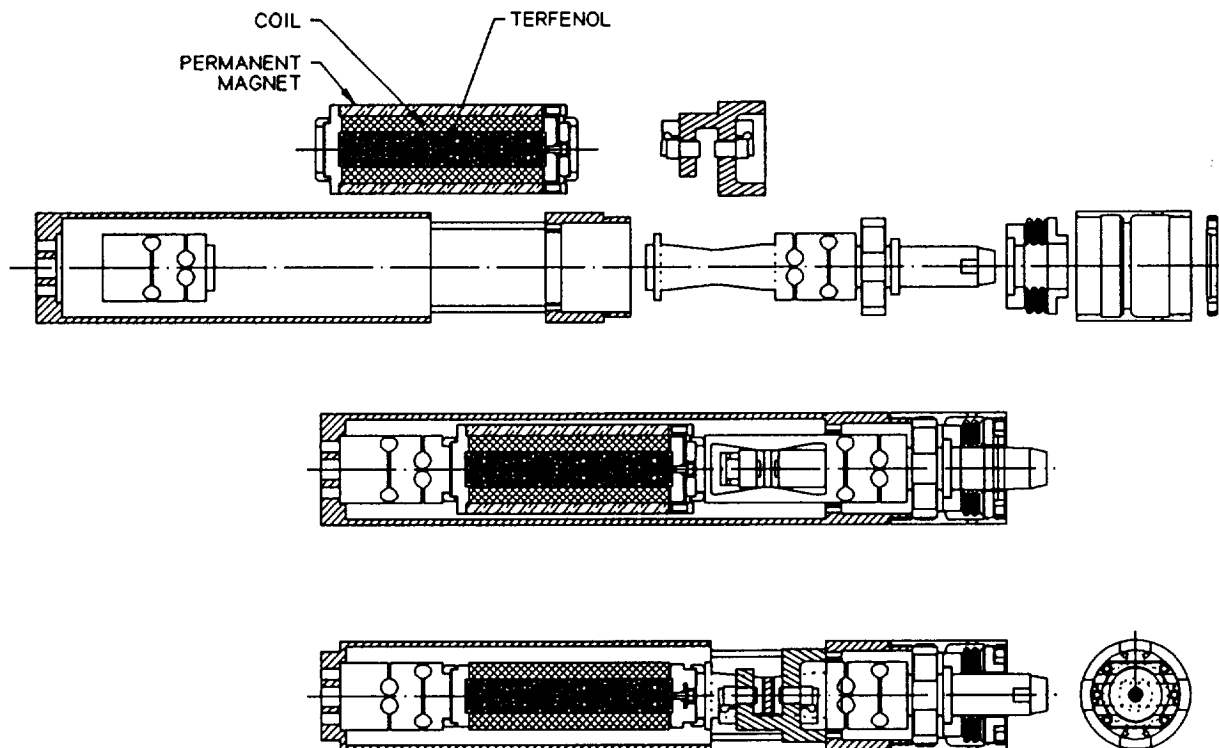


Figure 4-6. Final assembly drawing of the room temperature active strut.

Using this philosophy, the starting point of SatCon's room temperature mechanical design was a set of informal mechanical drawings provided by JPL. These

drawings were checked and modified for compatibility, and were entered into a CAD system, Personal Designer. Some parts, such as the central "long flexure", were simplified to reduce the number of machining operations while preserving the intended functionality. The tolerances were tightened on other parts to ensure sufficient material thickness in the worst case tolerance accumulation. Tighter tolerances were also required to ensure that relative motion of the parts in the active member occurred only at the flexures. Loose tolerances could allow parts to touch and slide during actuation, because of poor concentricity. Random contact within the active member could cause friction non-linearity and poor performance.

The original design called for "dead soft" aluminum crush washers at each end of the motor. It was determined that this material has such a low yield strength that the more powerful magnetostrictive motor could *extrude* the aluminum washer material radially. This action would limit the actuator force level and change the critical spacing and preload levels of the active member parts. The solution was to continue to use the relatively weak aluminum material, but to specify a harder anneal, such as used for aluminum shim material.

Although most of the changes to the JPL drawings for the room temperature active member were done to improve functionality, one change was done for aesthetics. The outside diameter of the housing was increased to match the outside diameter of the end cap to produce a constant diameter, smooth member envelope.

Another change was required, not for functional reasons, but to improve the manufacturability of the long flexure. This complex part has eight radial flexures that provide radial support of the central structure while allowing it to move axially with little resistance. To provide the necessary compliance requires thin, 0.010 inch (0.25 mm) flexures which are difficult to machine. Initial attempts by the fabricator to machine the flexures using electric-discharge machining (EDM) failed. The fragile flexures cracked when the recessed radius at the root of the flexure was cut on a lathe after the EDM process. It was determined that the depth of the recess could be reduced without excessively increasing the spring constant of the flexure. This reduced the length of the flexure and the degree that residual stresses would cause distortion of the material as the material was released during machining. The flexure was also changed by substituting a constant depth slot for the radiused feature. This change allow the use of a standard cutoff tool to machine the feature instead of a custom tool that tended to "pull" to the side and change the flexure thickness.

4.1.3 Room Temperature Active Member Sensors

The room temperature active member contains a displacement and flux sensor. These sensors are briefly discussed in this section.

4.1.3.1 Position Sensor System for Room Temperature Active Member

A differential eddy current position sensor is integrated into the magnetostrictive active member. The configuration and sensor model are based on the previous JPL design. The two sensor heads are mounted in a cage, which is fastened to the member housing. Each sensor head interacts with the opposite faces of a moving target web. The web is machined into the "long flexure", which moves as the magnetostrictive motor expands. Therefore the sensor measures the motion of the "free" end of the motor with respect to the member housing.

The particular sensor model used is the same as that used successfully in the JPL active members. The Kaman model KDM-7200D with 15N-004 sensor heads provides outstanding resolution and stability. Figure 4-7 lists the specifications for this sensor, and Figure 4-8 shows a drawing of the sensor heads. The equivalent RMS input noise specification quantifies the low sensor noise. The noise of $10^{-4} \mu\text{m}/\text{Hz}^{1/2}$ can be used to calculate the expected RMS position noise for any bandwidth. Even for sensor bandwidth of 10 kHz, the expected RMS position noise is only $10^{-2} \mu\text{m}$. This far exceeds the requirements of this application, where active member elongation must be accurately characterized. The quoted temperature stability of $<5\text{mV}/^\circ\text{F}$ is also adequate. A sensor calibrated for $\pm 200 \mu\text{m}$ will produce an output change less than $0.1 \mu\text{m}$ for each degree of temperature change.

Calibration of the room temperature active member sensor was done using a laser interferometer at JPL. The results of this procedure, including measured sensor linearity, is discussed below in Subsection 4.3 (Test Results).

4.1.3.2 Magnetic Flux Sensor for Room Temperature Active Member

A hall probe type magnetic field sensor was installed in the magnetic circuit of the active member. This sensor was used to help characterize the Terfenol-D material by measuring the magnetic field applied while measuring the elongation of the active member. As discussed in Section 4.3, a number of different locations for the sensor were tried. Because of the small volumes available for the flux sensor, a low width, A F. W. Bell model BH-301 Hall effect sensor was installed.

Performance

(typical for an aluminum target) -

Measuring range:

15N — Up to ± 0.035 -inch (± 0.889 mm).

20N — Up to ± 0.075 -inch (± 1.27 mm).

Nonlinearity: $\pm 0.1\%$ to $\pm 0.5\%$ FSO;
application dependent.

Output: KD-5100 — ± 10 Vdc max;

KDM-7200D/8200D — ± 9 Vdc max.

Long term stability (*nominal; stabilized at*
70°F [21°C] scale factor dependent): 5×10^{-6}
inches/month; 1.27×10^{-4} mm/month.

Thermal sensitivity at null: Application
dependent; < 5 mV per °F.

Frequency response: 22 kHz $\pm 5\%$ @ 3db.

Equivalent RMS input noise: $4 \times 10^{-9}/\sqrt{\text{Hz}}$
inches; $1 \times 10^{-7}/\sqrt{\text{Hz}}$ mm,
slightly higher in KDM-7200D/8200D.

Effective resolution: Equivalent RMS; input
noise $\times \sqrt{\text{bandwidth in Hz}}$.

Input voltage: ± 15 Vdc @ 70mA typical.

Power consumption (system): < 2 watts.

Power dissipation (sensors): < 50 μ W per
-15N sensor; < 2 mW per -20N sensor.

Output characteristics: < 5 Ω @ 5mA.

Operating temperature range:

Electronics: -4°F to 140°F (-20°C to 60°C).

Sensors: -62°F to 220°F (-52°C to 105°C).

Cryogenic 20N sensor: 4° Kelvin to 220°F
(105°C).

Storage temperature range:

Electronics: -4°F to 140°F (-20°C to 60°C).

Sensors: -62°F to 220°F (-52°C to 105°C).

Cryogenic 20N sensor: 4° Kelvin to 220°F
(105°C).

Weight:

15N-001 sensor with 5-ft. cable:

.61-oz. (17.3 gr.).

20N sensor + 5-ft. cable: .59-oz. (16.8 gr.)

Figure 4-7. KDM-2700D sensor specification.

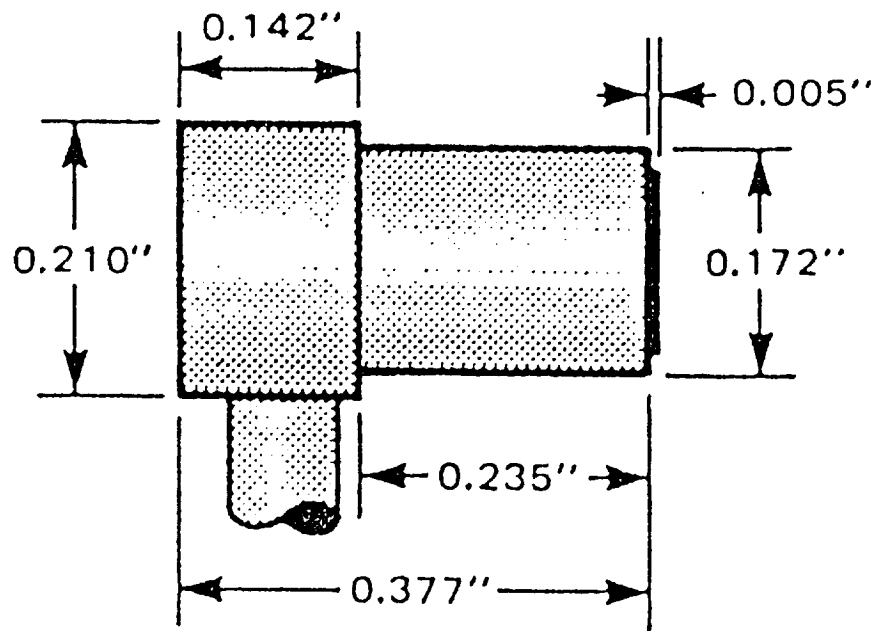


Figure 4-8 Drawing of sensor 15N-004 for use with the KDM-7200D systems.

4.2 Assembly of Room Temperature Active Member

Before assembling the room temperature active member, the parts were inspected at SatCon¹. The room temperature parts are shown in Figure 4-9. The parts at the bottom of the figure lie in the mechanical load path. These include, from left to right, the short flexure, the Terfenol-D rod, the long flexure, the preload spring, and the preload nut. Shown on either end of the Terfenol-D rod are Delrin alignment sleeves. Not shown are the aluminum crush washers. The parts in the middle of the photograph include, from left to right, the coil, the permanent magnet with attached end caps, the actuator flexure, the live end cap, and sensor cage and clips. The upper part of the

¹The original long flexure was found to have poorly toleranced flexure arms. The vendor attempted to machine this piece a number of times, but with the same result. Since these flexures were needed primarily to carry moments away from the magnetostrictive actuator, the active member could still be successfully used in laboratory testing where moments applied to the active member are small or non-existent. The long flexure was slightly redesigned, as discussed in the previous section, for the cryogenic active member and successfully fabricated. After its successful demonstration on the cryogenic actuator, the room temperature long flexure was redesigned to incorporate these changes, the part successfully fabricated, and incorporated into the room temperature active member.

photograph shows the outer housing and displacement sensors. Not shown are the flux sensors.

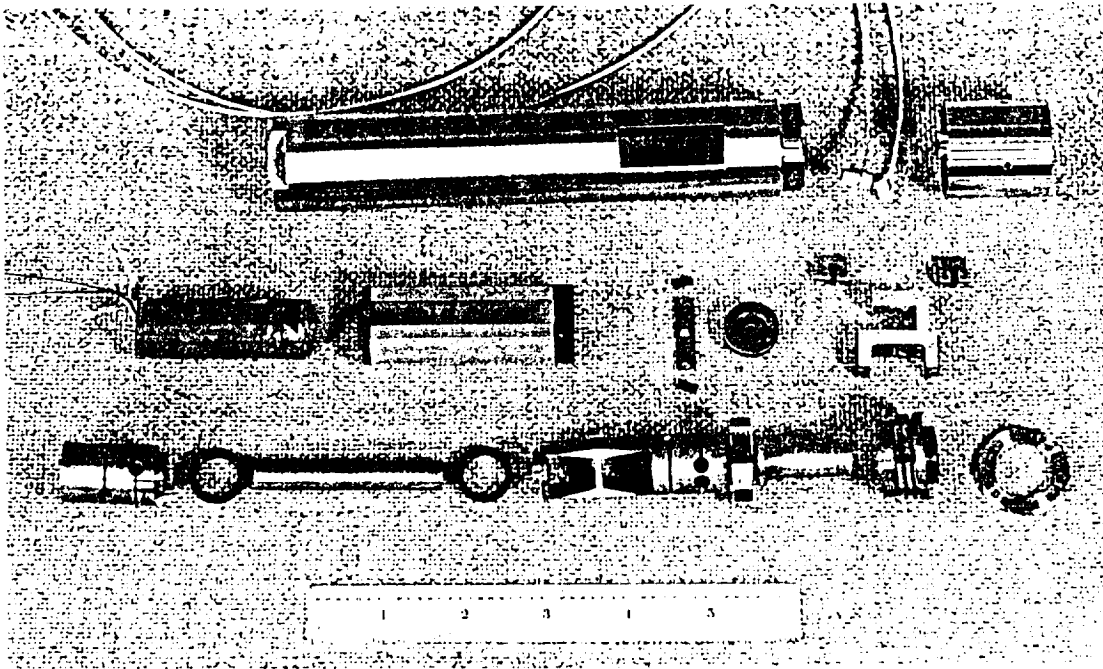


Figure 4-9. Photograph of unassembled room temperature active member.

The first assembly step was to attach the permanent magnets to their associated end caps, which also act as the Terfenol-D mount. The permanent magnets are attracted to these magnetic end caps and radially held in place by small step machined into the end caps. These were additionally held by epoxy. Later these glue bonds were found to have broken, which required reassembly. The Teflon anti-rust paint on the ends of the permanent magnets was removed for the second gluing and the end caps carefully cleaned. Recommended epoxy was used and better adhesion was obtained. After running at high current levels, however, the bonds were again found to have broken. At high negative current levels, the magnetic field produced by the coil acts to push the permanent magnets radially outward. Under normal operation, however, the permanent magnets are held in place by the self-attraction of the permanent magnets to the end caps.

After the end caps were glued to the permanent magnets and the live end-cap to the Terfenol-D, the coil and Terfenol-D rod were inserted into the permanent magnet

assembly. This is shown in Figure 4-10. Shown are the coil partially inserted in the permanent magnet assembly and the Terfenol-D rod being readied for assembly. During the first few times the magnetostrictive actuator was assembled, the permanent magnet assembly and the Terfenol-D rod were held in a milling machine, as shown in Figure 4-10. This allowed the Terfenol-D rod to be accurately placed into the permanent magnet assembly in the presence of the magnetically induced radial forces acting on the Terfenol-D. Because of the small size of this actuator, however, it was later found that this step could be satisfactorily completed by hand. After the Terfenol-D rod and coil were assembled with the permanent magnets, the live end flexure was assembled using the associated washers, screws and flexure clamps. The crush washers located between the Terfenol-D rods and end caps were chosen such that the flexure attachment point on the Terfenol-D end cap was axially slightly further out (one to two mils) than the flexure attachment points on the permanent magnet end caps. This insured that the crush washers were always under some compressive stress, even if the magnetostrictive actuator was not assembled into the active member. Unfortunately, however, this placed a tensile stress on the permanent magnet - end cap glue joint. The assembled magnetostrictive actuator, with permanent magnets, coil, Terfenol-D, end caps and flexure and seen in Figure 4-11.

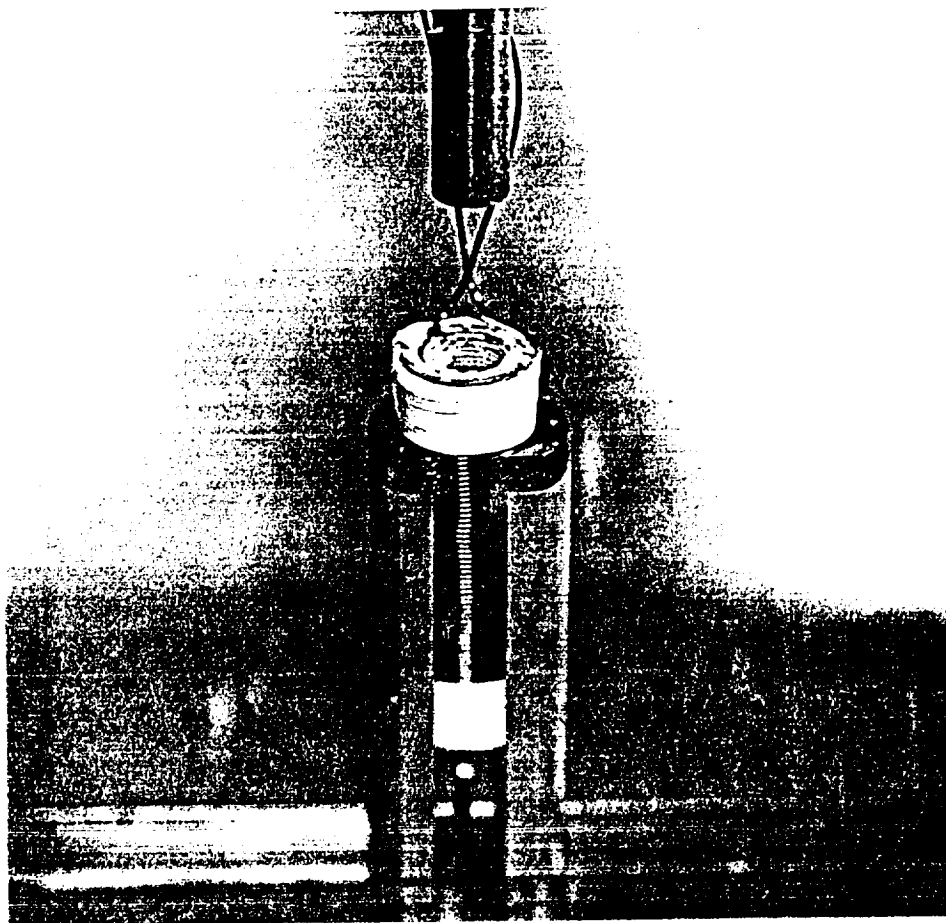


Figure 4-10. Photograph of room temperature magnetostrictive actuator being assembled.

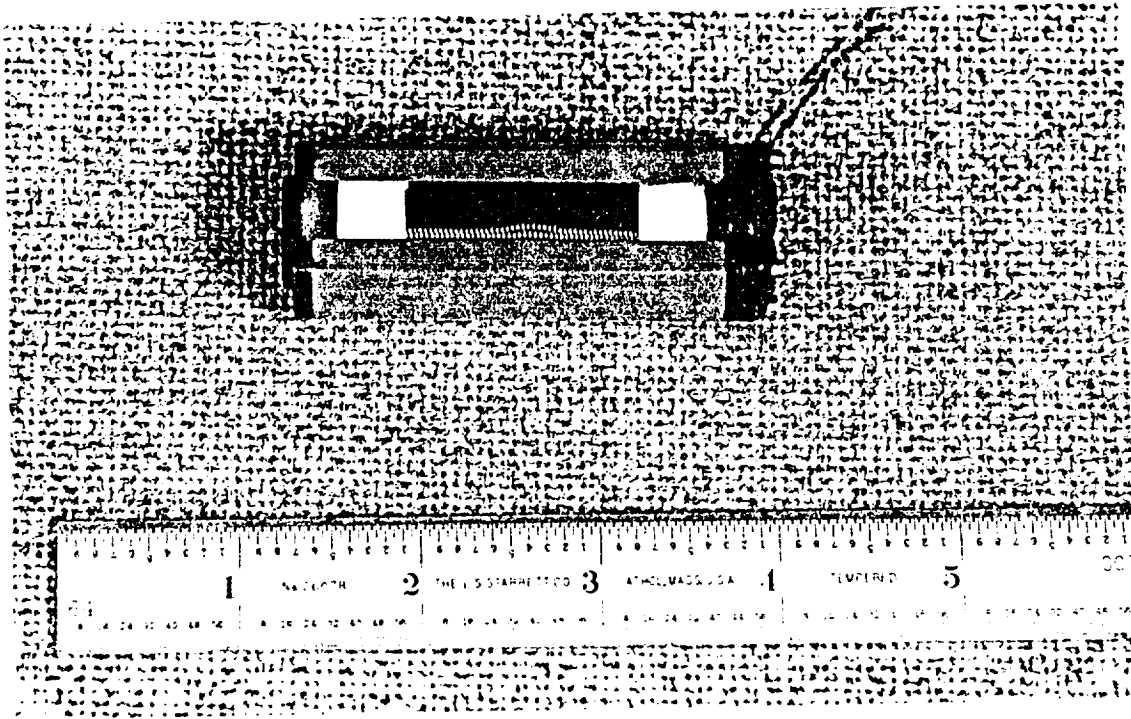


Figure 4-11. Photograph of room temperature magnetostrictive actuator assembled.

The assembly of the magnetostrictive actuator into the active member was relatively straight forward. Two shim thicknesses, however, had to be determined. The first was the thickness of the aluminum crush washers between the active member flexures and the magnetostrictive actuator. These were determined by assembling the short flexure, crush washers, and long flexure into the active member housing. The axial distance between the long flexure arms and the support notches in the active member housing were then measured. The crush washer thickness was selected to give between two and four mils of free motion between the flexure and housing. The housing end-cap was then threaded onto the housing, clamping the flexure arms against the housing support notches. The two to four mil unclamped clearance insured that axial load stack, including the crush washers, flexures, and magnetostrictive actuator were always maintained under some slight compressive stress, keeping the crush washers from moving.

The displacement sensors also required shimming to insure proper gaps. Aluminum targets were expoxied to either side of the cross-member of the long flexure. The thickness of these targets was chosen to yield a total sensor gap of 0.030 inches.

Furthermore, the thickness of the targets was chosen such that the gap was approximately 0.015 inches on either side. Shims placed between the sensor and sensor cage were also used to adjust these gaps.

The original location of the flux sensor was in a slot machined into the Terfenol-D end cap. This location did not give useful information, primarily because only a small amount of flux would cross the sensor, with most flux staying in the high permeability end-cap and not crossing the slot, and therefore, not being read by the sensor. A small notch was then machined on the outer circumference of the Terfenol-D live end cap, allowing the sensor to be placed in the radial air gap. Better readings were obtained in this position. The best readings, however, were found when the flux sensor was simply positioned in the radial air gap and attached to the inner radius of the permanent magnet end caps by a small amount of RTV.

The assembled active member, shown in Figure 4-12, was preloaded, excited, and then disassembled a number of times to check for correct shims. After the correct shim thicknesses had been determined, the test program for the active member began. The preload procedure is similar to the JPL technique, with the preload applied, via a specially machined cylinder, to end of the preload spring. The preload nut is then tightened until snug. As the external preload is released, the displacement sensor output is monitored. Based on monitoring the displacement sensor output, the compressive load is estimated to change less than five pounds when the preload changes from being carried by the external preload mechanism and the internal preload spring.



Figure 4-12. Photograph of room temperature active member assembled.

4.3 Test Results

An extensive test program was undertaken to determine the performance of the room temperature active member. The first tests were directed at verifying operation of the actuator and sensors, while later tests focussed on validating our models, especially the predictions of electromagnetic behavior. Testing the mechanical behavior of the strut, for example its torsional stiffness, was not stressed because this mechanical design has been used previously at JPL.

This section presents some highlights of these test results. The first subsection, 4.3.1, presents data taken at JPL using their laser interferometer displacement measurement system for active members. These tests were primarily used to calibrate the active member displacement sensor, but were also used to investigate the thermal displacement characteristics of the active member. The second subsection, 4.3.2, describes the active member testbed at SatCon. The third subsection, 4.3.3, presents data taken under "free boundary conditions", that is, when no external mechanical loads are placed on the active member. This tests include sinusoidal and random excitation. The last subsection, 4.3.4, presents similar data, but taken with the active member working against the stiffness of our active member testbed. This "partially clamped" data is used to validate our electromagnetic models.

4.3.1 Laser Interferometric Tests at JPL

Kaman Sensor Scale-Factor Calibration

One of the main reasons for bringing the room temperature active member to JPL was to use their laser interferometer displacement measurement rig for active members. This was needed to calibrate the Kaman differential eddy current sensors that are mounted internal to the room temperature active member. The laser test rig measures the deflection of the "output" shaft of the actuator via a mirror mounted to the end of the shaft. This test rig has been used to measure the displacement performance of a number of active members at JPL. The tests were run by providing a constant voltage to the active member, and recording the excitation voltage, laser interferometer output, and Kaman sensor electronics output. The active member was excited only long enough to record the measurements, approximately 10 seconds, so as to minimize thermal expansion effects.

The results of this test are given in the spreadsheet and associated graph (Figure 4-13) on the next page. The actuator was excited at approximately -3 volts, 3 volts, or 0

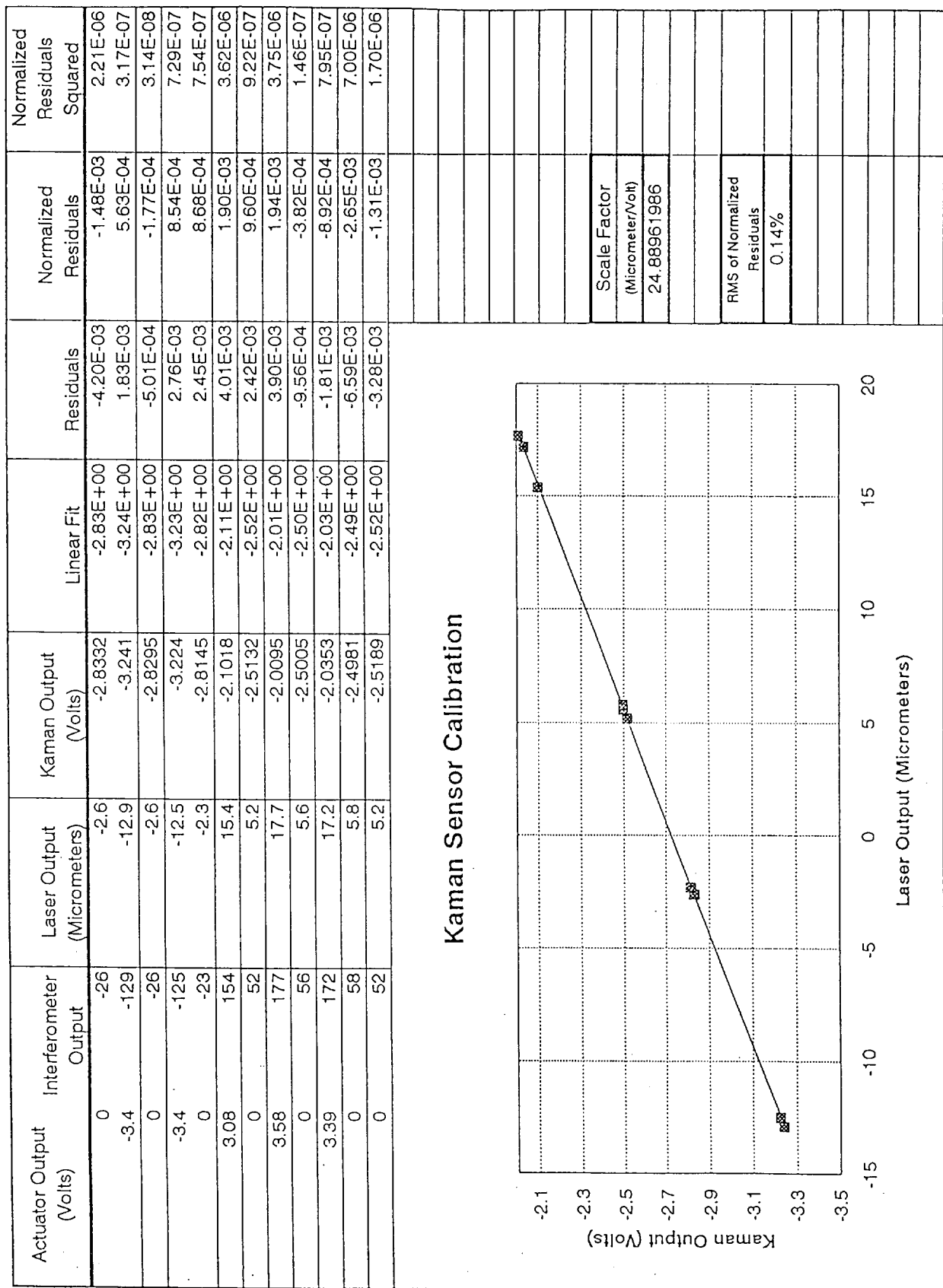


Figure 4-13. Laser interferometer test results.

volts, as is shown in the first column. This corresponds to approximately ± 1 amp or zero excitation current. This results in an approximately 31 micrometer displacement range, well over half the approximately 50 micrometer capability of the actuator. The third and fourth columns of the spread sheet contain the recorded laser interferometer output and the Kaman sensor output, respectively. The fifth column contains a linear least squares fit to the data. As can be seen in the accompanying graph, the linear fit is quite good. The "goodness" of this fit can be quantified by examining the difference between the measured Kaman sensor output and the linear fit, the so-called residuals. The RMS of the normalized residuals is less than 0.2 percent. The scale factor of the linear fit is 24.889 as indicated on the spreadsheet.

As discussed in previous progress reports, the scale factor of the Kaman sensors in this actuator was previously uncertain. As delivered from the vendor, the sensor had a scale factor of 0.001 inches per volt (25.4 micrometers/volt) when used against flat surfaces, as verified with a laser interferometer test rig. Our preliminary data, however, suggested that the scale factor was lower than this by approximately 10 percent. The vendor suggested that the geometry of the target surface in the actuator was responsible for a 10-15 percent reduction in sensor gain. We recalibrated the sensor electronics at SatCon with the sensor in place in the actuator, and found that the original sensor gain (scale factor) was indeed approximately 12 percent low. This recalibration, however, was not particularly accurate, being based on micrometer measurements of a limited (≈ 0.001 inch) range. The tests at JPL confirmed that the scale factor as recalibrated at SatCon was off by approximately 2 percent. Rather than recalibrate the sensor electronics, we will simply use the scale factor of 24.89 micrometers per volt as measured at JPL. This will allow us to reinterpret our previous results correctly, and use one scale factor for all our tests results, after we recalibrated the electronics at SatCon.

Thermal Effects on Displacement Sensing

Previous tests at SatCon and tests run at JPL indicated a significant thermal expansion of the actuator is caused by high current level excitation of the actuator coil. The following test was designed to answer two questions about this effect. The first is the scale and characteristic time constant of the coil induced thermal expansion. The second is the thermal effect on the measurement of displacement by the Kaman sensor. The test consisted of exciting the actuator with a constant voltage and measuring and recording the interferometer and Kaman sensor outputs versus time. The actuator was

excited with a constant voltage nominally producing a relatively high actuator current of approximately 2 amps. This excitation was held on for 19 minutes and then turned off.

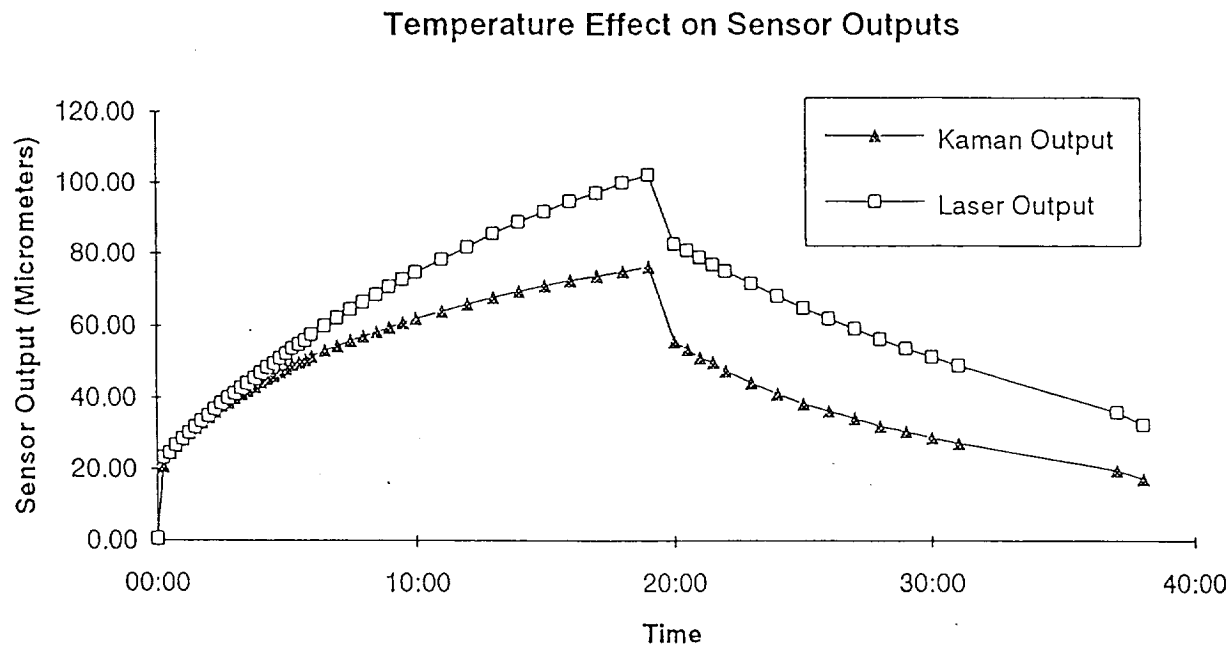


Figure 4-14. Exponential fit to displacement data.

The resulting laser interferometer and Kaman sensor output (scaled by its gain) are plotted versus time in Figure 4-14. The displacement jumps approximately 20 micrometers when the actuator is first excited just after zero time. For the first few minutes, the two displacement sensors track together. Gradually, however, the Kaman sensors begin to measure smaller displacements than the laser interferometer. This is most likely caused by thermal expansion of the actuator housing. The Kaman sensor measures the position of the actuator output shaft relative to the actuator housing where the Kaman sensors are mounted. The heat generated by the coil is transmitted via a combination of both convection and conduction to the actuator outer case. As the outer case temperature rises, it expands, reducing the Kaman sensor output. Another effect is elongation of the output shaft by thermal effects. The Kaman sensor measures the displacement of the output shaft close to its inner end near the magnetostrictive material. The laser interferometer, on the other hand, measures the displacement of the shaft at its output end. Most of the thermal expansion of this output shaft, therefore,

will be measured only by the laser interferometer and not by the Kaman sensors. By the 19-minute mark, when the actuator excitation was turned off, these temperature effects on the Kaman sensor output are quite significant, with the Kaman sensor reading approximately 20 percent less displacement than the laser interferometer.

An exponential curve was fit to the laser interferometer data to determine if a simple, on-state thermal model could accurately fit this data. The curve fit had three free parameters: the initial displacement d_0 , steady state displacement d_{\max} , and the time constant τ . The data and curve fit for the period when the actuator was excited are shown in Figure 4-15, where the exponential curve is seen to provide a very good fit to the data. The parameters of this least mean square curve fit are an initial displacement of 21.8 micrometers, a steady state displacement of 141.6 micrometers and a time constant of 1024 seconds. Similar curve fits were attempted on the "cooling off" time period when the actuator was not excited. These resulted in time constants of between 1100 and 1500 seconds, depending upon how this rather sparse data was weighted.

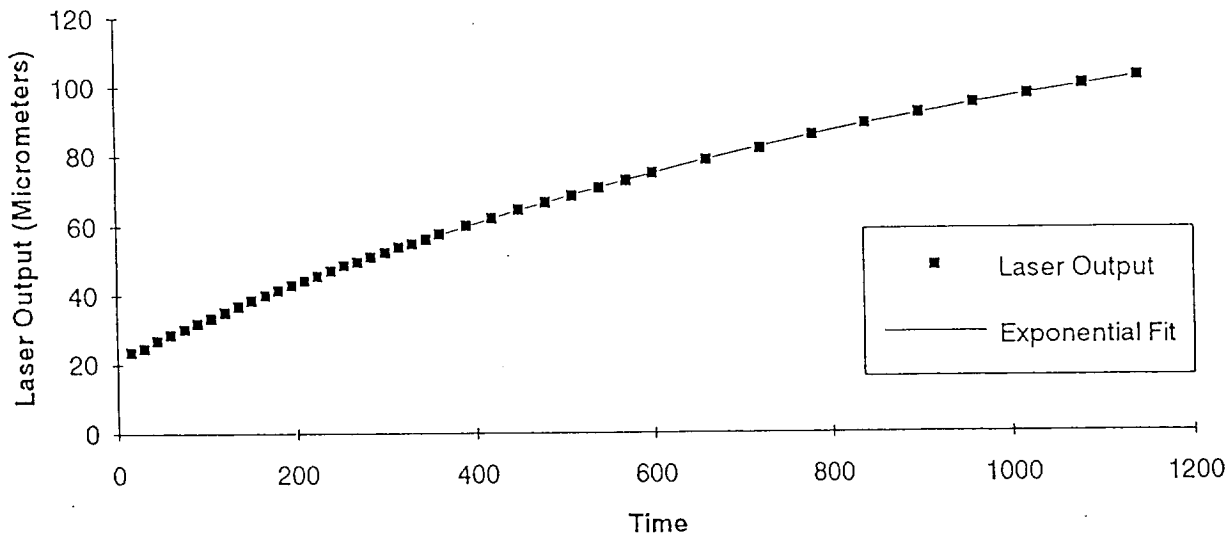


Figure 4-15. Displacement versus time at constant excitation.

Interpretation of this data is somewhat complicated by the fact that both the displacement and heat generation are nonlinear functions of the actuator excitation current. A couple of simple points, however, can be deduced. The first is that the thermal induced active member displacements can dominate the magnetostrictive displacements at very low frequencies. The simple thermal model predicts that 2 amps of dc excitation current will result in 120 micrometers of thermal expansion. Even at more reasonable current levels of 1 amp, the thermal expansion is predicted to be approximately 30 micrometers (since power is proportional to the square of current), which is greater than the approximately 15 to 20 micrometers of magnetostrictive expansion at this current level.

The frequencies at which the thermal effects dominate are quite low. For example, with the actuator excited with a one amp peak sinusoid at one hertz, the AC component of the thermal displacement is predicted to be approximately 0.03 peak micrometers at 2 hertz versus the approximately 15 micrometer peak fundamental magnetostrictive response at 1 hertz. At these levels, the nonlinearity in the magnetostrictive material will dominate the response at 2 hertz by at least one order of magnitude.

4.3.2 SatCon Active Member Testbed Description

The following is a discussion of the procedures and results of tests run at SatCon on the room temperature magnetostrictive active member. The active member was first tested under free end boundary conditions, then in the SatCon active member testbed under partially clamped boundary conditions². The preload and drive current levels were varied for both boundary condition investigations.

The principal components of SatCon's active member testbed can be seen in Figure 4-16, a schematic of the testbed. The top half of Figure 4-16 is the view of the testbed from above, the lower half of Figure 4-16 is the view of the testbed from the side. As shown the active member is held between a stationary support structure on the right side and a movable carriage on the left. The stationary support is rigidly attached to the testbed base. The other end of the active member is bolted to the movable

² The clamped boundary conditions are referred to as "partially" clamped because the stiffness of the SatCon testbed is not high enough to contain all the motion of the active member, as will be discussed.

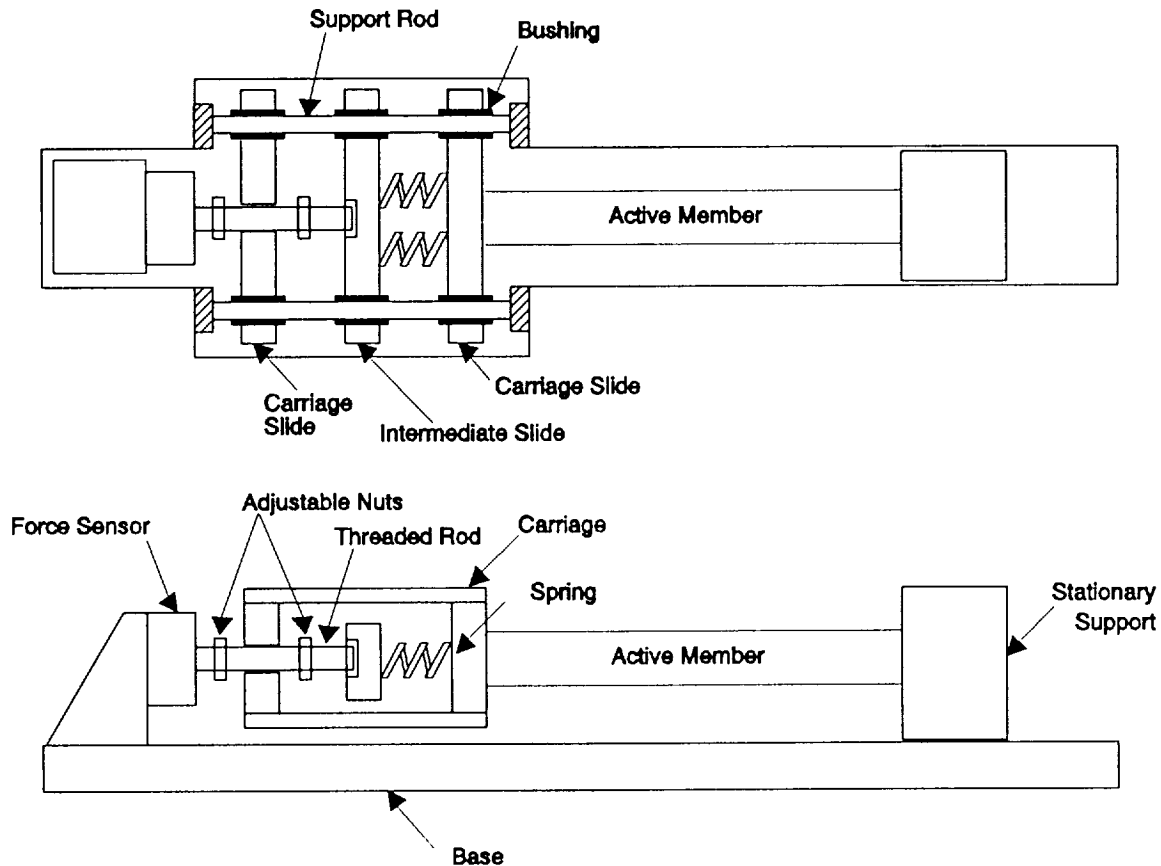


Figure 4-16. Active member testbed layout.

carriage. The movable carriage is constrained to motions along the axes of the active member by support rods and bushings. The mechanical mechanism around the movable carriage provides for three different operational modes, which provide "partially clamped", "constant spring", and "free motion" boundary (end) conditions for the active member. These operational modes are selected by changing the positions of the two adjustable nuts mounted on a threaded rod.

In the "partially clamped" mode, the two nuts are tightened against opposite sides of the movable carriage slide. This eliminates the ability of the carriage to move. In this case, the load path from the active member is through the carriage, through the tightened nuts to the threaded rod, and then through the force sensor to the testbed base. In this mode, the mechanical impedance seen by the active member is approximately 10 MN/m ($60,000 \text{ lb}_f/\text{in}$). This is caused by the finite stiffness of the mechanical elements, including the force sensor, threaded rod, adjustable nuts, etc.

In the "constant spring" mode, the right adjustable nut is tightened against the intermediate slide. The nut is adjusted to obtain the desired compressive force level. The combination of the relatively soft spring and threaded nut allows the compressive "preload" force to be accurately adjusted to within the five Newton (one pound-force) accuracy of the force sensor readout. In this case the load path is from the active member into the movable carriage. The load is then taken by the spring and transferred to the intermediate slide and then through the adjustable nut to the threaded rod and force sensor. In this mode, the mechanical impedance as seen by the active member is dominated by the spring with an approximately 300 kN/m (2000 lb_f/in) stiffness.

In the "free motion" mode, neither adjustable nut is tightened against either the carriage or intermediate slide. This configuration is shown in Figure 4-16. In this case, the movable carriage is free to move in the axial direction of the active member. Its axial motion is effected only by friction in the bushings that constrain its non-axial motion.

The active member testbed is instrumented with both an LVDT and a force sensor. The Schavitz LVDT, not shown in Figure 4-16, measures the motion of the carriage relative to the testbed base. It includes both analog signal output (3937 Volts/meter) and front panel numeric display. The force sensor is mounted to the same bracket that terminates the threaded rod, at the end of the testbed. The force sensor is used to meter the spring compression while preloading the active member, as well as measure the forces generated by the actuator during the "partially clamped" or "constant spring" tests. The force sensor and associated electronics are made by Sensotec. The force sensor is a dc strain gauge type model 572-05 with a 0-5000 lb_f (0-20,000 Newton) range. The associated electronics produces analog signal output (0.001 Volts/lb_f or 2.25×10^{-4} Volts/Newton) and front panel numeric display. The active member is instrumented with a displacement sensor and a flux field sensor. As previously described, the displacement sensor is a differential eddy current sensor that measures the motion of the magnetostrictive rod and flexures relative to the active member housing.

4.3.3 Free Boundary Condition Tests

The test procedures for the free boundary conditions involve driving the actuator with a 5 Hz sinusoidal signal and recording the time history of four measurements; the coil current, the flux field, the displacement, and the voltage. The 5 Hz signal was generated using a 2630 Tektronix spectrum analyzer. The five hertz excitation is low

enough to give quasi-static results and high enough to allow the data to be quickly collected. The active member coil was driven by a Techron 7520 power amplifier, which was under current control and amplified the 5 Hz sinusoidal signal. The four time history measurements, current, field, displacement, and voltage, were stored using the spectrum analyzer. The coil current was measured using a current probe. The field and displacement signals correspond to the active member sensors, as previously described. The voltage was taken at the output of the power amplifier.

The active member was excited with five hertz sinusoidal current waveforms at seven different peak current levels of 0.5, 1.0, 1.5, 2.0, 3.0, 4.0, and 5.0 amps. Data was taken with the magnetostrictive material in the active member mechanically preloaded at five different levels, consisting of 0 lb_f, 100 lb_f, 200 lb_f, 300 lb_f, and 400 lb_f. The preload stresses in the magnetostrictive material corresponding to these preload levels are given in Table I. The actuator was preloaded in the SatCon testbed, then tested at the different current levels. The power supply is under current control, hence for testing convenience, the transfer function from commanded voltage from the spectrum analyzer to the drive current has gain of one amp/volt. In order to reduce the thermal effects in the data, the "current on" time was minimized.

Table 4-2: Preload Forces and Stresses

Force		Stress	
lb	N	psi	MPa
100	445	905	6.2
200	890	1810	12.5
300	1330	2715	18.7
400	1780	3620	25

To adjust the mechanical preload, the active member was placed in the SatCon testbed in series with a steel cylinder. The steel cylinder rides between the bracket and the active member flexures. The inner diameter of the steel cylinder diameter is slightly larger than the diameter of the output shaft of the active member, allowing the cylinder to slip over the output shaft. The outer diameter of the cylinder is smaller than the

inner diameter of the preload nut, allowing the cylinder to rest on the preload spring. The preload is set using the "constant spring" configuration by turning the adjustment nut against the intermediate slide, as discussed earlier. One revolution of the adjustment nut will change the preload force by approximately 800 Newtons (200 lb_f). The force level is measured using the testbed force sensor. Once the desired preload was obtained, the housing preload nut was tightened down, using a custom wrench, to hold the active member flexures at the desired preload.

Figures 4-17 through 4-20 are time plots of the raw data at a current level of 2 Amps, as shown in Figure 4-17, and with the active member preloaded to 12.5 MPa (200 lb_f). Figure 4-18 is a plot of the flux field in units of Gauss. As shown, only very small levels of magnetic field were detected. Due to assembly requirements, the flux sensor is not located in a direct flux path and therefore cannot detect the actual flux density. Earlier flux data, taken before assembly, shows the flux field levels varying by over 1000 Gauss. Figure 4-19 is a plot illustrating the earlier flux field data, also taken at a current level of 2 Amps and a preload of 12.5 MPa (200 lb_f). Because that data was taken before assembly, the Hall probe was placed directly in the air gap, and depicts a more accurate level of magnetic flux. Figure 4-20 is a plot of the measured displacement of the magnetostrictive rod and flexures relative to the housing. The peak-to-peak displacement is approximately 48 micrometers. As can be seen from the dc level of the displacement, no attempt was made to force the sensor output to zero for zero input current, either through shimming the sensor cage or through conditioning the sensor output signal. Figure 4-21 is a plot of the actuator voltage versus time.

In Figure 4-22, the actuator displacement is plotted against the actuator current for the 2 amp peak, 5 hertz sinusoidal current input. This is the same data of in Figure 4-17 (current vs time) and Figure 4-20 (displacement vs time), but plotted as displacement versus current. This plot, therefore, shows the actuator output (displacement) as a function of actuator input (current). At this excitation level, the active member is reasonably linear but with significant hysteresis. Figure 4-23 contains a blown-up portion of Figure 4-22, which illustrates that the two cycles of the 5 Hz waveform have excellent repeatability.

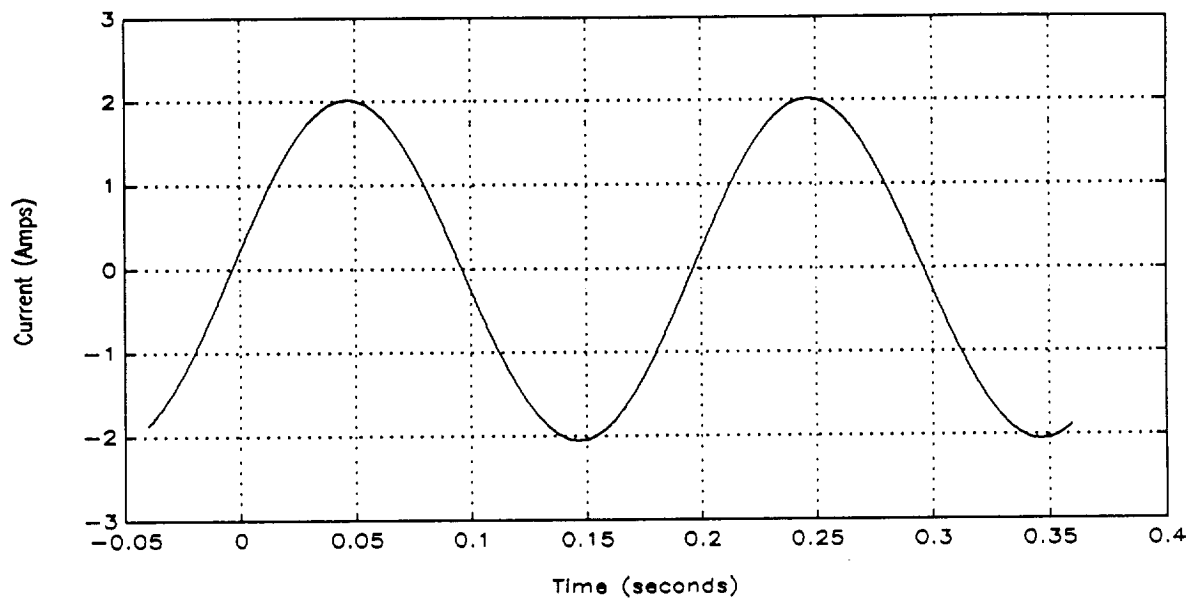


Figure 4-17. Time history of current (12.5 MPa preload free end conditions).

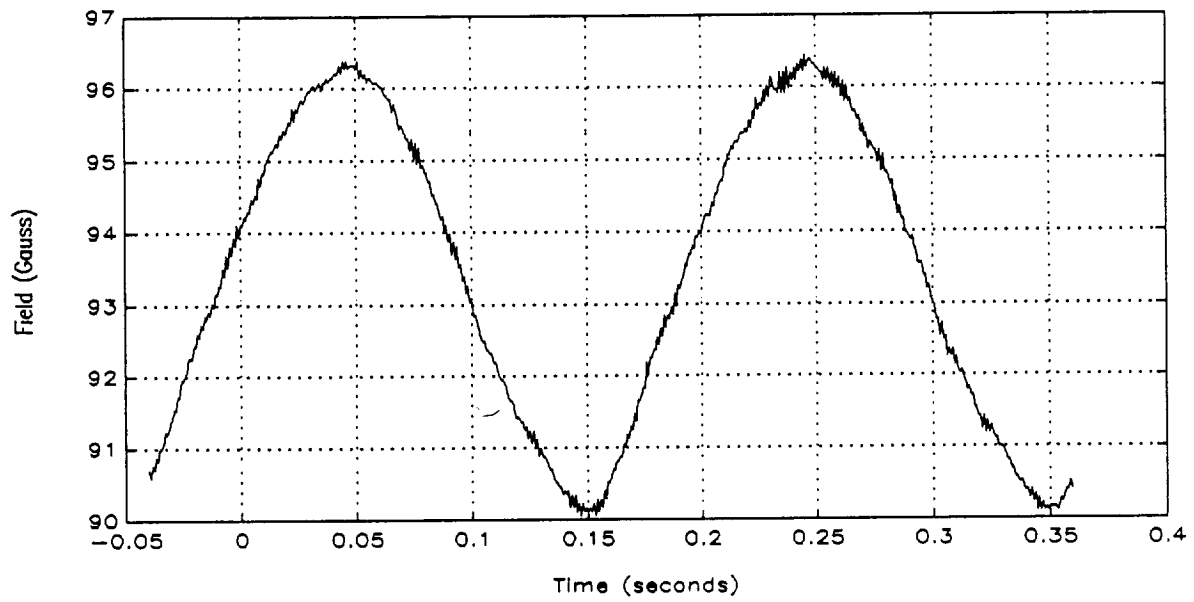


Figure 4-18. Time history of flux field (12.5 MPa preload, free end conditions).

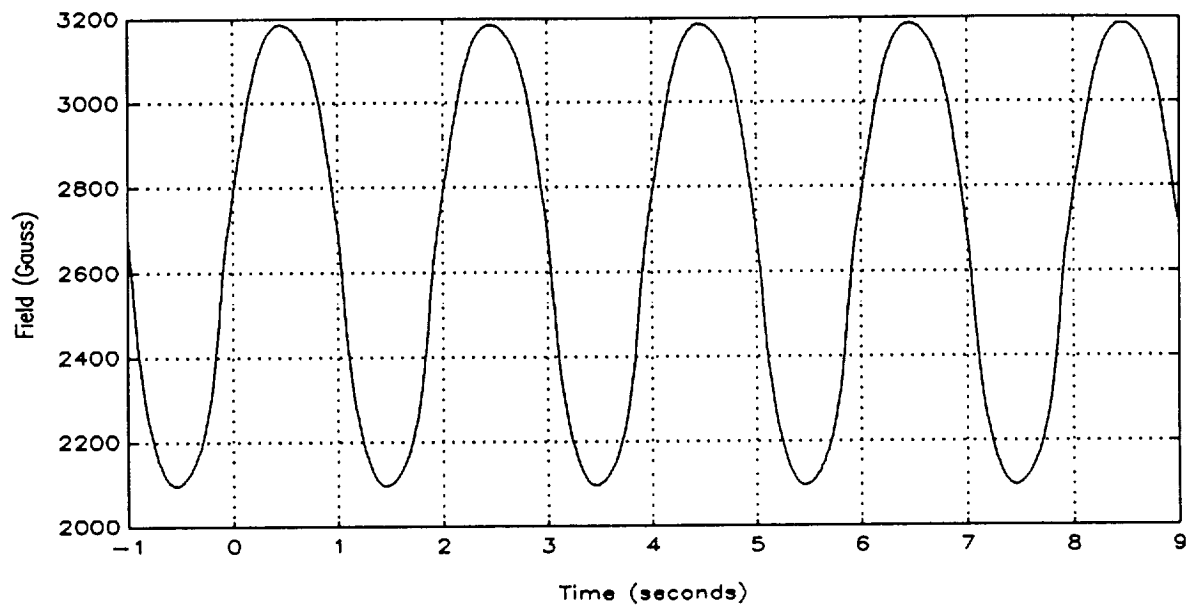


Figure 4-19. Time history of flux field before assembly (12.5 MPa preload, free end conditions).

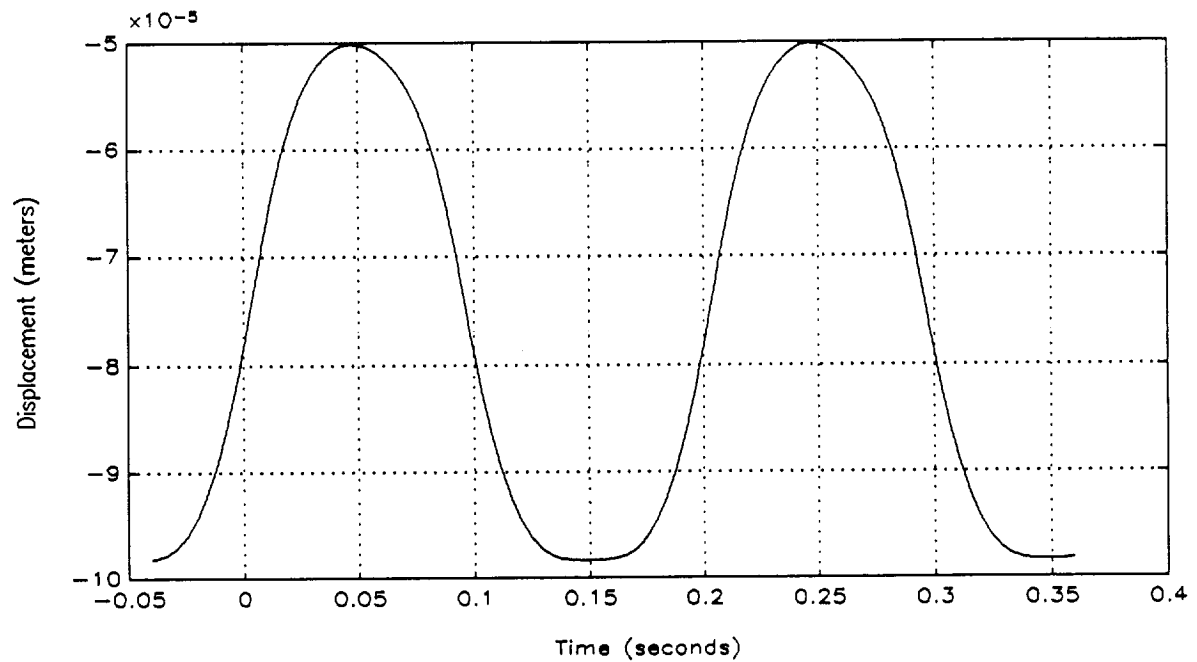


Figure 4-20. Time history of displacement (12.5 MPa preload, free end conditions).

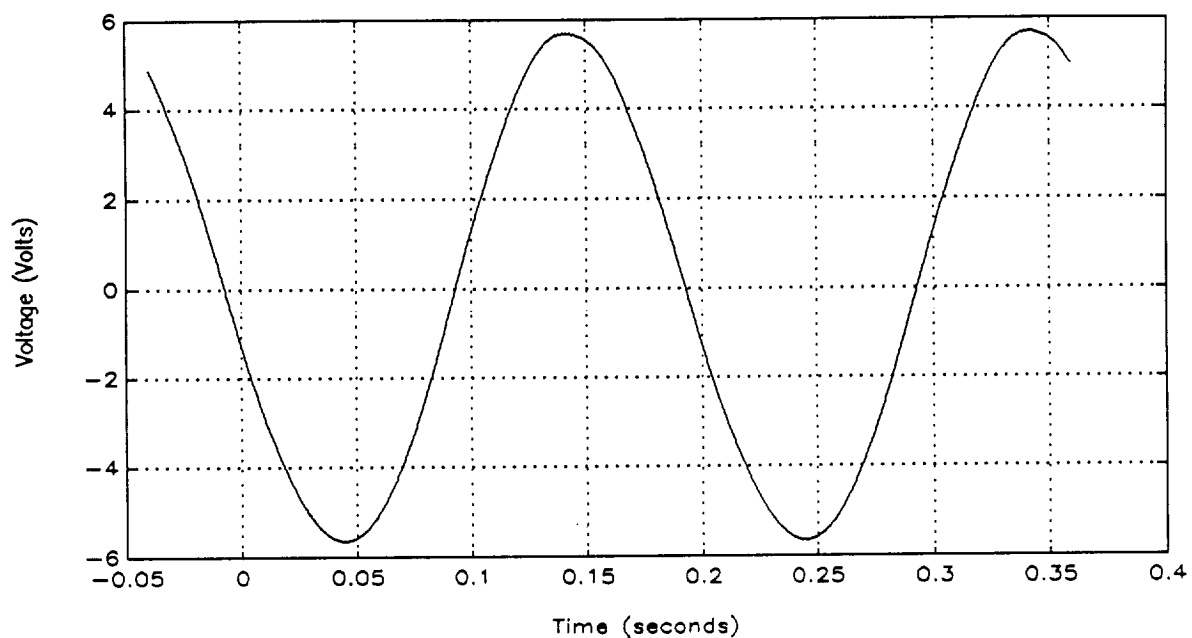


Figure 4-21. Time history of voltage (12.5 MPa preload, free end conditions).

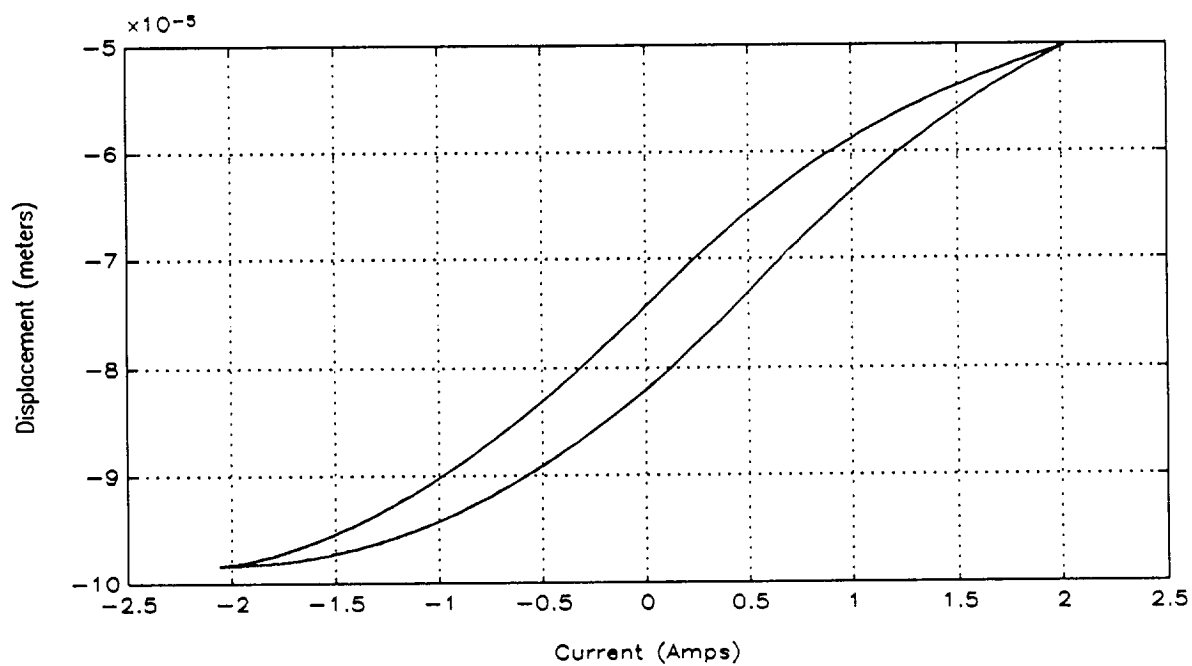


Figure 4-22. Displacement vs. current (12.5 MPa preload, free end conditions).

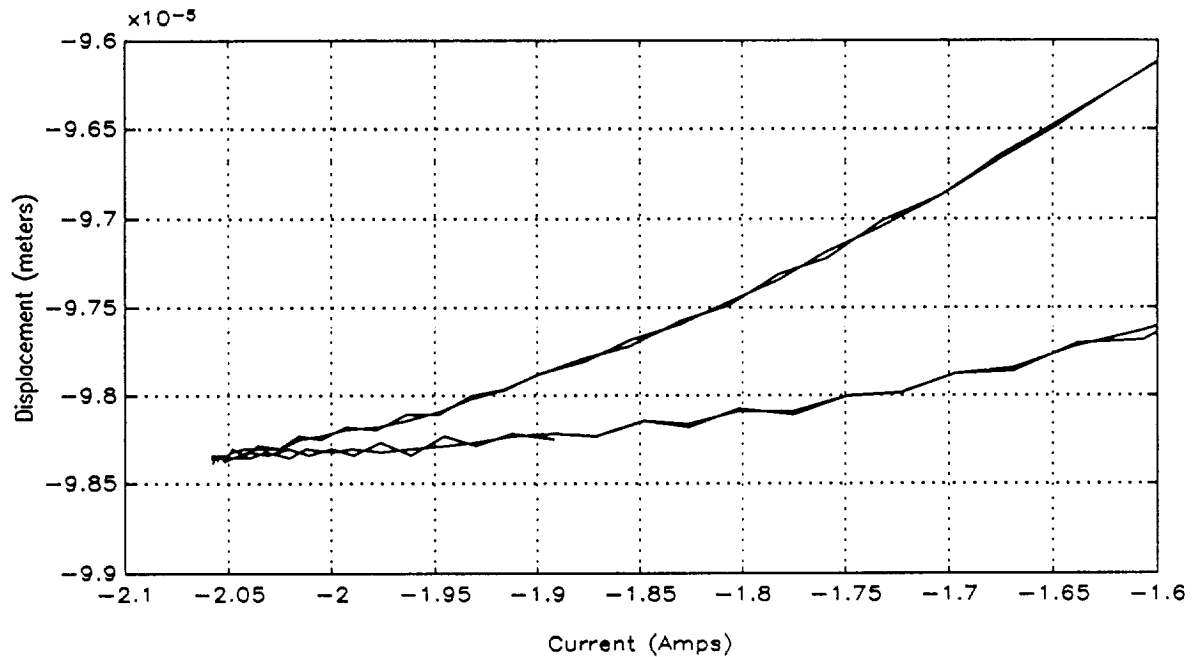


Figure 4-23. Displacement vs. current (12.5 MPa preload, free end conditions).

Figure 4-24 contains the raw displacement and current data for all the current levels at the 12.5 MPa l_b preload. As shown, a maximum displacement of approximately 66 micrometers was obtained at the current level of 5 Amps. The curves vary slightly due to thermal effects. Figure 4-25 is a plot of the same data, however, the thermal effects have been removed by sifting each of the displacement curves such that at the zero current points, the average of the two displacements is zero. Figure 4-26 is an identical plot to Figure 4-25 illustrating the displacement as a strain, with the minimum strain set to zero. As shown, the maximum strain obtained with a 5 Hz and 5 Amp excitation, at 12.5 MPa (200 l_b) preload, is approximately 1120 ppm.

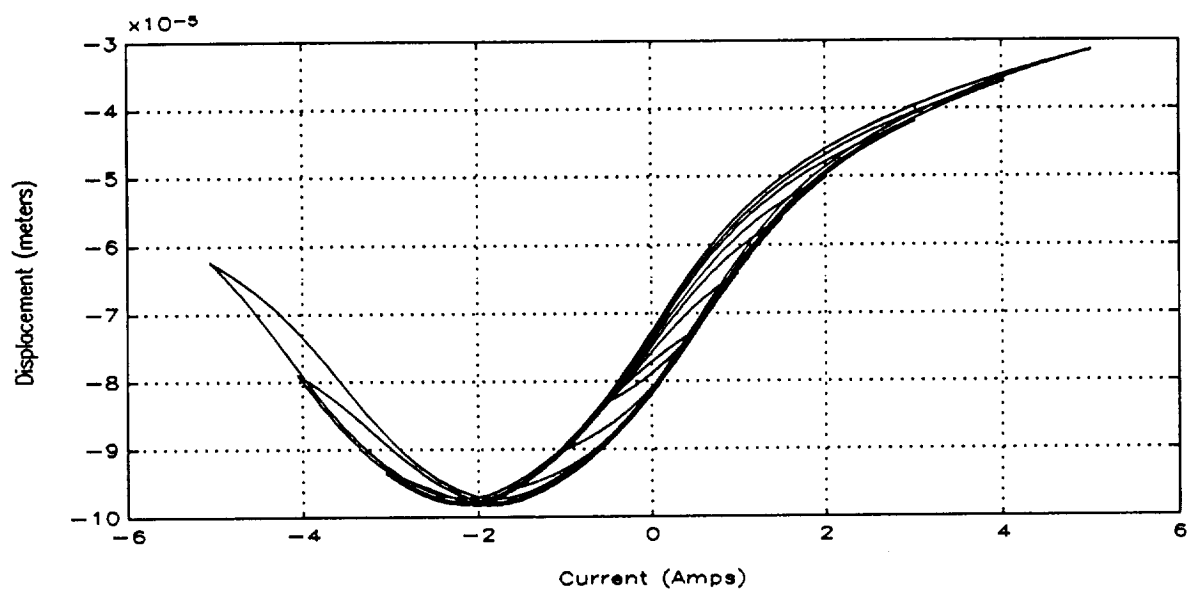


Figure 4-24. Displacement vs. current (12.5 MPa preload, raw data).

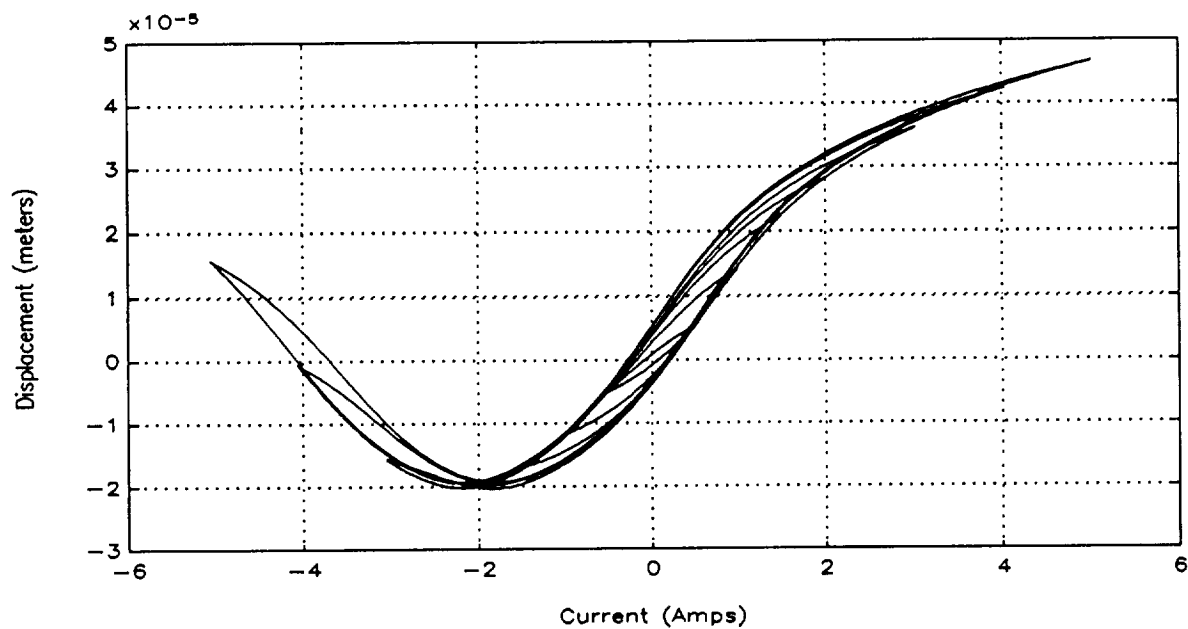


Figure 4-25. Displacement vs. current (12.5 MPa preload, cleaned data).

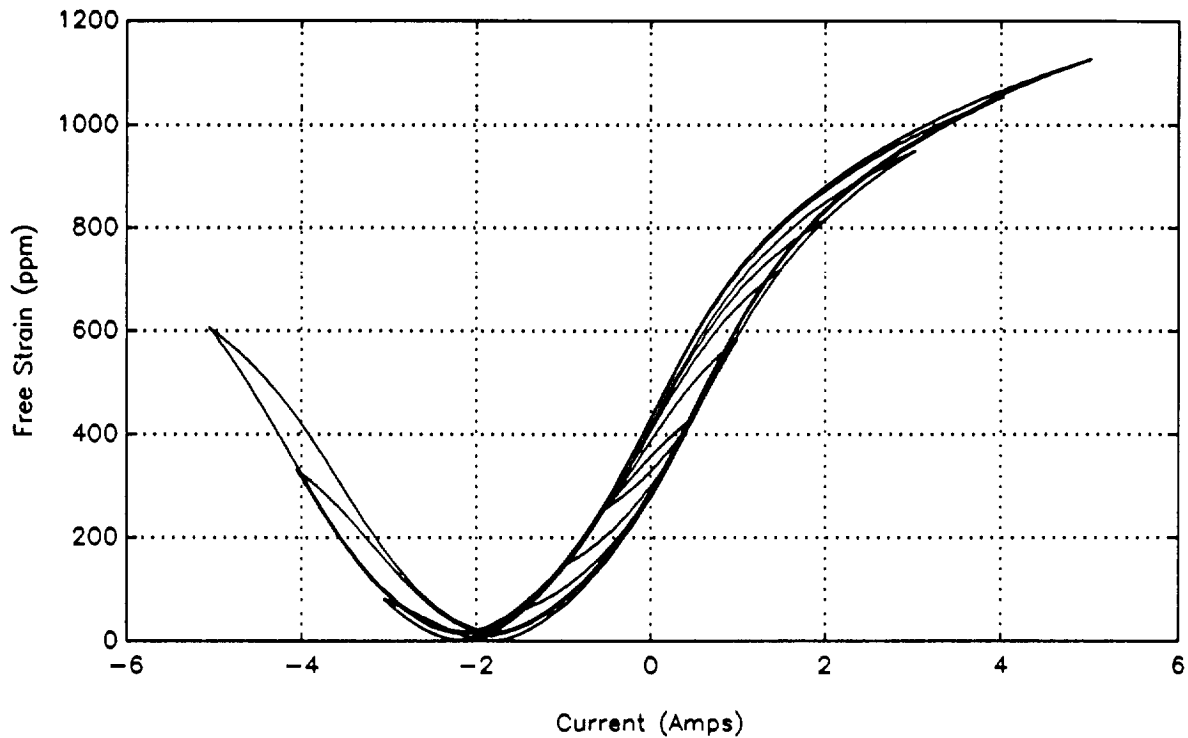


Figure 4-26. Free strain vs. current (12.5 MPa preload, cleaned data).

Figure 4-27 is a plot of the raw displacement versus current data for all the different preloads, with the same 2 amp peak, 5 Hertz sinusoid excitation. The number beside each curve is the preload stress in the magnetostrictive material as previously given in Table I. The same data in Figure 4-26 is shown in Figure 4-28 with the compressive and thermal displacements removed. This was done by again shifting the displacement curves such that at zero current, the average of the two displacements is zero. As shown, the largest strains occur at the 6.2 MPa and 12.5 MPa preload levels, for a current excitation of 2 Amps. Figure 4-29 is identical to Figure 4-27, except displaying the displacement as a strain in the magnetostrictive material. The maximum strain is approximately 840 ppm (at 6.2 MPa) for the current level of 2 Amps.

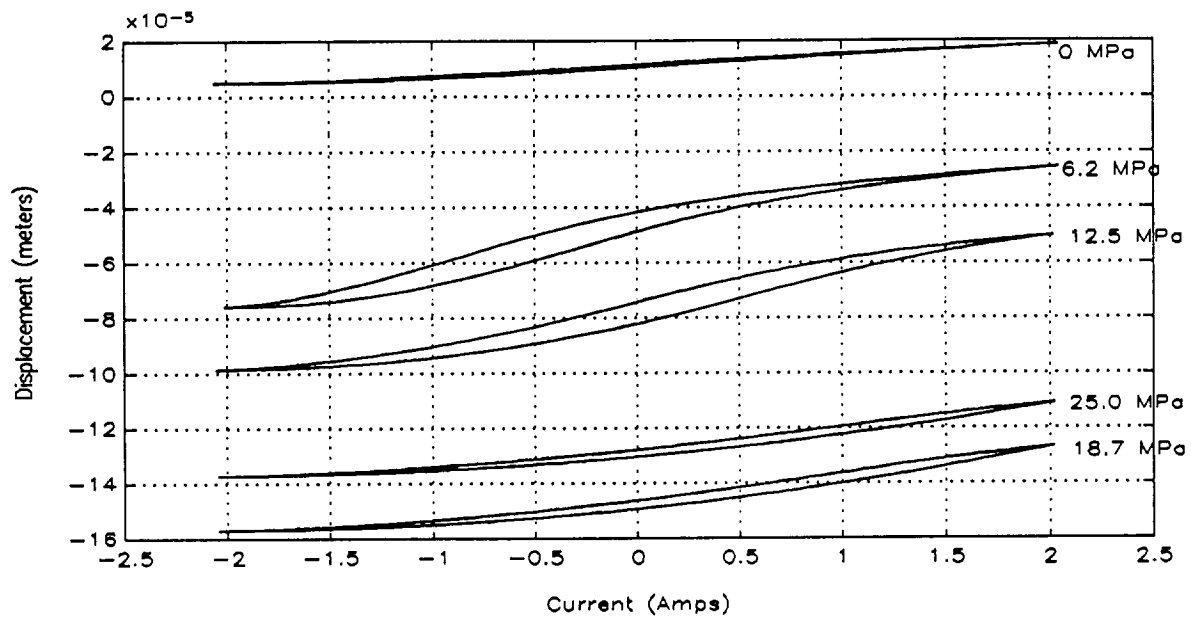


Figure 4-27. Displacement vs. current (2 amps, raw data).

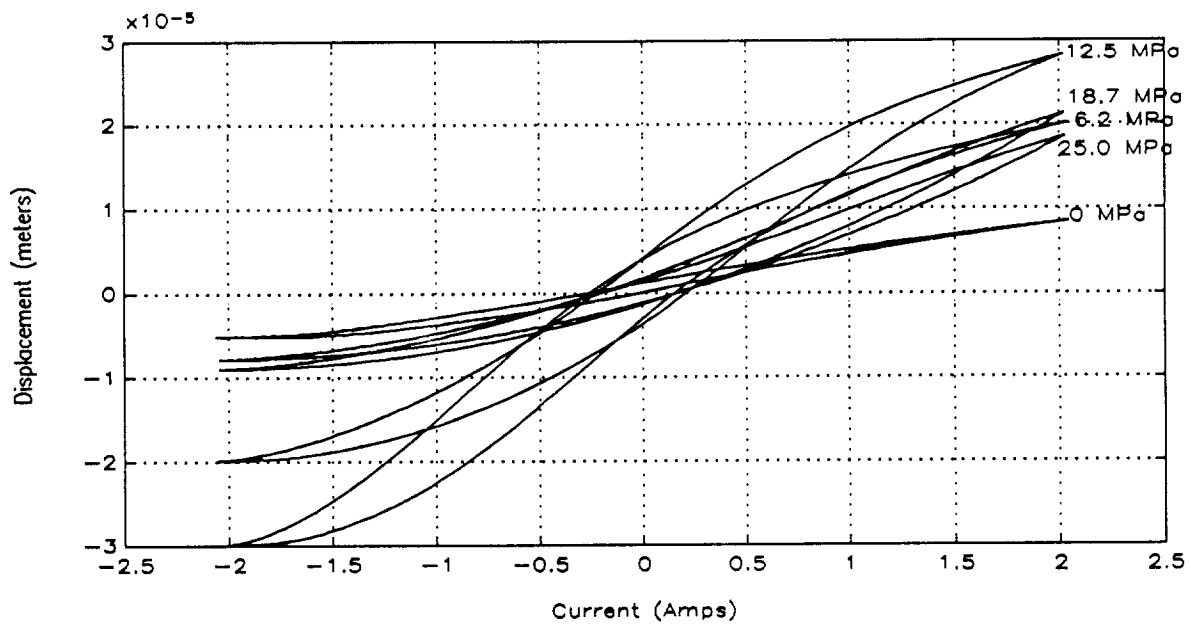


Figure 4-28. Displacement vs. current (2 amps, cleaned data).

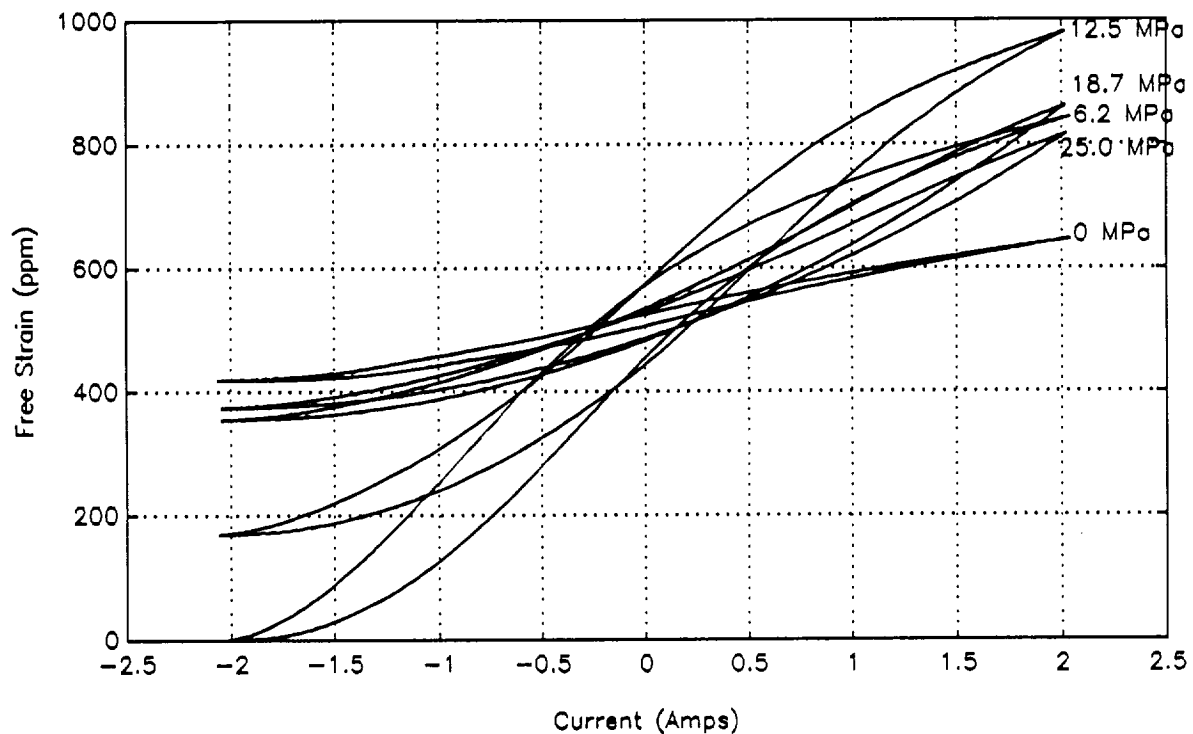


Figure 4-29. Free strain vs. current (2 amps, cleaned data).

The frequency response from the drive current to the active member displacement was measured using the spectrum analyzer. Figure 4-30 is a bode plot over the frequency range of 5 to 500 Hz. The upper plot is the magnitude of the transfer function and the lower plot the phase of the transfer function. The active member was preloaded to 12.5 MPa and excited with 100 mA rms white noise. As shown, the response is flat out to 450 Hz. The dc gain is approximately 10×10^{-6} meters per amp.

Because of the nonlinear response of the magnetostrictive material, its hysteresis characteristics, and incremental permeability effects, the frequency response of the actuator is a function of amplitude. This can be clearly seen in Figure 4-31, the frequency response magnitude between current and displacement for RMS current excitation levels of 100 mA, 0.5 A, and 1 A. As can be seen, at higher excitation levels, the dc gain is higher. The effect of hysteresis on these dc gain levels can be seen in Figure 4-32, a plot of displacement versus current for three different excitations. The

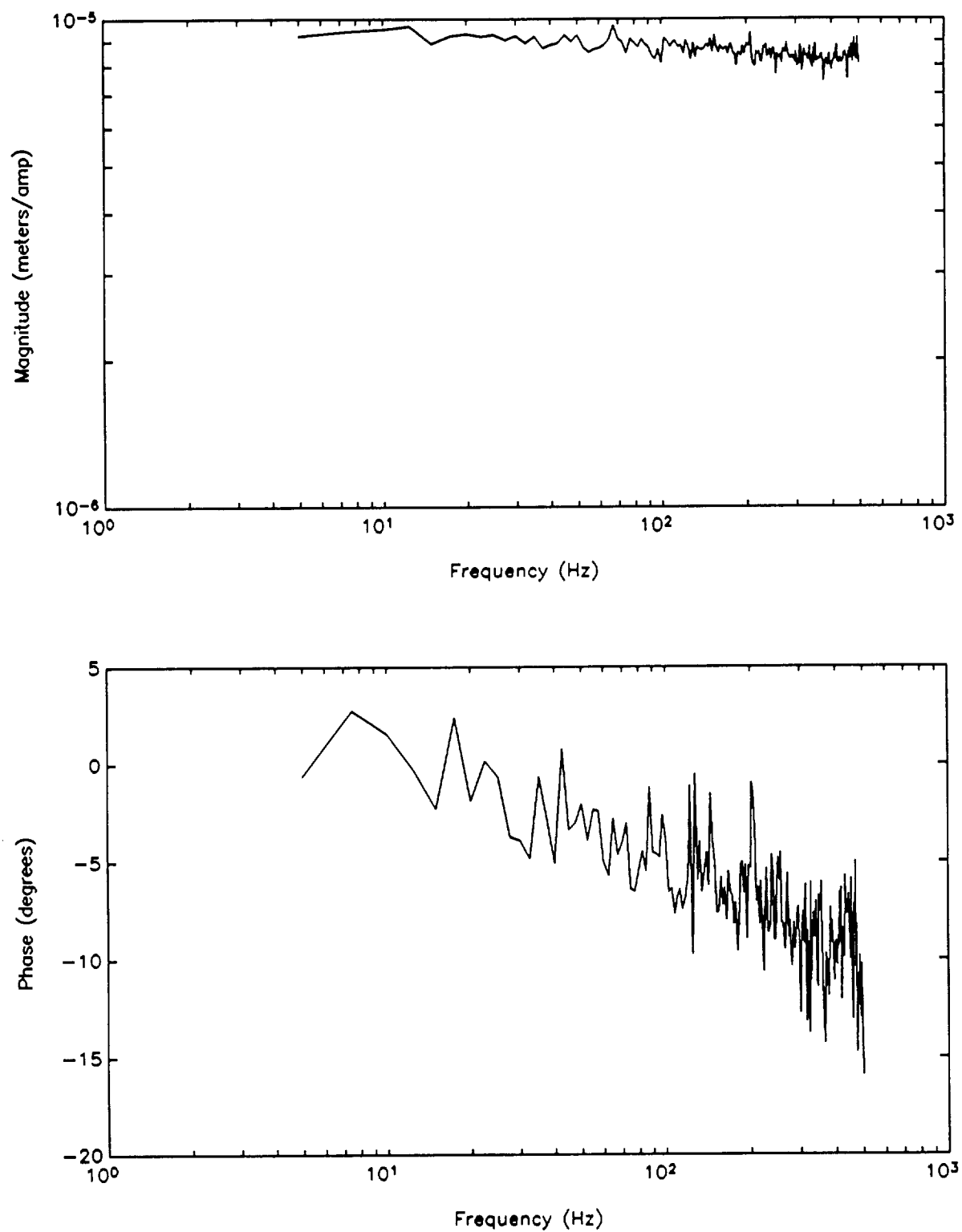


Figure 4-30. Current to displacement frequency response for 1 amp RMS excitation (12.5 MPa preload).

two solid curves are for the 5 Hz sinusoidal excitations shown previously, one with a 1 A peak amplitude and the other with a 2 A peak amplitude. The stars are data from white noise (0-500 Hz), 1 amp RMS excitation.

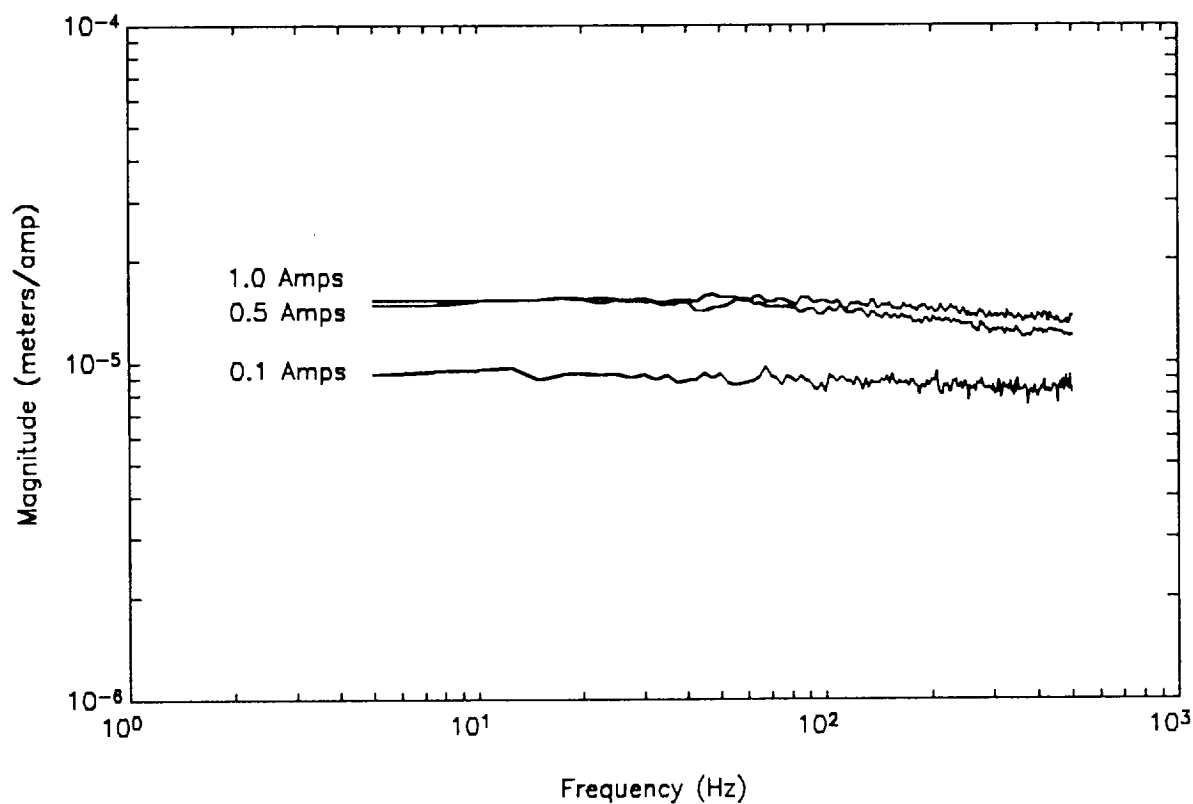


Figure 4-31. Comparison of the current to displacement frequency response for 0.1, 0.5, and 1.0 amps RMS excitation (12.5 MPa preload).

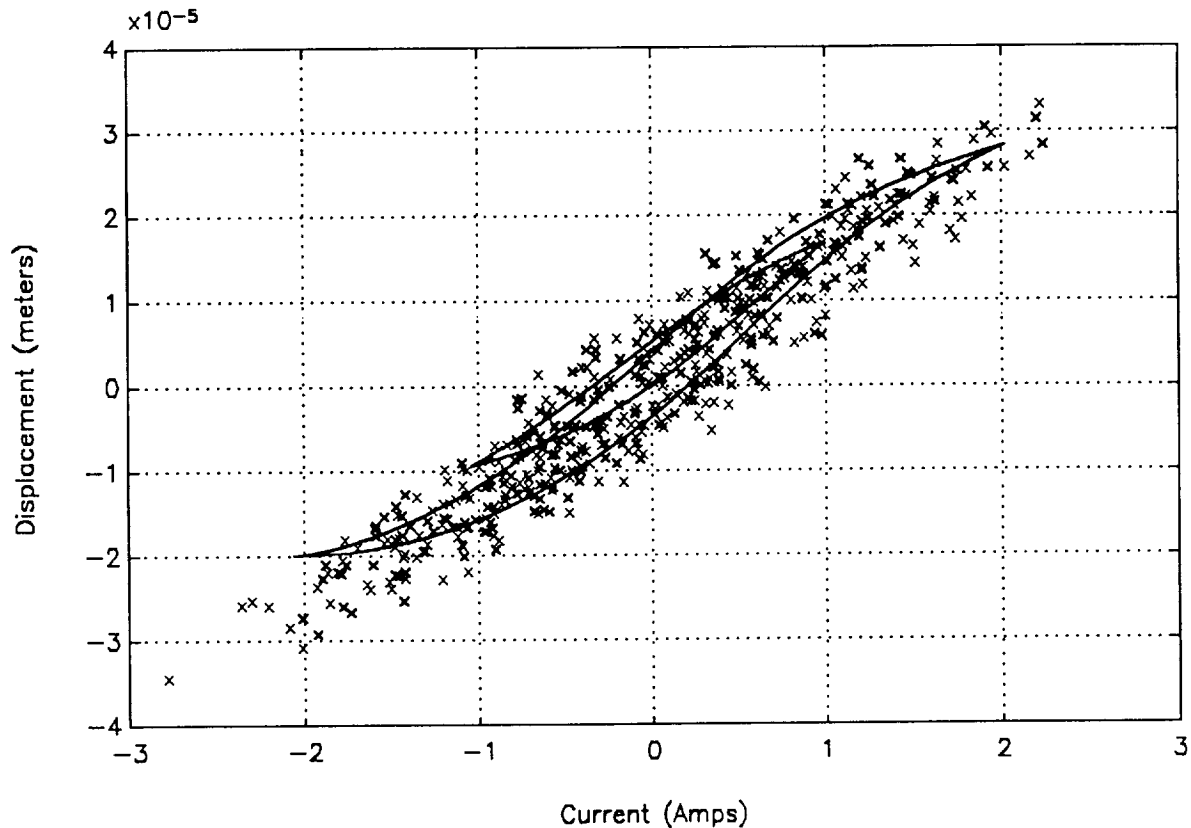


Figure 4-32. Comparison of the displacement versus current slopes for random and sinusoidal time history data.

Figure 4-33 is a swept sine bode plot of the displacement response to current input. These are plotted for two different amplitude excitations, 0.1 A and 1 A RMS. As for the random excitation, the active member gain is higher at the higher current levels. Figure 4-34 is a comparison of the random and swept sine excitations. Shown are the two bode magnitude plots for the same excitation level of 1 A RMS. The active member gain for these two excitation types is quite similar, with the sinusoidal excitation yielding cleaner data as is expected.

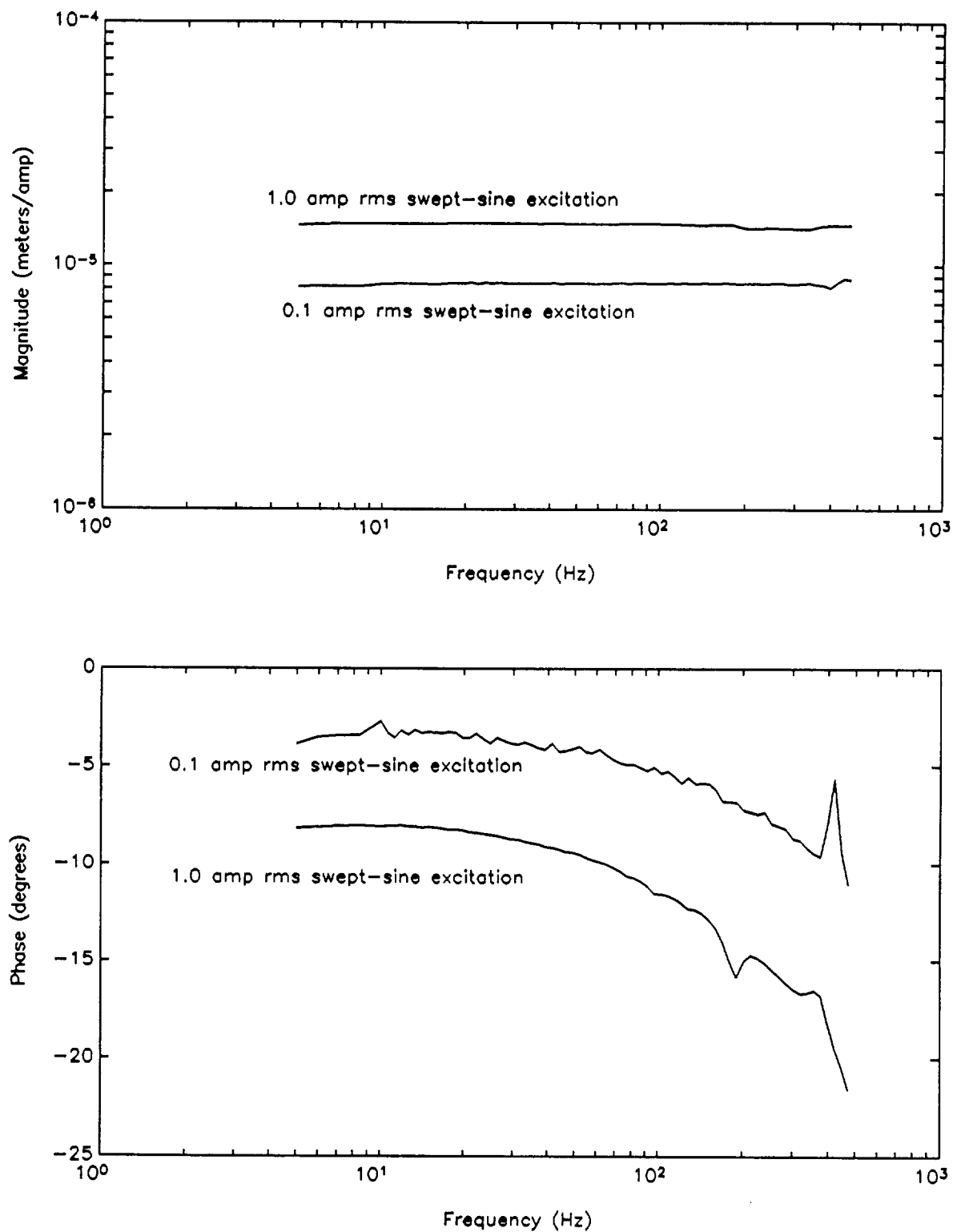


Figure 4-33. Current to displacement frequency response for swept-sine excitation.

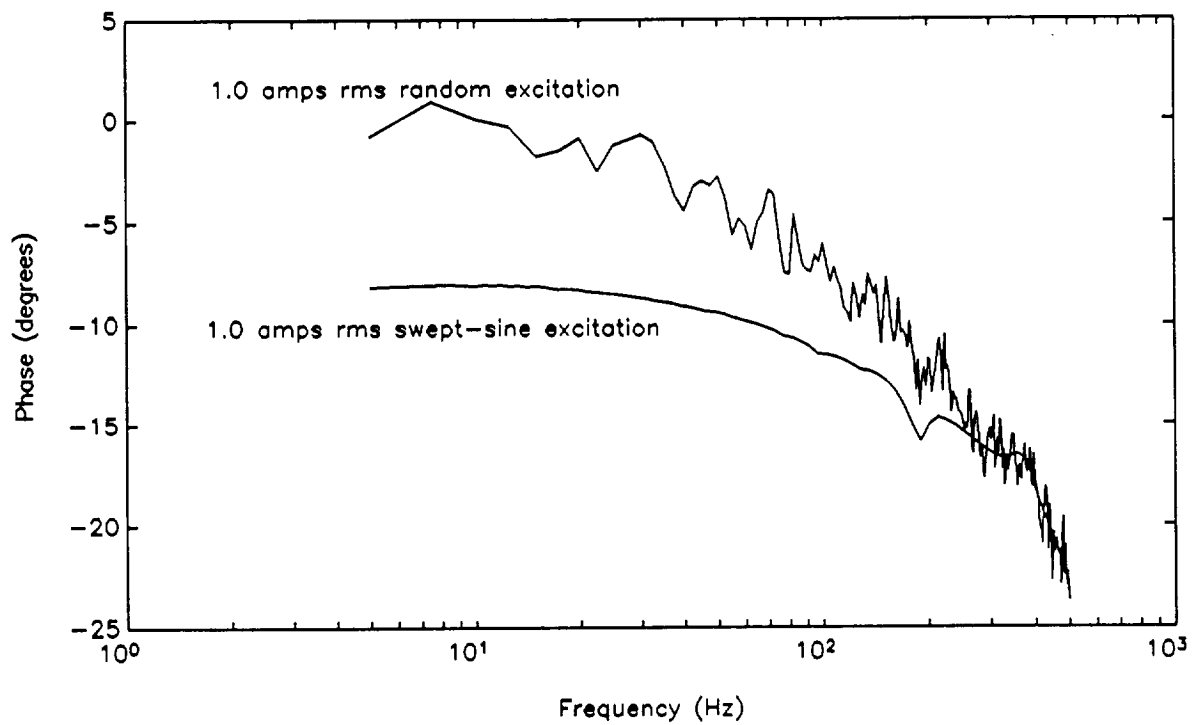
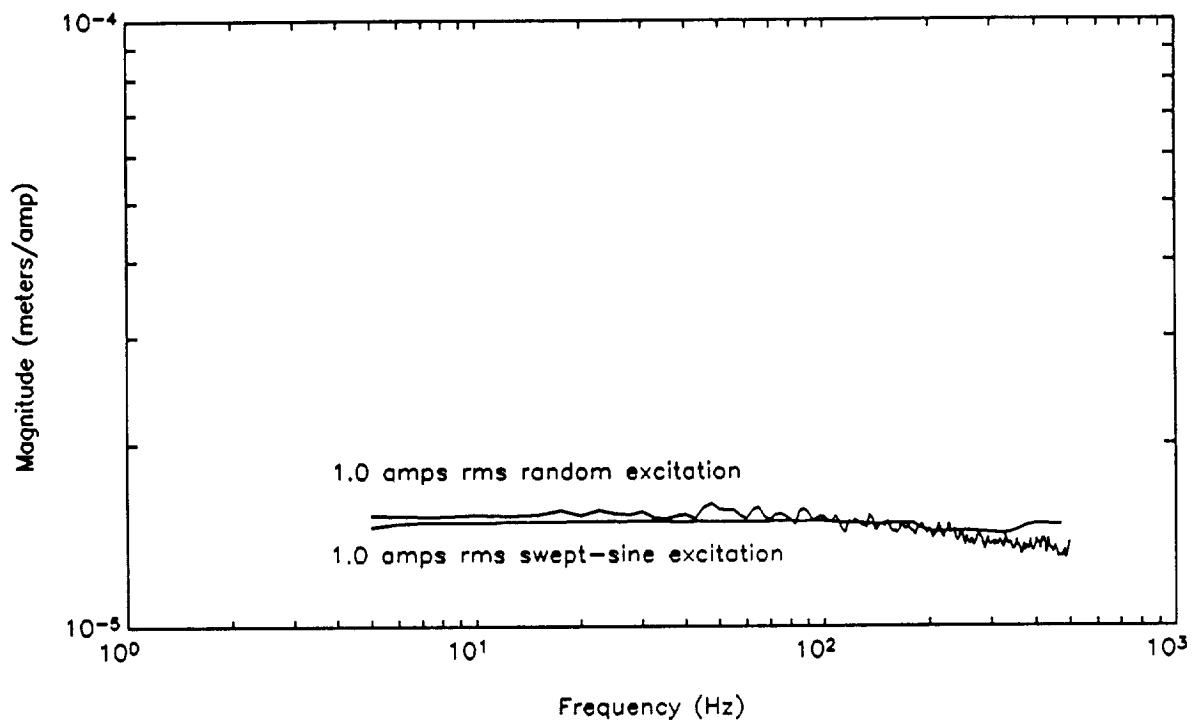


Figure 4-34. Comparison of random and swept-sine excitation (1 amp rms).

Figure 4-35 is a bode plot of the same transfer function, taken over the frequency range from 5 to 5000 Hz, with random excitation. Both the magnitude and phase of the frequency response are flat up to approximately 2000 Hz. As shown, the active member has a resonance at approximately 3300 Hz.

Figure 4-36 is a bode plot of the voltage to current response, or in other words, the impedance response, taken over the frequency range from 5 to 500 Hz. The figure compares the magnitude and phase plots for two random excitation levels, 0.1 A and 1 A RMS. The lower level excitation plot displays a higher break frequency.

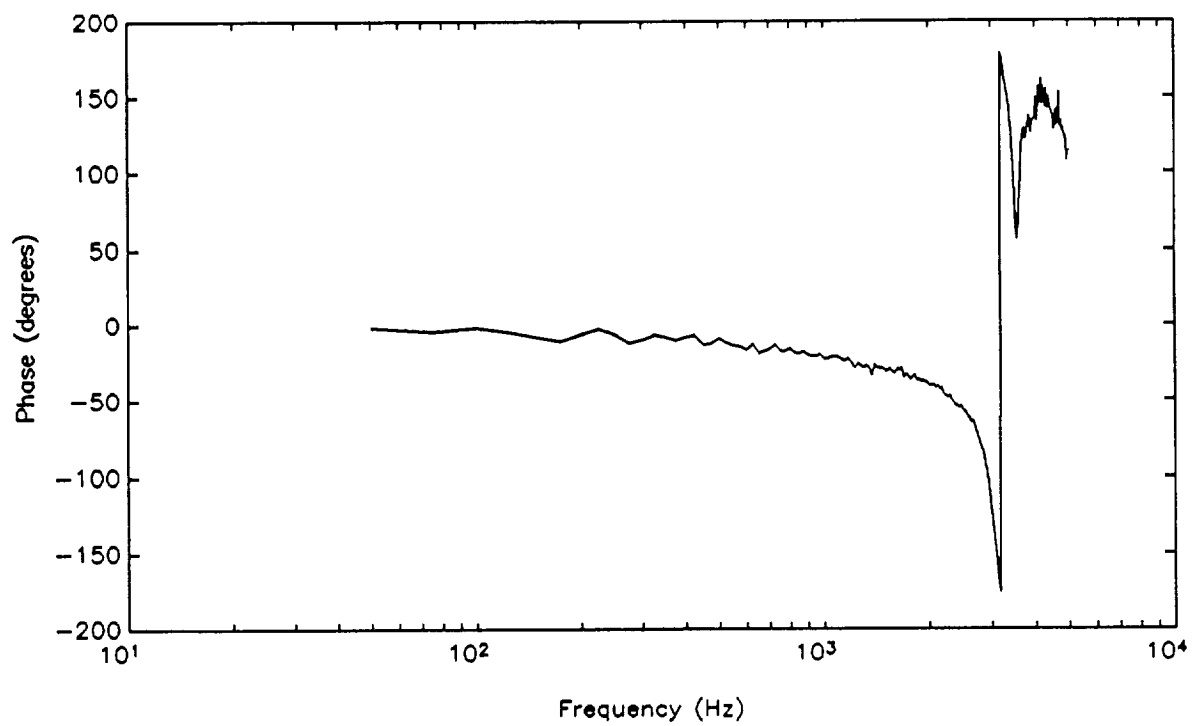
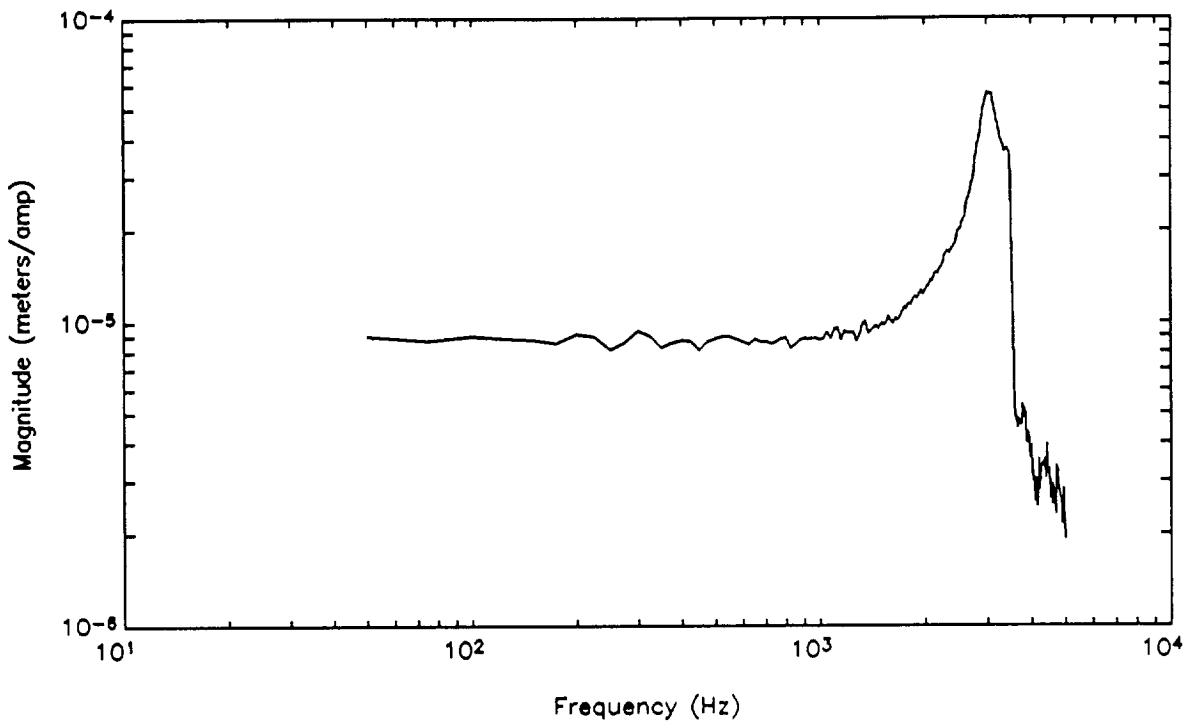


Figure 4-35. Current to displacement frequency response for 1 amp RMS excitation (12.5 MPa preload).

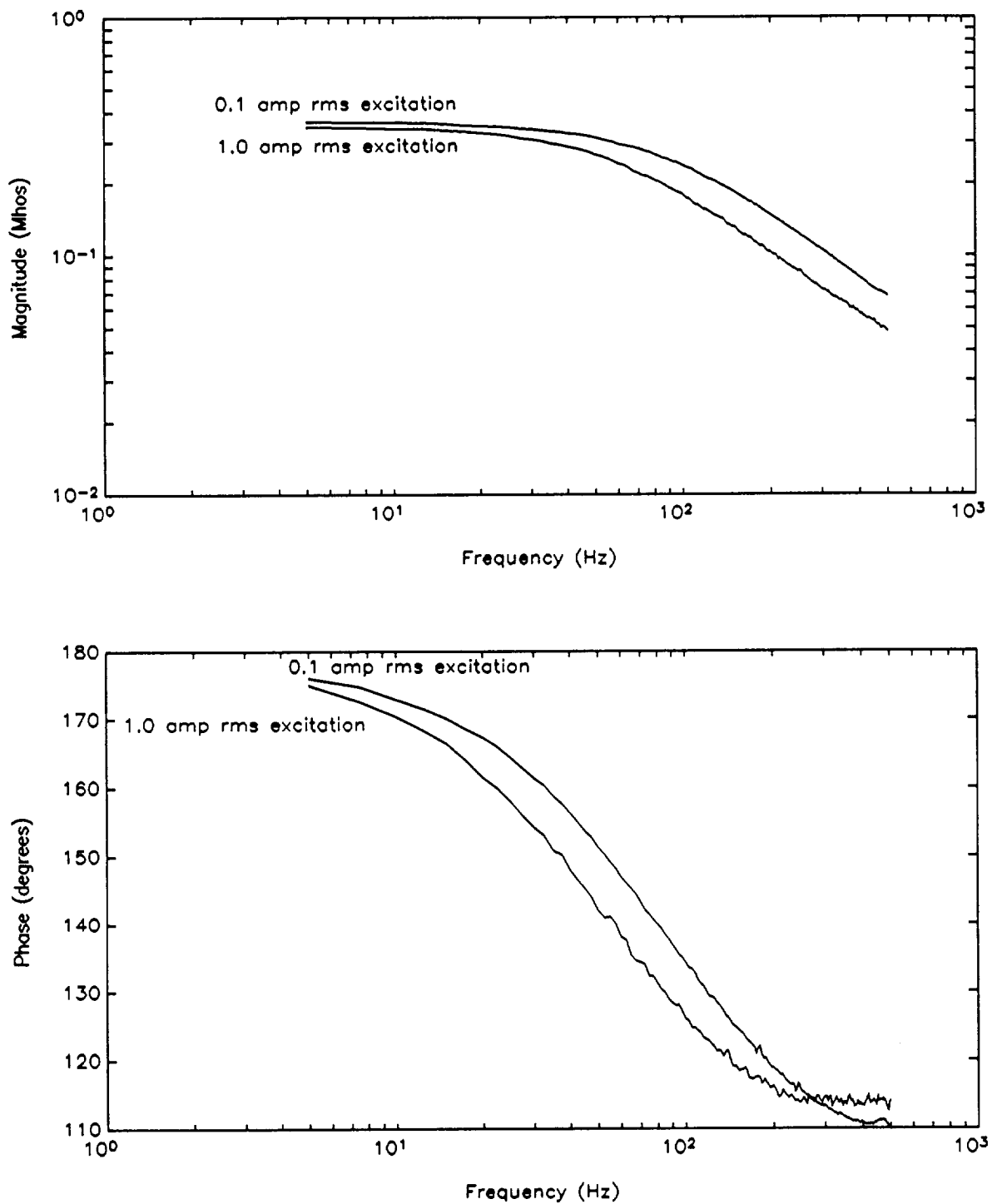


Figure 4-36. Voltage to current frequency response for random excitation (12.5 MPa preload, 0 A current bias).

4.3.4 Partially Clamped Boundary Condition Tests

This section discusses the partially clamped end condition procedures and results. The test procedures for the clamped end boundary conditions are similar to the free end conditions. Data was taken at the same current levels and preloads. Instead of voltage, the actuator clamped-force was measured. As previously mentioned, the testbed stiffness is lower than the actuator stiffness. Consequently, the boundary conditions for the clamped tests are not ideally clamped, and will be referred to as "partially" clamped. Data characterizing the testbed and actuator stiffnesses is discussed below.

For the clamped tests, the active member was placed in the SatCon testbed, and fastened to the end brackets with threaded screws. The movable end bracket was positioned such that no compressive or tensile forces were applied to the active member. Then both the nuts on the testbed threaded rod were torqued against the carriage end bar to prevent any motion. The nuts were torqued against each other, in such a manner as to not apply any forces on the active member. Using the frequency spectrum analyzer in series with a power amplifier, the actuator is driven with a 5 Hz sinusoidal signal, at current levels of 0.5, 1.0, 1.5, 2.0, 3.0, 4.0, and 5.0 amps, and at different internal preload conditions, consisting of 0, 6.2 MPa (100 lbs), 12.5 MPa (200 lbs), 18.7 MPa (300 lbs), and 25.0 MPa (400 lbs). Time histories of current, field, displacement, and force were measured.

The stiffness of the test assembly was determined by clamping the active member in the test assembly, following the procedures described above. Then the active member, internally preloaded to 12.5 MPa, was driven with a 5 Hz, 2 amps peak, sinusoidal signal. These preload and current levels are in the middle of the preload and current level ranges that were investigated, hence they were used as baseline conditions during the testbed stiffness test. The displacements of both the testbed brackets were measured using an eddy current sensor that was held by a portable clamp mount. Also measured was the force, from the testbed load cell, and the displacement of the active member. The actuator motion is given by the sum of the testbed bracket displacements.

Figure 4-37 is a plot comparing the actuator displacement measurement for the free end boundary conditions and clamped end boundary conditions. As shown, the clamped motion is approximately sixty percent of the free motion, hence the boundary conditions are not ideally clamped. An approximate testbed stiffness was determined from the force measurement and the displacement of one testbed bracket. Figure 4-38 is

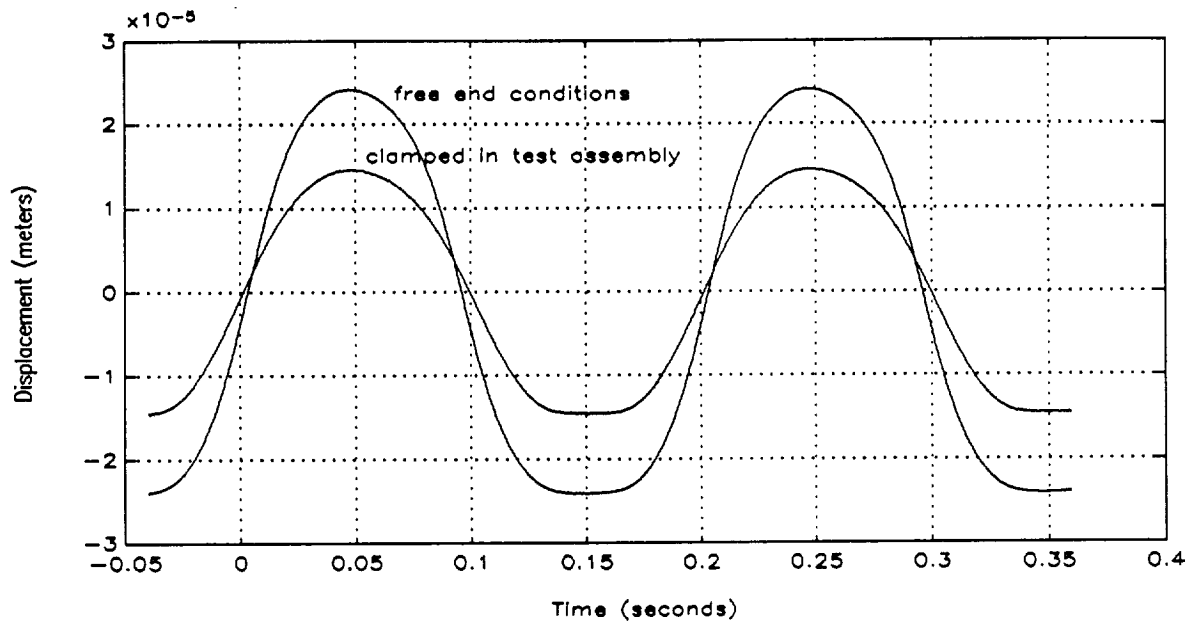


Figure 4-37. Actuator displacement for free and partially clamped boundary conditions.

a plot of the force versus displacement. The stiffness is approximately 9.3 MN/m (52,000 lb/in).

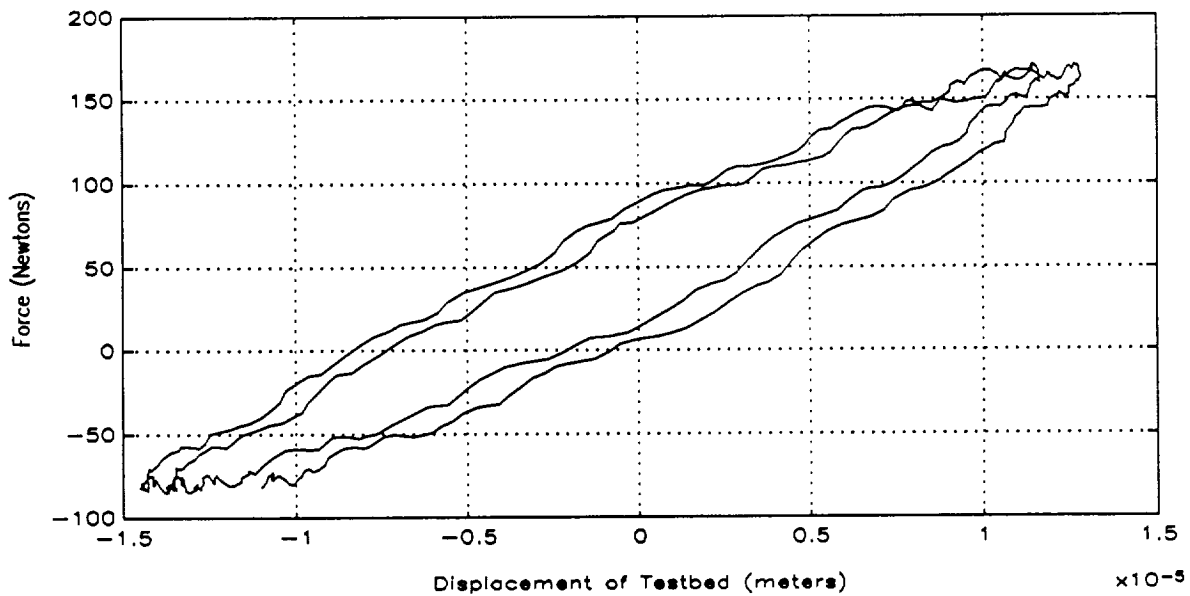


Figure 4-38. Testbed stiffness.

Figures 4-39, 4-40, and 4-41 are time history plots of the raw data, at a current level of 2 amps, and with the active member preloaded to 12.5 MPa. Figure 4-39 is a plot of the current versus time, and shows two cycles of the 5 Hz, 2 amps peak signal. From the free end testing discussion, the flux field sensor can only detect small levels of magnetic field because the Hall probe is not located in a direct flux path. The data for the partially clamped tests is similar to that of the free tests and will not be discussed.

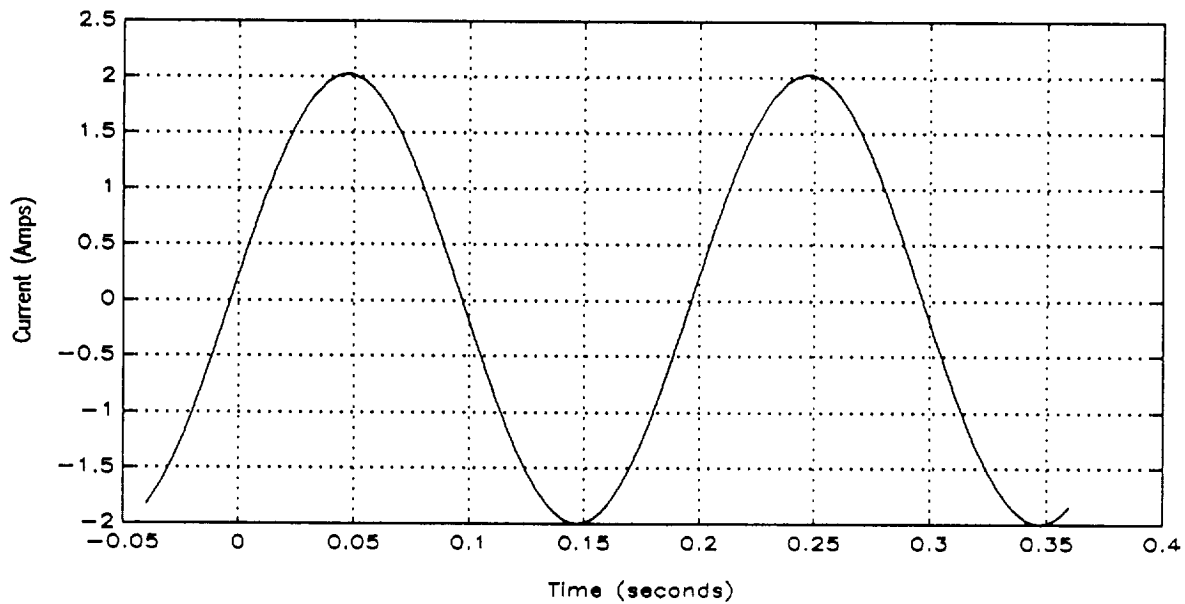


Figure 4-39. Time history of current (12.5 MPa preload; partially clamped end conditions).

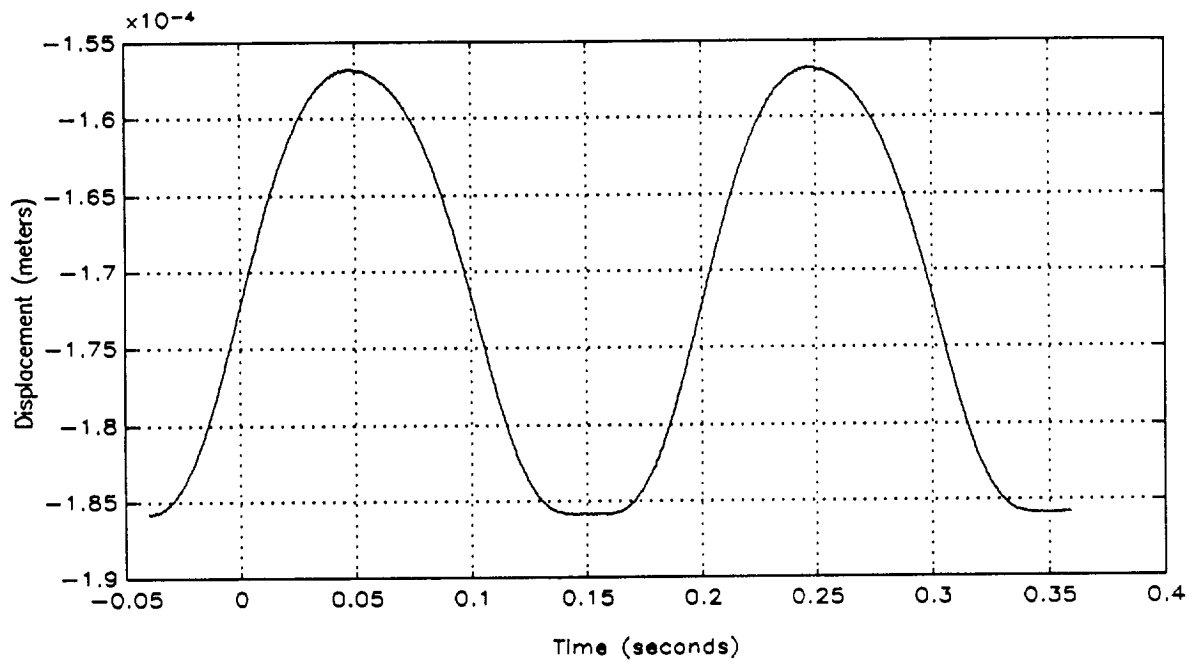


Figure 4-40. Time history of displacement (12.5 MPa preload, partially clamped end conditions).

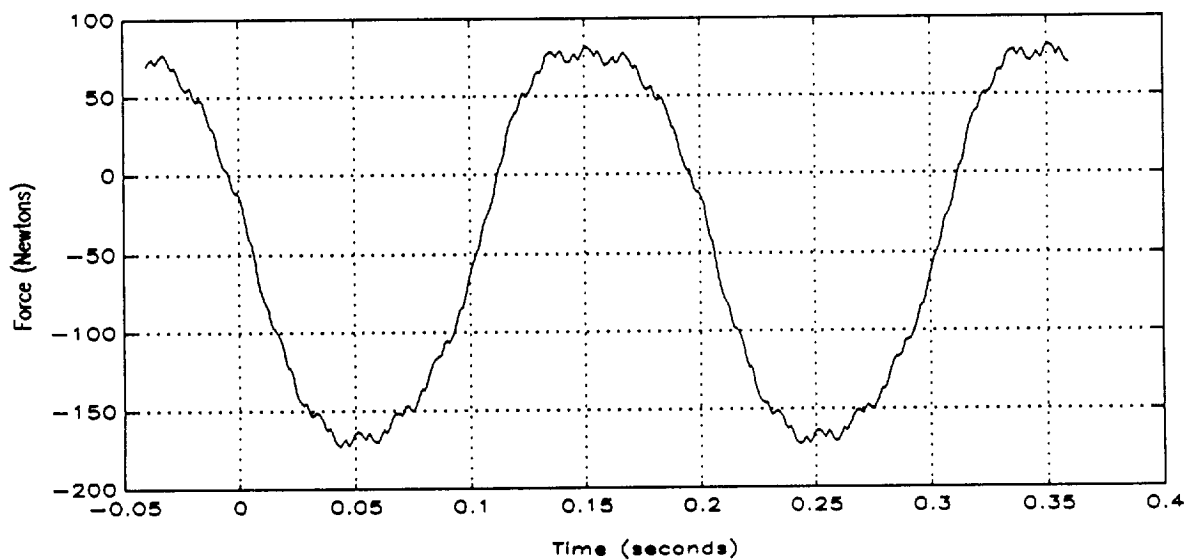


Figure 4-41. Time history of force (12.5 MPa preload, partially clamped end conditions).

Figure 4-40 is a plot of the displacement of the active member, under the partially clamped boundary conditions. The partially clamped peak-to-peak displacement is approximately 29 microns. The free peak-to-peak displacement, for the same current and preload levels, is approximately 48 microns. A plot of the force versus time, for the partially clamped boundary conditions, is illustrated in Figure 4-41. The force-signal input-channel of the spectrum analyzer was dc coupled, hence the force data has a dc offset. The high frequency noise shown on the 5 Hz force signal is predominately 60 Hz interference. As shown, the peak-to-peak force is approximately 250 Newtons. Figure 4-42 is a plot of the raw current data versus the raw force data. The plot consists of two cycles of data, and illustrates good repeatability. The curve of the current and displacement is depicted in Figure 4-43. As shown, the peak-to-peak displacement is approximately 29 microns. The displacement versus current data for partially clamped boundary conditions is required to characterize the active member performance under a varying stress load.

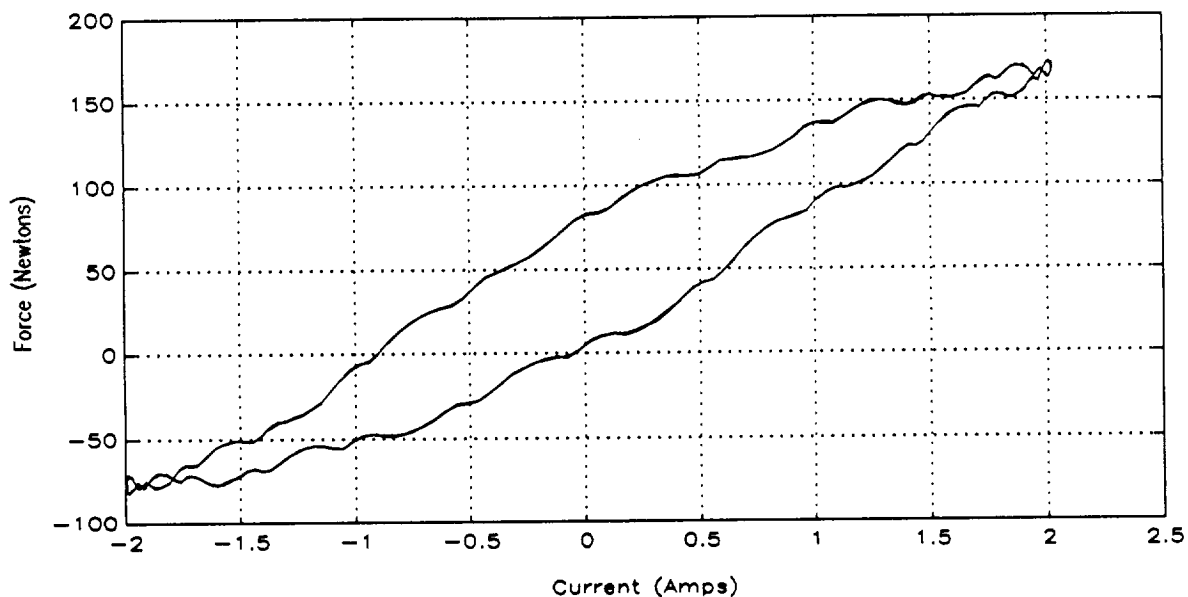


Figure 4-42. Force vs. current (12.5 MPa preload, partially clamped end conditions).

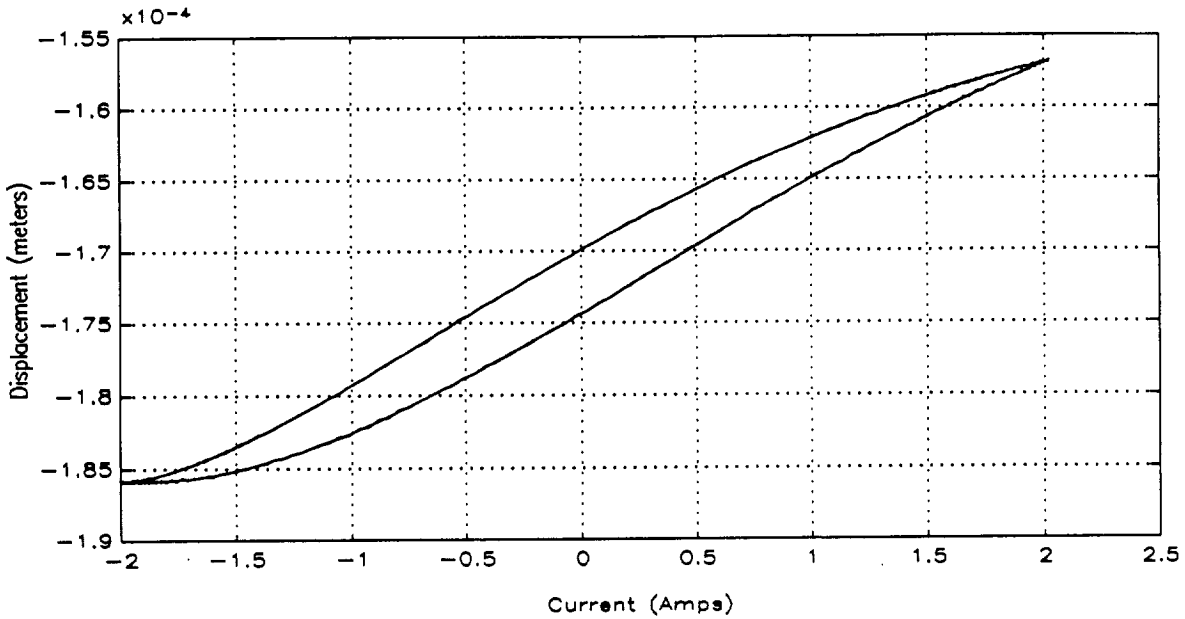


Figure 4-43. Displacement vs. current (12.5 MPa preload, partially clamped end conditions).

Figure 4-44 is a plot of force versus current, for all current levels, at an actuator preload of 12.5 MPa. The largest force of approximately 375 Newtons was obtained at the current level of 5 amps. A similar plot of displacement versus current is illustrated in Figure 4-45. Again, the actuator preload was 12.5 MPa, and the displacement was measured at all the current levels. The maximum displacement was approximately 42 microns, and was obtained at a current of 5 amps. Both Figure 4-44 and Figure 4-45 display the raw data.

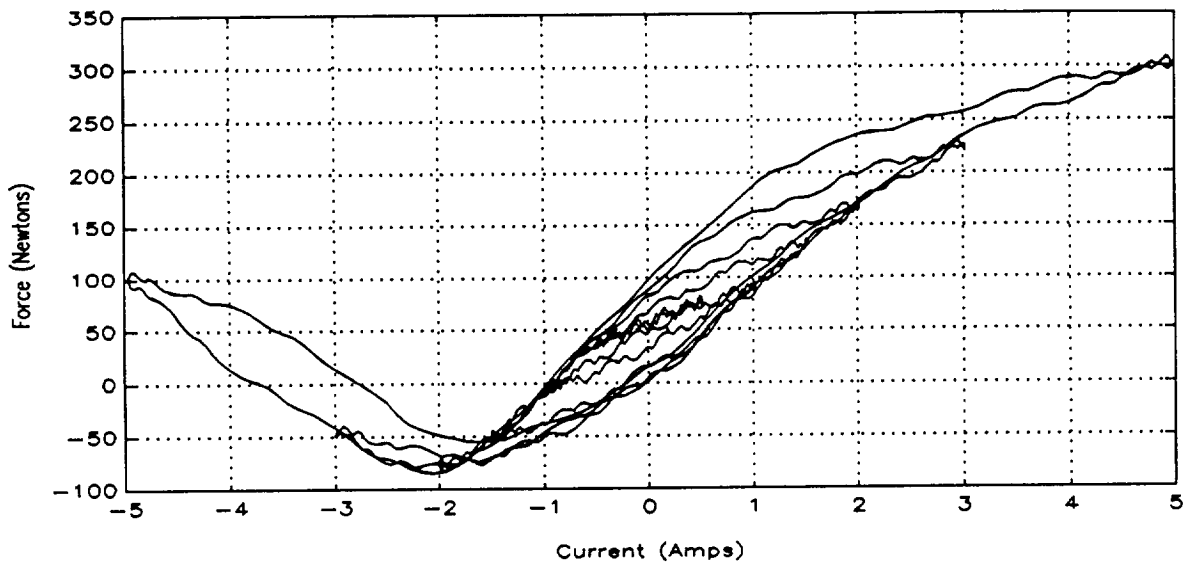


Figure 4-44. Force vs. current (12.5 MPa preload, raw data).

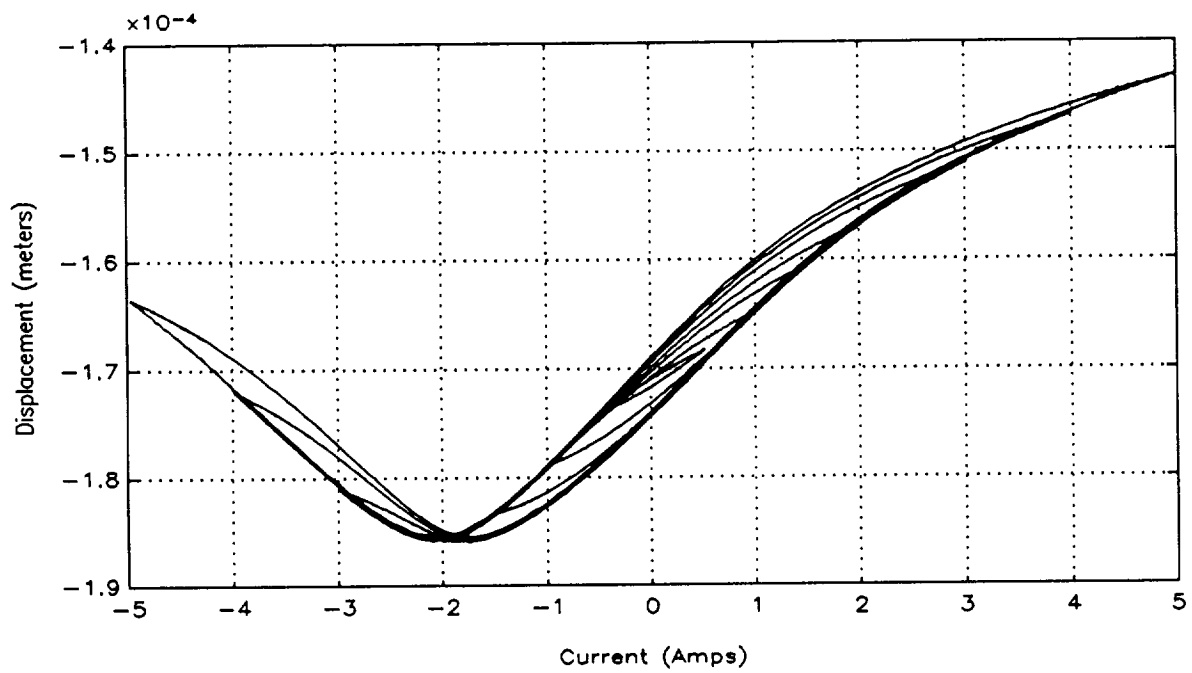


Figure 4-45. Displacement vs. current (12.5 MPa preload, raw data).

Figure 4-46 is a plot of the raw force versus current data for all the different preloads, at a current level of 2 amps. The different preloads levels that were tested are labeled in Figure 4-46. As previously mentioned, a list of the stresses and corresponding forces can be found in Table I. The raw displacement and current data is plotted in Figure 4-47. Figure 4-48 is a modified plot of the same data as in Figure 4-47. In order to compare the different preload results without thermal and other effects, the displacement curves have been averaged about the zero current point. As displayed in the plot, for a current excitation of 2 amps, the largest strains are obtained at the preload levels of 6.2 MPa and 12.5 MPa.

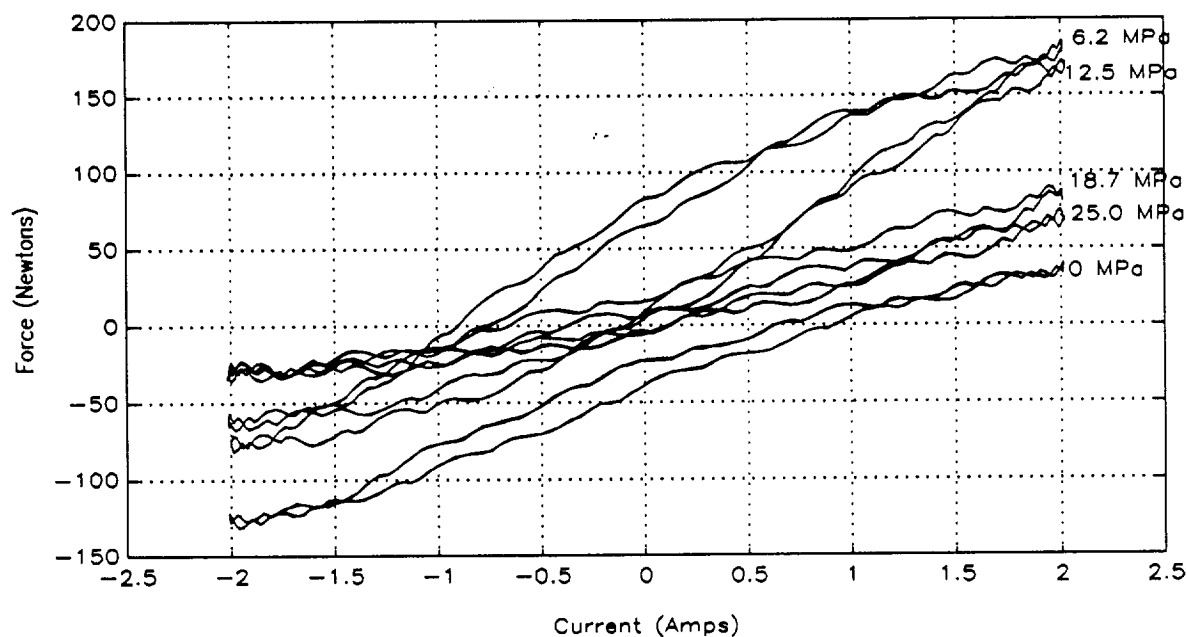


Figure 4-46. Force vs. current (2 amps, raw data).

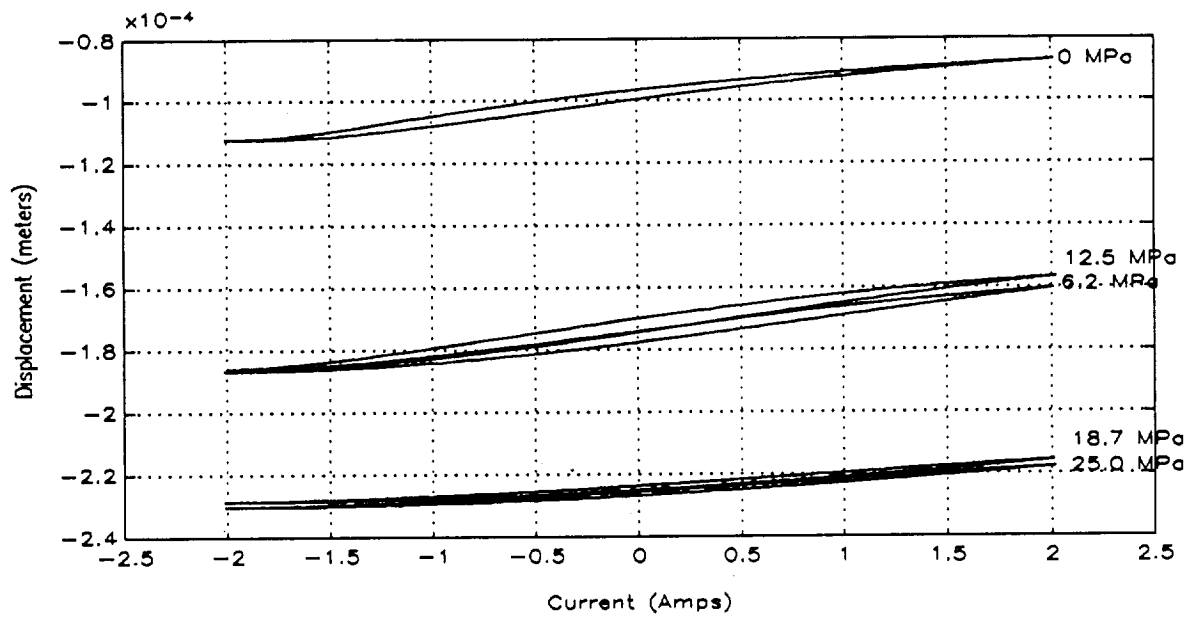


Figure 4-47. Displacement vs. current (2 amps, raw data).

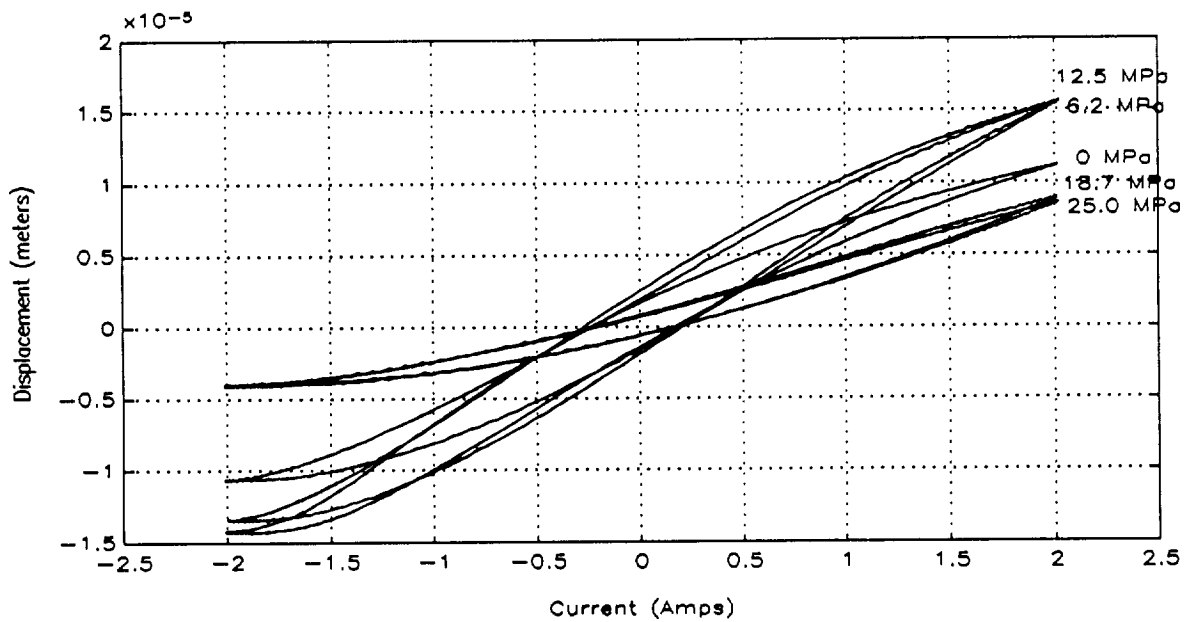


Figure 4-48. Displacement vs. current (2 amps, cleaned data).

The frequency response from the drive current to the partially clamped force was measured using the spectrum analyzer. Figure 4-49 is a bode plot of the transfer function over the frequency range of 10 to 500 Hz. The upper plot is the magnitude of the transfer function and the lower plot the phase of the transfer function. The active member was preloaded to 12.5 MPa and driven with a 70 mA peak swept-sine excitation. As shown, the response is flat over the frequency range from 10 through 50 Hz. Resonances at 60, 200, and 300 Hz are attributed to the test assembly dynamics. The dc gain is approximately 4.7 meters per amp. Figure 4-50 is a bode plot of the same transfer function, taken over the frequency range from 10 to 5000 Hz. Again, the actuator was driven with a 70 mA peak swept-sine excitation.

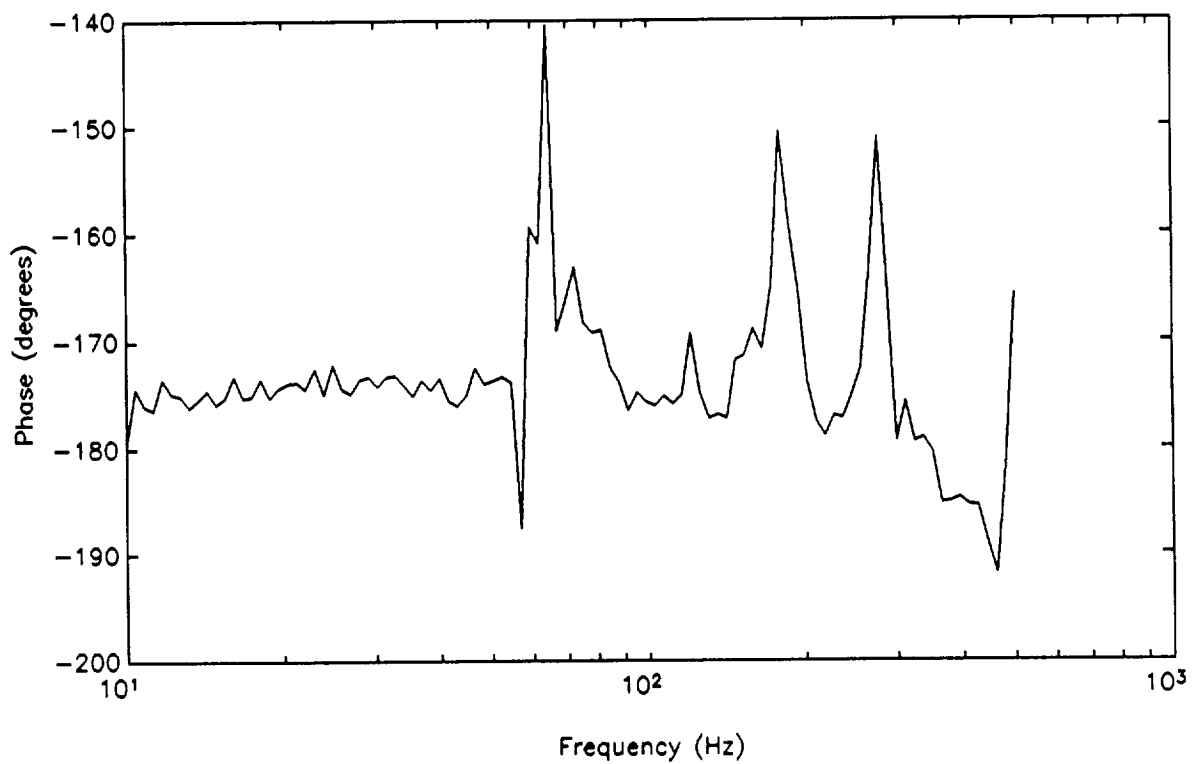
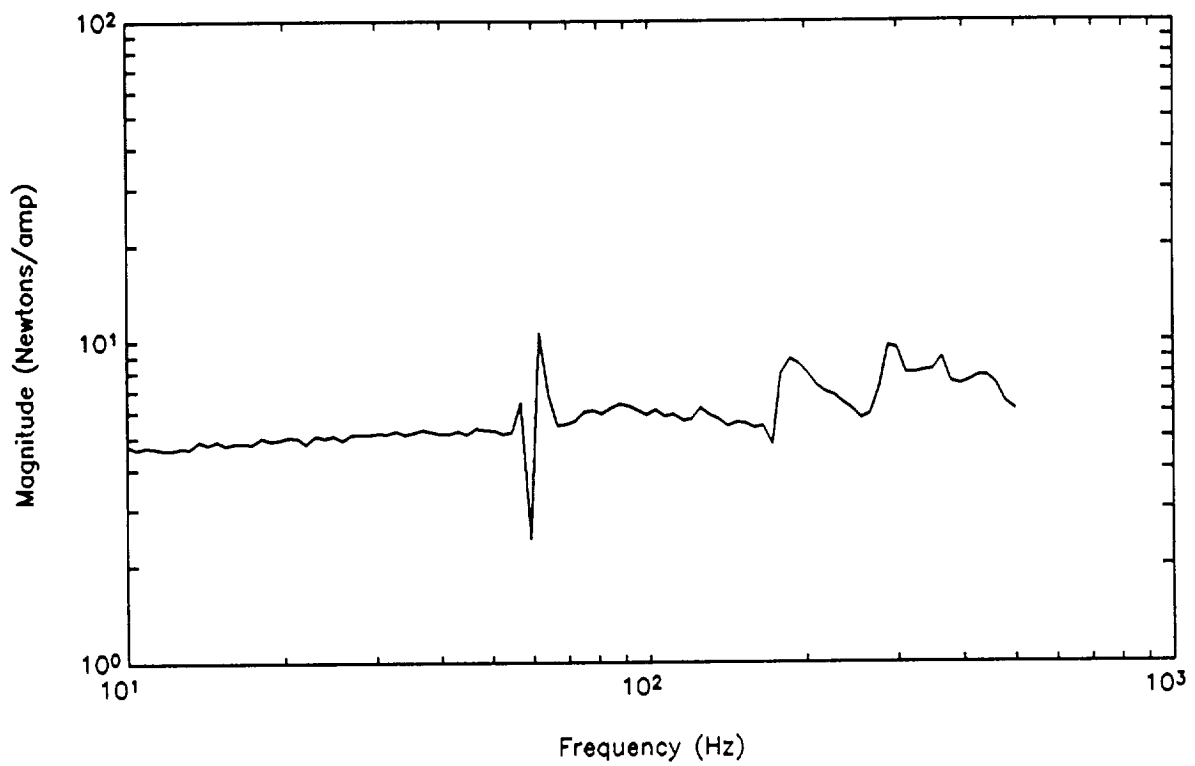


Figure 4-49. Frequency response from drive current to force (10 to 500 Hz).

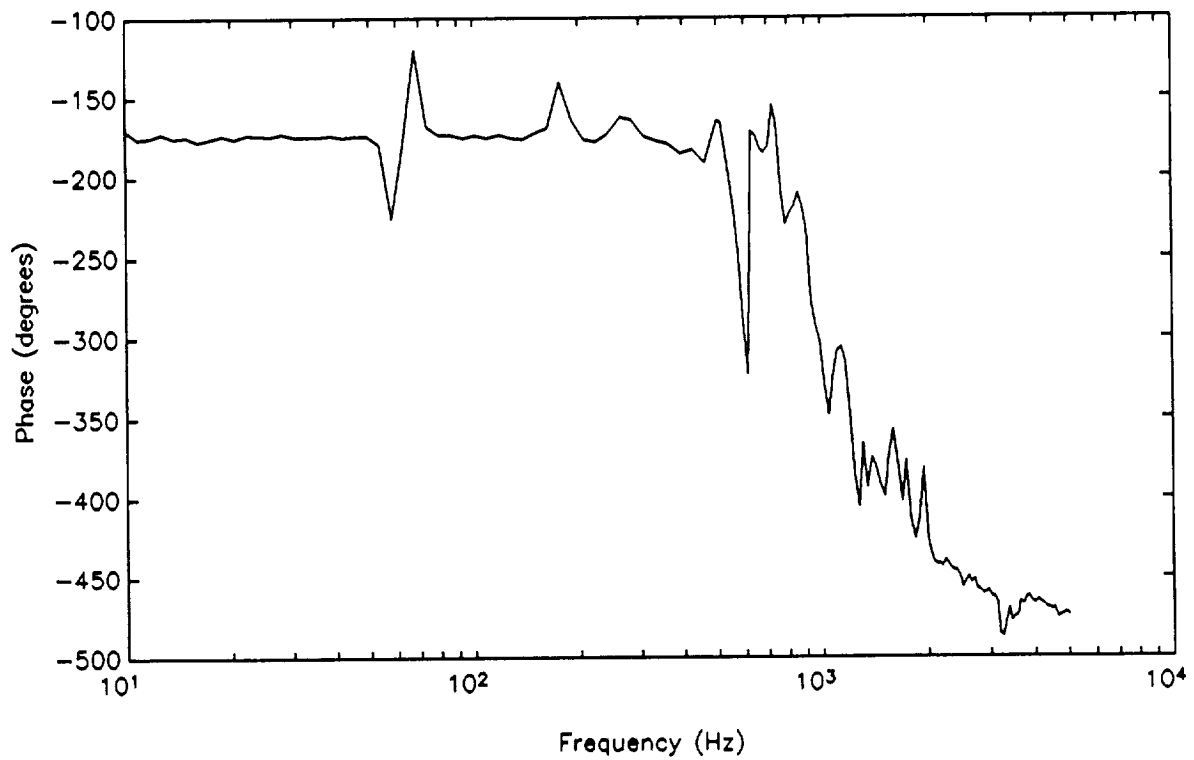
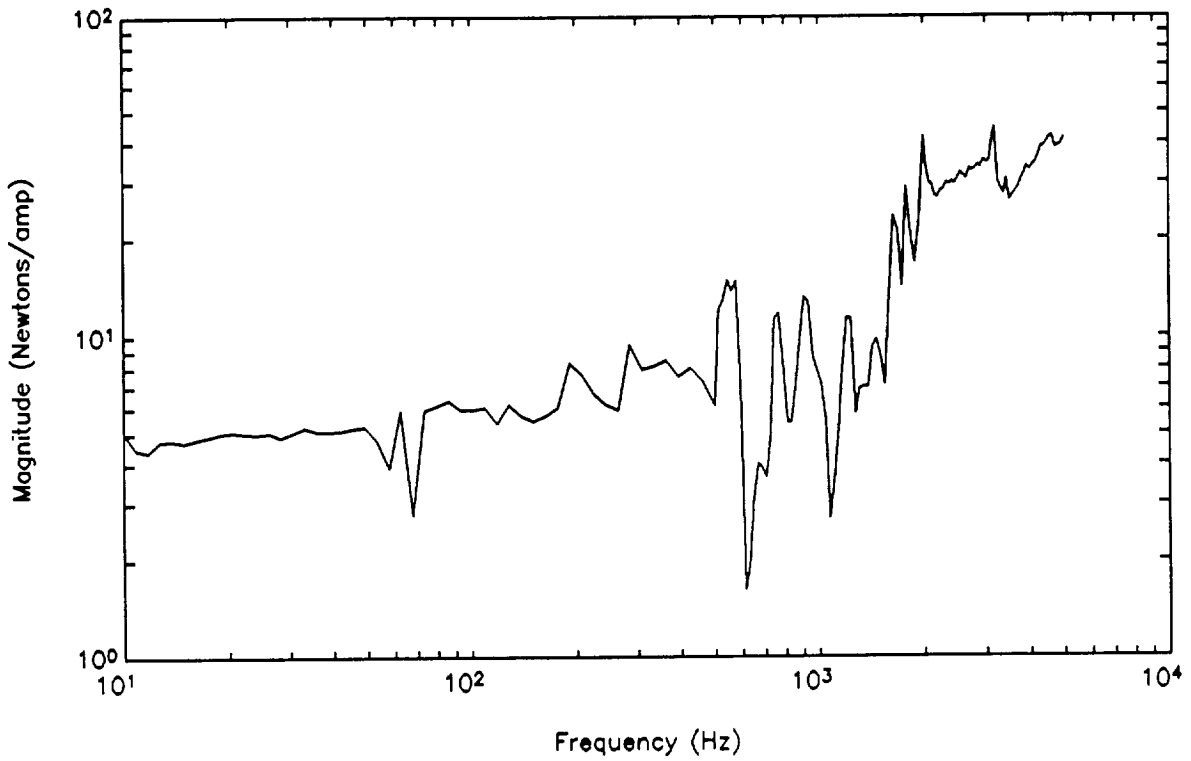


Figure 4-50. Frequency response from drive current to force (10 to 5000 Hz).

Figure 4-51 is the a plot of the frequency response from the drive current to the actuator displacement. The actuator was excited with 50 mA rms white noise, up to 500 Hz. The response is flat from 5 to 100 Hz. The higher frequency resonances may be attributed to both the actuator and the test assembly. The dc gain is approximately 3×10^6 meters per amp. Figure 4-52 is a plot of the same transfer function, from 5 to 5000 Hz. The predominate resonance at approximately 3300 Hz was also present in the free-end frequency response. This implies the effect is caused by the actuator dynamics and not the test assembly dynamics.

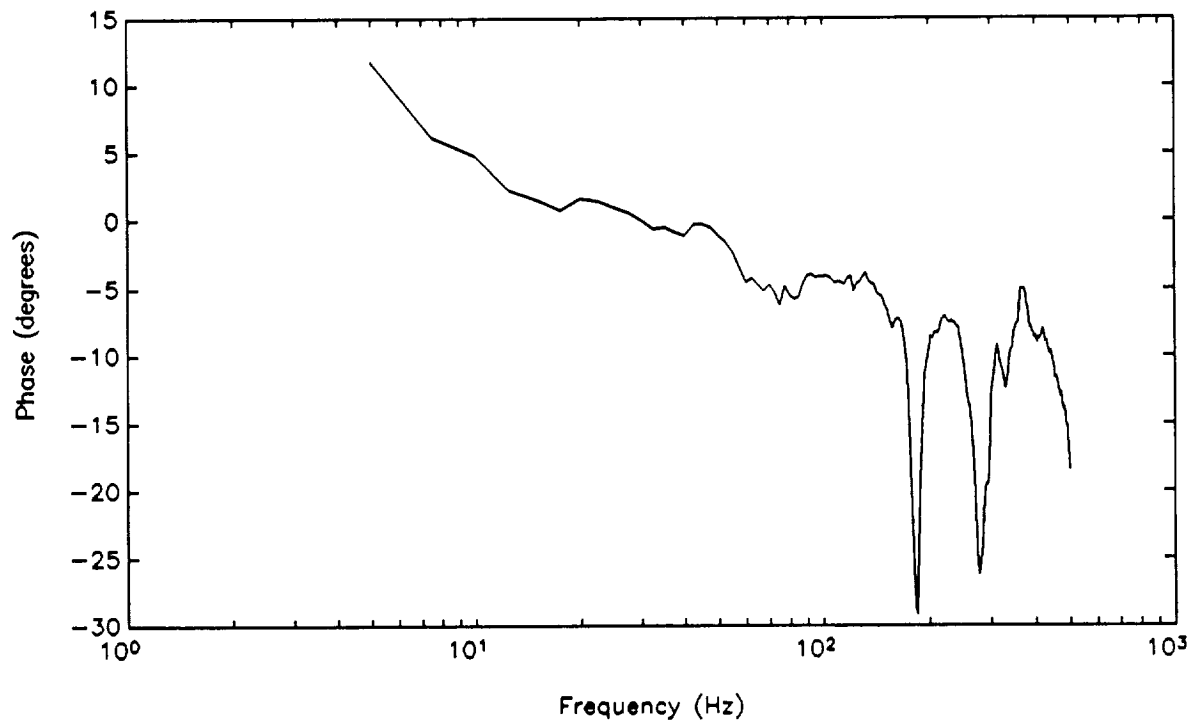
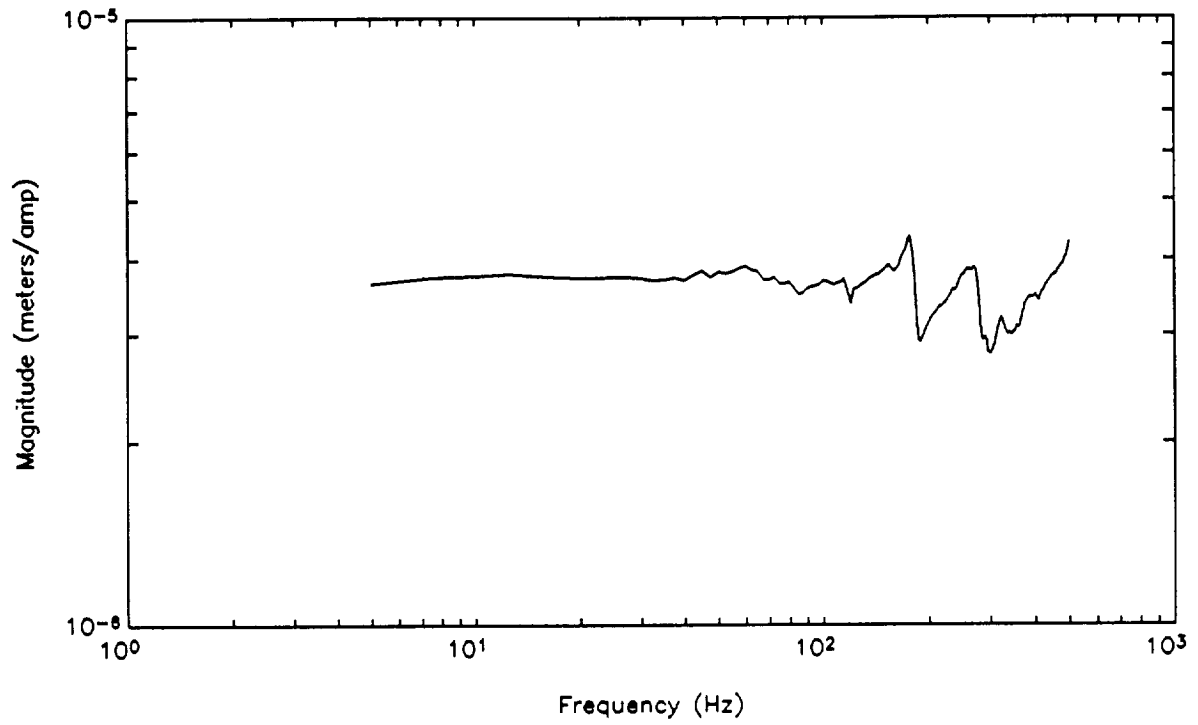


Figure 4-51. Frequency response from drive current to actuator displacement (5 to 500 Hz).

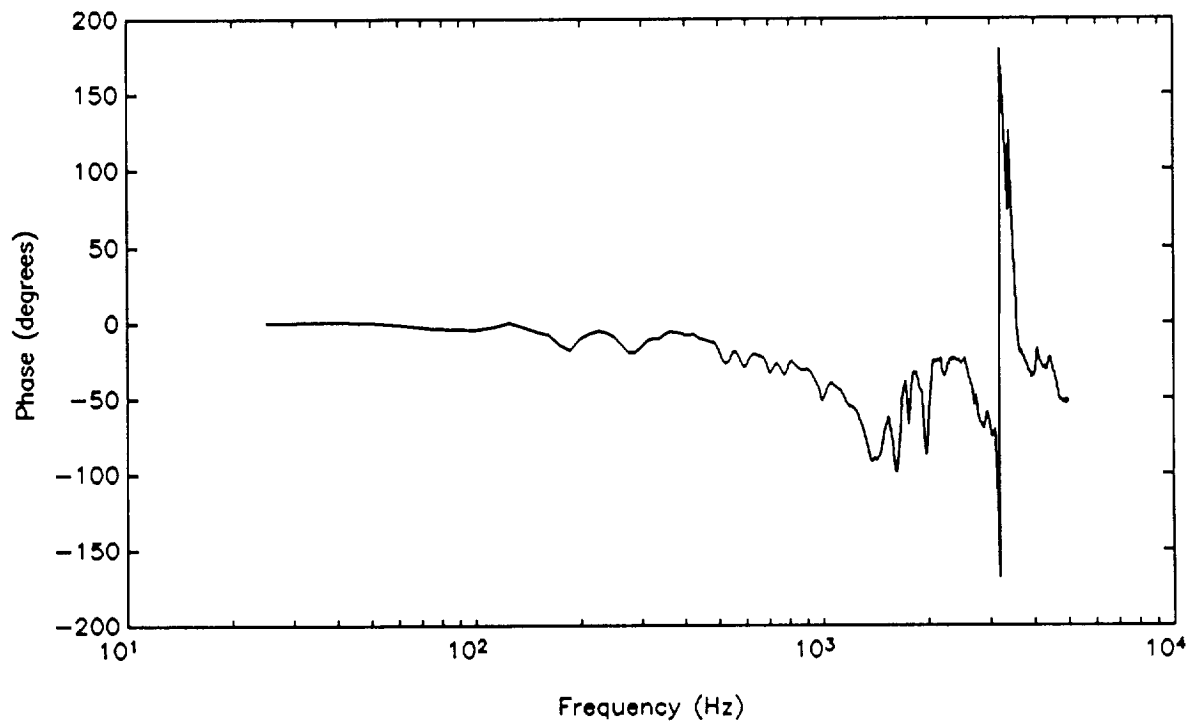
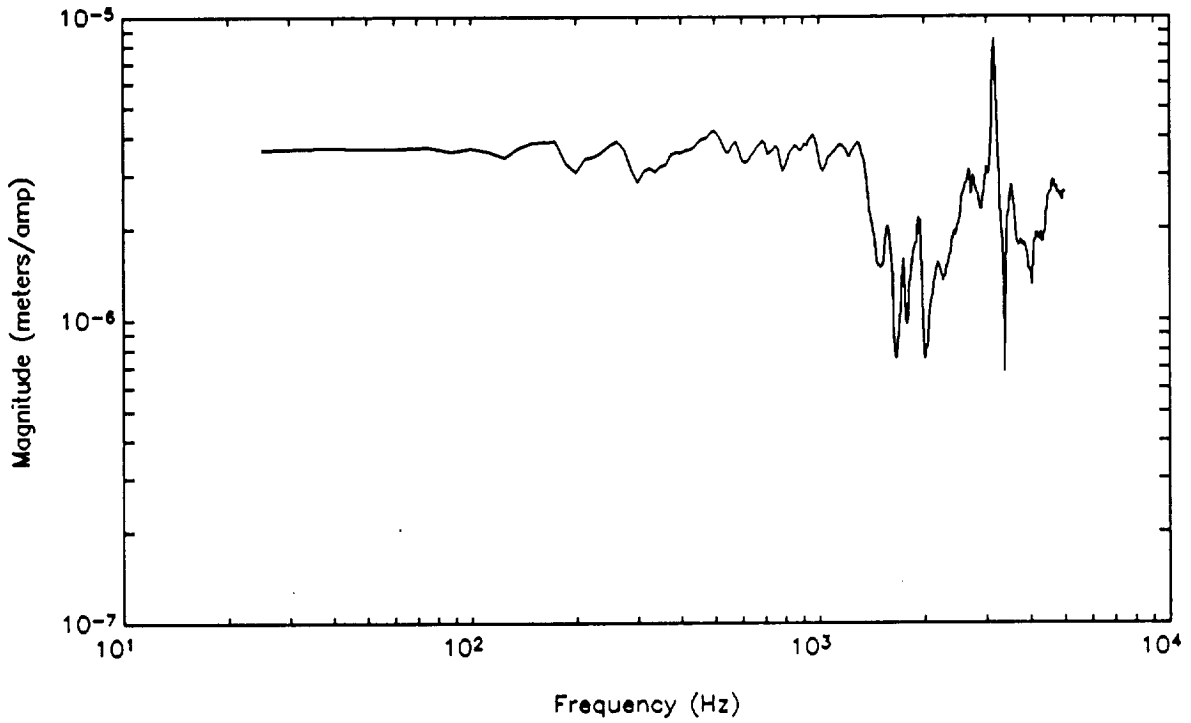


Figure 4-52. Frequency response from drive current to actuator displacement (10 to 5000 Hz).

4.4 Room Temperature Active Member Results Analysis

The anhysteretic magnetostrictive strain ϵ can be predicted as a function of coil current I , at constant stress, by using Eq. (3-7), together with the data in the literature for $\epsilon(B)$ and $\epsilon(H, \sigma)$ plotted in Figs. 3-2 and 3-3. For the room temperature actuator, we have the following parameters which are needed for Eq. (3-7):

$$A_{\text{mag}} = 1.07 \times 10^{-4} \text{ m}^2$$

$$A_{\text{Terf}} = 7.24 \times 10^{-5} \text{ m}^2$$

$$\ell_{\text{tot}} = 7.0 \times 10^{-2} \text{ m}$$

$$\ell_{\text{mag}} = \ell_{\text{Terf}} = 5.9 \times 10^{-2} \text{ m}^2$$

$$B_r = 1.1 \text{ tesla}$$

$$N = 800$$

$$r_{\text{ic}} = 5.0 \times 10^{-3} \text{ m}$$

$$r_{\text{oc}} = 9.5 \times 10^{-3} \text{ m}$$

Using these parameters, and expressing H_{Terf} in oersted and B_{Terf} in gauss, Eq. (3-7) becomes

$$H_{\text{Terf}} + B_{\text{Terf}}/47.6 = 340 + 165.5I \quad (4-4)$$

This equation shows that, regardless of the stress, the minimum strain, which occurs when H_{Terf} and B_{Terf} are both zero, should occur with a current $I = -340/165.5 = -2.03$ amps, which is very close to the $I = -1.95$ amps at which the minimum strain is observed in the test data (Fig. 4-26). To predict the strain at other values of I , it is most convenient to first find ϵ as a function of H_{Terf} using Fig. 3-3, then to find B_{Terf} as a function of ϵ using Fig. 3-2, and finally to find I as a function of ϵ using these results and Eq. (4-1). This should be valid for the test data at loads of 100 lbs or more (corresponding to 6.2 MPa or more), but will not be valid for the test data at zero load, because the $\epsilon(B)$ plotted in Fig. 3-2 is not valid for such low stress, for the reasons discussed in Sec. 3.6. For zero stress, $\epsilon(B)$ is close to zero for $B < 0.6B_{\text{sat}}$, and nearly equal to $\epsilon(B) - \epsilon(0.6B_{\text{sat}})$ from Fig. 3-2 for $B > 0.6B_{\text{sat}}$. Although data for $\epsilon(H)$ at $\sigma = 0$ is not given in Fig. 3-3, which was taken from Moffett et al., it is given in another paper by Clark.³

When this procedure is done, the predicted strain ϵ at a given current I is very close to the strain observed in our tests, usually within a few times 10^{-5} , or a few percent of the maximum strain. The following table compares the results for 5 different values of stress, corresponding to 0 lbs., 100 lbs., 200 lbs., 300 lbs., and 400 lbs. preload.

³A. E. Clark, "Giant Magnetostriction from Cryogenic Temperatures to 200 C", 1989(?).

Table 4-3. Predicted and observed dependence of strain on current and stress, for room temperature actuator.

σ (MPa)	H_{Teff} (Oe)	B_{Teff} (tesla)	I (amps)	Predicted ϵ (ppm)	Observed ϵ (ppm)
0	30	0.60	-1.11	60	35
"	100	0.62	-0.66	120	60
"	300	0.66	+0.60	240	150
"	500	0.70	+1.86	350	220
"	700	0.73	+3.10	440	290
"	900	0.76	+4.35	500	340
6.2	100	0.26	-1.14	200	170
"	200	0.43	-0.33	500	420
"	300	0.47	+0.30	600	620
"	400	0.52	+0.95	720	720
"	500	0.55	+1.58	770	820
"	700	0.60	+2.81	900	940
12.5	100	0.15	-1.28	70	90
"	200	0.24	-0.58	180	250
"	300	0.36	+0.16	380	460
"	400	0.44	+0.85	540	660
"	500	0.51	+1.53	720	800
"	600	0.56	+2.18	840	900
"	800	0.63	+3.44	1000	1020

σ (MPa)	H_{Terf} (Oe)	B_{Terf} (tesla)	I (amps)	Predicted ϵ (ppm)	Observed ϵ (ppm)
18.8	100	0.12	-1.31	40	20
"	200	0.20	-0.63	120	70
"	300	0.26	+0.03	200	150
"	400	0.33	+0.71	320	280
"	500	0.43	+1.43	500	430
"	600	0.50	+2.10	680	580
"	700	0.56	+2.76	820	740
"	800	0.62	+3.43	960	860
"	900	0.64	+4.04	1020	950
25	200	0.14	-0.71	60	70
"	300	0.19	-0.05	110	120
"	400	0.23	+0.59	170	210
"	500	0.29	+1.25	260	320
"	600	0.38	+1.95	420	480
"	700	0.46	+2.64	570	650
"	800	0.52	+3.30	720	780
"	900	0.59	+3.98	880	900
"	1000	0.62	+4.60	980	980

The discrepancy between the predicted ϵ and the observed ϵ tends to have the same sign for all values of current at a given stress, but can change sign in going from one value of stress to another. This suggests that the main source of error is in reading the data for $\epsilon(H)$ off of Fig. 3-3, or in interpolating the data in Fig. 3-3 between

different values of stress, or in measuring the stress in our tests or in the tests used to generate the data in Fig. 3-3. The greatest discrepancy is in the results for zero stress, where the test data consistently shows a strain close to two-thirds of the strain predicted from the data given by Clark.¹ However, we note that that paper also has strain data at higher stress that is not quite consistent with the more recent data plotted in Fig. 3-3, so perhaps the data it gives for zero stress is not very precise. In any case, at non-zero stress, it is clear that the approximations used in deriving Eq. (3-7) are good enough, and the properties of Terfenol-D are consistent enough, that it is possible to predict the strain of the room temperature actuator to within about 5% of the maximum strain.

The outer hysteresis loops for ϵ vs. I (in Fig. 4-26, for example) have a width $\Delta I \approx 0.3$ amp, corresponding to $2H_c = 50$ oersted, or $H_c = 25$ Oe, close to that seen in Fig. 3-3. The loops have width a few times narrower for $B > 0.6B_{sat}$, and for zero stress, where 70.52° domain wall motion contributes relatively little to the permeability, as discussed in Sec. 3.2.

To confirm the predicted relation between ϵ and B , independent of the relation between ϵ and I , we measured the inductance of the coil at different values of bias current and stress, and with ac currents of either 0.1 amp or 1 amp. With 0.1 amp excitation we expect that $\partial B / \partial H$ would be close to the initial permeability μ_{rot} , while at 1 amp $\partial B / \partial H$ should be close to the anhysteretic permeability μ_{an} in the case of room temperature Terfenol-D or TbDy at $77^\circ K$, both of which have H_c much less than the change in H associated with 1 amp of current. For cryogenic Terfenol-D at $77^\circ K$, H_c is so great that even with 1 amp $\partial B / \partial H$ will not be very close to μ_{an} , but it should be considerably closer to μ_{an} than it would be at 0.1 amp. (Actually, for TbDy, 0.1 amp excitation turned out to be a little too high to measure the initial permeability, see Sec. 5.4.)

The inductance was measured by finding the frequency dependence of both the magnitude and phase of I/V in the coil. If skin effects and hysteresis are ignored, so that the Terfenol can be treated as having a constant real permeability, then

$$V = (R + j\omega L)I \quad (4-5)$$

and R/L is the frequency at which the magnitude of I/V has fallen to $\sqrt{2}/2$ of its zero frequency value, and the phase of I/V is 45° . In fact, due to hysteresis, L has an imaginary part even at zero frequency, and due to skin effects L has an imaginary part which increases at high frequency, and a real part which decreases at high frequency. These contributions to L can be calculated using the model in Sec. 3.7, and they can also

be measured by measuring the phase of ϵ/I at different frequencies. It turns out that these contributions are typically small at the R/L frequency, making a small but measurable contribution to the phase of I/V , and a completely negligible contribution to the magnitude of I/V . For example, as shown in Fig. 4-33, the phase difference between ϵ and I , at $I_{\text{bias}} = 0$ at 200 lbs preload (12.5 MPa) is 3° at low frequency at 0.1 amp excitation, increasing to 5° at 100 Hz, while for 1 amp excitation it is 8° at low frequency, increasing to 12° at 100 Hz. The phase difference at low frequency is due to hysteresis, and the increase in phase difference at high frequency (which is proportional to ω^2) is due to skin effects. The skin effects are somewhat greater at higher excitation amplitude because μ_{an} is greater than μ_{rot} . At the R/L frequencies of interest, less than 100 Hz, the phase change due to both hysteresis and skin effects is substantially smaller than 45° , and the change in magnitude of L due to skin effects (which should be proportional to ω^4 at low ω) is completely negligible. We can therefore measure L quite accurately by measuring the frequency at which I/V falls to $\sqrt{2}/2$ of its value at much lower frequencies. (This is not true for TbDy at 0.1 amp excitation, as will be discussed in Sec. 5.4, because there is a large phase change due to hysteresis.)

The coil inductance L is just N^2 divided by the total reluctance seen by the source NI in the magnetic circuit shown in Fig. 3-1. Thus

$$L = N^2 / [\mathfrak{R}_{\text{ext}} + (\mathfrak{R}_{\text{Terf}}^{-1} + \mathfrak{R}_{\text{coil}}^{-1})^{-1}] \quad (4-6)$$

where $\mathfrak{R}_{\text{ext}}$ is defined in Eq. (3-6), $\mathfrak{R}_{\text{coil}}$ is defined in Eq. (3-5), and $\mathfrak{R}_{\text{Terf}}$ is defined by

$$\mathfrak{R}_{\text{Terf}} = \ell_{\text{Terf}} / \mu_T A_{\text{Terf}} \quad (4-7)$$

where $\mu_T = \partial B_{\text{Terf}} / \partial H_{\text{Terf}}$ is either the initial permeability μ_{rot} , the anhysteretic permeability μ_{an} , or something in between, depending on whether the amplitude of excitation ΔH is less than or greater than H_c . Using the parameters for the room temperature actuator, we find

$$L = N^2 A_{\text{Terf}} / \ell_{\text{Terf}} [(\mu_T + 1.37\mu_0)^{-1} + (40\mu_0)^{-1}] \quad (4-8)$$

Since μ_T is greater than $1.37\mu_0$ and less than $40\mu_0$ for room temperature Terfenol-D in the regime of interest, the reluctance of the Terfenol is the dominant contribution to the inductance, but the coil reluctance and the external reluctance both make significant contributions. (In the cryogenic actuator the coil reluctance is more important, since the coil is thicker radially and the Terfenol rod is thinner.) The coil resistance R is 2.85 ohms, so the frequency $\omega/2\pi$ (in Hz) at which the magnitude of I/V is $\sqrt{2}/2$ times its magnitude at much lower frequency should be

$$R/2\pi L = 520[(\mu_T/\mu_0 + 1.37)^{-1} + (40)^{-1}] \quad (4-9)$$

At $B = 0$, with 0.1 amp excitation, $\mu_T = \mu_{rot} \approx 6\mu_0$ at 12.5 MPa (corresponding to 200 lbs. preload), according to Eq. (3-13), and at $I_{bias} = 0$, which corresponds to $B = 0.33B_{sat}$, μ_{rot} should be slightly lower, perhaps $5.5\mu_0$, so we expect $R/2\pi L \approx 90$ Hz, while the observed value, from Fig. 4-36, is 89 Hz. At 1 amp excitation, at 12.5 MPa, $\mu_{an,wall} = 10\mu_0$ at $B = 0$, falling to $4.5\mu_0$ at $B = 0.33B_{sat}$ (since $\mu_{an,wall}$ goes approximately linearly to zero at $B = 0.6B_{sat}$), so $\mu_{an} = \mu_{an,wall} + \mu_{rot} \approx 10\mu_0$ at $B = 0.33B_{sat}$, a result that can also be read directly off Table 4-1. Then we expect $R/2\pi L = 58$ Hz, while the observed value, from Fig. 4-36, is 56 Hz. This excellent agreement between the predicted and observed values of inductance, as well as between the predicted and observed strain, shows that both $\epsilon(H)$ and $\epsilon(B)$ are in good agreement with the data in the literature.

The partially clamped data shows anhysteretic strain as a function of I that is in good agreement with the unclamped data at the same stress and I . Figures 4-42 and 4-43 show force and strain vs. current for a partially clamped test, around an equilibrium with a preload of 200 lbs (corresponding to a stress in the Terfenol-D of $\sigma = 12.5$ MPa) and no bias current. With the current varying by ± 2 amps, we found that the force varies by ± 125 newtons (corresponding to ± 1.73 MPa) and the length of the Terfenol-D rod varies by $\pm 1.25 \times 10^{-5}$ meters (or $\pm 2.12 \times 10^{-4}$ variation in strain ϵ). This means that the stiffness of the test bed is 1.0×10^7 newtons per meter, and $d\sigma/d\epsilon$ for the Terfenol-D is 8.14×10^9 Pa. This is less than the anhysteretic elastic modulus of Terfenol-D, about 2.3×10^{10} Pa, so the actuator is far from being completely clamped, but it is still a significant fraction of the Terfenol-D elastic modulus, so can provide some useful information. If we take a line with slope $d\sigma/d\epsilon = 8.14 \times 10^9$ Pa in Fig. 3-4, passing through the point with $\sigma = 12.5$ MPa and $H_{Terf} = 280$ Oe (corresponding to $I_{bias} = 0$), and use Eq. (4-1) to relate H_{Terf} to I , then we would predict that varying I by ± 2 amps would cause ϵ to vary by $\pm 2.7 \times 10^{-4}$, reasonably close to the observed variation of $\pm 2.12 \times 10^{-4}$. If the Terfenol-D were completely free, with $\sigma = 12.5$ MPa independent of strain, then a variation of ± 2 amps in current would cause ϵ to vary by $\pm 4 \times 10^{-4}$.

The hysteresis for the partially clamped data (Fig. 4-43) is nearly the same as for the unclamped data (Fig. 4-22), showing that the de-pinning of domain walls due to changes in stress, discussed in Sec. 3.2., is at most a relatively minor effect in room temperature Terfenol-D.

5. CRYOGENIC TEMPERATURE ACTIVE MEMBER

This chapter presents the design, fabrication, assembly, test, and performance analysis of the cryogenic temperature magnetostrictive active member. The Phase II research that was originally proposed included the test of cryogenic temperature magnetostrictive materials to determine their suitability for use in cryogenic temperature active members. After the start of this Phase II research, this goal was broadened to include the development of a full active member capable of operating at cryogenic (liquid nitrogen) temperatures. Furthermore, this program experimentally investigated the use of two different cryogenic temperature magnetostrictive materials, a cryogenic temperature version of Terfenol-D and pure Terbium-Dysprosium.

As discussed in Chapters 2 and 3, by slightly changing the chemical composition, Terfenol-D can be made to operate successfully at cryogenic temperatures. This cryogenic temperature Terfenol-D features larger strains and higher stiffness than the room temperature version, but with significantly higher hysteresis. The Terbium-Dysprosium has the largest magnetostrictive strains of approximately 0.5% when operated at liquid nitrogen temperatures. It also features low hysteresis and high permeability. Mechanically, however, it is a relatively soft material with low yield stress.

These two different magnetostrictive actuators were assembled and tested using the same mechanical and sensor assemblies to form cryogenic temperature active members. As is discussed in some detail below, the cryogenic active member was designed using the room temperature active member as a starting point. A number of changes were incorporated into the room temperature design, both to allow operation at cryogenic temperatures and to improve the design. The cryogenic active members developed under this program are the first to use magnetostrictive actuators. Of the two materials, the cryogenic Terfenol-D is the more mature, with previous cryogenic actuator development. For the less mature Terbium-Dysprosium technology, this program marks the first use of this material as actuator.

The structure of this chapter is similar to the previous chapter that presented the room temperature active member. The chapter starts with the design of the magnetostrictive active member. The electromechanical design section, Section 5.1.1, includes a discussion of both the cryogenic temperature Terfenol-D and Terbium-Dysprosium. Section 5.1.2 presents the mechanical design, primarily discussing differences between the cryogenic and room temperature designs. Section 5.1.3 briefly

discusses the displacement and flux sensors. A custom cryogenic dewar was developed under this program, which allows the active member to be integrated into a truss structure. The requirements for this dewar and its design are presented in Section 5.1.4.

Section 5.2 discusses the assembly procedure for the magnetostrictive actuators and active member. Section 5.3 presents highlights of the cryogenic temperature active member performance tests, for both the cryogenic temperature Terfenol-D and the Terbium-Dysprosium. Section 4.4 concludes the chapter by analyzing the test results. Again, the focus of the discussion is on the accuracy of our design models.

5.1 Cryogenic Temperature Active Member Design

Similar to the room temperature active member, the cryogenic active member design can be usefully divided into two activities, the design of the magnetostrictive actuator and the design of the mechanical assembly of the active member. Mechanically, the cryogenic active member was based on the room temperature design. Two types of changes were made to the room temperature design. The first type of changes were to allow operation at cryogenic temperatures. These included mechanical openings and clearances to allow liquid and gaseous nitrogen flow and material changes because of the low temperatures.

Two different cryogenic magnetostrictive materials were tested. As discussed in the next section, these were configured to use the same permanent magnet and coil assemblies.

5.1.1. Electromechanical Design

Originally we planned to use TbDy as magnetostrictive material in our cryogenic actuator, because it has higher magnetostrictive strain and somewhat higher permeability than cryogenic Terfenol-D, and much lower hysteresis, and because unlike cryogenic Terfenol-D, published data was available on strain and B as functions of H and stress. The actuator parameters were therefore optimized in the design to obtain close to the maximum strain, while still obtaining a reasonably high clamped force, as in the case of the room temperature actuator. Later, it was decided to use cryogenic Terfenol-D as well as TbDy, because TbDy has the disadvantage of a very low yield stress, and cryogenic Terfenol-D may be better for some applications, in spite of its large hysteresis. We were also able to obtain some unpublished data on strain and B vs. H , for one value of stress, in cryogenic Terfenol-D. Rather than design separate actuators for TbDy and

cryogenic Terfenol-D, we kept the design that had been optimized for TbDy, and checked to see that we could also expect to obtain a reasonably large strain and clamped force with cryogenic Terfenol-D.

At the time the cryogenic electromechanical design was done, the lugs holding the sensors had not yet been redesigned, so it was assumed that, as in the room temperature design, the permanent magnets had to fit in the spaces between the lugs azimuthally. With this assumption, as in the room temperature design, the cross-sectional area of the permanent magnets A_{mag} was somewhat less than optimal, even if the permanent magnets took up all of the available area and had the largest possible B_r . Therefore, the actuator was designed to have the permanent magnets take up all of this area, with an inner radius equal to the inner radius of the lugs, and the only free parameter in the design was r_T , the radius of the TbDy (or cryogenic Terfenol-D). The description of the design process below is thus based on the assumption that A_{mag} must be only 0.175 in^2 , the same as in the room temperature design, that the magnetostrictive material is TbDy, and that the only free parameter is r_T . Because this design gave a rather low bias field, the lugs were redesigned so that the magnets could fill up the entire 360° azimuthally (with small gaps to prevent eddy currents in the magnets from completely encircling the coil), and r_T and the inner radius of the magnets was kept the same. This resulted in a better bias field. It was then decided to use cryogenic Terfenol-D as well as TbDy, and this design was predicted to give satisfactory strain and clamped force with cryogenic Terfenol-D, so was not changed.

The vendor reported difficulty in manufacturing a TbDy rod of the full 5.9 cm length of the coil and magnets. A 3 cm length TbDy rod was successfully grown. If the rest of the length were filled in with a high permeability material such as silicon-iron, then the bias field would be 800 Oe, which was higher than desired, so a nonmagnetic spacer, 1/32 inch long, was designed to go between the TbDy and the silicon-iron extensions, in order to reduce the bias field to 500 Oe. As it turned out, this spacer was not really necessary, because the coil could be run at higher NI than conservatively estimated in designing it, and would have been able to produce enough H in the TbDy to reach the full magnetostrictive strain, except for the fact that the silicon-iron extensions saturated well before this point. The maximum strain in the TbDy occurred only when the silicon-iron was well into saturation, and the strain was somewhat higher without the nonmagnetic spacer, because the saturated silicon-iron increased the

reluctance of the magnetic path even more than a 1/32 inch nonmagnetic spacer would have, and using the spacer made the reluctance greater than optimal.

In retrospect, there was nothing that could have been done to increase the maximum strain obtainable from the TbDy rod, given the constraint that it could not be obtained in larger radius or length, and given the fact that the coil and permanent magnets were 5.9 cm long in order to maximize the strain of the cryogenic Terfenol-D. Increasing the coil cross-section would not have helped, because the coil could carry far more than enough NI to saturate the TbDy magnetostriction. Increasing the permanent magnet area would not have helped either, because the bias field was already almost high enough to saturate the silicon-iron. Although not originally designed with cryogenic Terfenol-D in mind, the cryogenic actuator was fairly well optimized to obtain a large strain when run with cryogenic Terfenol-D.

The procedure used to choose the optimal radius r_T for TbDy was similar to that used in the room temperature design, described in Sec. 4.1.2. As in the room temperature case, the external and coil reluctance were neglected in calculating the variation in H_{Terf} due to the coil current, although they were taken into account in calculating the bias H_{Terf} due to the permanent magnets. Unlike the room temperature case, we used the exact $B_{\text{Terf}}(H_{\text{Terf}}, \sigma)$, rather than just approximating it as $\mu_T B_{\text{Terf}}$ with constant μ_T . The length of the TbDy, coil and magnets is assumed to be $\ell = 2.25$ inches, the outer radius of the coil is $r_{\text{oc}} = 0.375$ inches, and the maximum possible cross-sectional area of the permanent magnets $A_{\text{mag}} = 0.175$ square inches, were all fixed by the outer dimensions of the actuator, which are supposed to be the same as those of other actuators used by JPL, as was the case in the room temperature design. The only significant free parameter was r_T . There was also the possibility of using permanent magnets with lower retentivity B_r , or smaller area A_{mag} , than the maximum available, or of replacing some of the coil volume with additional permanent magnet volume, but it turned out that neither of these options were worth doing.

For each of several different values of r_T , we calculated the maximum range of strain $\Delta\epsilon$ with constant stress, the maximum range of stress $\Delta\sigma$ under clamped conditions, and the optimum bias stress σ_{bias} at which these maxima were achieved. Unlike the room temperature case, the optimum bias magnetic field H_{bias} was always the highest field that could be obtained with the available permanent magnet area, and higher values of $\Delta\epsilon$ and $\Delta\sigma$ could certainly be achieved if more permanent magnet area were available. (However, better parameters could not be achieved, or could only marginally be

achieved, by increasing the permanent magnet area at the expense of the coils.) This difference between the cryogenic and room-temperature designs was due to TbDy having a higher permeability than Terfenol-D, so that it captured a substantial fraction of the flux supplied by the permanent magnet.

In order to do this calculation, the following data are needed: 1) Magnetization curves B vs. H for different fixed values of stress σ ; 2) Magnetostrictive strain ϵ vs. H (or B) curves for different fixed values of stress; 3) Stress vs. strain curve for one value of H , say $H = 0$. For Terfenol-D at room temperature, full data on H vs. ϵ vs. σ was available, but data on B vs. H was available only at $\sigma = 0$, and in addition some kind of average value of $\partial B / \partial H$ was given for clamped conditions. In that design, therefore, we took the permeability of the Terfenol-D as a constant $\mu_T = 9$ for free operation, and as a different constant $\mu_T = 5$ for clamped operation. For TbDy, the available data included B vs. H , as well as ϵ vs. H , for several values of σ , but there was no data for ϵ vs. σ , even at $H = 0$. However, the value of Young's modulus $\partial \sigma / \partial \epsilon$ at $H = 0$ and $\sigma = 10$ MPa was given, 1.5×10^{10} Pa, and it was possible to infer the saturation value of $\partial \sigma / \partial \epsilon$ at large σ because it could be determined, using the ϵ vs. H vs. σ curves, at large H and low σ , and theoretically it should have the same value, 3×10^{10} Pa, at high σ and low H . (This is the value of Young's modulus when the magnetization direction is pinned by high H or high σ , so that magnetomechanical effects are eliminated.) It was also possible to make a good guess at the σ required to reach this saturation value, and at the behavior of Young's modulus at lower σ , by comparison with the data for Terfenol-D at room temperature. For both Terfenol-D at room temperature, and TbDy at 77°K, the product of the saturated Young's modulus and the saturated magnetostriction was the same, 20 ksi. Since this is a measure of the stress at which saturation of magnetomechanical effects occurs, it is a reasonable guess that for both materials the approach from the $\sigma = 0$ value of Young's modulus to the $\sigma \rightarrow \infty$ value of Young's modulus occurs at about the same values of σ . Supporting this belief is the fact that Young's modulus at 10 MPa is about half of its saturation value, both for Terfenol-D and for TbDy. A similar comparison to Terfenol-D allowed us to make a reasonable guess for the behavior of Young's modulus at σ lower than 10 MPa, and ϵ vs. H for σ less than 7 MPa (1 ksi) which were not given in by Spano et al.

With all of this data, both given by Spano et al. and inferred, it was possible to make a more precise calculation of the maximum $\Delta \epsilon$ and $\Delta \sigma$ as a function of r_T than was done for the room-temperature actuator, since it was possible to determine μ_T at each

value of σ and H , rather than just using an average value. This is fortunate, since the permeability of TbDy is higher than that of Terfenol-D, and H_{bias} is a more sensitive function of μ_T than it is for Terfenol-D, so using accurate values of μ_T is more important. The procedure was done iteratively, since μ_T has to be known to find H_{bias} , H_{bias} has to be known to find the total H , and the total H has to be known to find μ_T .

Spano et al. only give data for stresses up to 25 MPa (3.5 ksi), and mentioned that at the highest stress used, the rod started to deform. For this reason, in calculating the maximum $\Delta\sigma$, it was always assumed that σ should not exceed 3.5 ksi, even if higher $\Delta\sigma$ could have been achieved by doing so. When that happened, there was no longer a unique bias stress that would lead to the maximum $\Delta\sigma$, but a range of bias stresses that would allow operation between 0 and 3.5 ksi, and for each value of the bias stress it was not necessary to use the full available range of coil current (positive or negative) to obtain this range of stresses. This is shown in the table, where in the data for clamped operation, for r_T less than or equal to 0.2 inches, a range of values is given. (For larger r_T , there is a unique value of bias stress which maximizes $\Delta\sigma$ subject to the constraint that the maximum stress not exceed 3.5 ksi, but larger $\Delta\sigma$ might be obtained if the maximum stress were allowed to exceed 3.5 ksi.)

Aside from the different properties of the magnetostrictive material (higher permeability, higher saturation magnetostriction, and lower Young's modulus, for TbDy than for Terfenol-D), another difference from the room-temperature case is that it should be possible to use a higher current density, because the resistivity of copper is about 10 times lower at 77°K than it is at room temperature. On the other hand, it is probably true that we cannot tolerate as great a temperature rise in the TbDy, in degrees, as we can in the Terfenol-D, because their properties are likely to change by the same amount when the temperature is changed by the same amount relative to the absolute temperature. This suggests that we can only tolerate $77/300 \approx 1/4$ as much of a temperature rise in the cryogenic actuator as in the room temperature actuator. If we assume that the actuators are inadequately cooled, and that we want to run them for a certain time without having the temperature rise too much, and that they have the same specific heat (a guess, since we do not have data on specific heats of these materials at 77°K), then the maximum current density at 77°K should be $(10/4)^{1/2}$ times the 4×10^6 A/m² that we allowed in the room temperature actuator, or 6.3×10^6 A/m². A more appropriate model might be that we want to run the actuator indefinitely, under certain cooling conditions (black-body radiation, or convection in air or in liquid nitrogen)

without having the equilibrium temperature rise exceed some value. However, such a model would not give us a maximum current density, but a maximum power, and higher current density could be used in thinner coils. Since we assumed a fixed maximum current density in analyzing the room temperature actuator, for consistency we have done the same thing for the cryogenic actuator.

For the permanent magnet, we assumed a retentivity $B_r = 1.2$ tesla, the maximum available, and assumed that it is a rare earth magnet, with $B \approx B_r - \mu_0 H$ for the modest values of H of interest. Although there are some differences in the properties of rare earth magnets at room temperature and 77°K, the differences are minor, only a few percent, and are not of concern for this calculation.

The results of our calculation are given in Table 5-1. Better parameters could certainly be achieved if a larger permanent magnet were used. For free operation, the minimum strain is always at $H = 0$. In all cases, the coil does not have to run at maximum current density (opposing the permanent magnet field) to reach $H = 0$, but could actually reverse the direction of H if there were any reason to do so. (The negative values of H that could be achieved are shown in parentheses in the table.) Similarly, for clamped operation, for some bias stresses, zero stress is reached when the coil is not running at maximum current density. (The lower values of H that could be achieved, which would result in negative (tensile) stress, are shown in parentheses in the table.) This means that more efficient use could be made of the coil if there were a bigger permanent magnet. We tried replacing 0.1 inch of coil thickness, or 0.05 inch of coil thickness, by an additional layer of permanent magnet, for $r_T = 0.2$ inches or 0.15 inches. For both cases, replacing 0.05 inches of coil by permanent magnet resulted in obtaining the same range of stress for clamped operation, and replacing 0.1 inches resulted in a lower range of stress. For larger or smaller r_T , this would clearly not be worth doing, since at larger r_T the coil is so thin that even a small reduction in its thickness would severely reduce the H it can generate, while at smaller r_T the H generated by the permanent magnet is already adequate. Clearly it would not be worthwhile to replace 0.05 inch of coil by permanent magnet, even if it gave marginally better results, since a permanent magnet only 0.05 inches thick would be quite fragile. On the other hand, these results do show that, in contrast to the room temperature case, an increase in the permanent magnet area would be advantageous, if it did not have to be done at the expense of the coils.

The highest product of maximum $\Delta\epsilon$ and maximum ΔF occurs for $r_T = 0.2$ inches. However, the maximum $\Delta\epsilon$ is obtained at a different bias stress than the maximum ΔF for this value of r_T , in contrast to lower and higher values of r_T , where the maximum $\Delta\epsilon$ and the maximum ΔF are achieved at about the same bias stress. This suggests that the maximum stored energy, which we have not calculated but which should scale roughly as the maximum $\Delta\epsilon \cdot \Delta F$, has a local minimum at $r_T = 0.2$ inches, and is higher at larger or smaller r_T , so $r_T = 0.2$ would not be a good choice. It is clearly better to go to smaller r_T , say 0.15 inches, than to larger r_T . For one thing, smaller r_T allows larger $\Delta\epsilon$, at the expensive of smaller ΔF , but large $\Delta\epsilon$ is probably more important than large ΔF for our application. For another thing, at smaller r_T the maximum ΔF is limited not by the available current, but by our concern that the rod start to deform if the stress exceeds 3.5 ksi. This means that if the rod is not clamped, but is allowed do work, it should still be possible to obtain the maximum range of stress, from 0 to 3.5 ksi, while this would not be true at larger r_T .

We conclude that the optimal design has $r_T = 0.15$ inches, and should be operated at a bias stress of about 1.85 ksi (13 Mpa). It can achieve a strain of 4×10^{-3} , and a clamped range of stress from 0 to 3.5 ksi. It requires using the full available area for a permanent magnet, with the maximum possible B_r of 1.2 tesla. It does not make full use of the available coil volume, because of the limited permanent magnet volume available.

Table 5-1 Dependence of maximum strain and maximum clamped force on radius of TbDy

r_T (inches)	0.10	0.15	0.20	0.25	0.30
max H, free (Oe)	890	740	600	450	310
μ_T/μ_0 at max H	30	30	30	30	25
min H, free (Oe)	0(-190)	0(-150)	0(-70)	0(-10)	0(-50)
μ_T/μ_0 at min H	20	20	20	20	20
bias H, free (Oe)	345	305	270	230	205
μ_T/μ_0 at bias H	27	25	23	22	20
optimum σ_{bias} , free (ksi)	1.85	1.85	1.85	1.85	1.85
max ϵ , free	4.5×10^{-3}	4.0×10^{-3}	3.3×10^{-3}	2.5×10^{-3}	1.65×10^{-3}
max σ , clamped (ksi)	3.5	3.5	3.5	3.5	3.5
H at max σ (Oe)	910 to 520	760 to 520	620 to 520	480	370
μ_T/μ_0 at max σ	23 to 22	23 to 22	23 to 22	22	15
min σ , clamped (ksi)	0.	0.	0.	0.25	1.4
H at min σ (Oe)	300(-250) to 0	200(-200) to 0	150(-150) to 0	0(-100)	30
μ_T/μ_0 at min σ	45	45	45	45	25
σ_{bias} , clamped (ksi)	0.1 to 2.4	0.2 to 2.1	0.5 to 1.0	1.6	2.5
H at σ_{bias} (Oe)	300 to 363	250 to 325	200	220	200
μ_T/μ_0 at σ_{bias}	45 to 17	45 to 18	45	25	17

The maximum clamped force was calculated for the cryogenic actuator, as actually built, with $A_{mag} = 0.29 \text{ in}^2$, rather than 0.175 in^2 as in the original design, and using cryogenic Terfenol-D. The clamped force was also calculated for TbDy, using the 3 cm long rod that was used, rather than the 5.9 cm length that was assumed in the original design. In calculating the maximum clamped force, we used Eq. (3-7), which takes into account the external and coil reluctances, for calculating the variation in H_{Terf} due to the

coil current, as well as for calculating the bias H_{Terf} due to the permanent magnets. We also calculated the stiffness for the actuator, both for cryogenic Terfenol-D and for TbDy.

The optimal preload stress for maximizing the clamped force with the cryogenic Terfenol-D is 21 MPa, according to our stress measurements, although as noted in the analysis of the results, there is reason to believe that our stress calibration is off for the cryogenic testbed, and the actual stress is about 15 MPa. With a coil current of ± 2 amps, the clamped stress goes from 14 MPa to 31 MPa (again, according to our stress measurements, which may be about 35% too high), for a total range $\Delta\sigma = 17$ MPa. At ± 4 amps, the clamped stress goes from 14 MPa to 38 MPa, so $\Delta\sigma = 24$ MPa. These are similar to the values for the room temperature actuator. In the case of TbDy, it would take quite modest currents (less than ± 1.5 amps) to make the stress range between the yield stress down to zero, so $\Delta\sigma$ is limited by the yield stress, about 25 MPa.

The elastic modulus of the cryogenic Terfenol-D (with no coil current) is about 1.4×10^{10} Pa at large amplitude, at a preload stress of 21 MPa (according to our stress measurements). Note that this is $\partial\sigma/\partial\lambda$ at constant I , not at constant H , so it cannot be directly read off of the anhysteretic stress vs. strain curves at constant H , in Fig. 3-7; first it is necessary to draw constant I contours on Fig. 3-7, for fixed permanent magnet flux. This elastic modulus corresponds to a stiffness for the actuator of 9×10^6 N/m. At small amplitude, according to Clark's unpublished data, it is 7.7×10^{10} Pa, corresponding to a stiffness of 4.2×10^7 N/m; we did not measure the modulus at small amplitude. The saturated elastic modulus, with no magnetomechanical coupling, is about 9.8×10^{10} Pa, according to Clark's data. For the TbDy, the elastic modulus at zero coil current should be about 1.4×10^{10} Pa at large amplitude, and the saturated elastic modulus, with no magnetomechanical coupling, is about 3×10^{10} Pa. Although we have no data on the small amplitude elastic modulus, it must be somewhere between the large amplitude modulus and the saturated modulus, and it is probably roughly halfway in between, because the initial permeability in TbDy is about half of the anhysteretic permeability. So a good guess would be 2×10^{10} Pa for the small amplitude elastic modulus of TbDy.

5.1.2 Mechanical Design of the Cryogenic Temperature Active Member

The second strut built in this program is designed to operate at cryogenic temperatures near typical on-orbit conditions of 100°K. This cryogenic strut can accept two types of cryogenic magnetostrictive materials. A modified formulation of the room

temperature Terfenol-D can be used, or a terbium-dysprosium alloy, which lacks iron, can be used. This environment required changes to the room temperature design. Other changes were made to simplify and improve the earlier design in other ways. The resulting cryogenic temperature active member is shown in Figure 5-1. Figure 5-2 shows the cryogenic active member with the components required to adapt it to the smaller terbium-dysprosium rod. A complete set of mechanical part drawings for the cryogenic temperature active member comprises Appendix B.

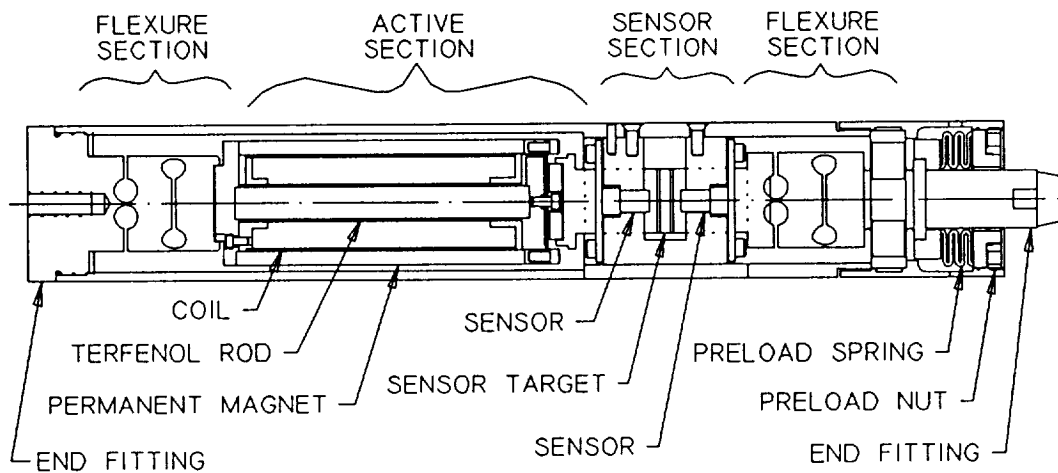


Figure 5-1. Assembly drawing of the cryogenic temperature active strut.

Design Implications of Cryogenic Operation

Operation at on-orbit temperatures or at 77° K in-house test temperatures required attention to active member material selection and differential contraction during cooling. The bulk of the components in the room temperature design were titanium for low mass. This material also has good toughness at cryogenic temperatures and so was retained for fabrication of the cryogenic version. Several parts in the room temperature design were made of 300 series stainless steel for their non-ferromagnetic properties, including the preload spring. The 300 series stainless steels are austenitic alloys and have excellent cryogenic toughness, and as such were retained unchanged for the low temperature design. The beryllium-copper flexure used to maintain clearance between the Terfenol-D and the solenoid coil is also a suitable cryogenic material. The

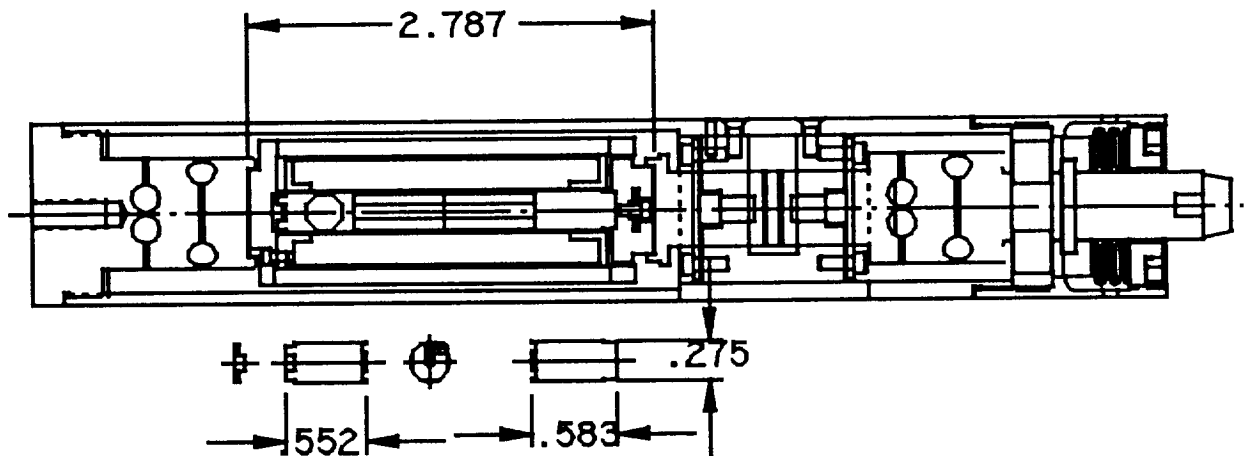


Figure 5-2. Drawing showing the adapters for the smaller terbium-dysprosium rod.

only part that was changed is the Delrin alignment insert. This part was eliminated to simplify the design and to avoid use of a plastic that is embrittled at cryogenic temperatures.

The second area of concern in the cryogenic design is maintenance of the Terfenol-D or terbium-dysprosium rod at the cryogen temperature. The main source of heat is the resistive dissipation of the coil immediately surrounding the magnetostrictive rod. A design was produced that allows liquid nitrogen to bath the magnetostrictive rod while boiling occurs and gaseous nitrogen escapes. This is accomplished by providing appropriate slots and gaps in the parts separating the central rod from the cryogenic environment. Three slots are provided in the housing to allow passage of the liquid and gaseous nitrogen. Inside the housing is an annular gap to allow the fluids to travel radially to the three slots between the permanent magnets on the outside of the motor. The fluid can reach the outside of the coil through these magnet slots. Other passages allow fluid to flow around the ends of the bobbin, which lines the inside of the coil, into the annular space between the bobbin and the magnetostrictive rod. In this way both the magnetostrictive material and the coil are kept very close to the temperature of boiling nitrogen.

Design Improvements Unrelated to Cryogenic Operation

Other evolutionary changes were made to the room temperature design that were not required by cryogenic operation. These include changes to the sensor mount, short flexure, coil mount, and preload spring.

The sensor is mounted using axial fasteners in the JPL design and the room temperature SatCon variation. This design has several drawbacks. One is the requirement for tabs extending radially inward, which accept the axial mounting screws. These tabs substantially reduce accessibility to the motor volume within the housing. They also require complex machining operations. The new design uses radial instead of axial fasteners. The sensor cage is mounted to the housing wall using fasteners penetrating the housing into the sensor cage. Another change is the use of a reinforced plastic, G10, to hold the eddy current sensor heads. This material has insignificant effect on the sensor fields because it is nonconductive. Conversely, the titanium which was used previously is conductive and requires recalibration of the sensor after installation in the active member. Another change to the sensor subsystem was the use of flexible straps to secure the sensor heads, instead of the previously used stiff cantilevers.

The original housing design had a blind hole in which the short flexure and motor were placed. This design was difficult to manufacture and required the housing wall to be welded to a plate that formed the housing end. The new design uses two parts connected by threads to avoid machining the blind hole. The end of housing is integrated with the short flexure, which prevents requirements for an additional part.

In the room temperature magnetostrictive member, the coil was restrained simply by the space in which it lay. In the cryogenic design, the coil is wound onto a bobbin, which has a flange with threaded holes. The bobbin and coil are firmly fastened to the structure of the active member using fasteners connecting the bobbin to the Terfenol mount.

During testing of the room temperature active member, it was apparent that the preload spring was too stiff. Only a small fraction of a turn of the preload nut was required to preload the Terfenol-D. The high stiffness limited the precision of preload forces and also violated to a degree the assumption that the Terfenol-D was preloaded at a constant level. The cryogenic design reduced the preload spring stiffness by fifty percent by reducing the springs leaves from 0.028 inches (0.71 mm) to 0.022 inches (0.56 mm).

5.1.3 Position Sensor System for the Cryogenic Active Member

The sensor used for the cryogenic active member was the same model used for the room temperature unit (see Subsection 4.1.4). The sensor heads are compatible with operation at cryogenic temperatures. This unit was calibrated at SatCon using another Kaman eddy current sensor.

A. F. W. Bell BH-301 hall effect magnetic field sensor was used to measure field and flux in the cryogenic active member.

5.1.4 Design of the Cryostat Used for Cryogenic Testing

Cryostat Requirements

Testing of the cryogenic active member required creating an environment similar to on-orbit cryogenic conditions. This goal was accomplished by designing a cryostat to allow bathing the active member in boiling liquid nitrogen, which approximates on-orbit temperatures. This application has special cryostat requirements. Most basic is the allowance for member length changes, which exerts the unusual requirement for a flexible cryostat. While the active member is allowed to expand with minimal reaction force, the components in series with the member must be stiff so that clamped force measurements are minimally affected.

Other requirements are that the member be operated at any angle between vertical and horizontal. This will allow integration into any position in a test truss irrespective of member orientation. Also required is cable access to the active member while installed. Coil power leads and position sensor leads must pass through the cryostat. For convenience, a cryostat that does not require periodic evacuation is required.

Cryostat Features

A cryostat was designed to meet these requirements by SatCon and Andonian Cryogenics, inc. of Newtonville, MA (Figure 5-3) and fabricated by Andonian Cryogenics. The design includes a dual bellows feature that allows free expansion of the central active member while it is bathed in liquid nitrogen. The sides of the cryostat are evacuated and filled with super-insulation while the ends are solid stainless steel plates that provide the required series stiffness. Although the cryostat ends are solid metal, the thickness and low thermal conductivity of the stainless steel provides acceptable insulating qualities.

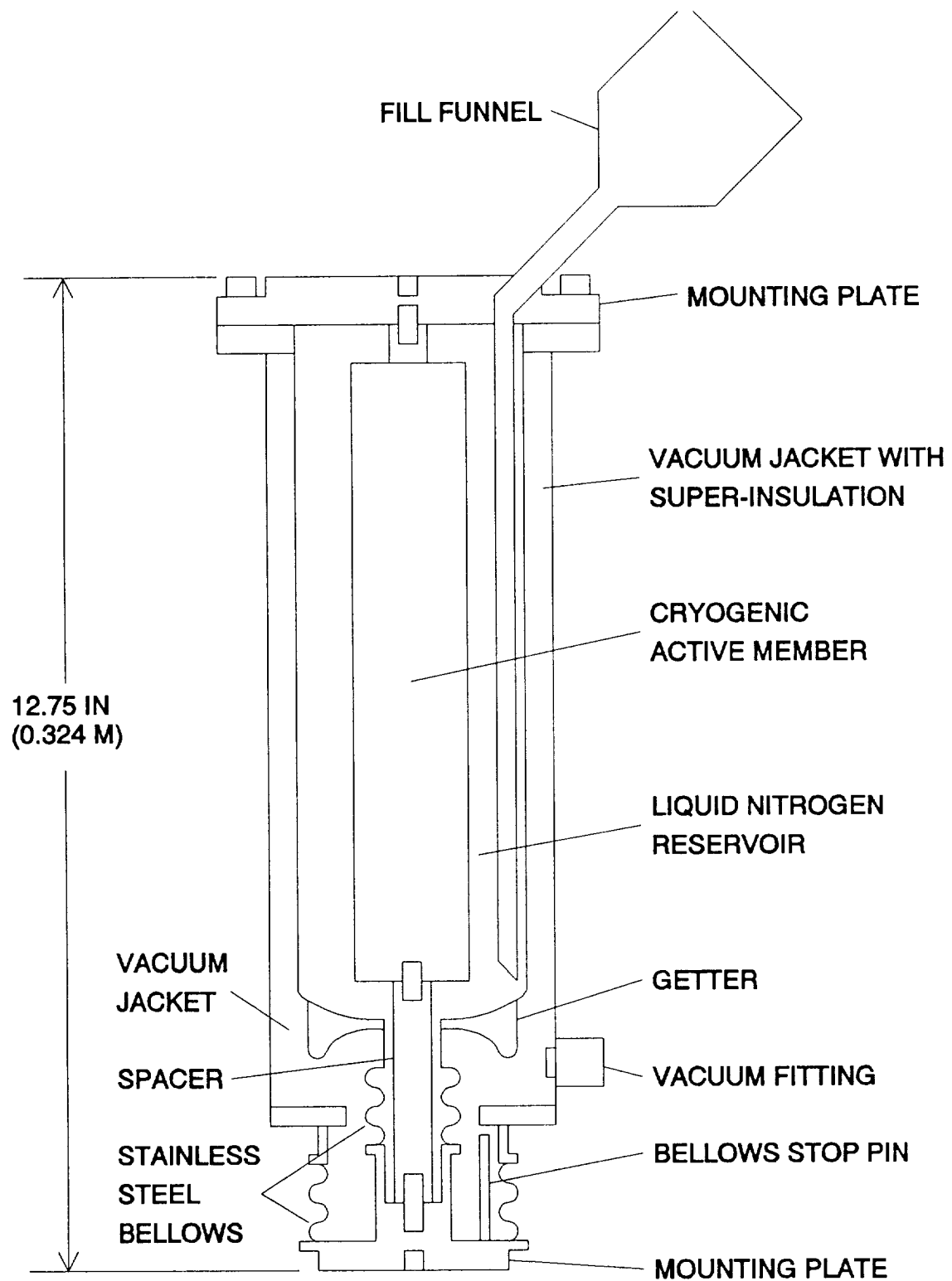


Figure 5-3. Fabricated cryostat with active member installed.

The cryostat has two large access ports in the top plate. A fill port has a funnel to facilitate liquid nitrogen addition, and a vent port allows gaseous nitrogen to escape without interfering with simultaneous nitrogen filling. The cabling fits through the 0.4 inch inside diameter vent port. The vacuum is maintained by a getter, which absorbs any outgas products that might accumulate over time. The flexible bellows are protected from complete collapse and possible damage by three stop pins. When the active member is installed, the bellows are extended and supported by the member. Approximately 25 pounds of constant force are applied to the active member by the differential pressure across the bellows. When the active member is not installed this 25 pounds is carried by the three stop pins after the bellows collapse by 0.06 inches.

5.2 Assembly of the Cryogenic Temperature Active Member

Because of the similarity between the room temperature and cryogenic temperature active members, their assembly procedures were similar. This section, therefore, will only discuss differences in the assembly.

The permanent magnet assembly for the cryogenic design used three separate cylindrical section magnets versus the two in the room temperature design. The cryogenic design featured more positive constraints on their placement, in both the radial and circumferential directions. Because the cryogenic design could use a full circle, the permanent magnets had full circle retainers on both top and bottom. This also contributed to a more robust assembly. In the cryogenic design, a coil bobbin was used, which allowed more accurate tolerancing. This bobbin was bolted to the bottom end cap, providing more accurate control of the spaces between the coil and magnetostrictive rods and the coil and permanent magnets. This was important to guarantee adequate nitrogen flow for cooling. Additionally, it provided a more robust mechanical assembly.

The assembly of the magnetostrictive actuator into the active member was similar to the room temperature case. The only important difference was that the slots between the permanent magnets were aligned with the slots in the active member housing, to allow more efficient liquid and gaseous nitrogen flow.

The active member was preloaded in the same manner as for the room temperature design. The active member testbed was placed in a vertical position. The dewar and active member were then mounted. The top was left off the dewar so that the preload nut could be accessed after the external preload was applied. After filling with liquid nitrogen, the preload was applied and the preload nut adjusted. We found that the preload level stayed constant within our measurement capability (approximately 5 to 10 %) even after the active member had been cycled to room temperature and back to cryogenic temperature.

We normally left the dewar top was off during testing for convenience. The active member was tested with the dewar fully assembled, however, to verify operation. At the completion of tests, the dewar was covered to decrease airflow into the dewar. This is important to stop the build-up of ice crystals that can damage the relatively fragile inner bellows. The dewar was also carefully cleaned of condensed water before filling with liquid nitrogen for the same reasons.

5.3 Cryogenic Temperature Test Results

The following is a discussion of the procedures and results of tests run at SatCon on the cryogenic temperature magnetostrictive active member. The active member was tested using two different magnetostrictive materials. The first set of tests were performed using cryogenic Terfenol-D, and the second set of tests used Terbium Dysprosium or TbDy. All active member tests were under free-end boundary conditions. The tests consisted of varying both the preload and drive current levels.

The cryogenic tests were performed using the SatCon active member testbed. Chapter 4 contains a detailed description of the testbed. The cryogenic tests used similar testbed components and instrumentation, with only slight modifications, to those described in Chapter 4. The active member was fastened to the bottom of the cryostat. The cryostat was then fastened to the movable carriage on the testbed via an interference plate. The SatCon active member testbed was oriented in a vertical fashion to allow for cryogenic liquid testing without the cryostat top. To expedite the testing, most tests were performed without the top. However, several tests were performed with the top to verify the cryostat effectiveness. The stationary support, used in the room temperature tests to provide clamped-end boundary conditions, was only required to adjust the preload in the cryogenic tests. The support, therefore, was removed during the vertical, free-end testing of the cryogenic active member.

The cryogenic test procedures are similar to those described in Chapter 4. The test procedures for both the Terfenol-D and the TbDy magnetostrictive materials, under free-end boundary conditions, involve driving the actuator with a 5 Hz sinusoidal signal and recording the time history of four measurements; the coil current, the flux field, the displacement, and the voltage. The 5 Hz signal was generated using a 2630 Tektronix spectrum analyzer. The five hertz excitation is low enough to give quasi-static results and high enough to allow the data to be quickly collected. The active member coil was driven by a Techron 7520 power amplifier, which was under current control and amplified the 5 Hz sinusoidal signal. The four time history measurements, current, field, displacement, and voltage, were stored using the spectrum analyzer. The coil current was measured using a current probe. The field and displacement signals correspond to the active member sensors, as previously described in Chapter 4. The voltage was taken at the output of the power amplifier.

5.3.1 Cryogenic Terfenol-D Tests

The active member, incorporating the cryogenic Terfenol-D magnetostrictive material, was excited with five hertz sinusoidal current waveforms at six different peak current levels of 0.5, 1.0, 1.5, 2.0, 3.0, and 4.0 amps. Data was taken with the magnetostrictive material in the active member mechanically preloaded at seven different stress levels, consisting of 0 MPa, 6.9 MPa, 13.7 MPa, 20.6 MPa, 27.4 MPa, 34.3 MPa, and 68.5 MPa. The preloads levels in the magnetostrictive material corresponding to these preload stresses are given in Table 5-2. The actuator was preloaded in the SatCon testbed, then tested at the different current levels. The power supply is under current control, hence for testing convenience, the transfer function from commanded voltage from the spectrum analyzer to the drive current has gain of one amp/volt.

Table 5-2. Cryogenic Terfenol-D preload forces and stresses

Force		Stress	
lb _f	N	Ksi	MPa
0		0	
50 lb	224	1	6.9
100 lb	448	2	13.7
150 lb	672	3	20.6
200 lb	896	4	27.4
250 lb	1120	5	34.3
500 lb	2240	10	68.5

Figures 5-4 through 5-7 are time plots of the raw data at a current level of 2 Amps, as shown in Figure 5-4, and with the active member preloaded to 20.6 MPa (150 lb_f). Figure 5-5 is a plot of the flux field. Because the level of magnetic field depends upon the location of the sensor, the information is somewhat arbitrary. The function of the plot is to illustrate that good flux data can be obtained. The units displayed in the plot are volts, the sensor output units. Figure 5-6 is a plot of the measured displacement

of the magnetostrictive rod and flexures relative to the housing. The peak-to-peak displacement is approximately 45 micrometers. As can be seen from the dc level of the displacement, no attempt was made to force the sensor output to zero for zero input current, either through shimming the sensor cage or through conditioning the sensor output signal. Figure 5-7 is a plot of the actuator voltage versus time.

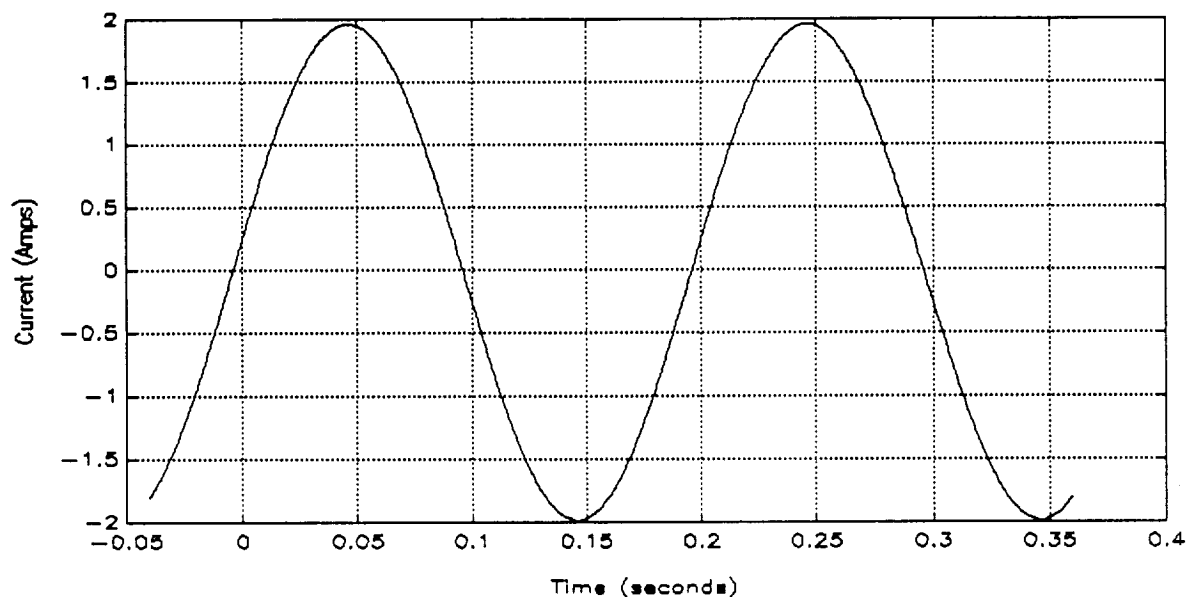


Figure 5-4. Time history of current (cryogenic Terfenol-D, 20.6 MPa)

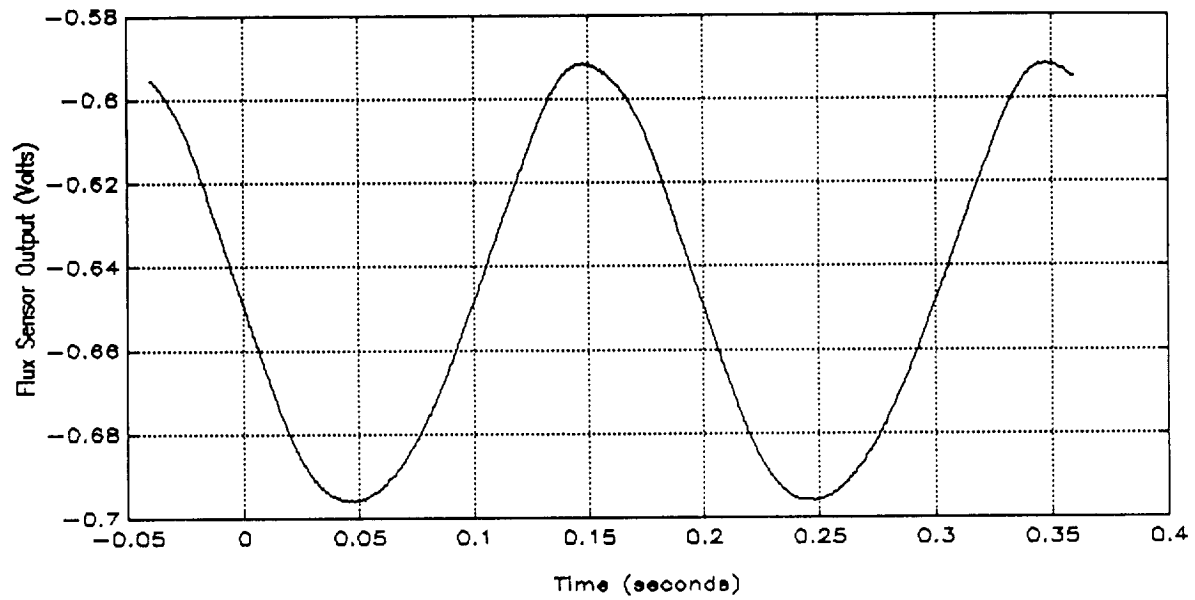


Figure 5-5. Time history of flux field (cryogenic Terfenol-D, 20.6 MPa)

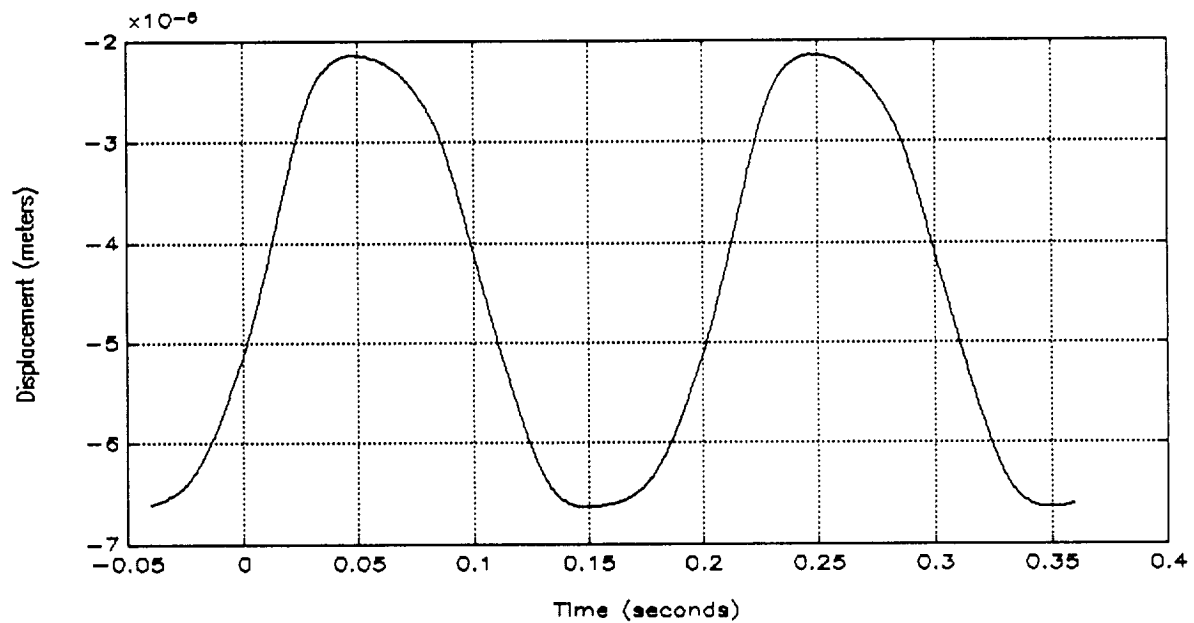


Figure 5-6. Time history of displacement (cryogenic Terfenol-D, 20.6 MPa)

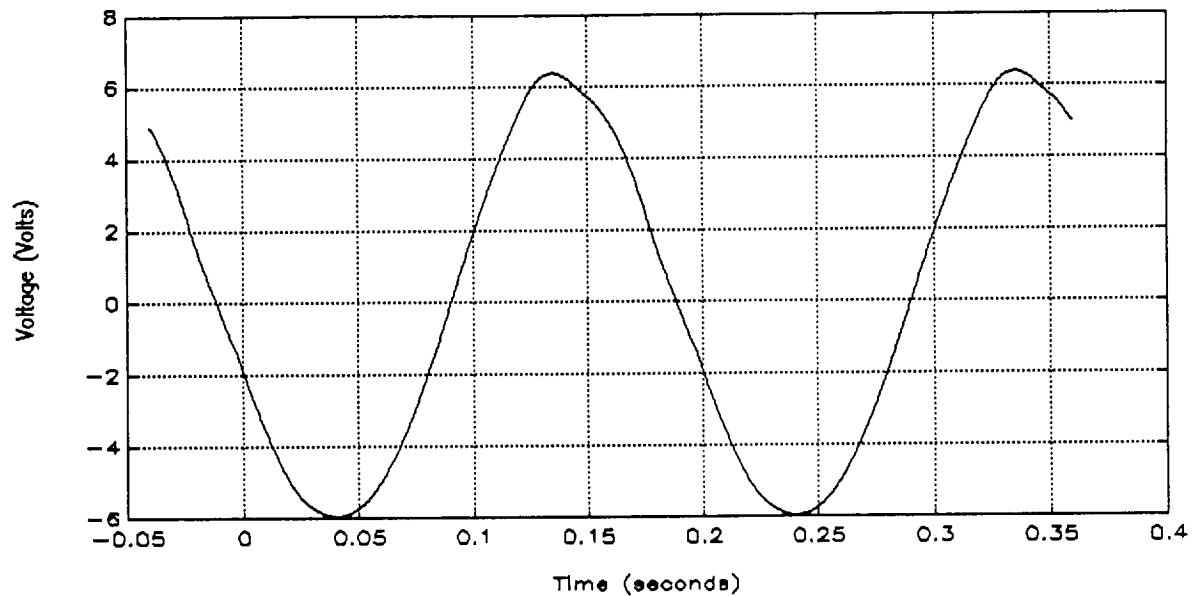


Figure 5-7. Time history of voltage (cryogenic Terfenol-D, 20.6 MPa)

In Figure 5-8, the actuator strain is plotted against the actuator current for the 2 amp peak, 5 hertz sinusoidal current input. This is the same data in Figure 5-4 (current vs time) and Figure 5-6 (displacement vs time), but plotted as displacement versus current, where the displacement is normalized to strain in the Terfenol-D rod. Again, the preload stress level is 20.6 MPa. This plot, therefore, shows the actuator output (strain) as a function of actuator input (current). At this excitation level, the active member is reasonably linear but with significant hysteresis. A plot of the same signals, at a different preload level, is shown in Figure 5-9. In Figure 5-9, the actuator preload stress is 13.7 MPa.

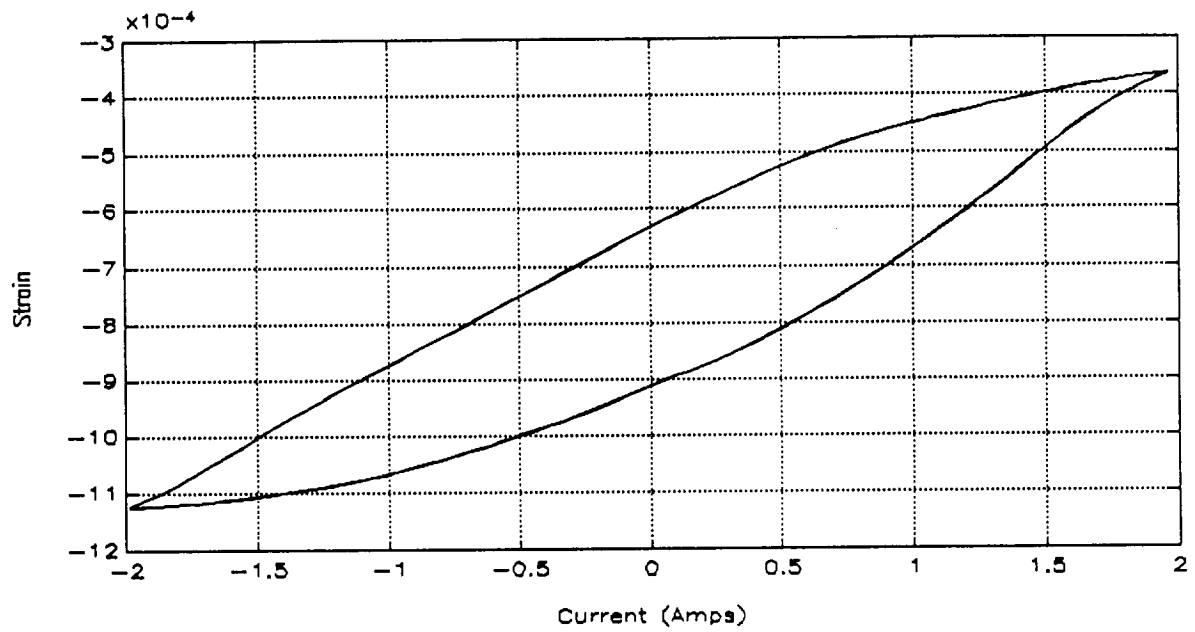


Figure 5-8. Strain vs. current (cryogenic Terfenol-D, 20.6 MPa)

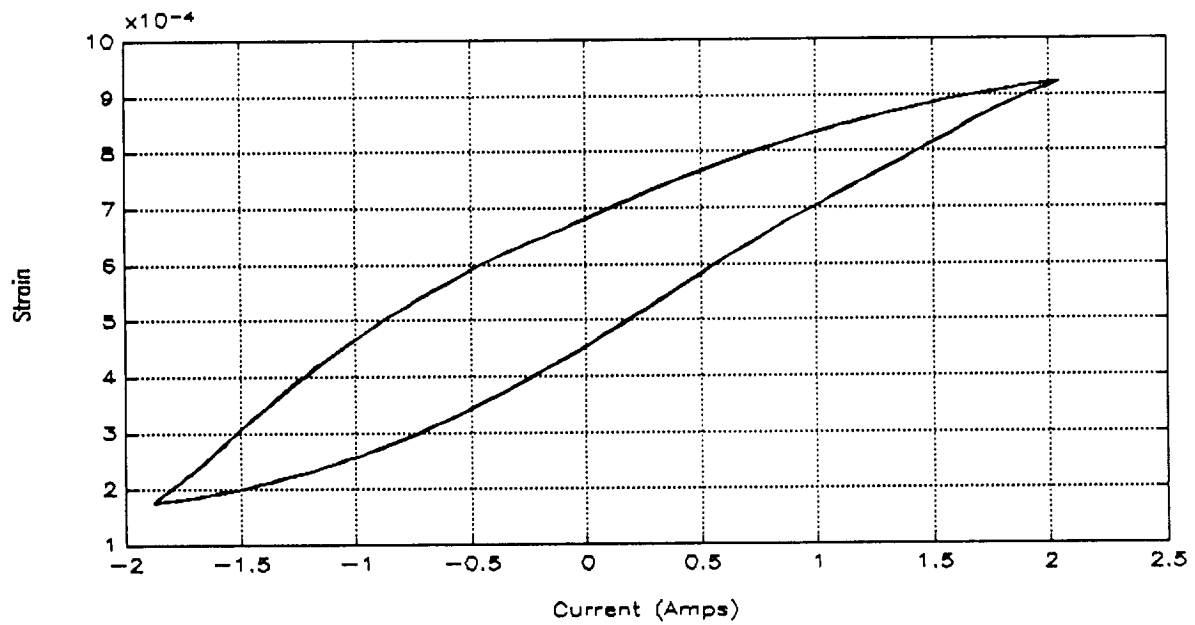


Figure 5-9. Strain vs. current (cryogenic Terfenol-D, 13.7 MPa)

Figure 5-10 contains the raw displacement and current data for all the current levels at the 20.6 MPa preload. As shown, a maximum displacement of approximately 52 micrometers was obtained at the current level of 4 Amps. Figure 5-11 is a similar plot, where the actuator has a preload stress level of 13.7 MPa. The maximum displacement obtained at 13.7 MPa was approximately 42 micrometers, at a current level of 4 Amps peak. This displacement data is presented as strain for all the current levels, as shown in Figures 5-13 and 5-14. For Figure 5-13, the actuator preload was 20.6 MPa and the maximum strain is approximately 1800 microstrain at 4 Amps peak. For Figure 5-14, the actuator preload was 13.7 MPa and the maximum strain is approximately 1450 microstrain at 4 Amps peak.

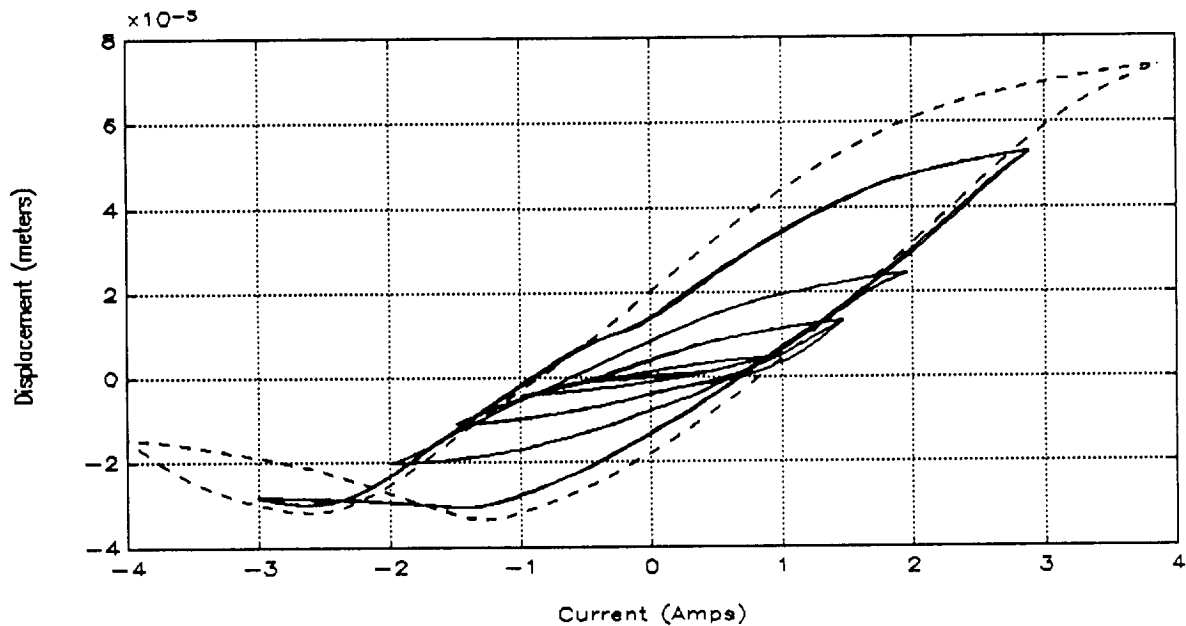


Figure 5-10. Displacement vs. current (cryogenic Terfenol-D, 20.6 MPa)

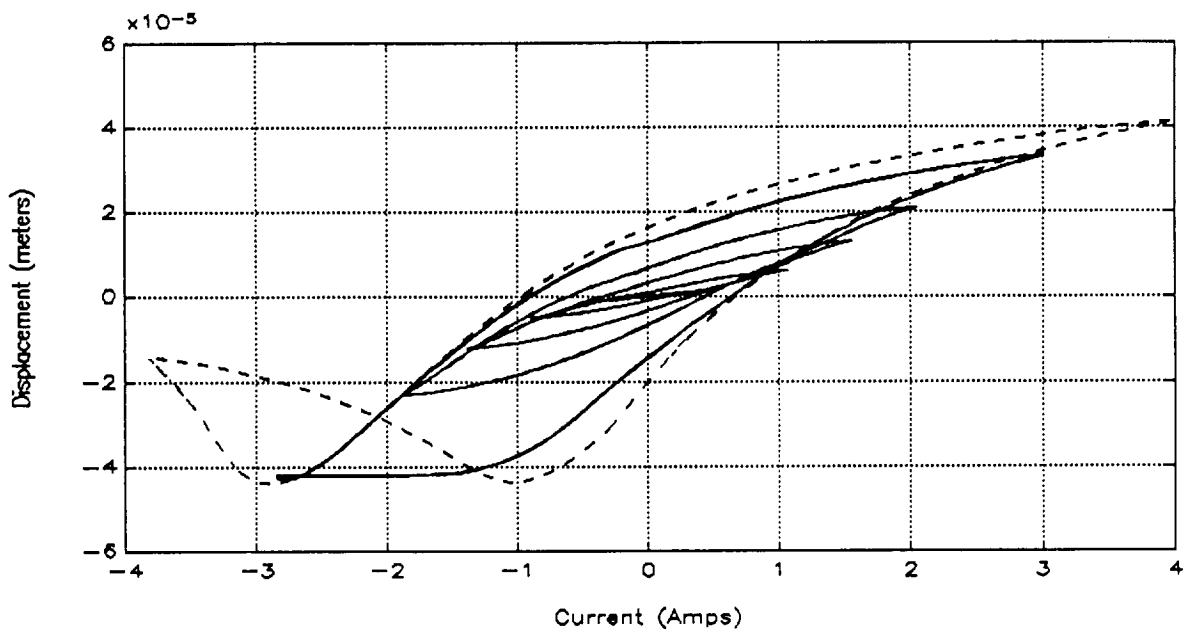


Figure 5-11. Displacement vs. current (cryogenic Terfenol-D, 13.7 MPa)

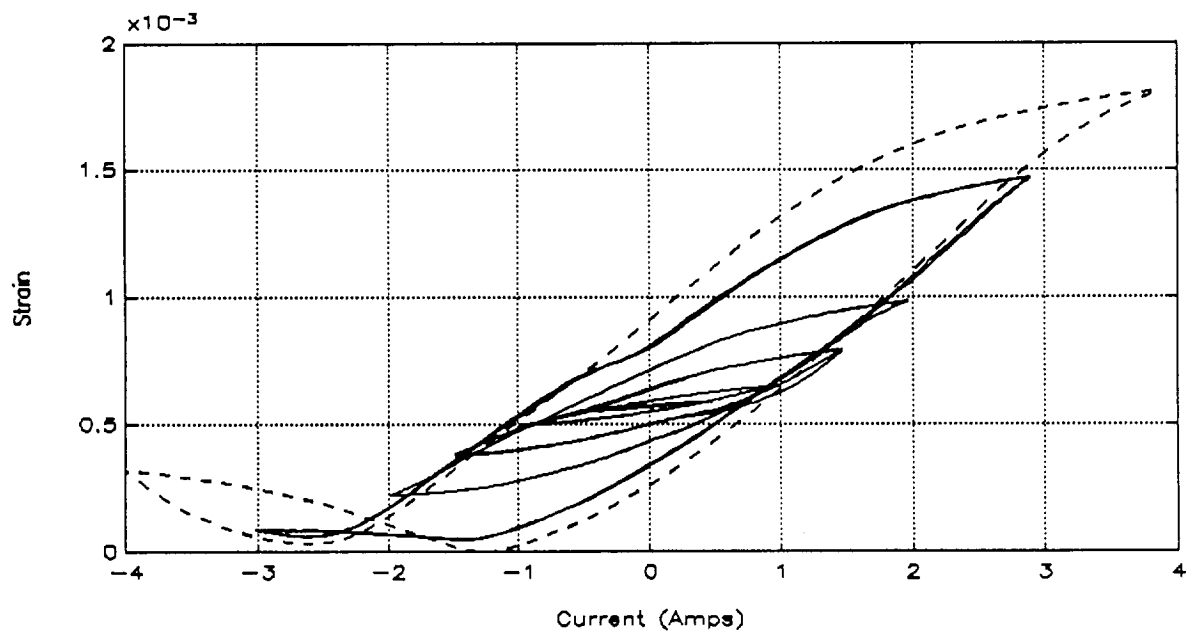


Figure 5-12. Strain vs. current (cryogenic Terfenol-D, 20.6 MPa)

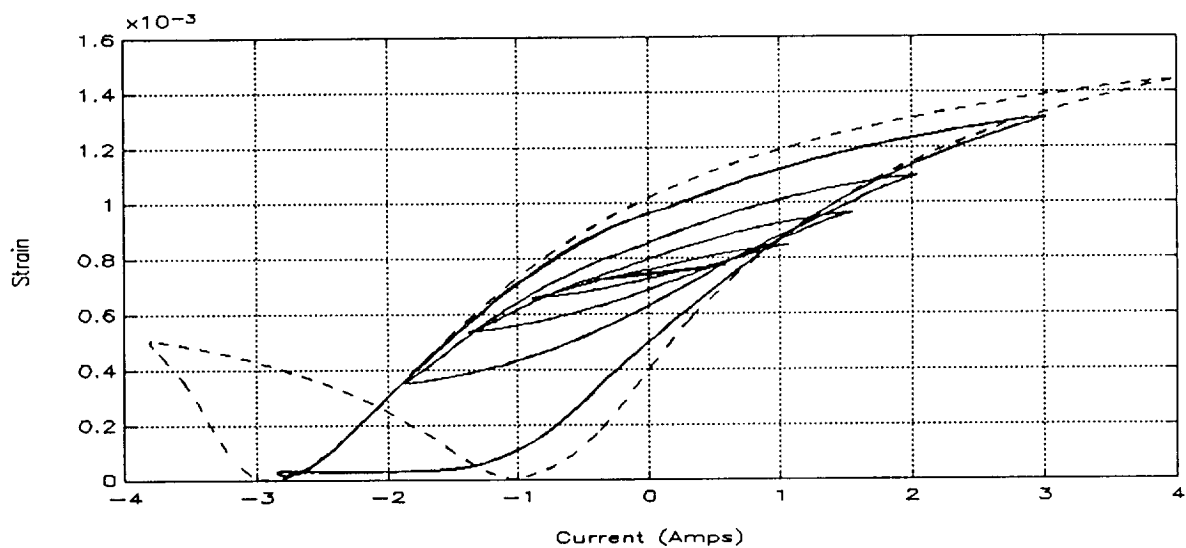


Figure 5-13. Strain vs. current (cryogenic Terfenol-D, 13.7 MPa)

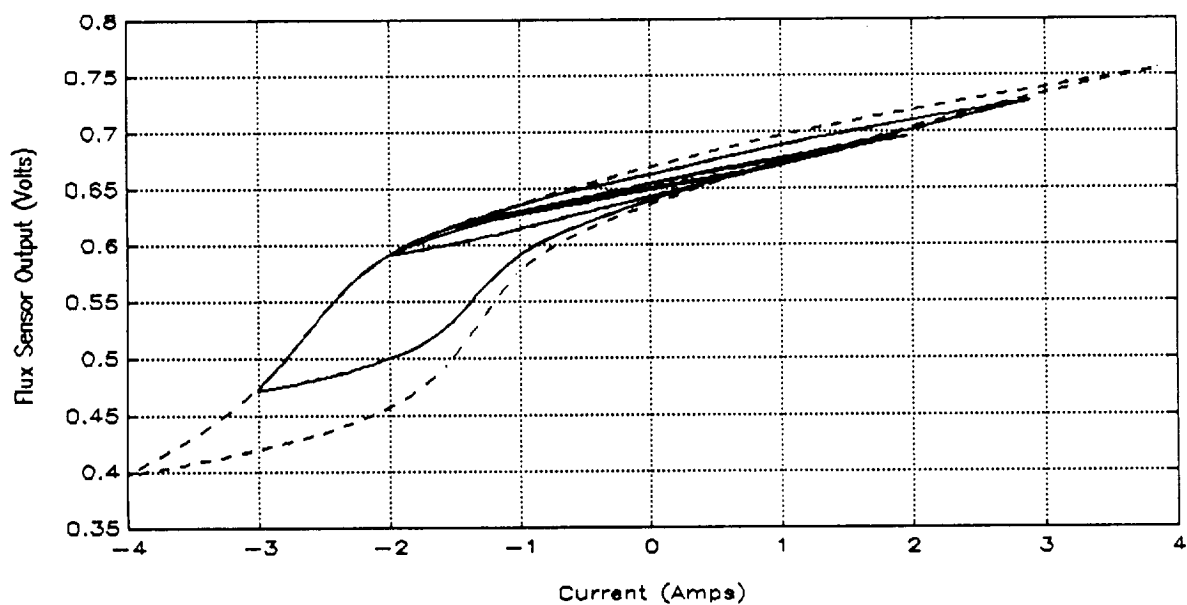


Figure 5-14. Flux sensor output vs. current (cryogenic Terfenol-D, 20.6 MPa)

Figure 5-14 is a plot of the flux sensor output in volts and the current. This data was obtained at the actuator preload level of 20.6 MPa. As shown, the flux is linear with current at the lower current levels. The strain and flux sensor output are plotted in Figure 5-15. Again, the actuator preload level was 20.6 MPa. Figures 5-14 and 5-15 both display two cycles of the 5 Hz waveform, illustrating clean flux data and good repeatability.

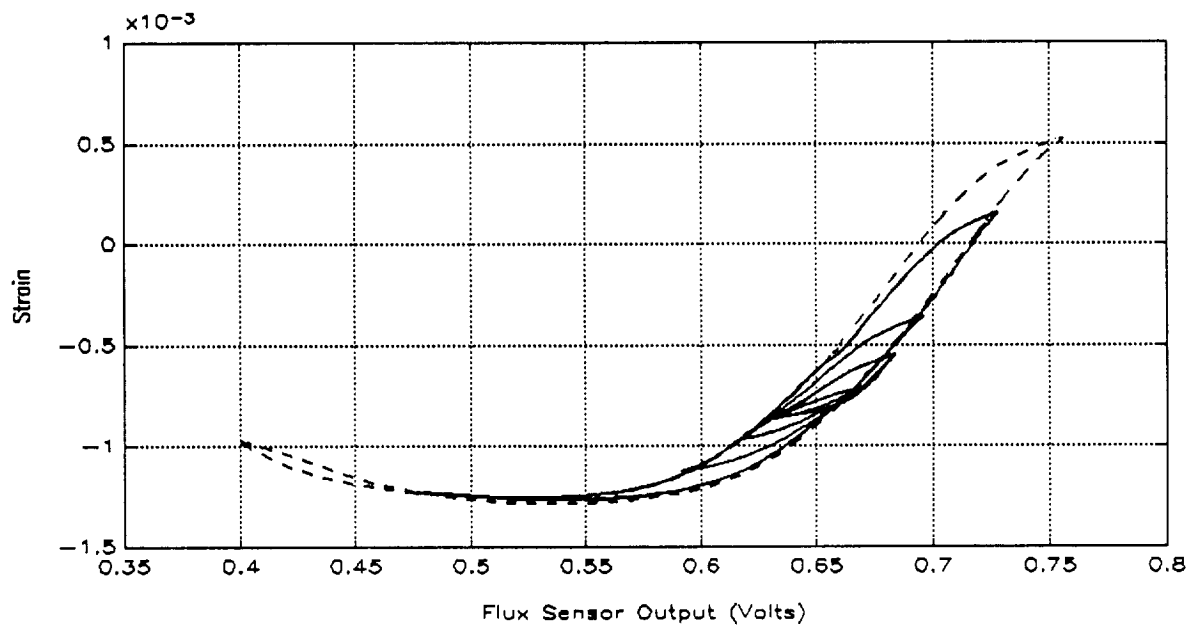


Figure 5-15. Strain vs. flux sensor output (cryogenic Terfenol-D, 20.6 MPa)

Figure 5-16 is a plot of the raw displacement versus current data for all the different preloads, with the same 2 amp peak, 5 Hertz sinusoid excitation. The number beside each curve is the preload stress in the magnetostrictive material as previously given in Table 5-2. The same data in Figure 5-16 is shown in Figure 5-17 with the compressive displacements removed. This was done by shifting the displacement curves such that at zero current, the average of the two displacements is zero. As shown, the largest strains occur at the 13.7 MPa and 20.6 MPa preload levels, for a current excitation of 2 Amps. Figure 5-18 is identical to Figure 5-17, except displaying the displacement as a strain in the magnetostrictive material. The maximum strain is approximately 760 ppm (at 20.6 MPa) for the current level of 2 Amps.

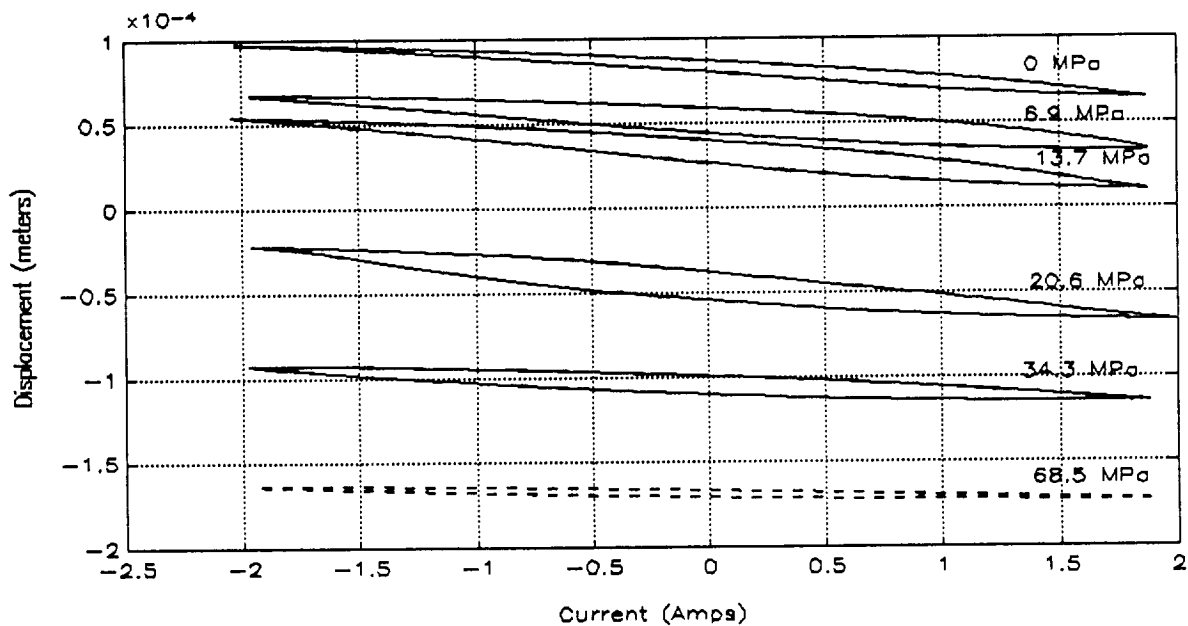


Figure 5-16. Displacement vs. current (cryogenic Terfenol-D, 2 amps, raw data)

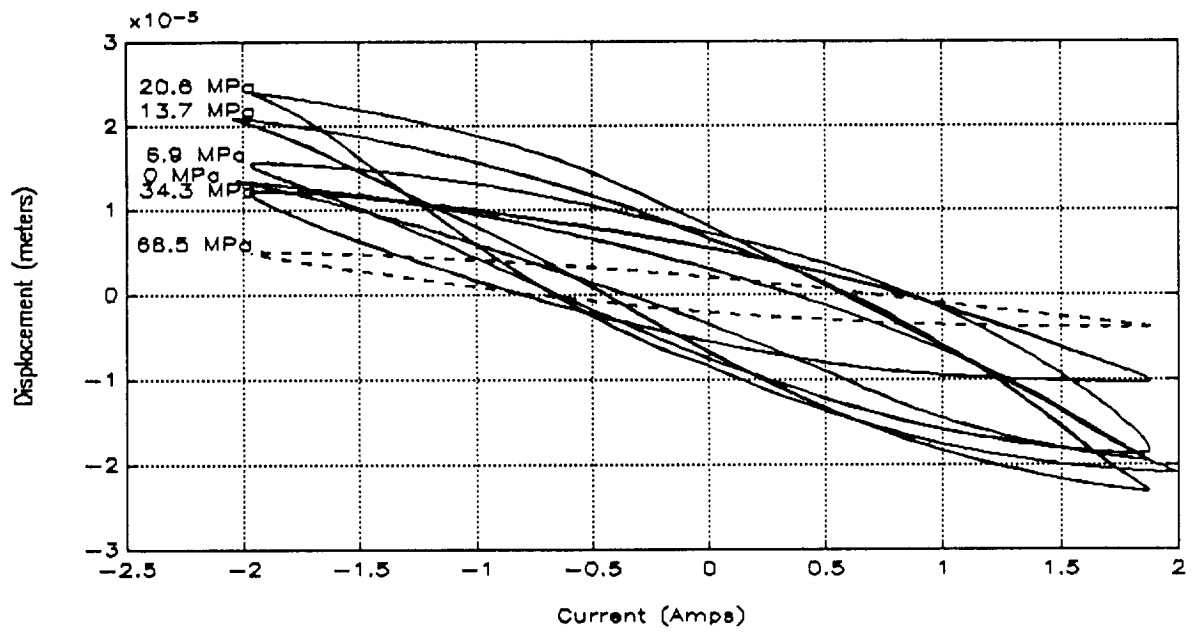


Figure 5-17. Displacement vs. current (cryogenic Terfenol-D, 2 amps, cleaned data)

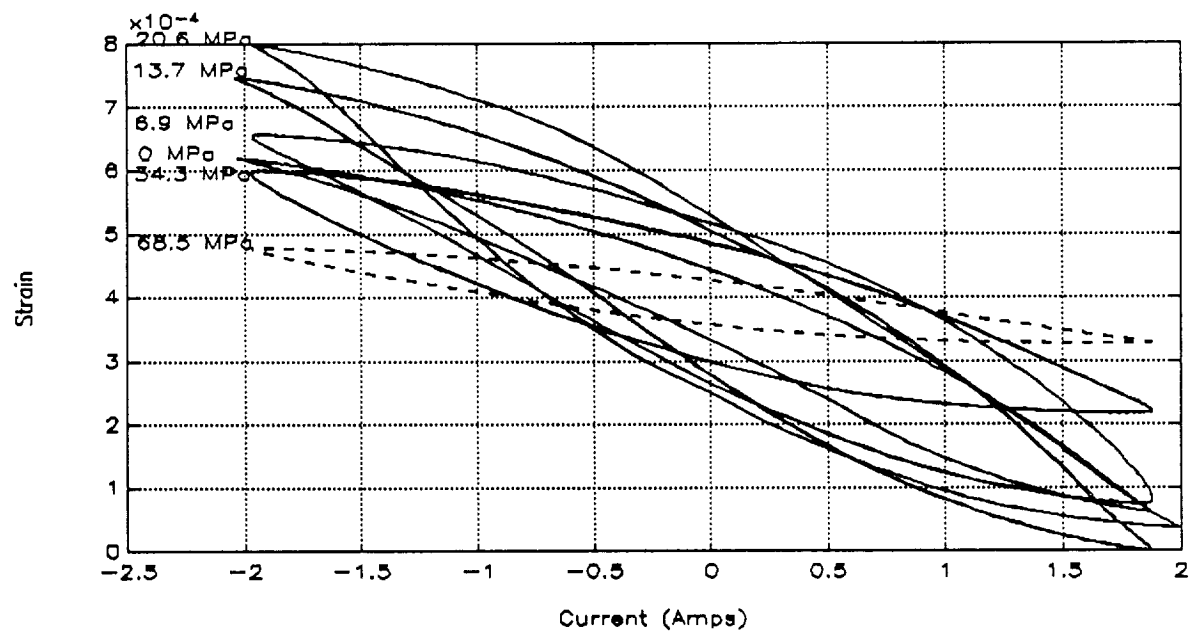


Figure 5-18. Strain vs. current (cryogenic Terfenol-D, 2 amps, cleaned data)

The frequency response from voltage to current was measured using the sweep-sine function of the spectrum analyzer. Figure 5-19 is the magnitude of the bode plot over the frequency range from 1 to 500 Hz. The active member was preloaded to 20.6 MPa and excited with 100 MA peak, sweep-sine excitation with no bias current. As shown, the response is flat out to approximately 10 Hz. The dc gain is almost 1 Mho, which corresponds to the resistive load of 1 Ohm.

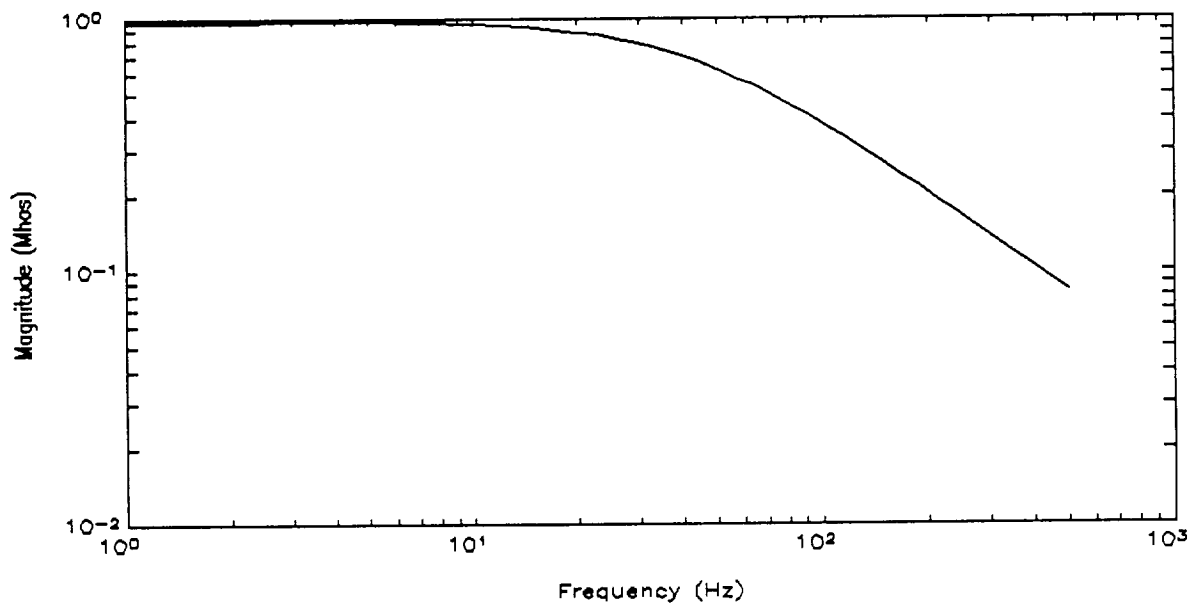


Figure 5-19. Voltage to current frequency response for 0.1 amp peak excitation (20.6 MPa)

Figure 5-20 is a plot of the voltage to current frequency response, from 1 to 500 Hz. The actuator was preloaded to 20.6 MPa and excited with 1.0 Amp peak swept-sine excitation. The plot compares the effect of the transfer function magnitude for two levels of the actuator bias current, 0 and 2 Amps. The 0 Amp bias curve has a higher dc gain, but rolls off at a lower frequency than the 2 Amp bias curve.

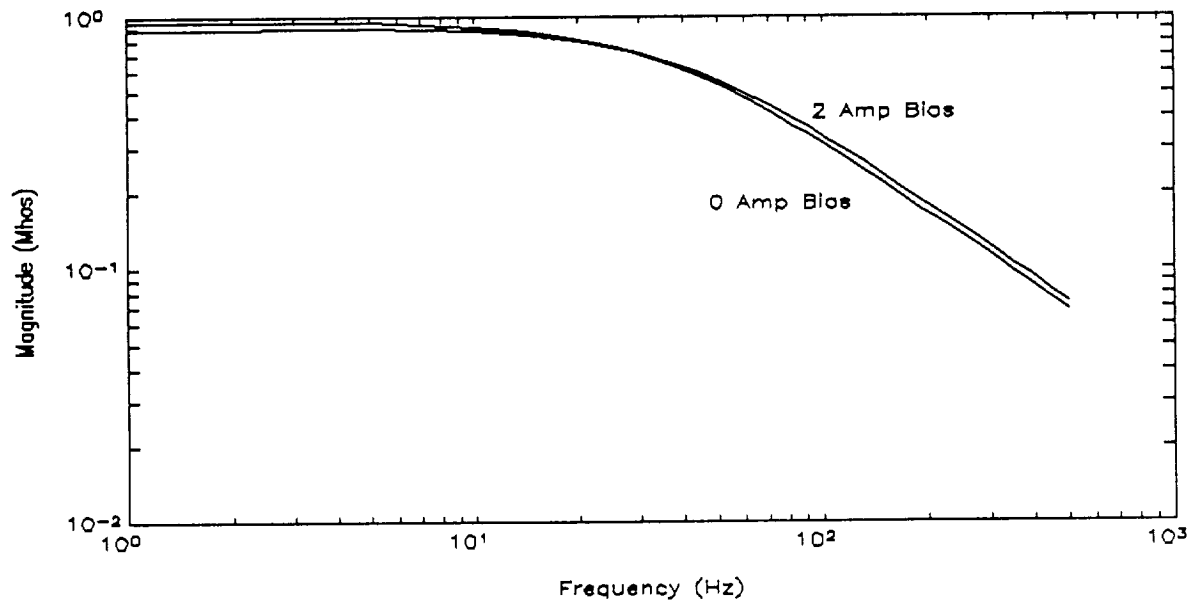


Figure 5-20. Comparison of the voltage to current frequency response at 1 amp P excitation, for 0 and 2 amp bias (20.6 MPa)

The frequency response from voltage to current for the various preload levels is illustrated in Figure 5-21. The preload level is label on the plot. The actuator was excited with a 1.0 Amp peak swept-sine excitation, at a 0 Amp bias level. Data was taken from 1 to 500 Hz. As shown, the break frequency increases with increasing preload.

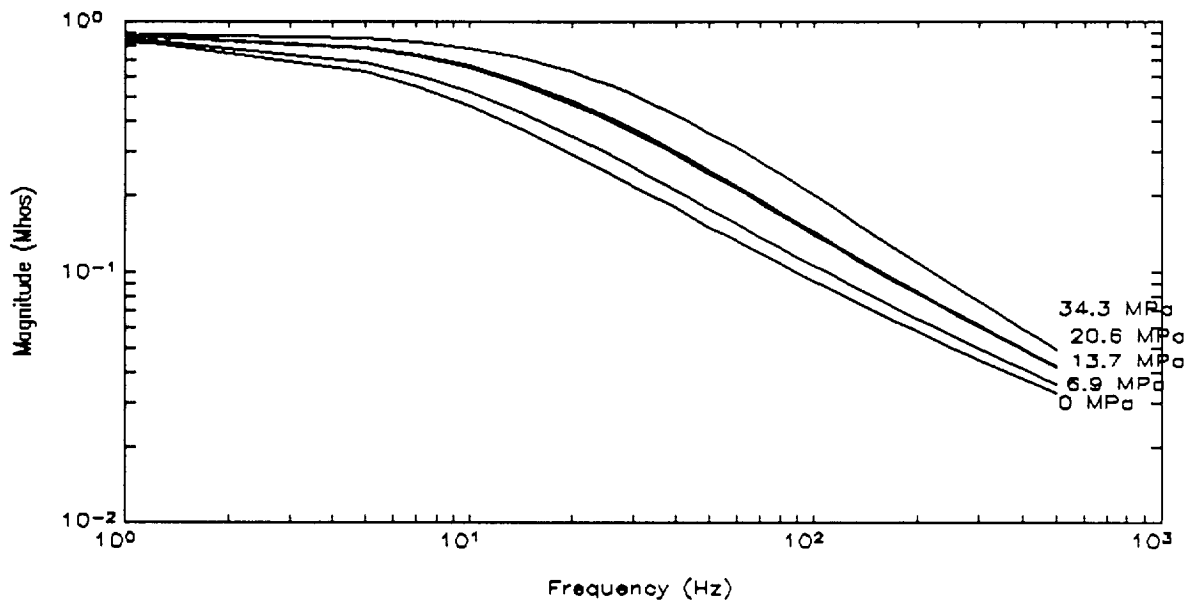


Figure 5-21. Comparison of the voltage to current frequency response at 1 amp P excitation, for the various preloads (cryogenic Terfenol-D, 0 bias)

Figure 5-22 is a swept-sine bode plot of the displacement response to current input. These are plotted for two different amplitude excitations, 0.1 Amp and 1 Amp peak. The upper plot is the magnitude of the transfer function and the lower plot is the phase of the transfer function. As for the swept-sine excitation, the active member gain is higher at the higher current levels. The actuator was preloaded to 20.6 MPa. As shown, the response is flat out to 200 Hz. The dc gain is approximately 1.9×10^{-6} meters per amp for the 0.1 Amp peak excitation and 16.3×10^{-6} meters per amp for the 1.0 Amp peak excitation.

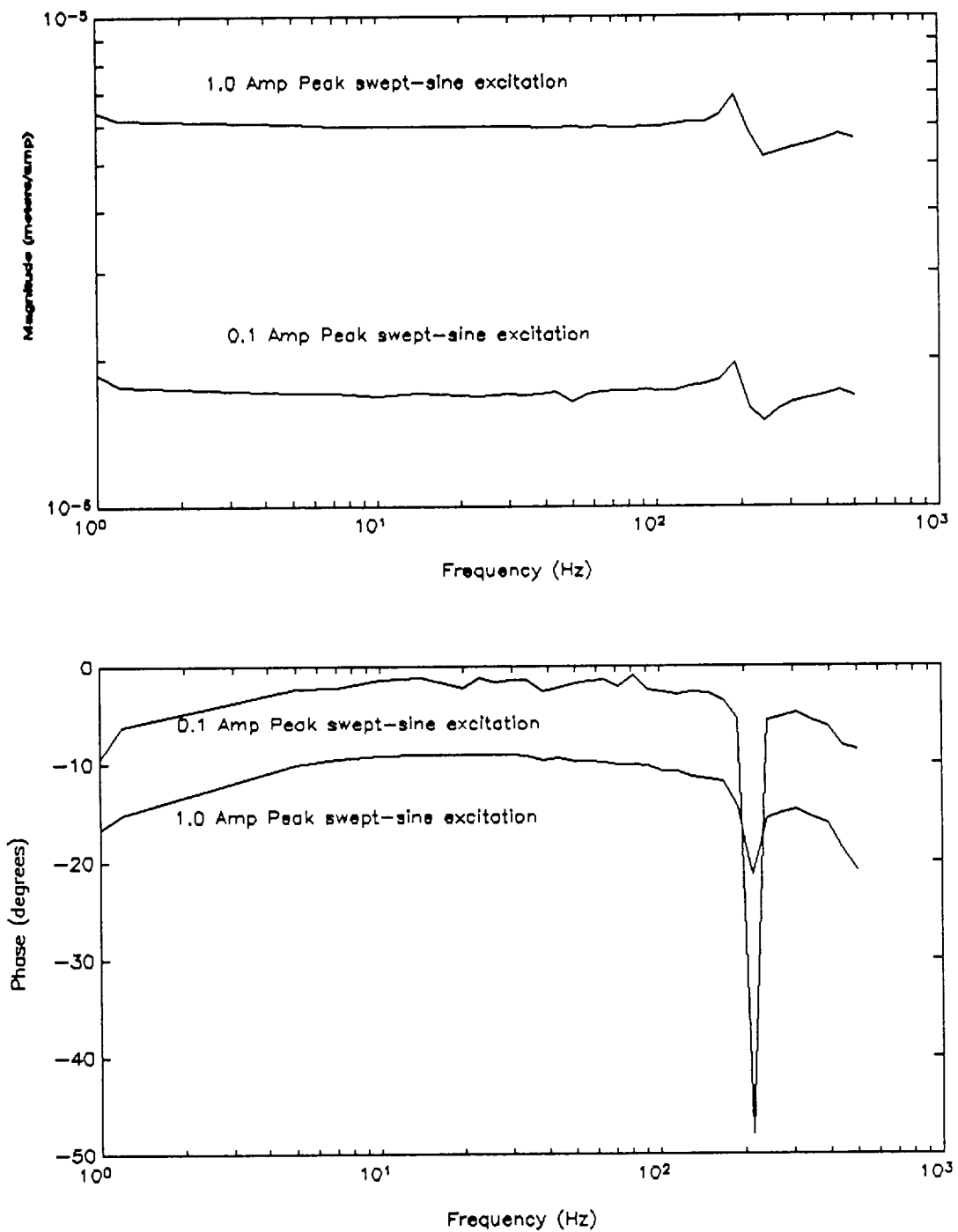


Figure 5-22. Current to displacement frequency response for 0.1 amp P and 1.0 amp P excitation at 0 amp bias (cryogenic Terfenol-D, 20.6 MPa)

The frequency response from the current to the flux sensor output is shown in Figure 5-23. The data is from 1 to 500 Hz, and compares the swept-sine excitation levels of 0.1 Amp peak and 1.0 Amp peak. The 1.0 Amp response has a higher gain and is flatter than the 0.1 Amp response. The phase of both responses begins to decrease at approximately 50 Hz. The actuator was preloaded to 20.6 MPa. The dc gain is approximately 8.0×10^{-3} volts per amp for the 0.1 Amp peak excitation and 1.0×10^{-2} volts per amp for the 1.0 Amp peak excitation.

Figure 5-24 is a swept-sine bode plot of the displacement response to the flux sensor input. Again, these are plotted for two different swept-sine excitations, 0.1 Amp and 1 Amp peak. As shown, the active member gain is higher at the higher current levels. The actuator was preloaded to 20.6 MPa. The responses are reasonably flat out to 100 Hz, and the 1.0 Amp response is flatter. The dc gain is approximately 1.1×10^{-4} meters per volt for the 0.1 Amp peak excitation and 3.1×10^{-4} meters per volt for the 1.0 Amp peak excitation.

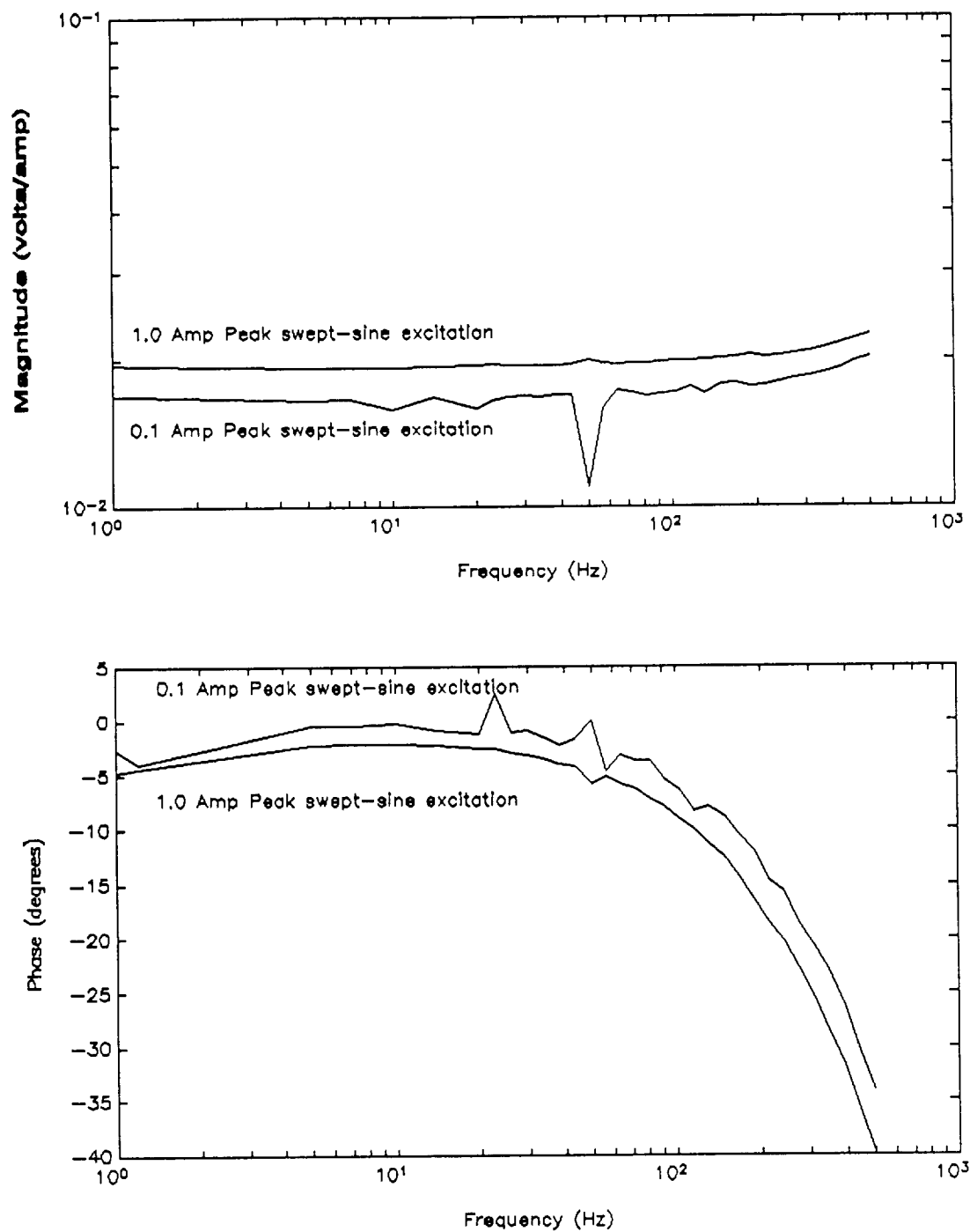


Figure 5-23. Current to flux sensor output frequency response for 0.1 amp P and 1.0 amp P excitation at 0 amp bias (cryogenic Terfenol-D, 20.6 MPa)

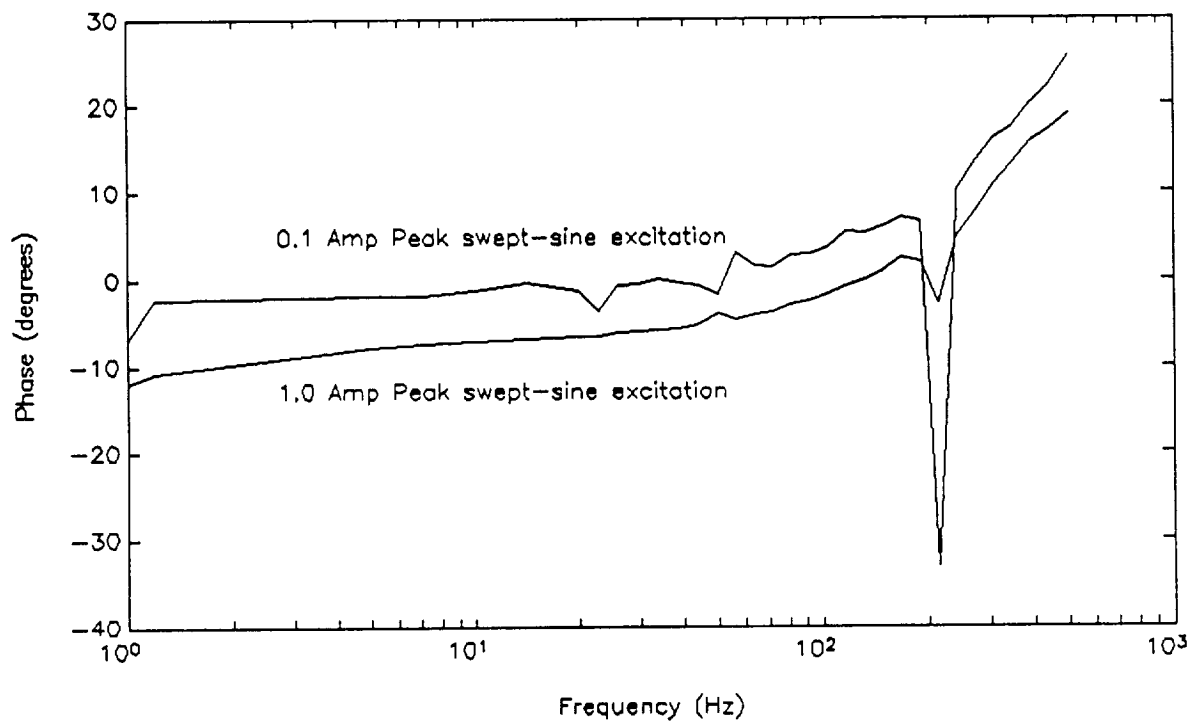
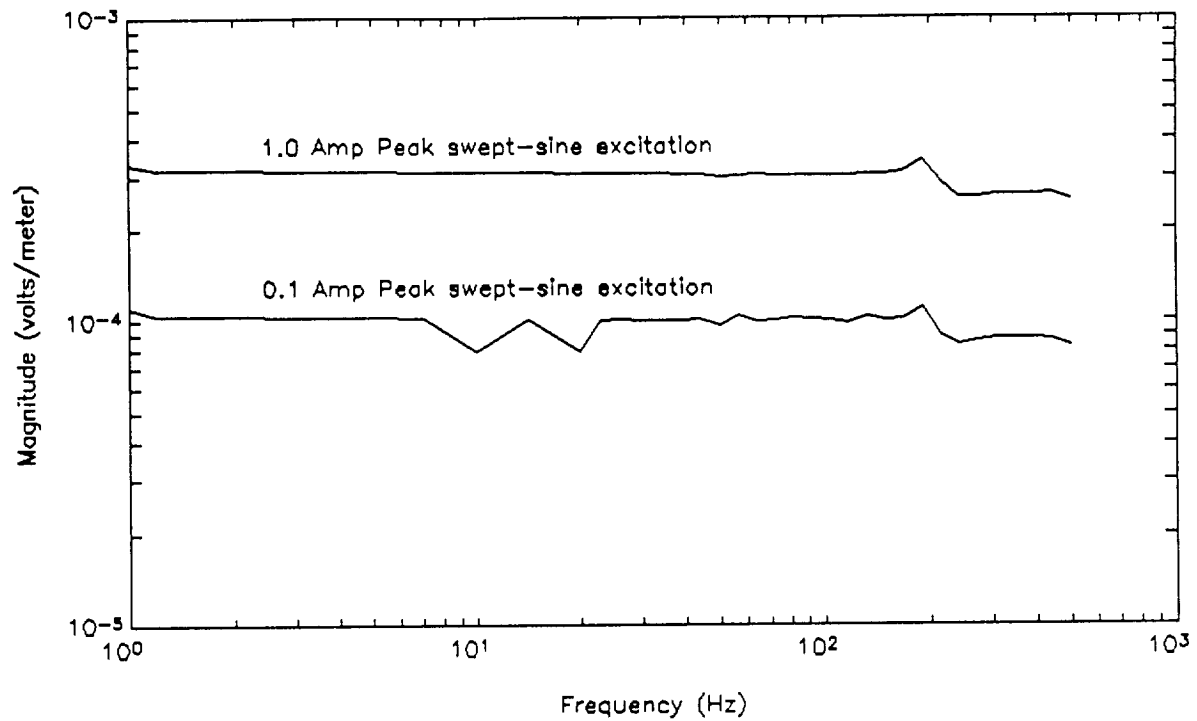


Figure 5-24. Flux sensor output to displacement frequency response for 0.1 amp P and 1.0 amp P excitation at 0 amp bias (cryogenic Terfenol-D, 20.6 MPa)

5.3.2 Terbium Dysprosium (TbDy) Tests

For the TbDy tests, the active member was excited with five Hertz sinusoidal current waveforms at six different peak current levels of 0.5, 1.0, 1.5, 2.0, 3.0, and 4.0 amps. Data was taken with the magnetostrictive material in the active member mechanically preloaded at three different stress levels, consisting of 2.7 MPa, 12.3 MPa, and 20 MPa. The preload levels in the magnetostrictive material corresponding to these preload stresses are given in Table 5-2. The TbDy rod was smaller than the cryogenic Terfenol-D rod, and therefore required spacer material to fit into the active member housing. The nominal "spacer" material was magnetic, and was used in testing the actuator at the nominal preload level of 20 MPa. A different spacer, one that was non-magnetic, was also used in the testing of the actuator at all three preload levels. For the following discussion of the data, the label "with spacer" refers to the configuration with the non-magnetic spacer, and "no spacer" refers to the configuration with the magnetic spacer. Similar to the cryogenic Terfenol-D tests, the actuator was preloaded in the SatCon testbed, then tested at the different current levels. The power supply is under current control, hence for testing convenience, the transfer function from commanded voltage from the spectrum analyzer to the drive current has gain of one amp/volt.

Table 5-3. TbDy preload forces and stresses

Force		Stress	
lb _f	N	Ksi	MPa
20	90	0.4	2.7
90	403	1.8	12.3
145	650	2.9	20

Figures 5-25 through 5-27 are time plots of the raw data at a current level of 1.5 Amps, as shown in Figure 5-25, and with the active member preloaded to 20 MPa (145 lb_f). Figure 5-25 is a plot of the flux field. Because the level of magnetic field depends upon the location of the sensor, the information is somewhat arbitrary. The function of the plot is to illustrate that good flux data can be obtained. The units displayed in the plot are volts, the sensor output units. Figure 5-27 is a plot of the measured

displacement of the magnetostrictive rod and flexures relative to the housing. The peak-to-peak displacement is approximately 100 micrometers. As can be seen from the dc level of the displacement, no attempt was made to force the sensor output to zero for zero input current, either through shimming the sensor cage or through conditioning the sensor output signal.

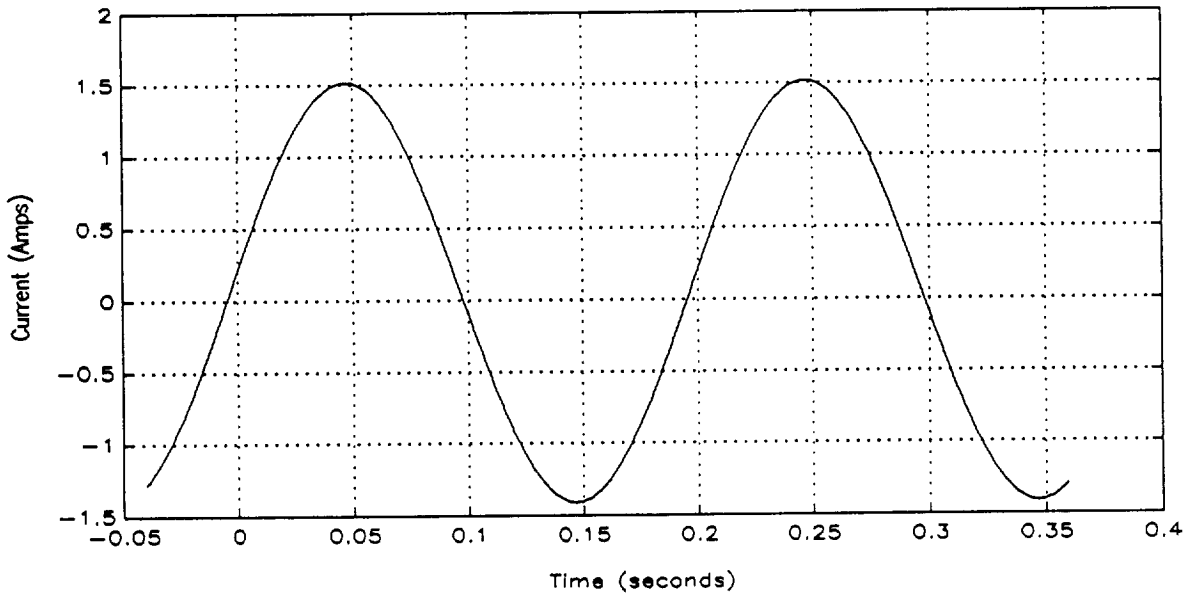


Figure 5-25. Time history of current (TbDy, 20 MPa, no spacer)

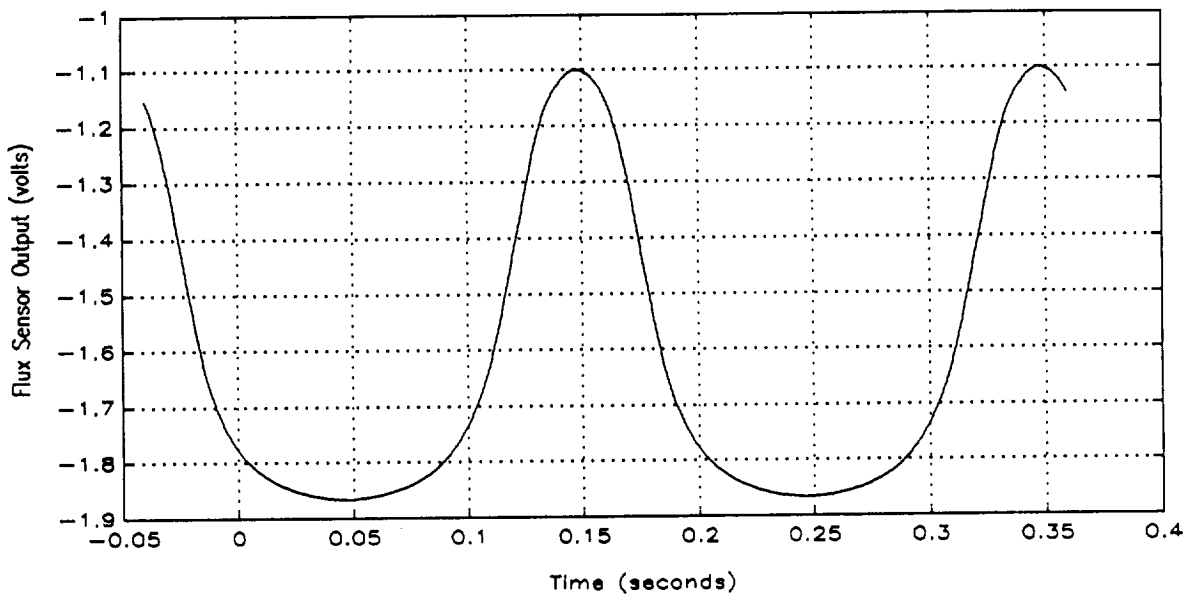


Figure 5-26. Time history of flux sensor output (TbDy, 20 MPa, 110 spacer)

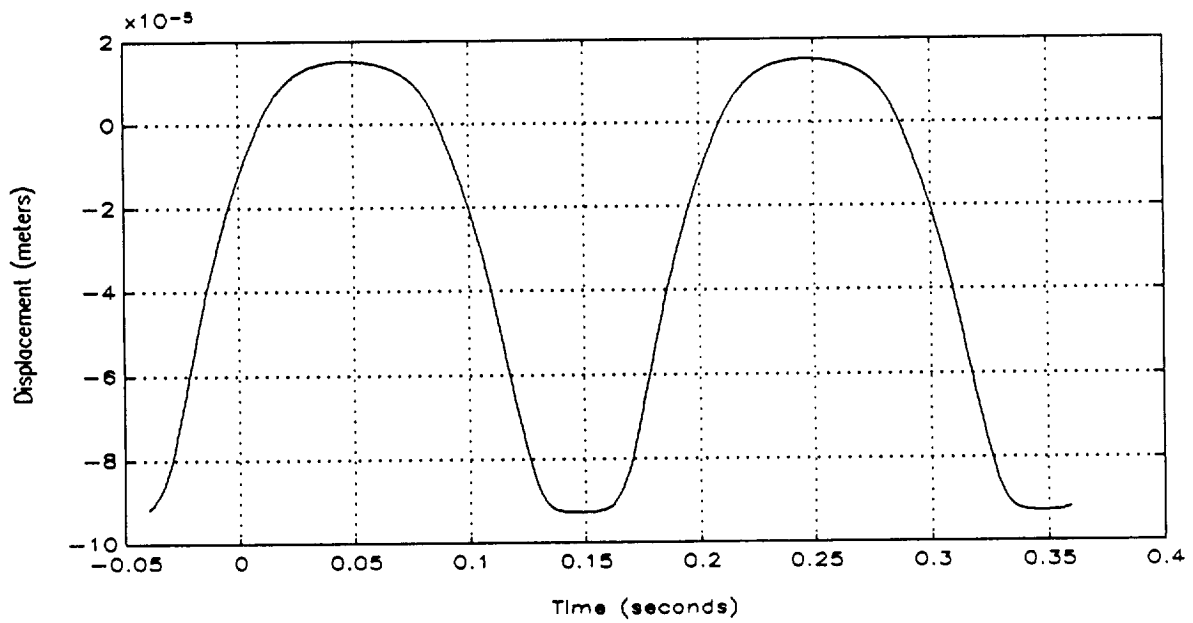


Figure 5-27. Time history of displacement (TbDy, 20 MPa, no spacer)

In Figure 5-28, the actuator displacement is plotted against the actuator current for the 1.5 amp peak, 5 hertz sinusoidal current input. This is the same data in Figure 5-25 (current vs time) and Figure 5-27 (displacement vs time). Figure 5-29 is a similar plot where the displacement is normalized to strain of the TbDy rod. The peak-to-peak strain is approximately 3600 microstrain. Again, the preload stress level is 20 MPa. This plot shows the actuator output (strain) as a function of actuator input (current). At this excitation level, the active member is reasonably linear with small hysteresis.

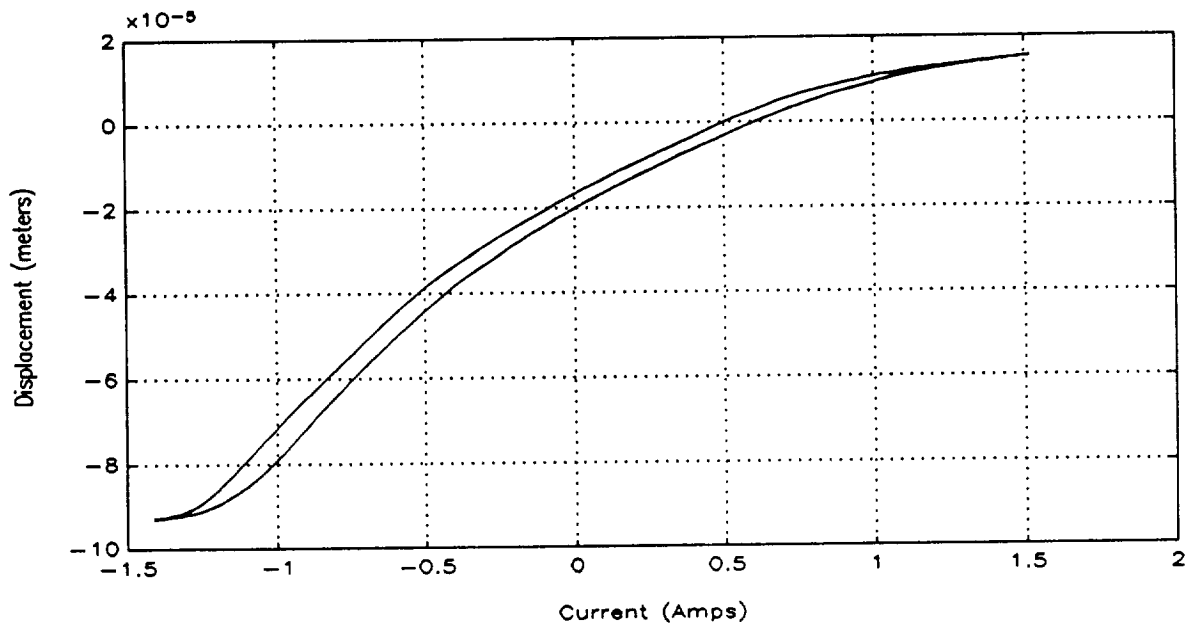


Figure 5-28. Displacement vs. current (TbDy, 20 MPa, no spacer)

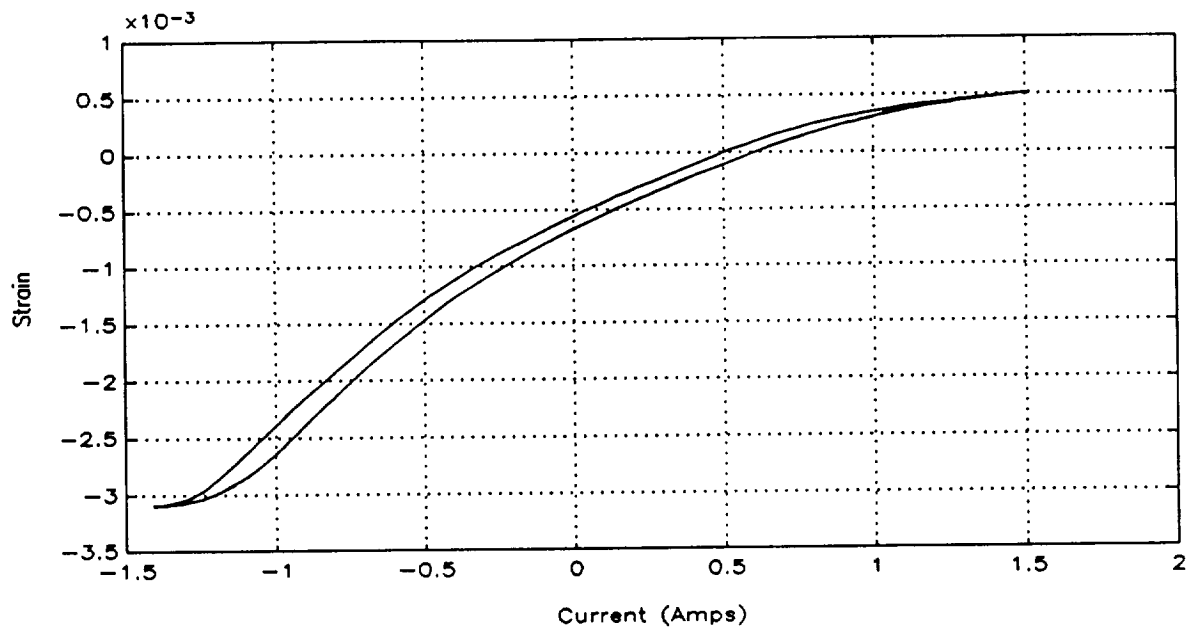


Figure 5-29. Strain vs. displacement (TbDy, 20 MPa, no spacer)

Figure 5-30 contains the strain and current data for all the current levels at the 12.3 MPa preload, and with the spacer. The strain curves were shifted, such that at zero current, the average of the two strains is zero. As shown, a maximum strain of approximately 2400 microstrain was obtained at the current level of 4 Amps. Figure 5-31 is a similar plot, where the actuator has the spacer and a preload stress level of 20 MPa. The maximum strain obtained at 20 MPa was approximately 3400 microstrain, at a current level of 4 Amps peak. To compare with Figure 5-31, Figure 5-32 is a plot of the strain and current data, where the actuator does not have the spacer, but does have the preload stress level of 20 MPa. The maximum strain obtained was approximately 4000 microstrain, at the same current level of 4 Amps peak.

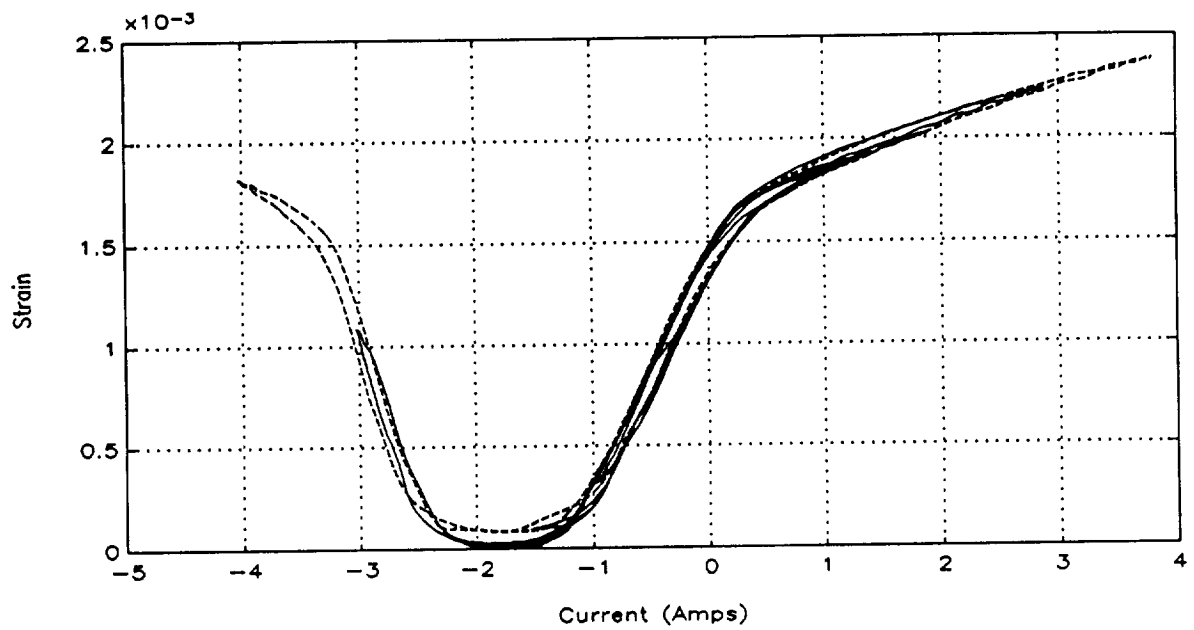


Figure 5-30. Strain vs. current (TbDy, 20 MPa, 1 spacer)

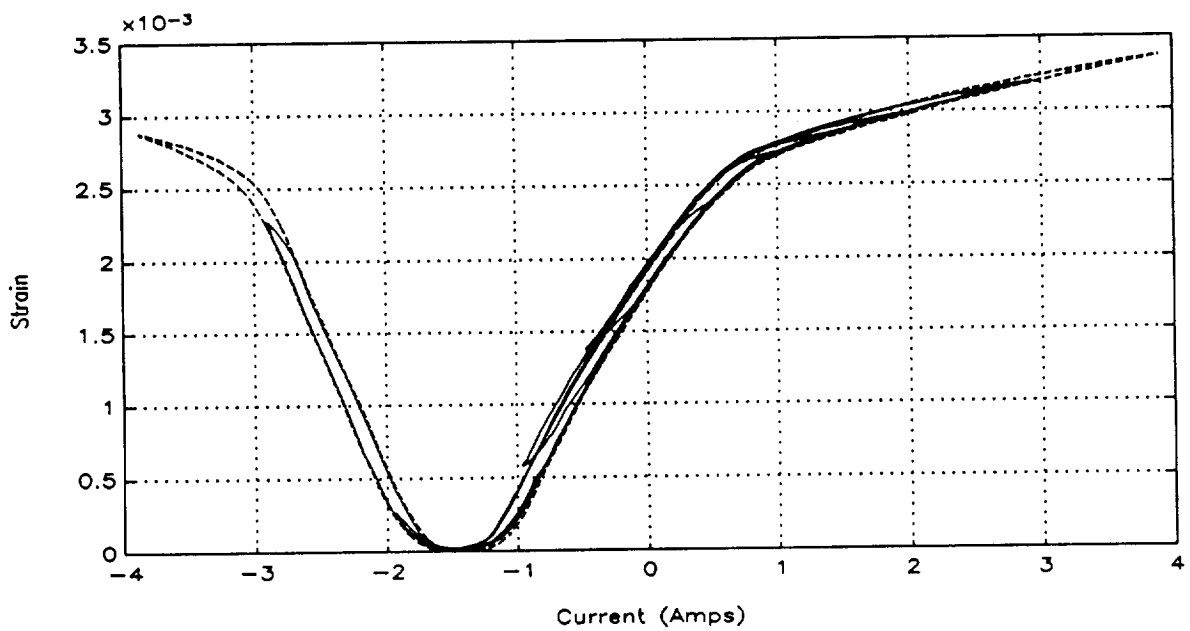


Figure 5-31. Strain vs. current (TbDy, 20 MPa, spacer)

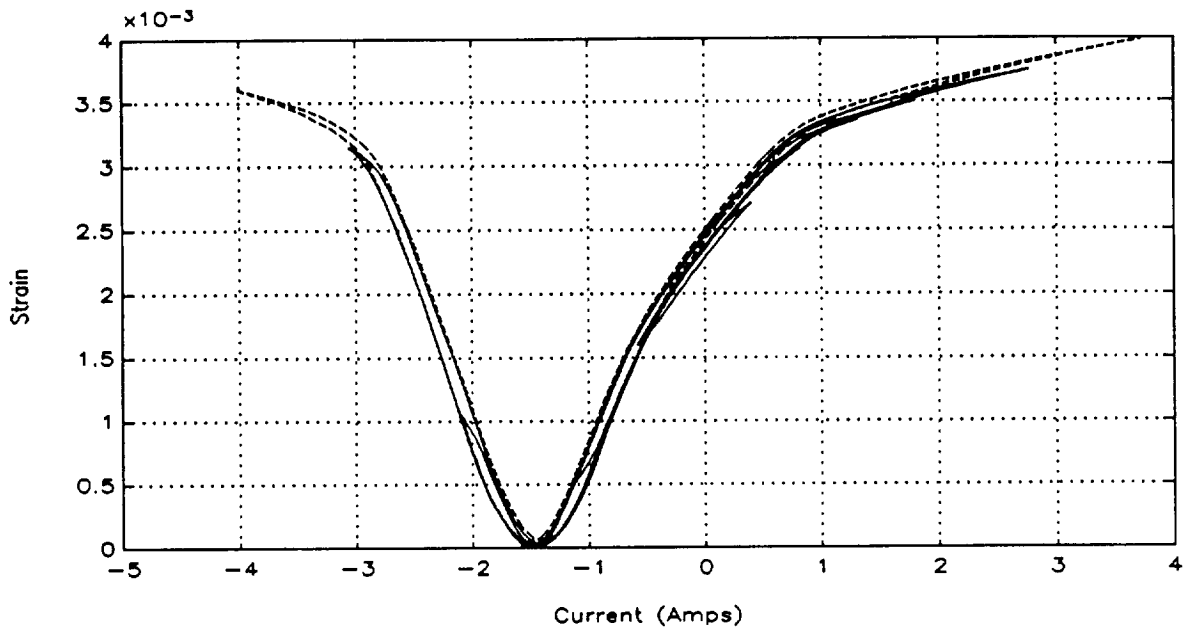


Figure 5-32. Strain vs current (TbDy, 20 MPa, no spacer)

Figure 5-33 is a plot of the flux sensor output in volts and the current. This data was obtained at the actuator preload level of 20 MPa, with no spacer. As shown, the flux has a highly linear range, with very little hysteresis. The strain and flux sensor output are plotted in Figure 5-34. Again, the actuator preload level was 20 MPa, and has no spacer. Figures 5-33 and 5-34 both display two cycles of the 5 Hz waveform, illustrating clean flux data and good repeatability. Figures 5-30 through 5-34 all display extremely low levels of hysteresis, especially when compared with the cryogenic Terfenol-D data.

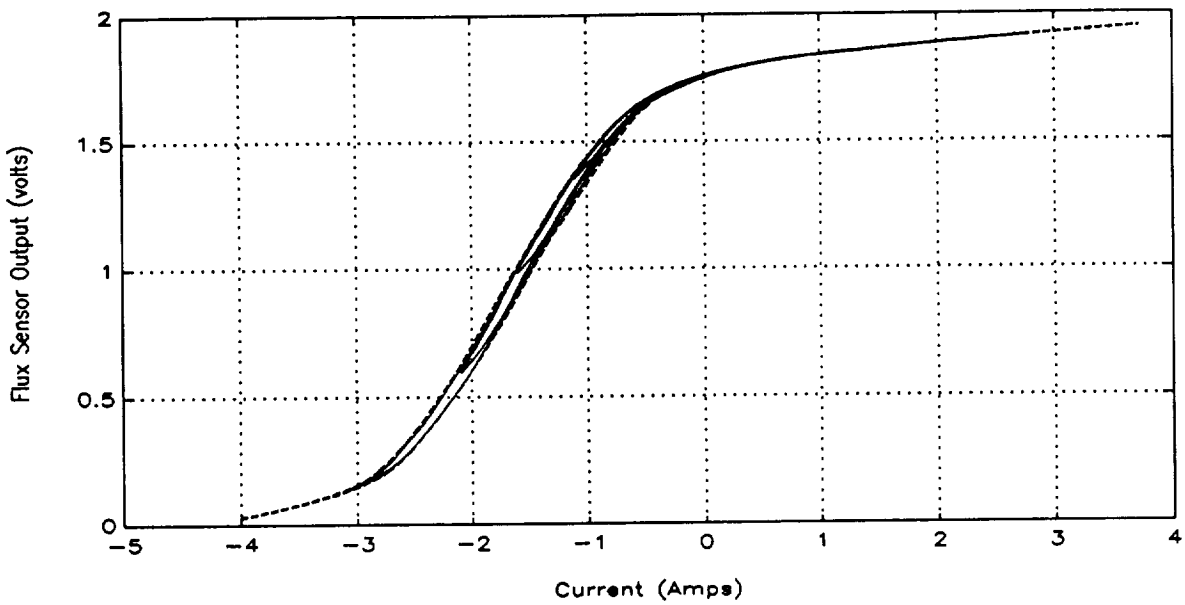


Figure 5-33. Flux sensor output vs. current (TbDy, 20 MPa, no spacer)

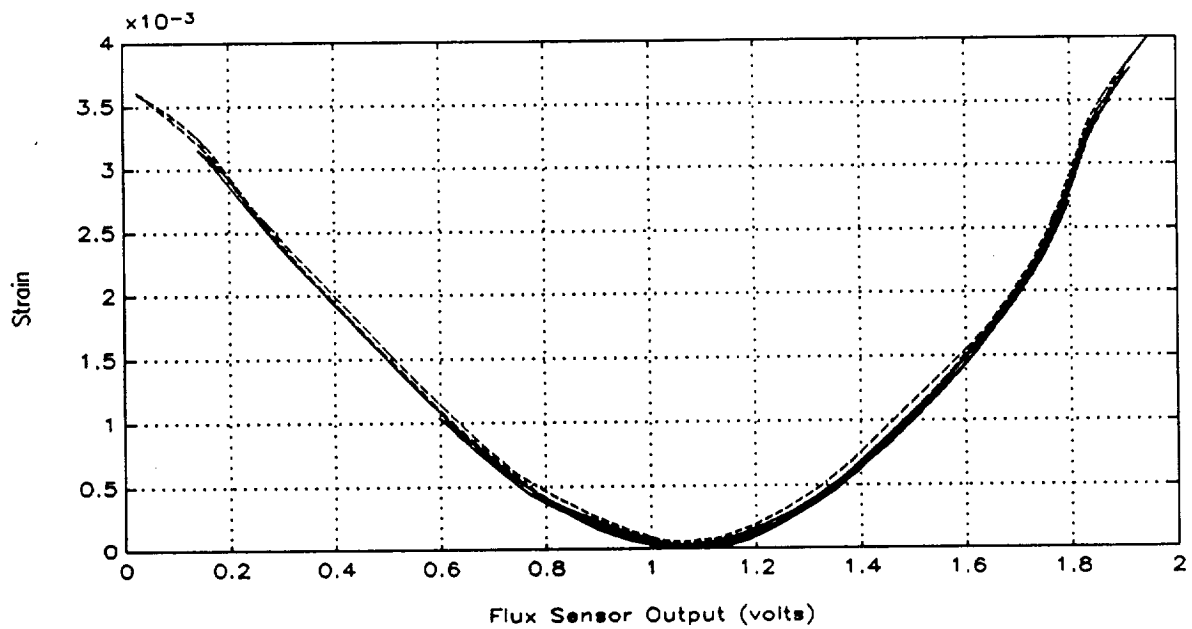


Figure 5-34. Strain vs. flux sensor output (TbDy, 20 MPa, no spacer)

The frequency response from voltage to current was measured using the swept-sine function of the spectrum analyzer. Figure 5-35 is the magnitude of the bode plot over the frequency range from 1 to 500 Hz. The active member was preloaded to 20 MPa, and has no spacer. The swept-sine excitation level was 100 MA peak. The plot compares the magnitude responses for various bias current levels. As shown, the break frequency increases with increasing bias level. The dc gain is approximately 1.0 Mho, which corresponds to the resistive load of 1.0 Ohms.

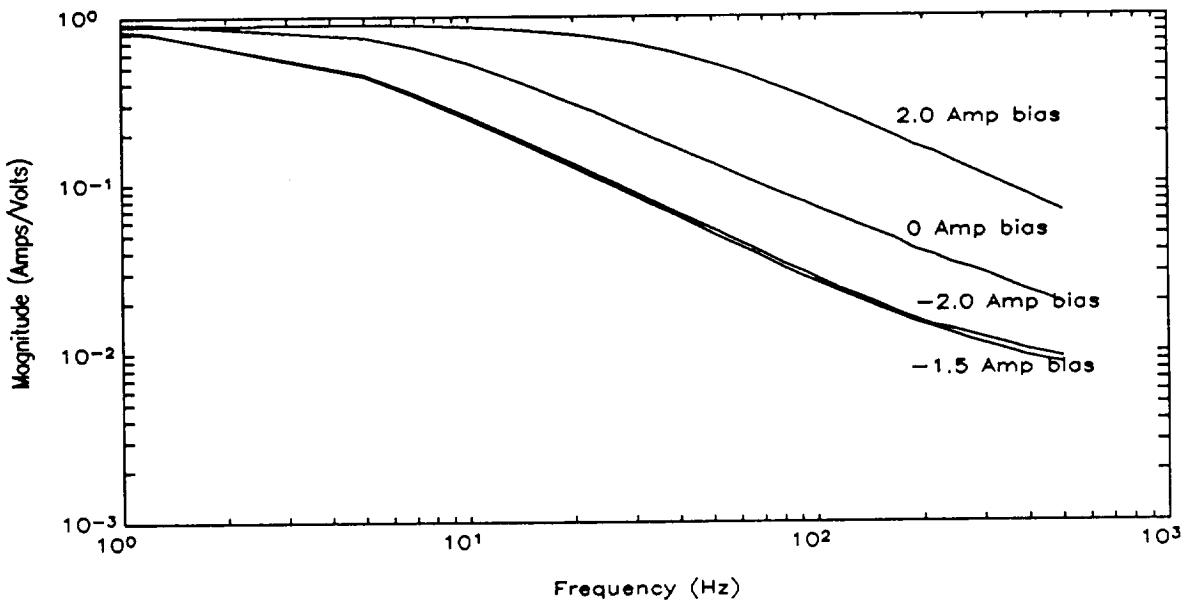


Figure 5-35. Voltage to current frequency response for 1 Amp P excitation, comparing various bias levels (TbDy, 20 MPa, no spacer)

Figure 5-36 is a plot of the voltage to current frequency response, from 1 to 500 Hz. The upper plot is the magnitude of the transfer function and the lower plot is the phase of the transfer function. The actuator excited with 100 mA peak swept-sine excitation, at a bias level of -2 Amps. The plot compares the effect of the transfer function magnitude for two levels of the actuator preload 12.3 MPa and 20 MPa. Data for the 20 MPa preload is identical with and without the spacer. The gain of the 12.3 MPa preload is lower than the 20 MPa preload up until approximately 100 Hz.

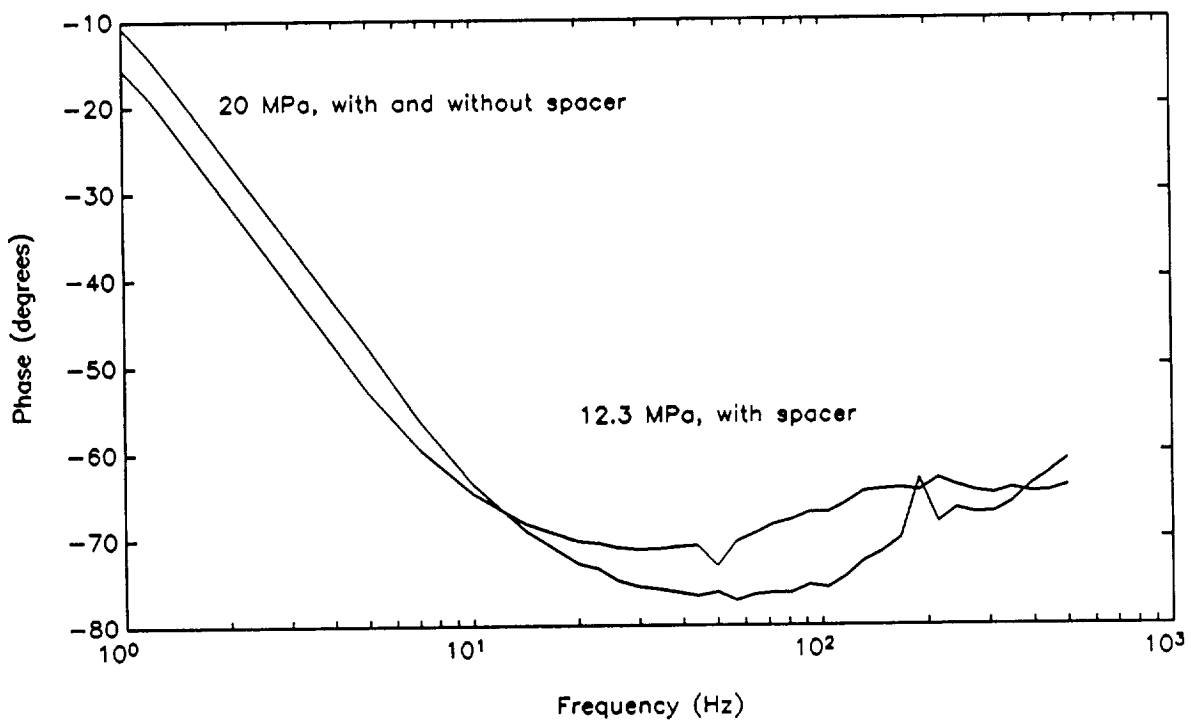
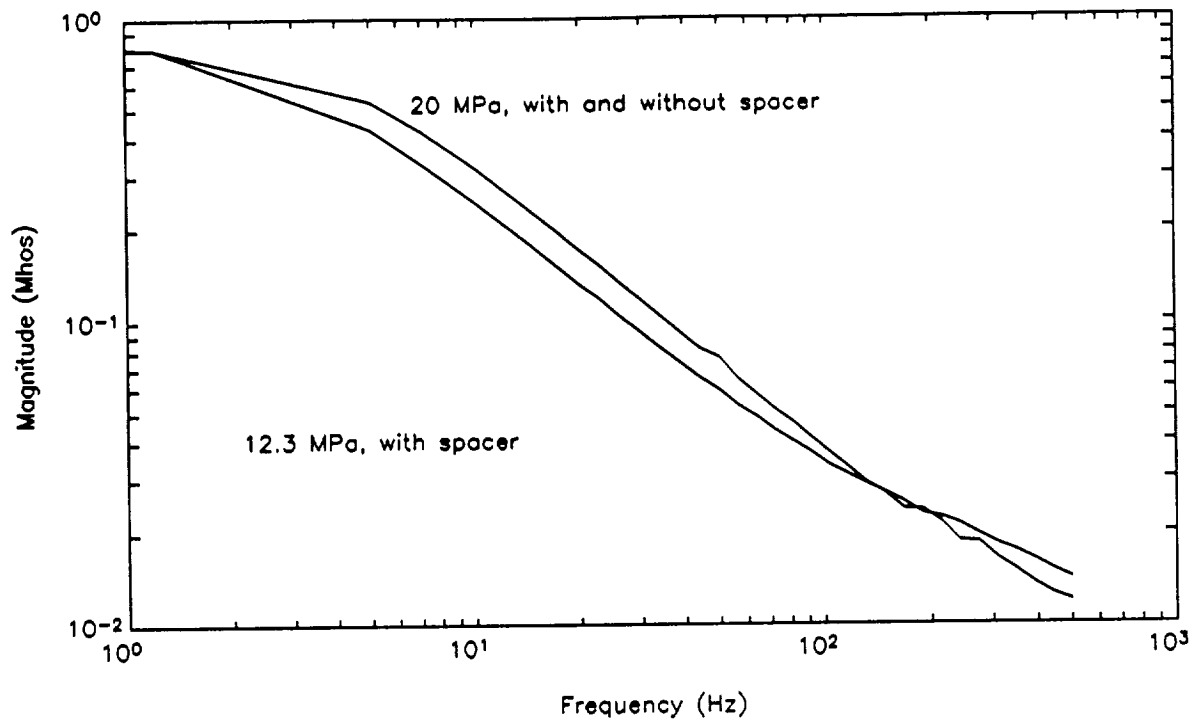


Figure 5-36. Voltage to current frequency response for 100 mA P excitation for various preloads at -2 Amp bias (TbDy)

Figure 5-37 is a swept-sine bode plot of the displacement response to current input. The actuator was excited with a swept-sine 0.1 Amp peak excitation and preloaded to 20 MPa, with no spacer. As shown, the response is flat out to 200 Hz. The dc gain is approximately 2.4×10^{-5} meters per amp.

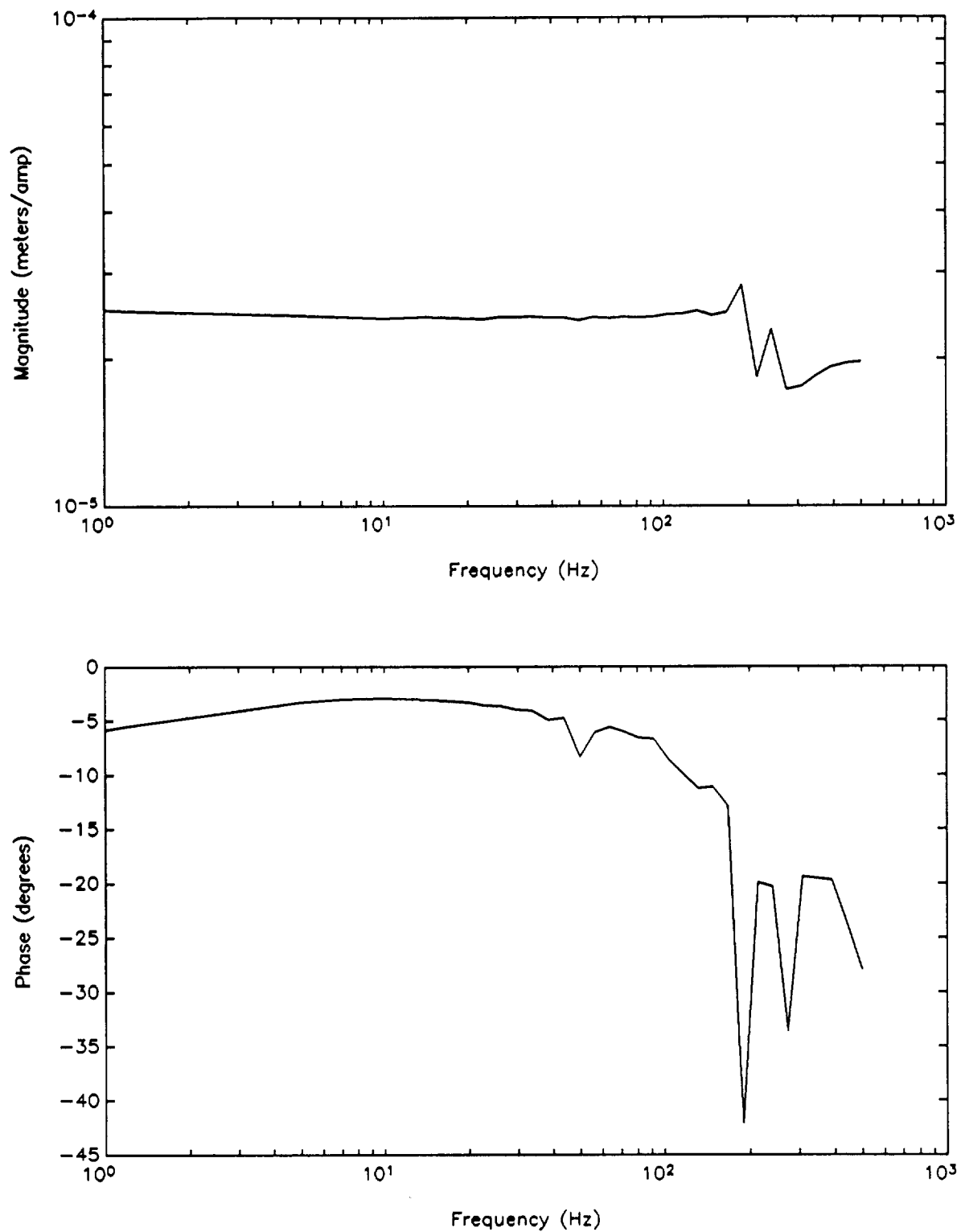


Figure 5-37. Current to displacement frequency response for 100 mAmp P excitation with 0 bias (TbDy, 20 MPa, no spacer)

The frequency response from the current to the flux sensor output is shown in Figure 5-38. The data is from 1 to 500 Hz, and illustrates both the magnitude and phase response to a swept-sine excitation level of 0.1 Amp peak, with zero bias. The phase begins to decrease at approximately 20 Hz. As in Figure 5-37, the actuator was preloaded to 20 MPa, with no spacer. The dc gain is approximately 3.5×10^{-2} volts per amp.

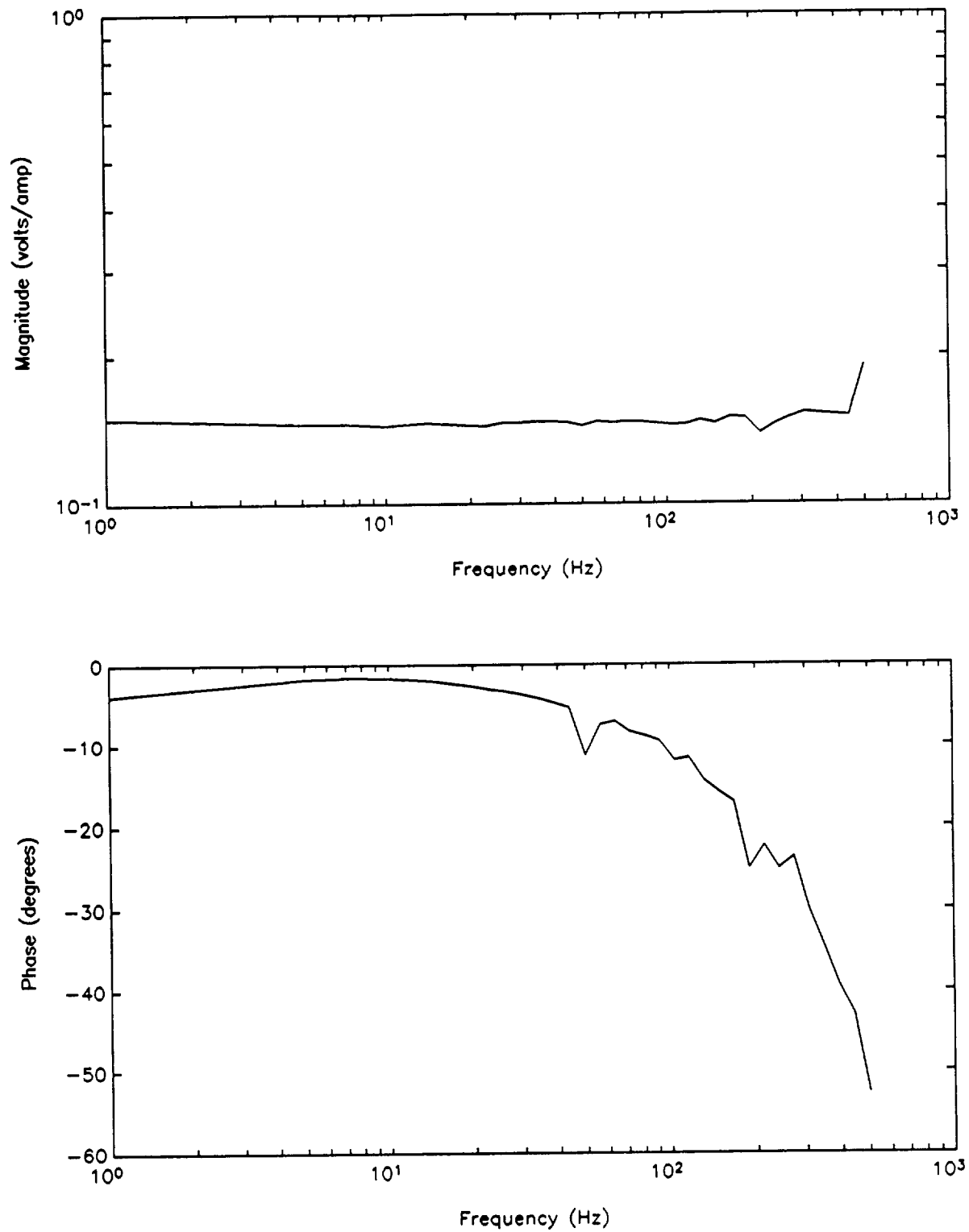


Figure 5-38. Current to flux sensor output frequency response for 100 mAmp P excitation with 0 bias (TbDy, 20 MPa, no spacer)

Figure 5-39 is a swept-sine bode plot of the displacement response to the flux sensor input. Again, the swept-sine excitation level is 0.1 Amps peak, and the actuator was preloaded to 20.6 MPa, with no spacer. The response is very flat out past 100 Hz. The dc gain is approximately 6.5×10^{-5} meters per volt.

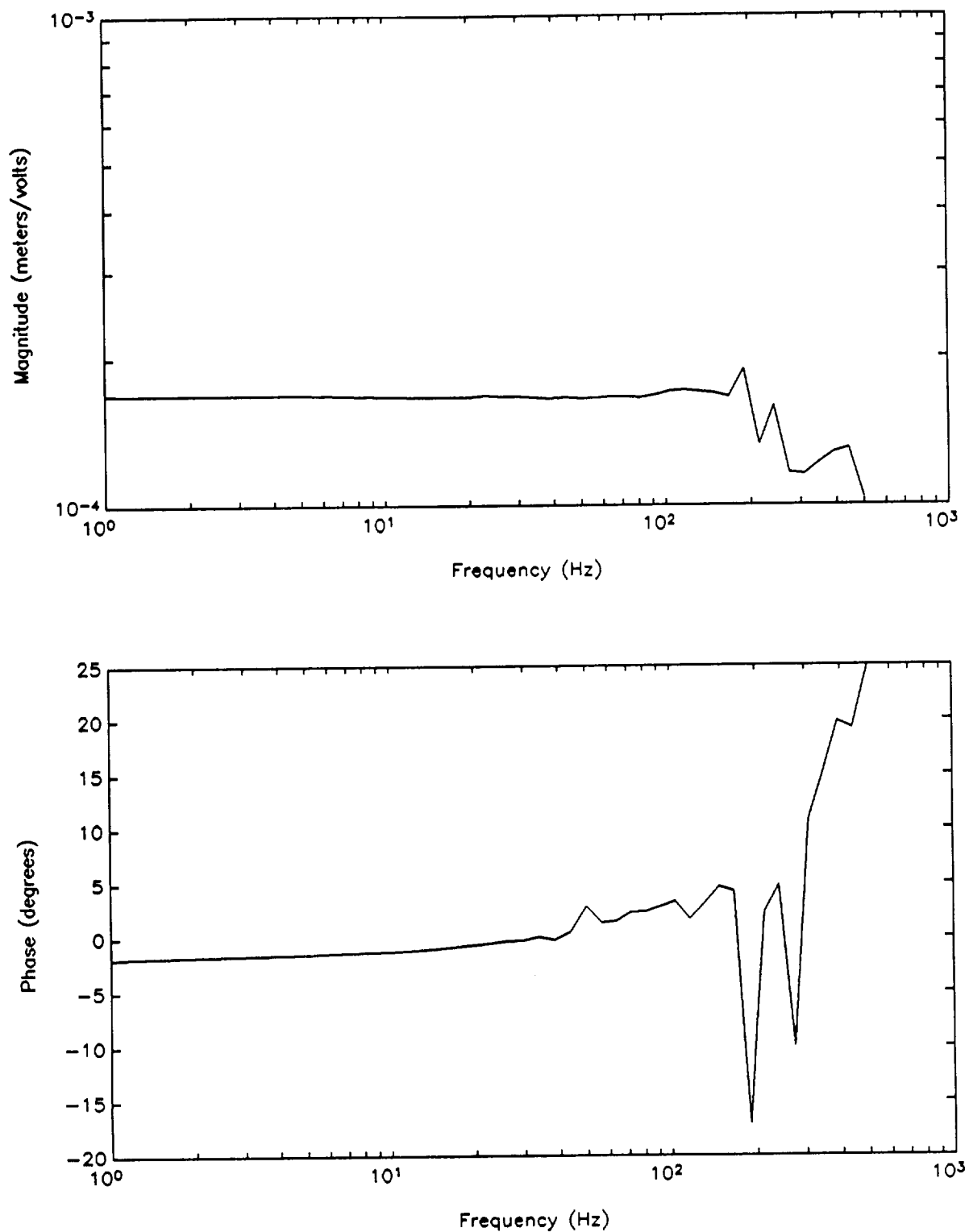


Figure 5-39. Flux sensor output to displacement frequency resonance for 100 mAmp P excitation with 0 bias (TbDy, 20 MPa, no spacer)

5.4 Cryogenic Temperature Results Analysis

This section is divided into two subsections. The first, Section 5.4.1, discusses the cryogenic Terfenol-D test results and the second, Section 5.4.2, discusses the Terbium-Dysprosium test results.

5.4.1 Results Analysis for Cryogenic Terfenol-D

As in the case of the room temperature actuator, we can predict the anhysteretic strain ϵ as a function of coil current I , by using Eq. (3-7), together with the data on $\epsilon(B)$ in Fig. 3-2, and the data on $\epsilon(H, \sigma)$ in Fig. (3-5) or Fig. (3-6), for TbDy, and Clark's unpublished data for cryogenic Terfenol-D. The parameters for the cryogenic actuator using cryogenic Terfenol-D are:

$$\begin{aligned} A_{\text{mag}} &= 1.88 \times 10^{-4} \text{ m}^2 & A_{\text{Terf}} &= 3.17 \times 10^{-5} \text{ m}^2 \\ \ell_{\text{tot}} &= 7.0 \times 10^{-2} \text{ m} & \ell_{\text{Terf}} &= 5.97 \times 10^{-2} \text{ m} \\ \ell_{\text{mag}} &= 5.84 \times 10^{-2} \text{ m} & N &= 1200 \\ r_{\text{ic}} &= 4.96 \times 10^{-3} \text{ m} & r_{\text{oc}} &= 9.14 \times 10^{-3} \text{ m} \\ B_r &= 1.0 \text{ tesla} \end{aligned}$$

The permanent magnet retentivity B_r was not actually measured at 77°K, but was estimated to be 1.0 tesla based on a guess that it would be reduced by about 10% from its room temperature value. Then Eq. (3-7) becomes (with H_{Terf} in oersted, B_{Terf} in gauss, and I in amps) seen in Figs. 5-12 and 5-13.

$$H_{\text{Terf}} + B_{\text{Terf}}/114 = 518 + 243.5I \quad (5-1)$$

The minimum strain, for any stress, should occur when $I = -518/243.5 = -2.13$ amps, close to the observed value of -2.0 amps seen in Figs. 5-12 and 5-13.

Using Clark's unpublished data for $\epsilon(H)$ and $B(H)$ at 15.5 MPa, we find fair agreement with our data (Fig 5-12) at 14 MPa at lower H , but poor agreement at higher H , where the strain continues to increase linearly with H in Clark's data, but starts to saturate in our data. However, our data at 21 MPa is in much closer agreement with Clark's data at 15.5 MPa, both at low H and high H . The reason that our cryogenic Terfenol-D does not reach full strain at 14 MPa is that this stress is not sufficient to force all of the domains to have magnetization perpendicular to the rod axis at $H = 0$. As in the case of zero stress discussed in Sec. 3.6, a substantial fraction of the domains

are still magnetized in the easy direction 35.26° from the rod axis at $H = 0$, and these domains do not contribute to the magnetostrictive strain because they are subject to 180° domain wall motion. There is direct evidence for this from inductance measurements, to be described later in this section. At 21 MPa, almost all of the domains are magnetized perpendicular to the rod axis at $H = 0$, and the full magnetostrictive strain is reached, as found by Clark at 15.5 MPa. It is possible that the transition between the two regimes occurs rapidly between 14 MPa and 15.5 MPa, or that the stress at which the transition occurs is sensitive to the processing of the Terfenol-D, but it is more likely that either we or Clark made an error in measuring the stress, and that in fact the stress is nearly the same in our tests done at a nominal stress of 21 MPa and Clark's tests done at a nominal stress of 15.5 MPa. The stress vs. strain curves at constant H in Fig. 3-7 are plotted assuming that our stress measurements are correct, but they could be off by 25% or so if Clark's stress measurement is correct.

Using Eq. (5-1) and Clark's data at 15.5 MPa, we compare the predicted $\epsilon(I)$ with our test data for $\epsilon(I)$ at 21 MPa and at 14 MPa, as was done in Table 4-2 for the room temperature actuator. The results are plotted in Table 5-4.

The outermost hysteresis loops in our strain vs. current data for cryogenic Terfenol-D have a width $\Delta I \approx 1.6$ amps, corresponding to $H_c \approx 200$ oersted, for measured stress between 14 and 28 MPa, at low B , and $\Delta I \approx 2.5$ amps, corresponding to $H_c \approx 300$ oersted, at 7 MPa and at 35 MPa and 70 MPa. Clark's data taken at 15.5 MPa (which seems to correspond to 21 MPa in our data) has $H_c \approx 300$ oersted, so it may be that our outermost hysteresis loops at 14 to 28 MPa are not truly the outer hysteresis loops. In Fig. 5-12 there is an odd glitch in the loop going between ± 3 amps which is repeatable, and which we cannot explain, but this does suggest that it may be difficult to get to the outer hysteresis loop.

Table 5-4. Predicted and observed dependence of strain on current for the cryogenic Terfenol-D actuator.

H_{Terf} (oersted)	B_{Terf} (tesla)	I (amps)	Predicted ϵ (ppm)	Observed ϵ , 14MPa	Observed ϵ , 21MPa
0	0.	-2.13	0	5	5
100	0.25	-1.63	50	40	50
200	0.37	-1.17	160	250	170
300	0.50	-0.71	340	500	350
400	0.61	-0.26	500	650	500
500	0.72	+0.19	730	820	650
600	0.80	+0.63	960	940	820
700	0.85	+1.06	1150	1020	1000
1000	1.05	+2.36	1750	1280	1520
1200	1.20	+3.20	2020	1360	1750
1900	1.30	+6.13	2450	--	--

Measurements of inductance were made for the cryogenic Terfenol-D actuator, using the method described in Sec. 4.4 for the room temperature actuator. Using Eqs. (4-3) and (4-4), with the parameters for the cryogenic Terfenol-D actuator, we find

$$L = N^2 A_{\text{Terf}} / \ell_{\text{Terf}} [(\mu_T + 4.07\mu_0)^{-1} + (100\mu_0)^{-1}] \quad (5-2)$$

Unlike the case of the room temperature actuator, the coil reluctance term, the $4.07\mu_0$ appearing in Eq. (5-2), is very important in the cryogenic actuator. It is the dominant term at low excitation amplitude, where μ_T is equal to the initial permeability μ_{rot} , which is only about $2\mu_0$, less than $4.07\mu_0$. The coil resistance R at 77°K is 1.05 ohms, and the frequency (in Hz) at which the magnitude of I/V is $\sqrt{2}/2$ times its magnitude at much lower frequency is

$$R/2\pi L = 230[(\mu_T/\mu_0 + 4.07)^{-1} + (100)^{-1}] \quad (5-3)$$

At low excitation amplitude, 0.1 amps, $\mu_T = \mu_{rot} \approx 2\mu_0$ at stresses below 35 MPa, according to Eq. (3-14), and we find $R/2\pi L = 40$ Hz, while the measured $R/2\pi L$ from Fig. 5-19 is 43 Hz. The difference could be due to the fact that the coil is about 10% shorter than the Terfenol in the cryogenic actuator, only 5.33 cm long, so the coil reluctance \mathfrak{R}_{coil} and the external reluctance \mathfrak{R}_{ext} are probably about 5% or 10% less than the expressions given by Eqs. (3-5) and (3-6), which assume that the coil is the same length as the Terfenol. This would cause $R/2\pi L$ to increase by 5% or 10%.

At higher excitation amplitude, μ_T should approach μ_{an} , and $R/2\pi L$ should be lower. Because the hysteresis is so great in cryogenic Terfenol-D, however, it would take an enormous excitation current to make μ_T close to its asymptotic value, and in any case this would be an average μ_{an} over the range of excitation, not the μ_{an} at the bias point. As a compromise, we used an excitation current of 1 amp, and measured $R/2\pi L$ at bias currents of +2 amps, 0 amps, and -2 amps, at several values of stress. From examining the minor hysteresis loops of Figs. 5-12 and 5-13, we expect that the average $\partial B/\partial H$ at 1 amp excitation, at $I_{bias} = 0$, is about twice μ_{rot} , the limiting $\partial B/\partial H$ for small amplitude excitation, so $\mu_T \approx 4\mu_0$ at stresses below 35 MPa. Putting $\mu_T = 4\mu_0$ into Eq. (5-3) yields $R/2\pi L = 31$ Hz, while the observed $R/2\pi L$ in our tests, at $I_{bias} = 0$, is 35 Hz, nearly independent of stress (see Fig 5-20). Again the small difference could be due to the coil being slightly shorter than the Terfenol. At $I_{bias} = +2$ amps, $R/2\pi L$ is observed to be 40 Hz in our test data (see Fig. 5-20), nearly independent of stress, which makes sense because μ_T should decrease slightly as B gets slightly closer to B_{sat} . The measured amplitude of I/V as a function of frequency, from which $R/2\pi L$ is derived, is shown in Fig. 5-20, for $I_{bias} = 0$ and +2 amps, at 21 MPa.

At $I = -2$ amps, corresponding to $H = 0$, on the other hand, $R/2\pi L$ is observed to be much lower, and sensitive to stress, as shown in Fig. 5-21. It is 6 Hz at zero stress, 7.5 Hz at 7 MPa, 11.5 Hz at 14 MPa, 12 Hz at 21 MPa, and 20 Hz at 35 MPa. From Eq. (5-3), these values of $R/2\pi L$ correspond to μ_T/μ_0 equal to 63, 50, 25, 23.5, and 13. These large values of $\partial B/\partial H$ near $H = 0$ are due to 180° domain wall motion, and provide a measure of the extent to which the domains have magnetization in the easy direction 35.26° from the rod axis at $H = 0$. At zero stress, as discussed in Sec. 3.6, most of the domains have magnetization in one of the easy directions 35.26° from the rod axis at $H = 0$, rather than in one of the easy directions perpendicular to the rod axis.

As H is increased, the increase in B is initially due almost entirely to 180° domain wall motion, which does not result in any change in strain. A change in I of 1 amp causes H to go to about 160 oersted, and since the average $\partial B/\partial H$ is $63\mu_0$ in this range, B must increase to 1.0 tesla, about 80% of B_{sat} . At this point there are almost no more 180° domain walls, and as H is further increased, the increase in B is due mostly to rotation of magnetization away from the easy direction toward the rod axis, and to a smaller extent to 70.52° domain wall motion, since there are a few domains magnetized perpendicular to the rod axis. These processes do result in a change in strain, but the total strain is much less than it would be if there were no 180° domain walls at low H . At 7 MPa, the average $\partial B/\partial H$ between $H = 0$ and $H = 160$ oersted is almost as great as it is at zero stress, indicating that most of the domains are still magnetized in one of the easy directions 35.26° from the rod axis at $H = 0$, and the total magnetostrictive strain should still be much less than at higher stress. A transition occurs at 14 MPa and 21 MPa. By 35 MPa, almost all of the domains are magnetized perpendicular to the rod axis at $H = 0$. If we attribute the difference in $\partial B/\partial H$ at $I_{\text{bias}} = -2A$ and $\partial B/\partial H$ at $I_{\text{bias}} = 0$ to 180° domain wall motion, then at 35 MPa the change in B between $H = 0$ and $H = 200$ oersted, due to 180° domain wall motion, is only 0.18 tesla, about 15% of B_{sat} . (As noted previously, there is some question about the accuracy of our stress measurements, and the transition which we have stated occurs around 14 to 21 MPa may actually occur around 11 to 15 MPa.) It should be possible to reach the full magnetostrictive strain at 35 MPa, although it will require higher H to reach it than at somewhat lower stress. These conclusions are consistent with our measurements of maximum strain achieved (at $I = +4$ amps, the highest current used), which increases with stress up to 21 MPa, as may be seen by comparing Figs. 5-12 and 5-13.

5.4.2. Results Analysis for Terbium-Dysprosium

For TbDy, the parameters are the same as for cryogenic Terfenol-D, except that
 $A_{\text{Terf}} = 2.98 \times 10^{-5} \text{ m}^2$ (an octagon 6 mm across)
 $\ell_{\text{Terf}} = 3.0 \times 10^{-2} \text{ m}$

With these parameters, Eq. (5-1) would become

$$H_{\text{Terf}} + B_{\text{Terf}}/63 = 1036 + 487I \quad (5-4)$$

(We still use the symbols A_{Terf} , ℓ_{Terf} , B_{Terf} and H_{Terf} , even though the material is TbDy rather than Terfenol-D.) This would result in a bias field of $H \approx 800$ oersted when $I = 0$, which is somewhat higher than desired. We therefore added a nonmagnetic spacer, of thickness $\ell_{\text{space}} = 1/32$ ", to the end of the TbDy rod, which would appear as a reluctance in series with the Terfenol in the magnetic circuit shown in Fig. 3-1,

$$\mathfrak{R}_{\text{space}} = \ell_{\text{space}} / \mu_0 A_{\text{Terf}} \quad (5-5)$$

Then the left hand side of Eq. (3-7) would have an additional term

$\pi \ell_{\text{space}} \ell_{\text{tot}} B_{\text{Terf}} / 4 \mu_0 \ell_{\text{Terf}}$, and Eq. (5-2) would become

$$H_{\text{Terf}} + B_{\text{Terf}} / 27 = 1036 + 487I \quad (5-6)$$

which would give a bias field at $I = 0$ of $H \approx 500$ oersted, right in the middle of the linear regime according to Fig. 3-5.

We measured the strain vs. current for the TbDy actuator, at a measured stress of 12.5 MPa and 20 MPa, with the spacer, and at 20 MPa without the spacer. The results are shown in Figs. 5-30, 5-31 and 5-32. Equations (5-4) and (5-6) imply that the minimum strain ($H_{\text{Terf}} = B_{\text{Terf}} = 0$) should occur when $I = -2.13$ amps, but in fact the minimum strain is observed to occur at $I = -1.75$ amps at 12.5 MPa with the spacer, at $I = -1.5$ amps at 20 MPa with the spacer, and at $I = -1.4$ amps at 20 MPa without the spacer. This implies that the permanent magnet term in Eqs. (5-4) and (5-5), 1036 oersted, should be reduced by 30% to about 750 oersted, with some minor (± 80 oersted) dependence on the permeability of the TbDy. This discrepancy did not occur in the case of the room temperature Terfenol-D or cryogenic Terfenol-D actuators, where Eq. (3-7) predicted the current at which $H_{\text{Terf}} = 0$ correctly to within 5%, so we believe that the discrepancy is due to the geometry of the TbDy actuator, which has silicon-iron extensions at the ends of the TbDy, because it was not possible to order a rod of TbDy of the same length as the rods of Terfenol-D. Evidently about 30% of the flux entering the silicon-iron extensions does not go through the TbDy, but leaks around it. In analyzing the data from TbDy, we therefore used 750 oersted instead of 1036 oersted in Eqs. (5-4) and (5-6).

Comparing our results with the TbDy data (from Spano et al) plotted in Figs. 3-2 and 3-5, we find good agreement with our data at a measured stress of 12.5 MPa and their data at 7.4 MPa, and good agreement (both with and without a spacer) between our data at a measured stress of 20 MPa and their data at 13.2 MPa. This is the same

discrepancy in stress noted in our cryogenic Terfenol-D data, and is apparently due to a problem with the calibration of our stress measurement in the cryogenic testbed. The predicted strain for 7.4 MPa and measured values of strain at a nominal stress of 12.5 MPa are shown as a function of current in Table 5-5, and similar data for the predicted strain at 13.2 MPa and the measured strain at nominal stress of 20 MPa are shown in Table 5-6. Our strain data does depart substantially from the predicted strain for B_{Teff} above a certain value, and this is obviously due to the saturation of the silicon-iron, which should occur at about 1.7 tesla. (The full saturation magnetization for silicon-iron is 2.0 tesla, but the effective saturation, when the permeability becomes less than that of TbDy, occurs at about 85% of the full saturation, when there is no more domain wall motion and the permeability is due entirely to domain rotation.) To zero order we would expect the B in the silicon-iron to be the same as the B in the TbDy, so that the sharp break in the strain vs. current data should occur when $B_{\text{Teff}} = 1.7$ tesla. In fact, the break occurs at $B_{\text{Teff}} \approx 1.4$ tesla, which indicates that B_{Teff} (the B in the TbDy) is about 20% less than B in the silicon-iron, in qualitative agreement with the 30% flux leakage inferred from the I required to obtain $H_{\text{Teff}} = 0$.

Examination of the minor hysteresis loops in Figs. 5-30, 5-31 and 5-32 shows that, for TbDy, the initial permeability μ_{rot} is equal to about half of the total permeability, for B well below saturation. This result (not previously reported in the literature, to our knowledge) implies that rotation and domain wall motion make approximately equal contributions to the permeability. In this respect TbDy at 77° K resembles room temperature Terfenol-D rather than cryogenic Terfenol-D, because TbDy, with its hexagonal crystal structure, has a much lower anisotropy (in the basal plane) than cryogenic Terfenol-D at 77° K.

The outer hysteresis loops of the strain vs. current data for TbDy have width $\Delta I \approx 0.10$ amps when there is a spacer, and $\Delta I \approx 0.15$ amps when there is no spacer, corresponding to $H_c \approx 15$ oersted in both cases, in agreement with the data of Spano, et al. shown in Fig. 3-5.

Table 5-5. Comparison of predicted strain at 13.2 MPa with measured strain at nominal stress of 20 MPa, with and without a spacer.

H_{Terf} (Oe)	B_{Terf} (tesla)	predicted ϵ (ppm)	I (amps) with spacer	I (amps) no spacer	measured ϵ (ppm) with spacer	measured ϵ (ppm) no spacer
0	0	0	-1.54	-1.54	0	100
100	0.23	170	-1.16	-1.23	130	200
200	0.46	550	-0.78	-0.92	750	650
300	0.80	1250	-0.32	-0.66	1500	1250
400	1.20	2150	+0.19	-0.33	2100	2000
500	1.50	2800	+0.63	-0.02	2600	2350
600	1.80	3300	+1.06	+0.28	2750	2700
700	2.10	3850	+1.49	+0.58	2900	3100
800	2.40	4300	+1.93	+0.88	3000	3250

Inductance data was taken for TbDy, at an excitation amplitude of 100 mA, and a few different bias currents, for the three cases shown in Tables 5-5 and 5-6, i.e. at a nominal stress of 20 MPa without a spacer, and at nominal stress of 20 MPa and 12.5 MPa with a spacer and is shown in Fig. 5-36. Data was also taken at an excitation amplitude of 1 amp, at a nominal stress of 20 MPa without a spacer, for a few different values of bias current shown in Fig. 5-35. If there is no spacer, then Eq. (4-3) applies, and we may derive an expression for $R/2\pi L$, similar to Eq. (4-6) and Eq. (5-3). The same coil and permanent magnets were used for TbDy as for the cryogenic Terfenol-D, and the cross-sectional area of the rod A_{Terf} is nearly the same. The only difference between the cryogenic Terfenol-D and the TbDy is that the length of the rod, ℓ_{Terf} , is 5.9 cm in the case of cryogenic Terfenol-D but only 3.0 cm in the case of TbDy. Then, instead of Eq. (5-3), we have

$$R/2\pi L = 115[(50)^{-1} + (\mu_T/\mu_0 + 4.07)^{-1}] \quad (5-7)$$

If there is a spacer, then $\mathfrak{R}_{\text{Terf}}$ in Eq. (4-3) must be replaced by $\mathfrak{R}_{\text{Terf}} + \mathfrak{R}_{\text{space}}$. Then Eq. (5-7) becomes

$$R/2\pi L = 115\{(50)^{-1} + [(\mu_0/\mu_T + \ell_{\text{space}}/\ell_{\text{Terf}})^{-1} + 4.07]^{-1}\} \quad (5-8)$$

Table 5-6. Comparison of predicted strain at 7.4 MPa with measured strain at nominal stress of 12.5 MPa, with a spacer.

H_{Terf} (Oe)	B_{Terf} (tesla)	predicted ϵ (ppm)	I (amps)	measured ϵ (ppm)
0	0	0	-1.54	50
100	0.37	300	-1.05	200
200	0.74	900	-0.56	800
300	1.12	1500	-0.07	1350
400	1.47	2100	+0.40	1700
500	1.79	2650	+0.85	1850
600	2.11	3200	+1.30	1950

For excitation amplitude much greater than the width of the hysteresis loop, μ_T should be the anhysteretic permeability, which is $37\mu_0$ at low B at the lower stress (12.5 MPa according to our measurement, but apparently corresponding to 7.4 MPa in the data of Fig. 3-5), and $23\mu_0$ at low B at the higher stress (20 MPa according to our measurement, corresponding to 13.2 MPa in Fig. 3-5). Then, at I_{bias} between -1 and -2 amps, we expect

$$R/2\pi L = 7.35 \text{ Hz}$$

at a nominal stress of 12.5 MPa with a spacer,

$$R/2\pi L = 8.56 \text{ Hz}$$

at a nominal stress of 20 MPa with a spacer, and

$$R/2\pi L = 6.55 \text{ Hz}$$

at a nominal stress of 20 MPa without a spacer. Since the width of the hysteresis loop is 0.1 or 0.15 amps, we would want to use an excitation amplitude of about 1 amp, and for this excitation amplitude we have data only for the last case. The measured $R/2\pi L$ is 4.0 Hz, which is within a factor of 2 of our prediction, but not nearly as close to the predicted value as was the case for the inductance measurements of room temperature and cryogenic Terfenol-D. As in the case of the predictions of strain vs. current, we believe that the discrepancy is due to the peculiar geometry of the TbDy actuator, with its silicon-iron extensions compensating for the shorter length of the TbDy rod. A more accurate prediction could probably be obtained by numerically solving for the fields in this geometry.

Inductance data at an excitation amplitude of 0.1 amp was taken for all three cases, at $I_{\text{bias}} = -2$ amps. Using our usual criterion of defining R/L as the frequency at which I/V falls to $\sqrt{2}/2$ of its amplitude at much lower frequency, as explained in Sec. 4.4, our data give (see Fig 5-36)

$$R/2\pi L = 3.7 \text{ Hz}$$

at a nominal stress of 12.5 MPa with a spacer,

$$R/2\pi L = 5.3 \text{ Hz}$$

at a nominal stress of 20 MPa with a spacer, and

$$R/2\pi L = 3.2 \text{ Hz}$$

at a nominal stress of 20 MPa without a spacer. The ratios of the values of $R/2\pi L$ are nearly the same as the ratios of the predicted values for 1 amp excitation. We note that in the last case, the measured $R/2\pi L$ at 0.1 amps excitation, 3.2 Hz, is less than the measured $R/2\pi L$ at 1 amp, 4.0 Hz, and at first this seems surprising, since we would expect μ_T to be lower at lower excitation amplitude, approaching μ_{rot} for sufficiently small excitation, and this should result in higher $R/2\pi L$. Since μ_{rot} is about half of the anhysteretic permeability for TbDy, we would expect $R/2\pi L$ to be somewhat less than twice as great at very small excitation amplitude (much less than 0.1 amp) as at large excitation amplitude (much greater than 0.1 amp). However, at an excitation of 0.1 amp, comparable to the width of the hysteresis loop, there is a large phase shift between B and H due to hysteresis, and L has a large imaginary part, comparable to its real part. In this case, it is no longer true that I/V falls to $\sqrt{2}/2$ of its low frequency amplitude when $\omega = R/L$. Rather, I/V falls more than this at $\omega = R/L$, because $j\omega L$ and R are now less than 90° apart in phase. This explains why, using our usual criterion for

defining R/L in terms of the decrease in amplitude of I/V , we would obtain a slightly lower value of R/L at 0.1 amp excitation than at 1 amp excitation.

A better estimate of R/L at 0.1 amp excitation might be made by defining R/L as the frequency at which the phase of I/V changes by 45° from its value at much lower frequency. In this case we find (from Fig. 5-36)

$$R/2\pi L = 5.5 \text{ Hz}$$

at a nominal stress of 20 MPa with no spacer, which is greater than the value of 4.0 Hz found (with either definition of R/L) with 1 amp excitation, as expected. We also find

$$R/2\pi L = 6.5 \text{ Hz}$$

at a nominal stress of 20 MPa with a spacer, and

$$R/2\pi L = 4.5 \text{ Hz}$$

with a nominal stress of 12.5 MPa with a spacer. With either definition, we would expect to find higher R/L at excitation amplitude much less than 0.1 amp, where hysteresis is very small.

At $I_{\text{bias}} \geq 0$, we find higher R/L in all cases, as expected, because the permeability of the TbDy is lower at higher values of B_{Teff} . In addition, the silicon-iron starts to saturate at these values of I_{bias} , and this increases R/L even more. In the case of a nominal stress of 20 MPa with no spacer, and an excitation amplitude of 1 amp, for example, $R/2\pi L = 4.0 \text{ Hz}$ at $I_{\text{bias}} = -2 \text{ amps}$ and -1.5 amps , as noted above, but $R/2\pi L = 7.5 \text{ Hz}$ at $I_{\text{bias}} = 0$, and $R/2\pi L = 38 \text{ Hz}$ at $I_{\text{bias}} = +2 \text{ amps}$ (well into the regime where the silicon-iron is saturated).

6. CONCLUSIONS AND RECOMMENDATIONS

This Phase II SBIR program developed room temperature and cryogenic temperature magnetostrictive active members for space structure control. One of the goals of this program is to compare the performance of these magnetostrictive active members with similarly sized piezoelectric and electrostrictive active members developed at JPL. This section briefly summarizes what was accomplished during this program, compares the magnetostrictive actuator performance to piezoelectric and electrostrictive alternatives, and discusses recommendations for future development efforts.

6.1 Summary of Results

The following important milestones were established by this project.

- 1) Design, fabrication, test, and delivery of a room temperature magnetostrictive active member whose performance can be directly compared with existing JPL active members that use alternative actuators.
- 2) Design, fabrication, and test of the first cryogenic temperature magnetostrictive active member. This active member, and its associated cryostat, can be used in ground based space structure testbeds, such as those at JPL. This provides the ability to both demonstrate the technical feasibility of using cryogenic temperature active members and investigate their performance directly in a space structure.
- 3) The first use of Terbium-Dysprosium in a magnetostrictive actuator.
- 4) Improvements in magnetostrictive actuator design and analysis tools, especially in the areas of hysteresis prediction and cryogenic temperature operation.

The magnetostrictive active members performed close model predictions. The test results are summarized in Tables 6-1 through 6-3 below. In general the magnetostrictive active members have higher stiffnesses and produce larger strains than the piezoelectric and electrostrictive active members. This occurs at a cost of higher mass but with lower amplifier volt-amp requirements. These comparisons can be seen

in Table 6-4. The piezoelectric (PZT) and electrostrictive (PMN) results are taken from Anderson et al¹. All hysteresis and drive currents and voltages are at 5 Hz for the magnetostrictive actuators. The hysteresis values are at 1 Hz for the PZT and PMN. The amplifier current values are at 25 Hz for the PZT and PMN. Values for the TbDy active member assume a full length (5.9 cm) crystal. Values for the magnetostrictive active members are the nominal, not the maximum achievable except where noted. The lowest values have been used for the magnetostrictive material stiffnesses.

¹ Anderson, E.H., Moore, D.M., Fanson, J.L., and M.A. Ealey, "Development of an Active Member Using Piezoelectric and Electrostrictive Actuation for Control of Precision Structures.", 31st Structural Dynamics and Materials Conference, Long Beach, CA, April 1990.

Table 6-1. Room temperature Terfenol-D performance

	Nominal (± 2 Amps)	Maximum (± 4 Amps)
Free Stroke (microns)	50	65
Free Strain (microstrain)	800	1150
Clamped Force (N)		
Predicted	1000	1500
Extrapolated from "clamped" data	≈ 650	
Clamped Stress (MPa)	17	24
Actuator Stiffness (MN/m)		
Predicted (Material)	28 - 48	
Measured ²	> 10	
Material Modulus (GPa)	23 - 40	
Resistance (Ohms)	2.3	
Inductance (milliHenries)	5 - 10	
Break Frequency (Hz)	55 - 90 Hz	
Coil # of Turns	800	
Power (peak - Watts)	9.2	37

²Not very accurately.

Table 6-2 Cryogenic Terfenol-D performance.

	Nominal (± 2 Amps)	Maximum (± 4 Amps)
Free Stroke (microns)	42	95
Free Strain (microstrain)	750	1650
Clamped Force (Newtons)	540	770
Clamped Stress (MPa)	17	24
Stiffness (MN/m)	18-42	
Material Modulus (GPa)	33 - 77	
Resistance (Ohms)	1.05	
Inductance (milliHenries)	4 - 5	
Break Frequency (Hz)	35 - 45 Hz	
Coil # of Turns	1200	
Power (peak - Watts)	4.2	17

Table 6-3. Cryogenic TbDy performance.

	Nominal (± 1.5 Amps)	Maximum (± 4 Amps)
Free Stroke (microns)	105	120
Free Strain (microstrain)	3500	4000
Clamped Force ³ (Newtons)	750	750
Clamped Stress (MPa)	25	25
Stiffness (MN/m)	14 - 20	
Material Modulus (GPa)	14 - 20	
Resistance (Ohms)	1.05	
Inductance (milliHenries)	12 - 23	
Break Frequency (Hz)	7.3 - 14	
Coil # of Turns	1200	
Power (peak - Watts)	2.4	17

³Clamped force and stress limited by material strength ≈ 25 MPa.

Table 6-4. Comparison of active members.

Property	PZT	PMN	R.T. Terfenol-D	Cryo. Terfenol-D	Cryo TbDy
Displacement [μm] ¹	63.4	39.5	50 (65)	42 (95)	205 (240) ⁴
Force [N] ⁵	505	455	1000	540	750 ⁶
Hysteresis [percent] ⁷	16.0	1.2	16 (4)	31 (16)	5.3 (1.7)
Stiffness ¹ [N/ μm]	14.6	9.75	28	18	14
Mass [grams]	240	190	457	500	495
Maximum Operating Voltage [V] ²	1000	300	5.5	2.1	1.6
Normal Bias Voltage [V]	500	150	0	0	0
Current [amps peak] ⁸	0.046	0.180	2	2	1.5
Peak V-A (volt-amps) ⁹	46	54	11	4.2	2.4

Notes for Table 6-4.

1. At 1 Hz for PZT and PMN, at 5 Hz for magnetostrictives. Value in parenthesis for magnetostrictive is for maximum excitation. Other value is for nominal excitation.
2. Assumes full length TbDy rod.
3. At 1 Hz for PZT and PMN, at 5 Hz for magnetostrictives. Clamped force predicted for magnetostrictives at nominal excitation.
4. Limited by material yielding.
5. Maximum width of displacement loop divided by peak-to-peak displacement. At 1 Hz for PZT and PMN, at 5 Hz for magnetostrictives. Measured between voltage and displacement for PZT and PMN. Measured between current and displacement for magnetostrictives. Values for magnetostrictives in parentheses are between measured flux and displacement.
6. Short circuit for PZT and PMN. Lowest value for magnetostrictives.
7. Below R/L break frequency for magnetostrictives, which ranges from 10 to 70 Hz for the different magnetostrictive actuators.
8. At 25 Hz for PZT and PMN.
9. At 25 Hz for PZT and PMN. At low frequencies below R/L break for magnetostrictives. This is approximately 10 Hz for cryogenic active members, over 50 Hz for room temperature magnetostrictive active member.

6.2 Recommendations for Future Research

This program has successfully demonstrated the feasibility of using magnetostrictive actuators in active members, both at room and cryogenic temperatures. A number of follow-on research paths are indicated by this work. These include:

1. Demonstration and performance testing of the room temperature and cryogenic temperature active members in a ground-based space structure testbed.
2. Demonstration of flux-feedback operation of these active members, to reduce hysteresis effects.
3. Integration of magnetostrictive actuator design tools into space structure system trade-off models. This would allow control-structure interaction (CSI) researchers to investigate the system level tradeoffs between alternative actuators.
4. Development of a passive magnetostrictive active member.
5. Investigation of the use of Holmium to decrease hysteresis in cryogenic temperature Terfenol-D and increase permeability in TbDy.
6. Development and demonstration of a superconducting magnetostrictive actuator, ideally using high-temperature superconductors.

Appendix A - Room Temperature Active Member Drawing Package

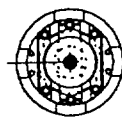
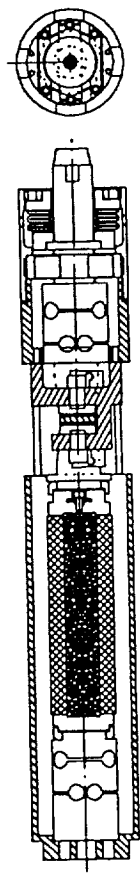
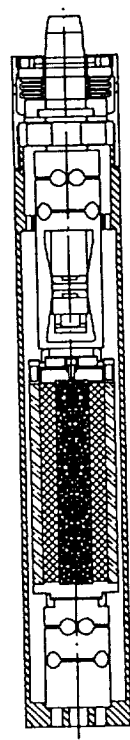
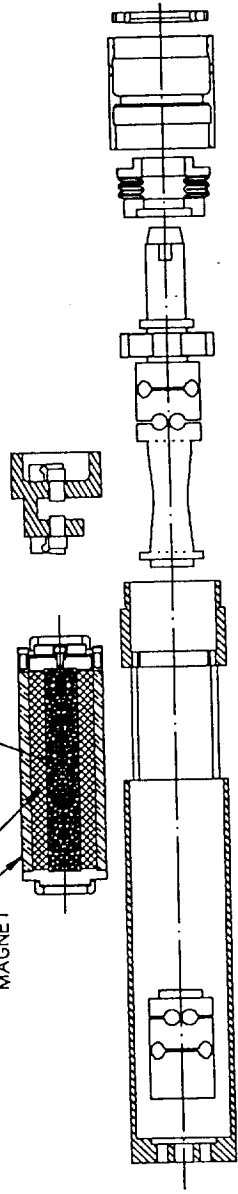
Title	No.
Layout - Actuator	1037300
End Cap - Live End Active Member	1037200
Preload Nut	1037201
Sensor Clip	1037202
Alignment Insert	1037203
Crush Washer	1037204
Crush Washer Terfenol	1037205
Magnet	1037206
Terfenol	1037207
Mount 1 Terfenol	2037208
Washer Shoulder	1037209
Washer Flat	1037210
Magnet Support Upper	1037211
Strap Magnet Support Upper	1037212
Clamp Flexure	1037213
Flexure	1037214
Housing Active Member	1037301
Flexure - Long Active Member	1037302
Flexure - Short Active Member	1037303
Preload Spring	1037304
Sensor Cage	1037305
Layout - Actuator	1037306
Mount 2 Terfenol	1037307
Flexure - Long Modified	1037310

1 2 3 4

REVISIONS		DWG	CHK	APPL	DATE
REV	DESCRIPTION				

COIL
PERMANENT
MAGNET

TERFENOL



DWG. NO. 1037300
SH

		LAYOUT - ACTUATOR		REV
		SIZE C	FSCM NO. 1037300	3
CONTRACT NO. DRAWN K. AVAKIAN 17OCT81 CHECKED ENGINEER APPROVED SATCON APPROVED		SCALE 1/1 SHEET 1		
UNLESS OTHERWISE SPECIFIED CAPACITOR VALUES ARE IN OHMS RESISTOR VALUES ARE IN OHMS DIMENSIONS ARE IN INCHES TOLERANCE ON DECIMALS .XX ± .01 ANGLES ± .5 .XXX ± .005 DO NOT SCALE THIS DRAWING WATER		NEXT ASSY USED ON APPLICATION		

JAN 20 1992

4 3 1

DWG. NO.
1037201

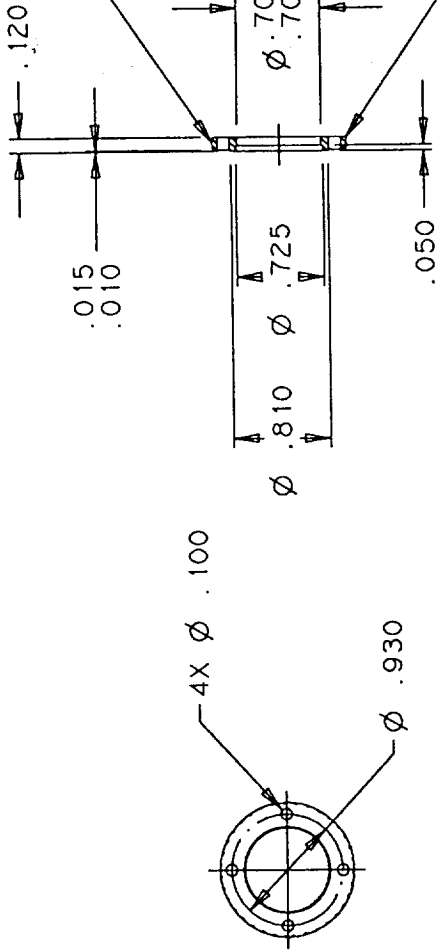
SH
1

REVISIONS

REV	DESCRIPTION	DWN	CHK	APPVL/DATE
A	INITIAL RELEASE PER ECR 91024	KMARF		86J/08NOV91

NOTES:
1. FINISH ALL OVER $\sqrt{32}$

2. REMOVE BURRS AND BREAK SHARP EDGES .01 MAX



SatCon
Technology Corporation

PRELOAD NUT

UNLESS OTHERWISE SPECIFIED CAPACITOR VALUES ARE IN RESISTOR VALUES ARE IN OHMS DIMENSIONS ARE IN INCHES TOLERANCE ON		CONTRACT NO.	
DECIMALS	ANGLES	DRAWN	K AVAKIAN 07OCT91
.XX \pm .01	\pm °	CHECKED	R FENN 08NOV91
.XXX \pm .005		ENGINEER	R FENN 08NOV91
DO NOT SCALE THIS DRAWING		APPROVED	B JOHNSON 08NOV91
MATERIAL		APPROVED	
		SATCON APPROVED	
NEXT ASSY	USED ON	SIZE	FSCM NO.
APPLICATION		B	1037201
		SCALE	1/1
		SHEET	1

4 3 2 1

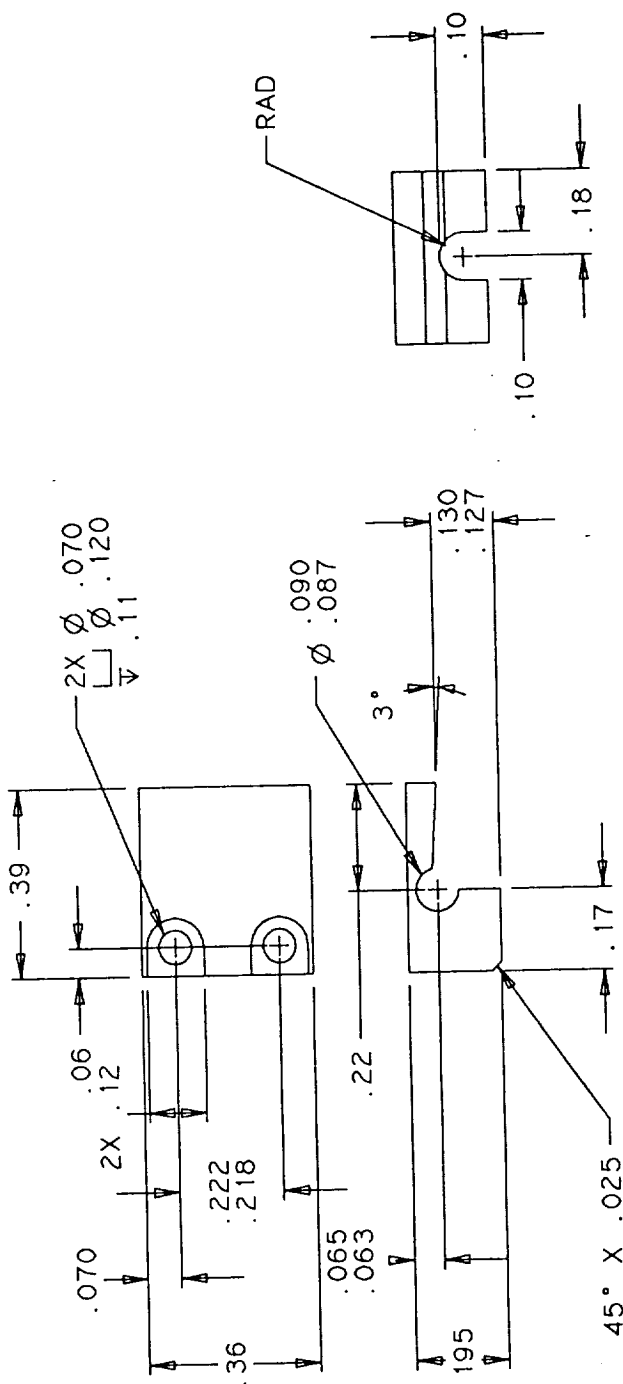
DWG. NO.	SH				
1037202	1				
REVISIONS					
REV	DESCRIPTION		DWN	CHK	APPLV./DATE
A	INITIAL RELEASE PER ECR 91024		KMA	RF	BGJ/08NOV91

REV	DESCRIPTION	DWN	CHK	APPVL/DATE
A	INITIAL RELEASE PER ECR 91024	KMA	RF	BGJ/08NOV81

REV	DESCRIPTION	DWN	CHK	APPVL/DATE
A	INITIAL RELEASE PER ECR 91024	KMA	RF	BGJ/08NOV81

NOTES:

- ES:
1. FINISH ALL OVER $\bigtriangledown^{32/}$
 2. REMOVE BURRS AND BREAK SHARP EDGES .01 MAX

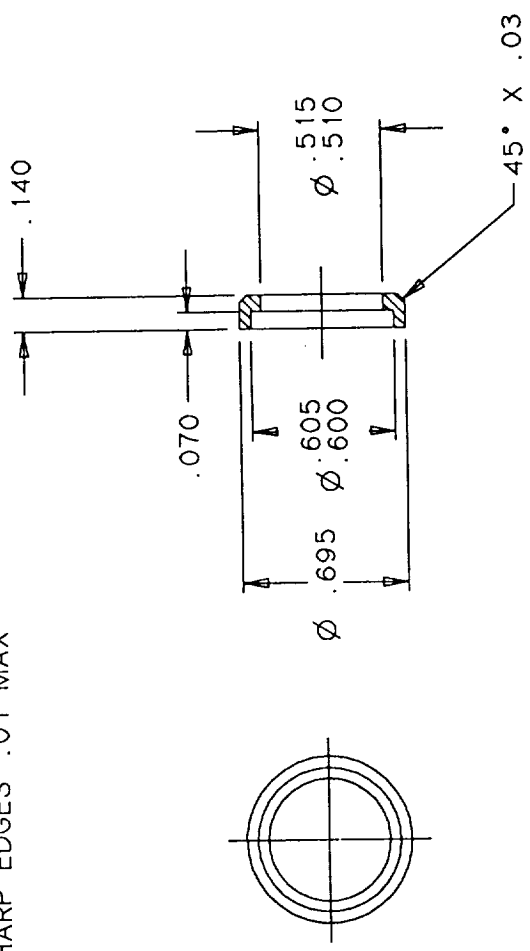
[illegible]

DWG. NO.	SH	1	1
1037203			

REVISIONS			
REV	DESCRIPTION	DWN	CHK APPVL/DATE
A	INITIAL RELEASE PER ECR 91024	KMARF	BGJ/08NOV91

NOTES: 32/

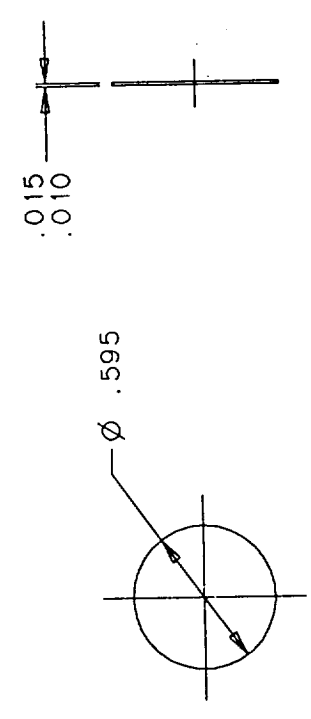
1. FINISH ALL OVER
2. REMOVE BURRS AND BREAK SHARP EDGES .01 MAX



UNLESS OTHERWISE SPECIFIED CAPACITOR VALUES ARE IN OHMS RESISTOR VALUES ARE IN OHMS DIMENSIONS ARE IN INCHES TOLERANCE ON		CONTRACT NO.		SatCon Technology Corporation	
		DRAWN	K AVAKIAN	16OCT91	
DECIMALS		CHECKED	R FENN	08NOV91	
ANGLES		ENGINEER	R FENN	08NOV91	
.XX ± .01 .XXX ± .005		APPROVED B JOHNSON		08NOV91	
DO NOT SCALE THIS DRAWING		APPROVED			
MATERIAL		SATCON APPROVED			
DELTRIN					
NEXT ASSY	USED ON	FSCM NO.		DRAWING NO.	REV
APPLICATION		B		1037203	A
		SCALE		2/1	SHEET 1

REVISIONS				
REV	DESCRIPTION	DWN	CHK	APPVL/DATE
A	INITIAL RELEASE PER ECR 91024	KMARF		BGJ/08NOV91

- NOTES:
1. FINISH ALL OVER $\sqrt[32]{}$
 2. REMOVE BURRS AND BREAK SHARP EDGES .01 MAX
 3. MATERIAL: ALUM 1100-0 DEAD SOFT CONDITION



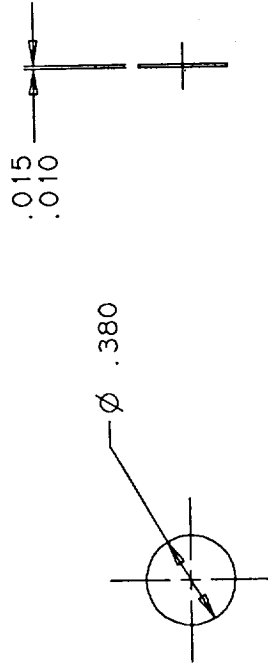
UNLESS OTHERWISE SPECIFIED DIMENSIONS ARE IN INCHES TOLERANCES ARE IN INCHES		CONTRACT NO.		SatCon Technology Corporation	
		DRAWN K AVAKIAN 16OCT91		CRUSH WASHER	
DECIMALS		CHECKED R FENN 08NOV91		SIZE FSCM NO.	
ANGLES		ENGINEER R FENN 08NOV91		DRAWING NO.	
.XX ± .01		APPROVED B JOHNSON 08NOV91		1037204	
.XXX ± .005		APPROVED		REV	
DO NOT SCALE THIS DRAWING		SATCON APPROVED		A	
MATERIAL		SEE NOTE 3		SCALE 2/1	
NEXT ASSY		USED ON		SHEET 1	
APPLICATION					

DWG. NO.	SH	1
1037205		

REVISIONS			
REV	DESCRIPTION	DWN	CHK
A	INITIAL RELEASE PER ECR 91024	KMA	TH
		BG/08NOV91	

NOTES:

1. FINISH ALL OVER $\sqrt{32}$
2. REMOVE BURRS AND BREAK SHARP EDGES .01 MAX
3. MATERIAL: ALUM 1100-0 DEAD SOFT CONDITION



UNLESS OTHERWISE SPECIFIED CAPACITOR VALUES ARE IN OHMS RESISTOR VALUES ARE IN OHMS DIMENSIONS ARE IN INCHES TOLERANCE ON		CONTRACT NO.	
DECIMALS	ANGLES	DRAWN	K AVAKIAN 06NOV91
.XX ± .01	± -	CHECKED	T HAWKEY 08NOV91
.XXX ± .005		ENGINEER	T HAWKEY 08NOV91
DO NOT SCALE THIS DRAWING		APPROVED	B JOHNSON 08NOV91
MATERIAL		APPROVED	SATCON APPROVED
SEE NOTE 3			
NEXT ASSY	USED ON	SIZE	FSCM NO.
APPLICATION		B	1037205
		SCALE	2/1
			SHEET 1

SATCON
Technology Corporation

CRUSH WASHER
TERFENOL

NOV 12 1991

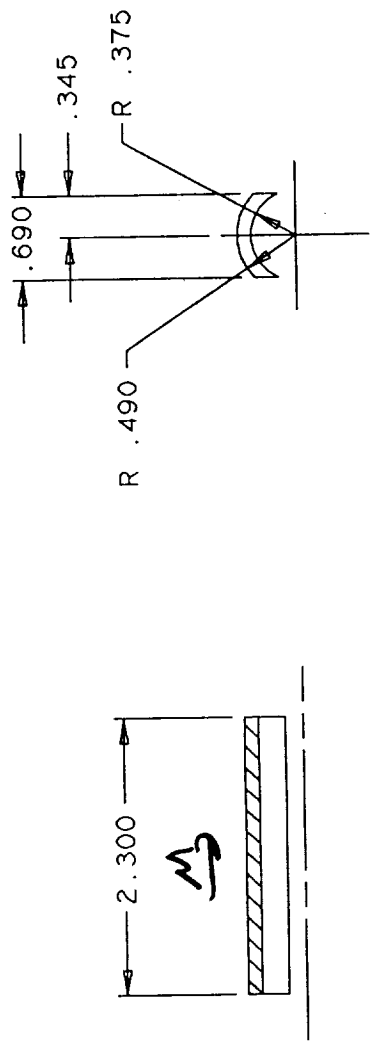
4 3 1

DWG. NO. 1037206 SH 1

REVISIONS			
REV	DESCRIPTION	DWN	CHK
A	INITIAL RELEASE PER ECR 91024	KMA	TH
			APPVL/DATE
			BGJ/08NOV91

NOTES: 32/

1. FINISH ALL OVER
2. REMOVE BURRS AND BREAK SHARP EDGES .01 MAX
3. RUST PROTECT



SATCON Technology Corporation

MAGNET

UNLESS OTHERWISE SPECIFIED CAPACITOR VALUES ARE IN INCHES RESISTOR VALUES ARE IN OHMS DIMENSIONS ARE IN INCHES TOLERANCE ON		CONTRACT NO.	
DECIMALS		DRAWN K AVAKIAN 23OCT91	
ANGLES		CHECKED T HAWKEY 08NOV91	
.XX ± .01		ENGINEER T HAWKEY 08NOV91	
.XXX ± .005		APPROVED B JOHNSON 08NOV91	
DO NOT SCALE THIS DRAWING		APPROVED	
MATERIAL		SATCON APPROVED	
Nd Fe35			
NEXT ASSY USED ON			
APPLICATION			

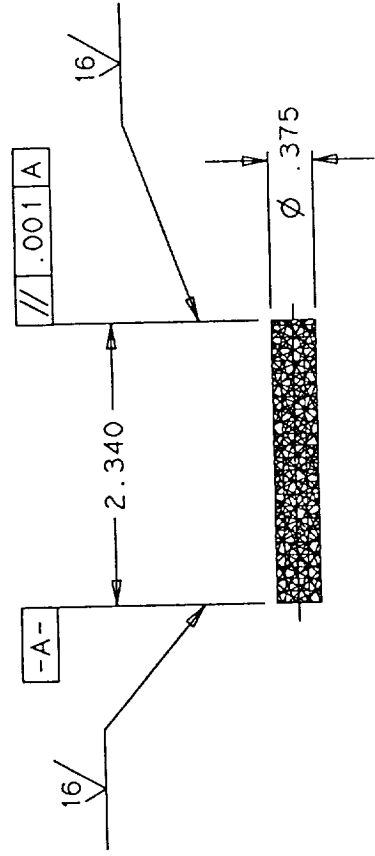
SIZE	FSCM NO.	DRAWING NO.	REV
B		1037206	A
SCALE	1/1		SHEET 1

4 3 2 1

NOV 12 1991

DWG. NO.		1037207		SH	1
REVISIONS					
REV	DESCRIPTION			DWN	CHK
A	INITIAL RELEASE PER ECR91023			KMATJH	0610 NOV91

- NOTES:
1. FINISH ALL OVER $\sqrt{32}$ EXCEPT AS NOTED
 2. REMOVE BURRS AND BREAK SHARP EDGES .01 MAX



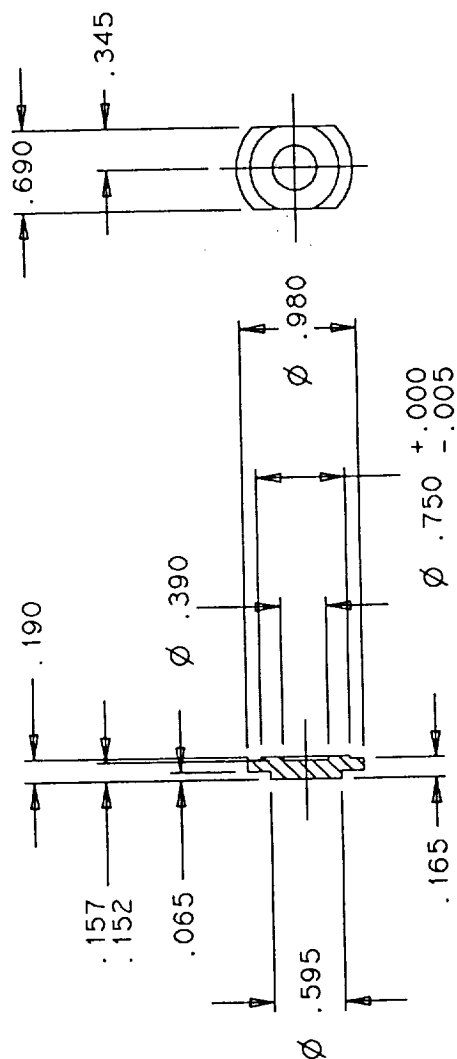
UNLESS OTHERWISE SPECIFIED CAPACITOR VALUES ARE IN OHMS RESISTOR VALUES ARE IN OHMS DIMENSIONS ARE IN INCHES TOLERANCE ON		CONTRACT NO.		SatCon Technology Corporation	
DECIMALS	ANGLES	DRAWN	K AVAKIAN	24OCT91	TERFENOL
.XX ± .01	± -	CHECKED	T HAWKEY	01NOV91	
.XXX ± .005		ENGINEER	T HAWKEY	01NOV91	
DO NOT SCALE THIS DRAWING		APPROVED	B JOHNSON	01NOV91	
MATERIAL		APPROVED		SATCON APPROVED	
TERFENOL		APPROVED		SATCON APPROVED	
NEXT ASSY		USED ON		APPLICATION	
APPLICATION		APPLICATION		APPLICATION	
SIZE		FSCM NO.		DRAWING NO.	
B				1037207	
REV		A		REV	
A		A		A	
SCALE		1/1		SHEET	
1		1		1	

4

1037208	REVISONS			
REV	DESCRIPTION	DWN	CHK	APPVL/DATE
A	INITIAL RELEASE PER ECR 91024	KMA	TH	BGJ/08NOV91

NOTES:

- ES:
- | | | | |
|----|------------------------------------|----------|-----|
| 1. | FINISH ALL OVER | 32/ | ✓ |
| 2. | REMOVE BURRS AND BREAK SHARP EDGES | .01 | MAX |
| 3. | HEAT TREAT PER DRAWING NO. | 1009-107 | |
| 4. | BLACK OXIDE AFTER HEAT TREAT | | |

[illegible]

1

NOV 12 1991

4

3

DWG. NO.
1037209SH
1

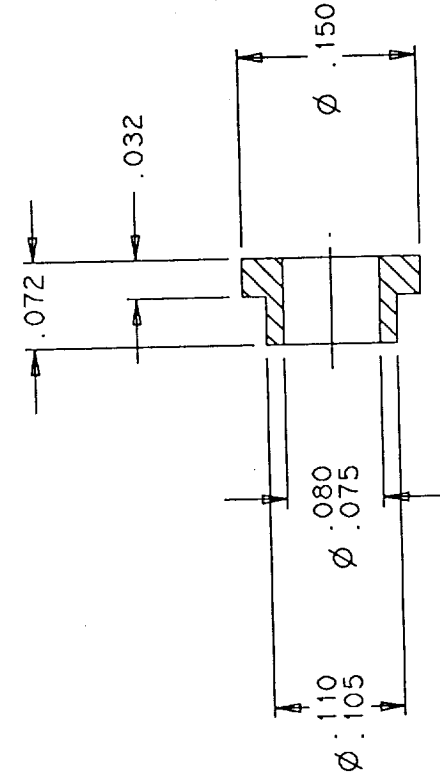
1

REVISIONS

REV	DESCRIPTION	DWN	CHK	APPLV/DATE
A	INITIAL RELEASE PER ECR 91024	KMA	TH	BGJ/08NOV91

NOTES:

1. FINISH ALL OVER $\sqrt{32}$
2. REMOVE BURRS AND BREAK SHARP EDGES .01 MAX

SatCon
Technology CorporationWASHER
SHOULDERUNLESS OTHERWISE SPECIFIED
CAPACITOR VALUES ARE IN OHMS
RESISTOR VALUES ARE IN OHMS
DIMENSIONS ARE IN INCHES
TOLERANCE ONDECIMALS ANGLES
.XX ± .01 ±
.XXX ± .005 ±

DO NOT SCALE THIS DRAWING

MATERIAL

ST ST TYPE
303 OR EQUIV
(NON-MAGNETIC)

NEXT ASSY USED ON

APPLICATION

CONTRACT NO.

DRAWN K AVAKIAN 28OCT91

CHECKED T HAWKEY 08NOV91

ENGINEER T HAWKEY 08NOV91

APPROVED B JOHNSON 08NOV91

APPROVED

SATCON APPROVED

SIZE FSCM NO. DRAWING NO. REV

B 1037209 A

SCALE 10/1 SHEET 1

3

2

1

4

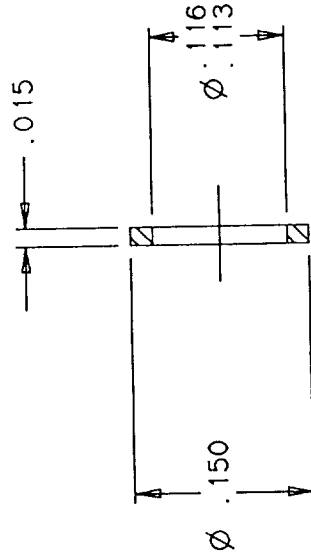
NOV 12 1991

4 3 1

DWG. NO. 1037210 SH 1

REVISIONS			
REV	DESCRIPTION	DWN	CHK
A	INITIAL RELEASE PER ECR 91024	KMA	TH
		APPVL/DATE	
		BGJ/08NOV91	

- NOTES:
1. FINISH ALL OVER $\sqrt{32}$
 2. REMOVE BURRS AND BREAK SHARP EDGES .01 MAX



SatCon
Technology Corporation

WASHER
FLAT

CONTRACT NO.	
DRAWN	K AVAKIAN 28OCT91
CHECKED	T HAWKEY 08NOV91
ENGINEER	T HAWKEY 08NOV91
APPROVED	B JOHNSON 08NOV91
APPROVED	
SATCON APPROVED	

UNLESS OTHERWISE SPECIFIED
DIMENSIONS ARE IN INCHES
TOLERANCE ON

DECIMALS ANGLES
.XX ± .01 ± °
.XXX ± .005

DO NOT SCALE THIS DRAWING

MATERIAL
ST ST TYPE
303 OR EQUIV
(NON-MAGNETIC)

SIZE	FSCM NO.	DRAWING NO.	REV
B		1037210	A
SCALE 10/1		SHEET 1	

4 3 2 1

NOV 12 1991

4 3 1

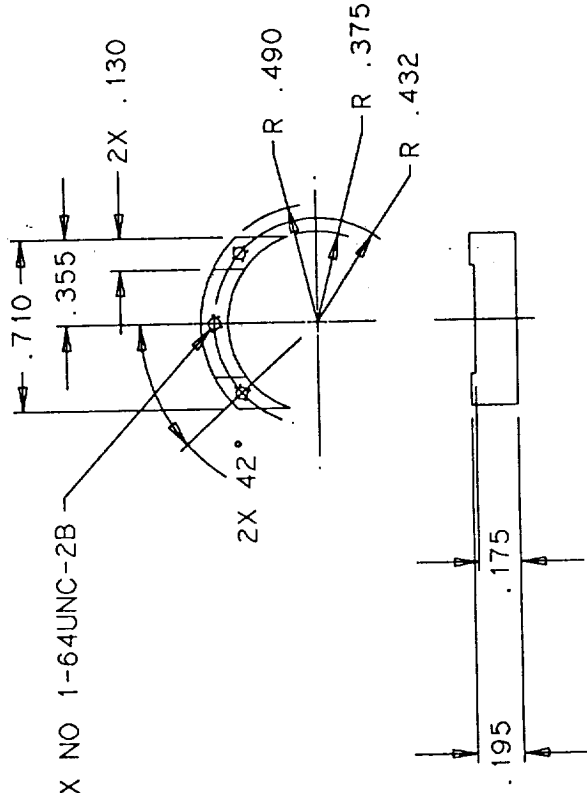
DWG. NO.
1037211 SH
1

REVISIONS			
REV	DESCRIPTION	DWN	CHK APPVL/DATE
A	INITIAL RELEASE PER ECR 91024	KMA TH	BGJ/08NOV91

NOTES:

1. FINISH ALL OVER 32/
2. REMOVE BURRS AND BREAK SHARP EDGES .01 MAX
3. HEAT TREAT PER DRAWING NO. 1009-107
4. BLACK OXIDE AFTER HEAT TREAT

3X NO 1-64UNC-2B



<p>SATCON Technology Corporation</p> <p>MAGNET SUPPORT UPPER</p>		CONTRACT NO.	
		DRAWN K AVAKIAN 05NOV91	CHECKED T HAWKEY 08NOV91
<p>UNLESS OTHERWISE SPECIFIED DIMENSIONS ARE IN INCHES TOLERANCE ON</p>		<p>ENGINEER T HAWKEY 08NOV91</p>	
<p>DECIMALS ANGLES</p> <p>.XX ± .01 ± -</p> <p>.XXX ± .005</p>		<p>APPROVED B JOHNSON 08NOV91</p>	
<p>DO NOT SCALE THIS DRAWING</p>		<p>APPROVED</p>	
<p>MATERIAL</p> <p>Si-Fe</p>		<p>SATCON APPROVED</p>	
NEXT ASSY	USED ON	SIZE	FSCM NO.
APPLICATION		B	1037211
		SCALE	2/1
		SHEET	1

4 3 2 1

NOV 12 1991

DWG. NO. 1037212 SH 1

1

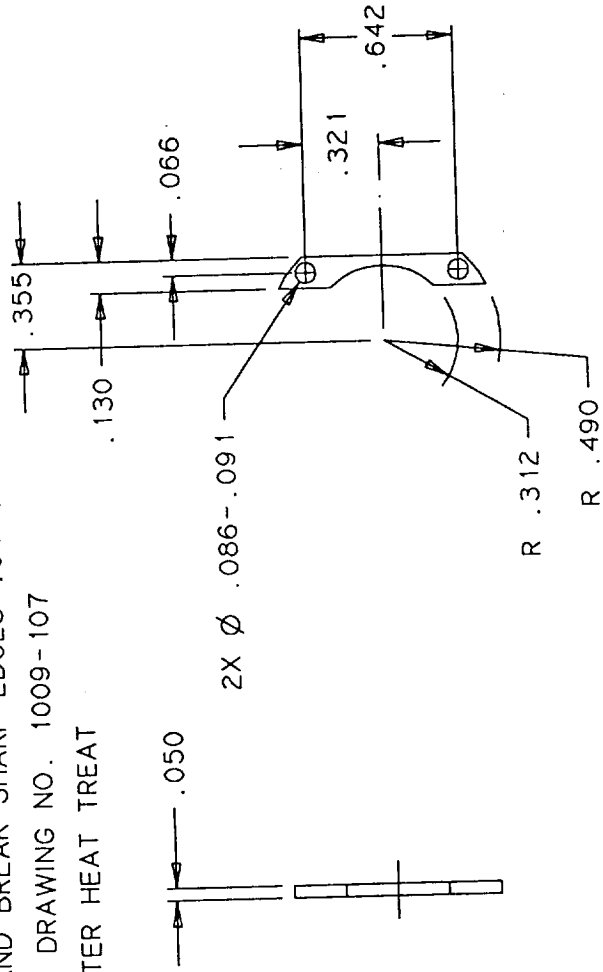
3

4

REVISIONS			
REV	DESCRIPTION	DWN	CHK
A	INITIAL RELEASE PER ECR 91024	KMA	TH
		BGJ/08NOV91	

NOTES: 32/

1. FINISH ALL OVER ∇
2. REMOVE BURRS AND BREAK SHARP EDGES .01 MAX
3. HEAT TREAT PER DRAWING NO. 1009-107
4. BLACK OXIDE AFTER HEAT TREAT



SatCon Technology Corporation

STRAP
MAGNET SUPPORT
UPPER

UNLESS OTHERWISE SPECIFIED DIMENSIONS ARE IN INCHES TOLERANCES ARE IN INCHES		CONTRACT NO.	
DECIMALS		DRAWN K AVAKIAN 05NOV91	
ANGLES		CHECKED T HAWKEY 08NOV91	
.XX \pm .01		ENGINEER T HAWKEY 08NOV91	
.XXX \pm .005		APPROVED B JOHNSON 08NOV91	
DO NOT SCALE THIS DRAWING		APPROVED	
MATERIAL		SATCON APPROVED	
NEXT ASSY		USED ON	
APPLICATION			

SIZE	FSCM NO.	DRAWING NO.	REV
B		1037212	A
SCALE	2/1		SHEET 1

1

2

3

4

NOV 12 1991

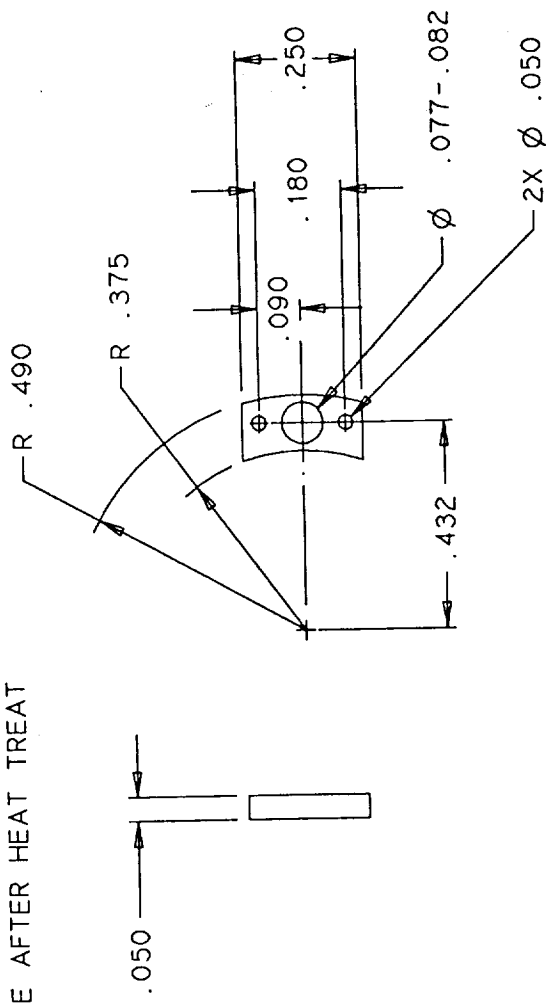
4 3 1

DWG. NO. 1037213 SH 1

REVISIONS			
REV	DESCRIPTION	DWN	CHK
A	INITIAL RELEASE PER ECR 91024	KMA	TH
		BGJ/08NOV91	

NOTES: 32/

1. FINISH ALL OVER
2. REMOVE BURRS AND BREAK SHARP EDGES .01 MAX
3. HEAT TREAT PER DRAWING NO. 1009-107
4. BLACK OXIDE AFTER HEAT TREAT



SATCON Technology Corporation

CLAMP FLEXURE

UNLESS OTHERWISE SPECIFIED CAPACITOR VALUES ARE IN OHMS RESISTOR VALUES ARE IN OHMS DIMENSIONS ARE IN INCHES TOLERANCE ON		CONTRACT NO.	
DECIMALS		DRAWN K AVAKIAN 05NOV91	
ANGLES		CHECKED T HAWKEY 08NOV91	
.XX ± .01		ENGINEER T HAWKEY 08NOV91	
.XXX ± .005		APPROVED B JOHNSON 08NOV91	
DO NOT SCALE THIS DRAWING		APPROVED	
MATERIAL		SATCON APPROVED	
NEXT ASSY USED ON		SIZE FSCM NO. DRAWING NO. REV	
APPLICATION		B 1037213 A	
		SCALE 4/1 SHEET 1	

4 3 2 1

NOV 12 1991

DWG. NO. 1037214 SH 1

1

3

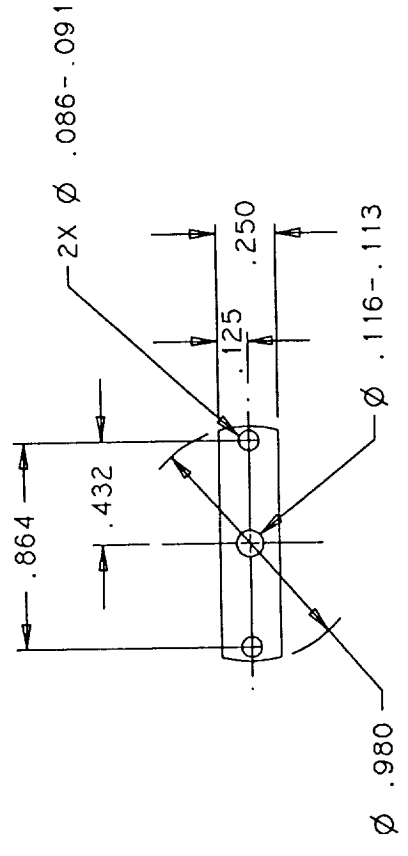
4

REVISIONS

REV	DESCRIPTION	DWN	CHK	APPL/DATE
A	INITIAL RELEASE PER ECR 91024	KMA	TH	BGJ/08NOV91

NOTES: 32/

1. FINISH ALL OVER
2. REMOVE BURRS AND BREAK SHARP EDGES .01 MAX



SATCON Technology Corporation

FLEXURE

UNLESS OTHERWISE SPECIFIED
CAPACITOR VALUES ARE IN OHMS
RESISTOR VALUES ARE IN OHMS
DIMENSIONS ARE IN INCHES
TOLERANCE ON

CONTRACT NO.	DRAWN	K	AVAKIAN	05NOV91
CHECKED	T	HAWKEY	08NOV91	
ENGINEER	T	HAWKEY	08NOV91	
APPROVED	B	JOHNSON	08NOV91	

APPROVED
SATCON APPROVED

DO NOT SCALE THIS DRAWING
MATERIAL
Be-Cu
.010 AND
.015 THK

NEXT ASSY USED ON
APPLICATION

SIZE	FSCM NO.	DRAWING NO.	REV
B		1037214	A
SCALE	2/1		SHEET 1

2

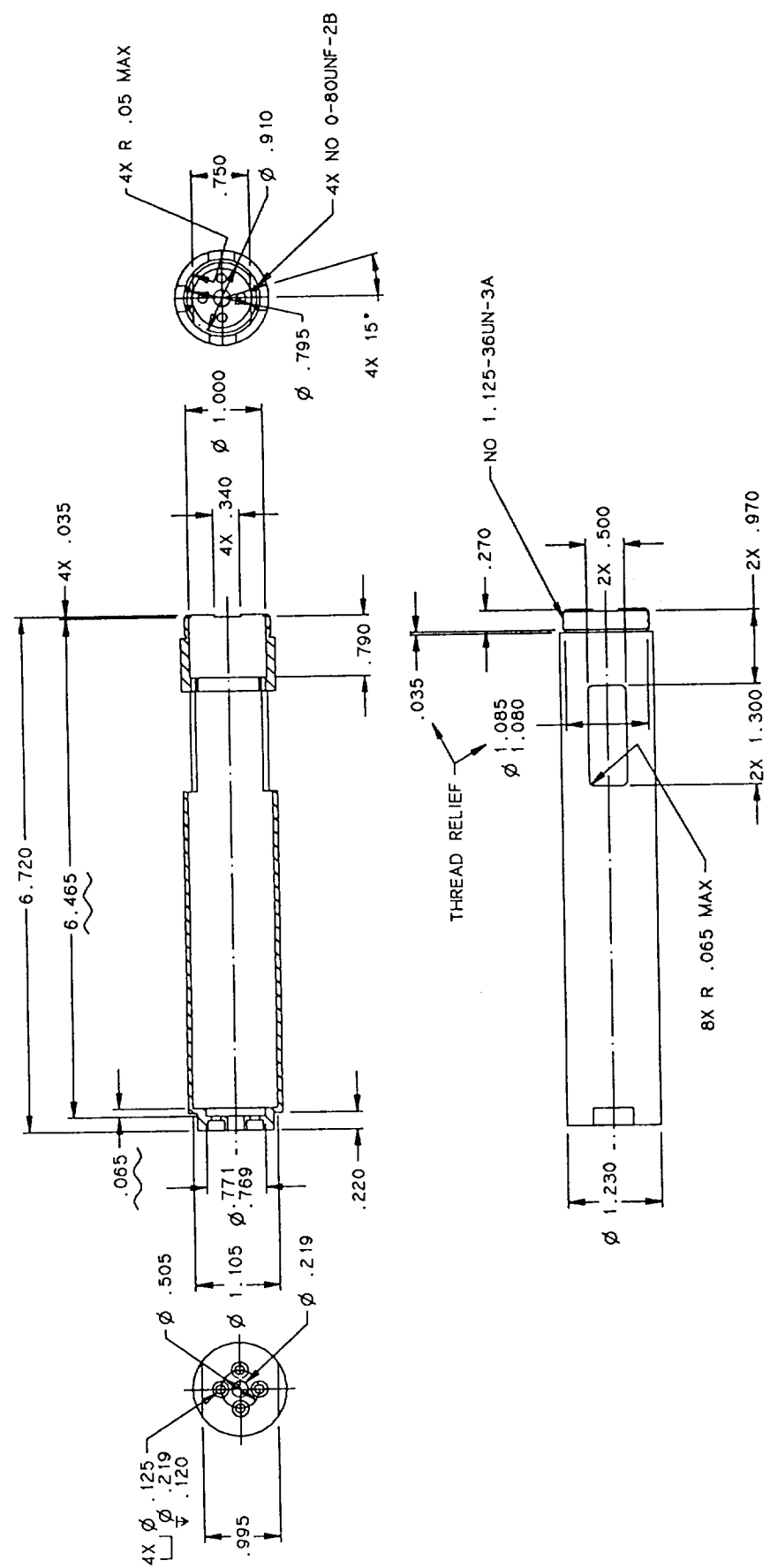
3

4

NOV 12 1991

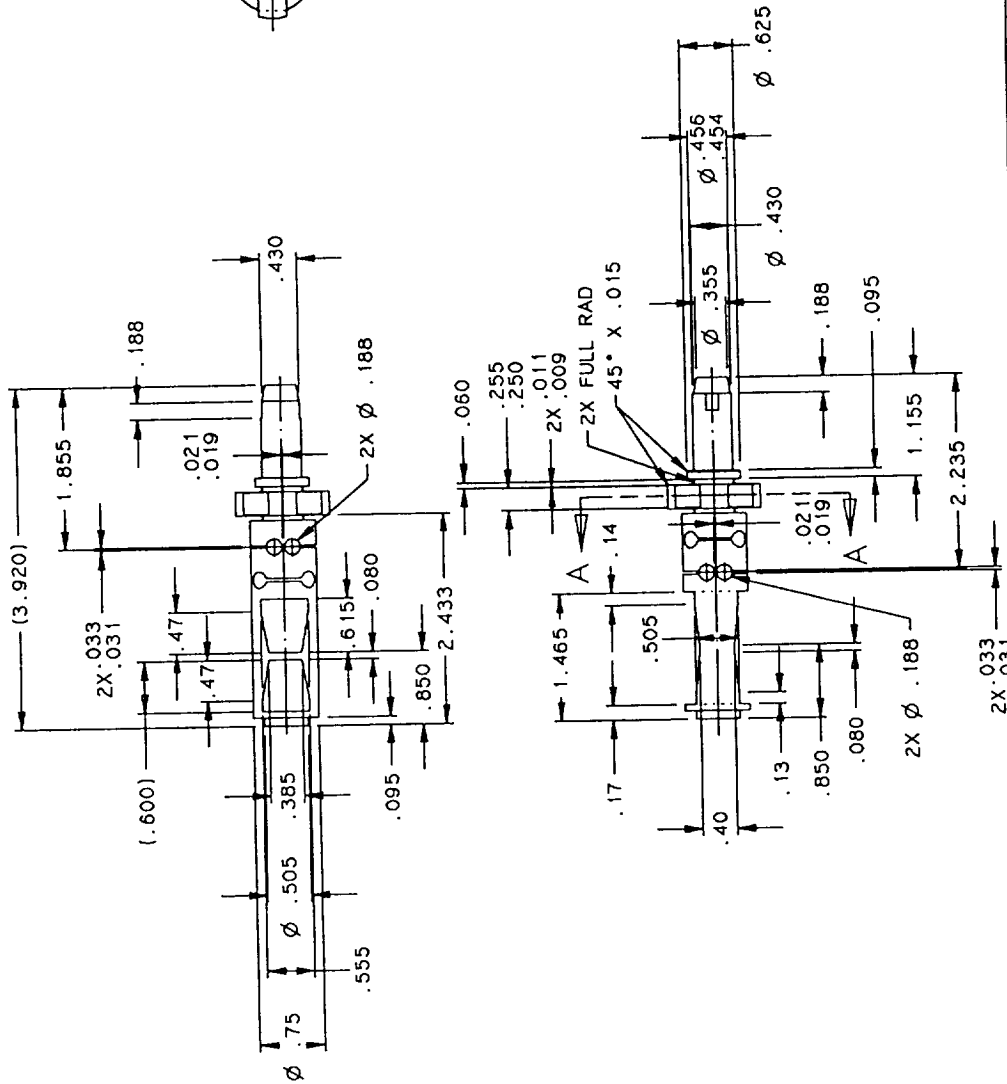
NOTES:

1. FINISH ALL OVER $\sqrt{32}$
2. REMOVE BURRS AND BREAK SHARP EDGES .01 MAX

[illegible]

NOTES:

1. FINISH ALL OVER $\sqrt{32}$
2. REMOVE BURRS AND BREAK SHARP EDGES .01 MAX



UNLESS OTHERWISE SPECIFIED CAPACITOR VALUES ARE IN RESISTOR VALUES ARE IN OHMS DIMENSIONS ARE IN INCHES TOLERANCE ON		TI 6A1-4V	
DECIMALS	ANGLES	DO NOT SCALE THIS DRAWING	MATERIAL
.XX ± .01	± .5		
.XXX ± .005			
NEXT ASSY USED ON APPLICATION			

CONTRACT NO.	K AVAKIAN 070CT91
DRAWN	R FENN 08NOV91
CHECKED	R FENN 08NOV91
ENGINEER	R FENN 08NOV91
APPROVED	B JOHNSON 08NOV91
SATCON APPROVED	

FLEXURE- LONG ACTIVE MEMBER	
SIZE FSCM NO.	1037302
DRAWING NO.	1037302
REV	A
SCALE	1/1
SHEET	1

SATCON

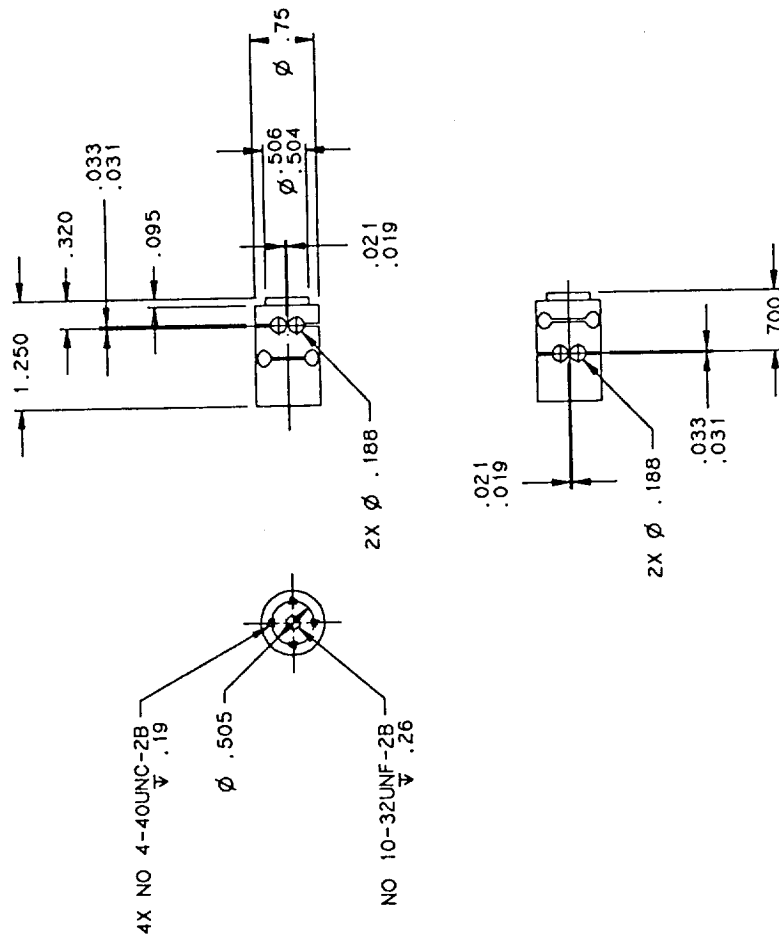
SECTION A-A

REV	DESCRIPTION	DATE	CHK	APPLY/DATE
A	INITIAL RELEASE PER ECR 91024	KMAIRF	BOLNOVOY	

TES: 32/

1. FINISH ALL OVER

1. FINISH ALL OVER $\sqrt{}$
2. REMOVE BURRS AND BREAK SHARP EDGES .01 MAX

[illegible]

Ti 6Al-4V

NEXT ASSY	USED
APPLICATION	

1

SCALE 1/1

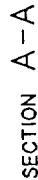
SCALE	1/1
-------	-----

SHEET 1

1

--	--

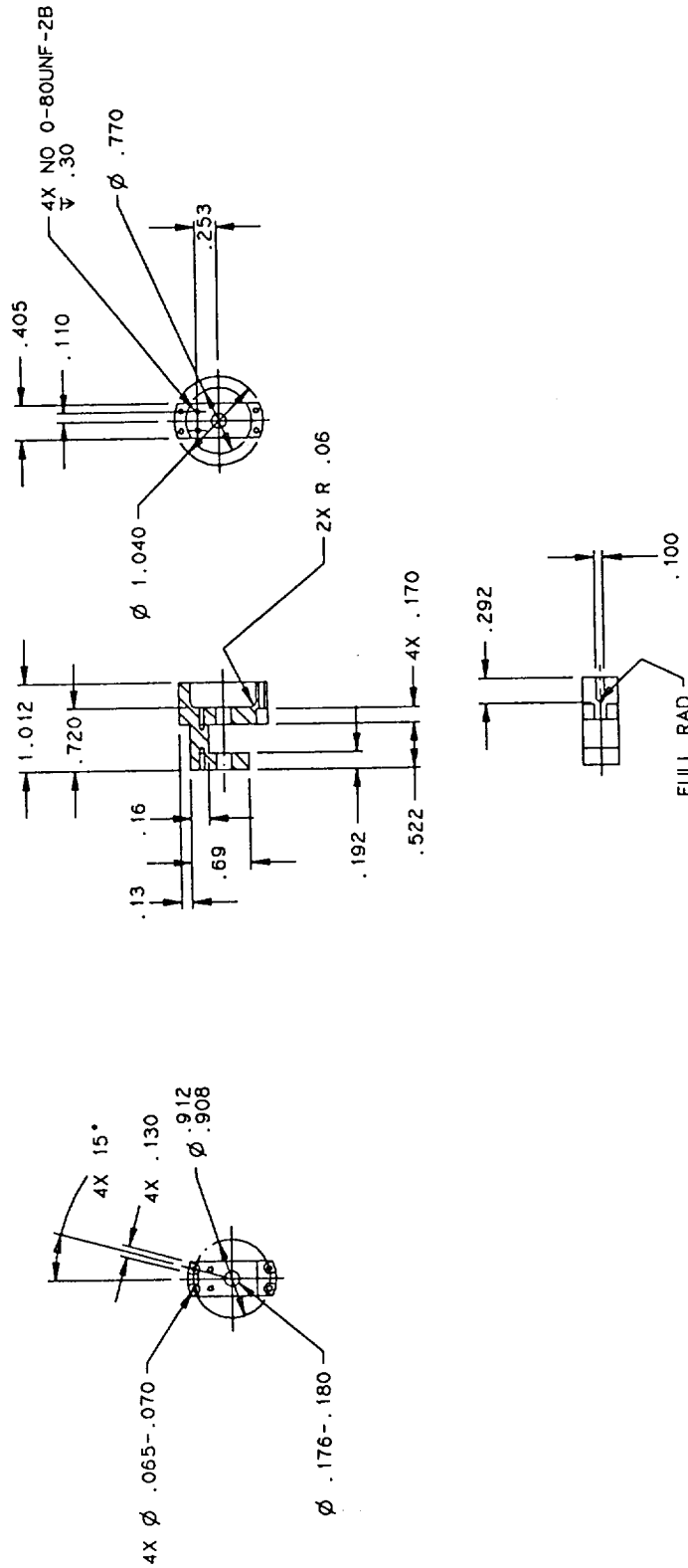
1. FINISH ALL OVER A
2. REMOVE BURRS AND BREAK SHARP EDGES .01 MAX



150

NOTES:

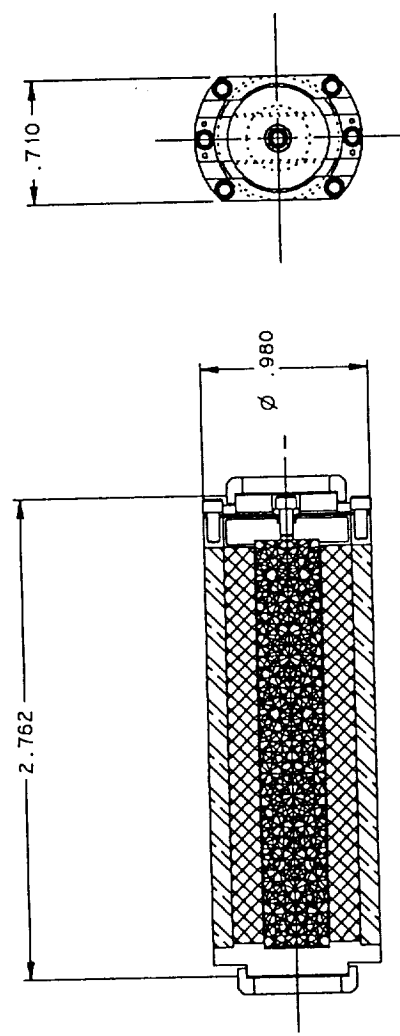
1. FINISH ALL OVER $\sqrt{32}$
2. REMOVE BURRS AND BREAK SHARP EDGES .01 MAX



SatCon		SENSOR CAGE	
CONTRACT NO.	K AVAKIAN 080CT91	SIZE	C
DRAWN	R FENN 08NOV91	FSCM NO.	1037305
CHECKED	R FENN 08NOV91	DRAWING NO.	1037305
ENGINEER	R FENN 08NOV91	REV	A
APPROVED	B JOHNSON 08NOV91	SCALE	1/1
DO NOT SCALE THIS DRAWING	SHEET 1		
MATERIAL	TI 6Al-4V		
NEXT ASSY	APPLICATION		

4 3 2 1

REVISIONS			
REV	DESCRIPTION	DWN	CHK



D C B A

1037306
DWG NO

SATCON
Aerospace Corporation

LAYOUT - ACTUATOR

SIZE	FSCM NO.	DRAWING NO.	REV
C	1037306	1037306	-

UNLESS OTHERWISE SPECIFIED DIMENSIONS ARE IN INCHES TOLERANCES ARE IN INCHES	
CONTRACT NO.	K AYAMIAN 27NOV91
DRAWN	CHECKED
ENGINEER	APPROVED
SATCON APPROVED	

NEXT ASSY	USED ON
APPLICATION	

SCALE 1/1

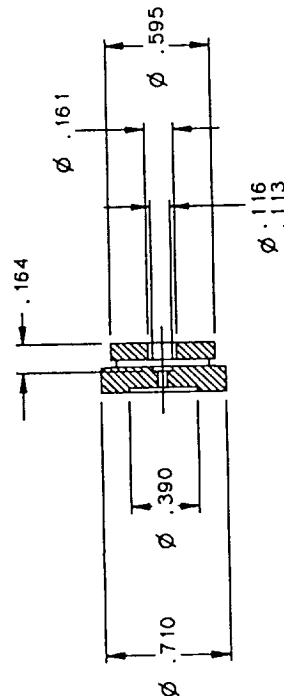
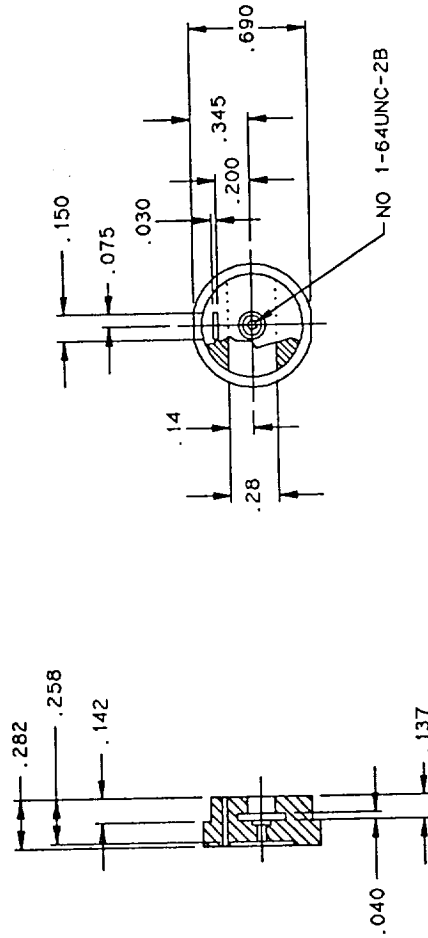
SHEET 1

1
IAN 20 1997

D C B A

NOTES:

1. FINISH ALL OVER ³²✓
2. REMOVE BURRS AND BREAK SHARP EDGES .01 MAX
3. HEAT TREAT PER DRAWING NO. 1009-107
4. BLACK OXIDE AFTER HEAT TREAT



REV	DESCRIPTION	DWN	CHK	APPLD/DATE
A	INITIAL RELEASE PER ECR 91024	KMA	RF	BOUNDOV91
B	REVISED PER ECR 91025	KMA	TH	BOUNDOV91

SatCon

MOUNT 2
TERFENOL

SIZE	FSCM NO.	DRAWING NO.	REV
C		1037307	B
SCALE	2/1	SHEET	1

CONTRACT NO.	DRAWN	K AVAKIAN	24OCT91
CHECKED	R FENN	08NOV91	
ENGINEER	R FENN	08NOV91	
APPROVED	B JOHNSON	08NOV91	
SATCON APPROVED			

UNLESS OTHERWISE SPECIFIED
CAPACITOR VALUES ARE IN OHMS
RESISTOR VALUES ARE IN OHMS
DIMENSIONS ARE IN INCHES
TOLERANCE ON

DECIMALS ANGLES
.XX ± .01
.XXX ± .005

DO NOT SCALE THIS DRAWING

MATERIAL

SI-Fe

NEXT ASSY	USED ON	APPLICATION
-----------	---------	-------------

3

2

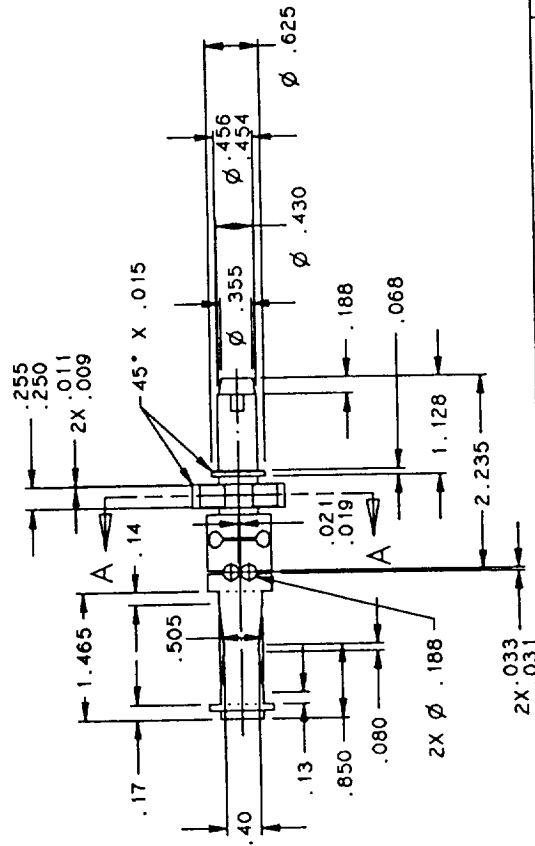
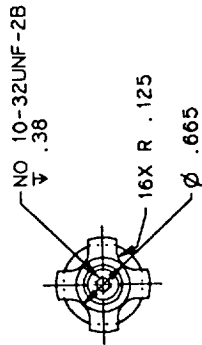
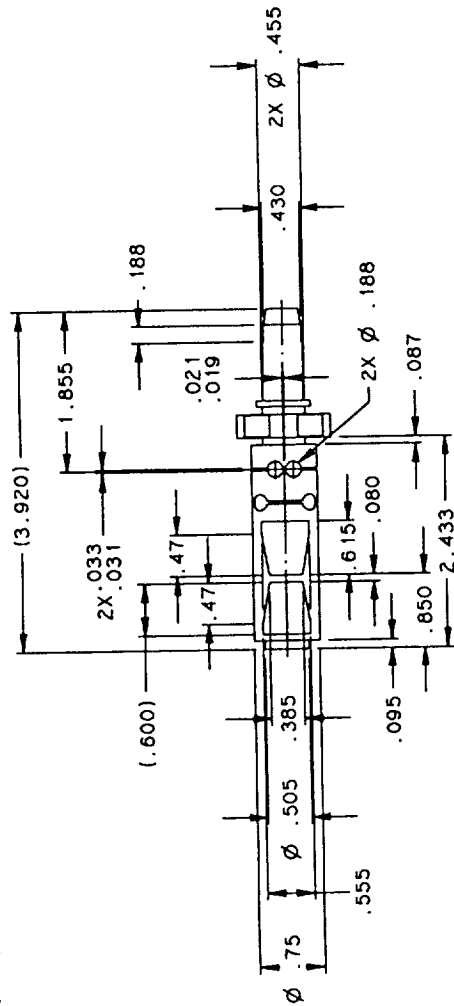
1

DWG. NO. 1037307

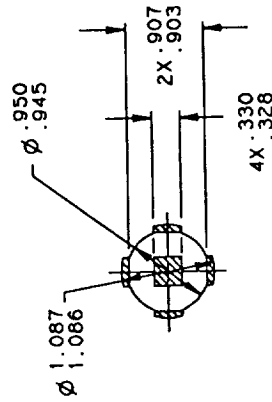
REVISIONS				
REV	DESCRIPTION	DWN	CHK	APPLY DATE
A	INITIAL RELEASE PER ECR 92011		KMARF	190228ZMAR82

NOTES:

- TES:
1. FINISH ALL OVER $\sqrt{32}$
 2. REMOVE BURRS AND BREAK SHARP EDGES .01 MAX



SECTION A-A

[illegible]

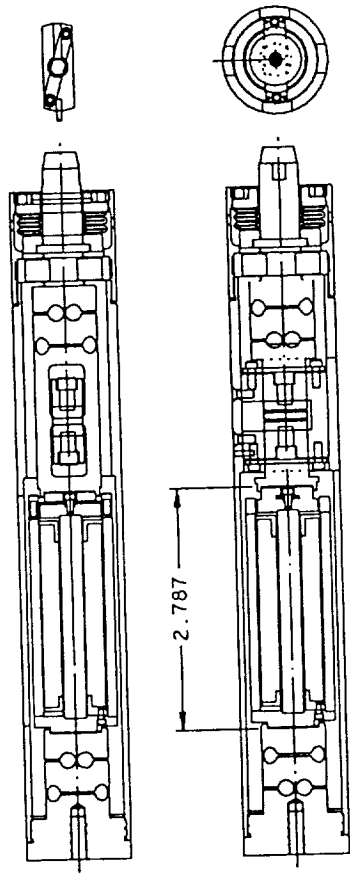
Appendix B - Cryogenic Active Member Drawing Package

Title	No.
Layout - Actuator	1037350
End Cap - Live End Active Member	1037250
Preload Nut	1037251
Sensor Strap	1037252
Crush Washer	1037254
Crush Washer Terfenol	1037255
Magnet	1037256
Cryogenic Temperature Magnetostrictive Rod	1037258
Washer Shoulder	1037259
Washer Flat	1037260
Magnet Support Upper	1037261
Clamp Flexure	1037263
Flexure	1037264
Bobbin - Upper	1037265
Adapter - TbDy	1037266
Adapter - G10 Side TbDy	1037267
Spacer - TbDy	1037268
Housing Active Member	1037351
Flexure - Long Active Member	1037352
Flexure - Short Active Member	1037353
Preload Spring	1037354
Sensor Cage	1037355
Coil Bobbin	1037356
Mount 2 Terfenol	1037357
Mount 1 Terfenol	1037358
Coil Bobbin Bottom	1037359
Sensor Cage (Titanium)	1037360
Layout - Actuator TbDy	1037361

1 2 3 4

D C B A

REVISIONS			
REV	DESCRIPTION	DWN	CHK
A	INITIAL RELEASE PER ECR 92001	KMARF	10/12/1992



1037350
REV 1

SATCON

LAYOUT - ACTUATOR

CONTRACT NO.	K AVAKIAN 22JAN92
DRAWN	R FENN 21FEB92
CHECKED	R FENN 21FEB92
ENGINEER	R FENN 21FEB92
APPROVED	B JOHNSON 21FEB92
APPROVED	R HOCKNEY 21FEB92
SATCON APPROVED	

UNLESS OTHERWISE SPECIFIED
CAPACITOR VALUES ARE IN OHMS
RESISTOR VALUES ARE IN OHMS
DIMENSIONS ARE IN INCHES
TOLERANCE ON
DECIMALS .XX ± .01 ANGLES ± .5
.XXX ± .005
DO NOT SCALE THIS DRAWING
WATERMARK

NEXT ASSY	USED ON
APPLICATION	

SIZE	FSCM NO.	DRAWING NO.	REV
C		1037350	A
SCALE	1/1	SHEET	1

1 2 3 4

4 3 1

DWG. NO.
1037250

SH

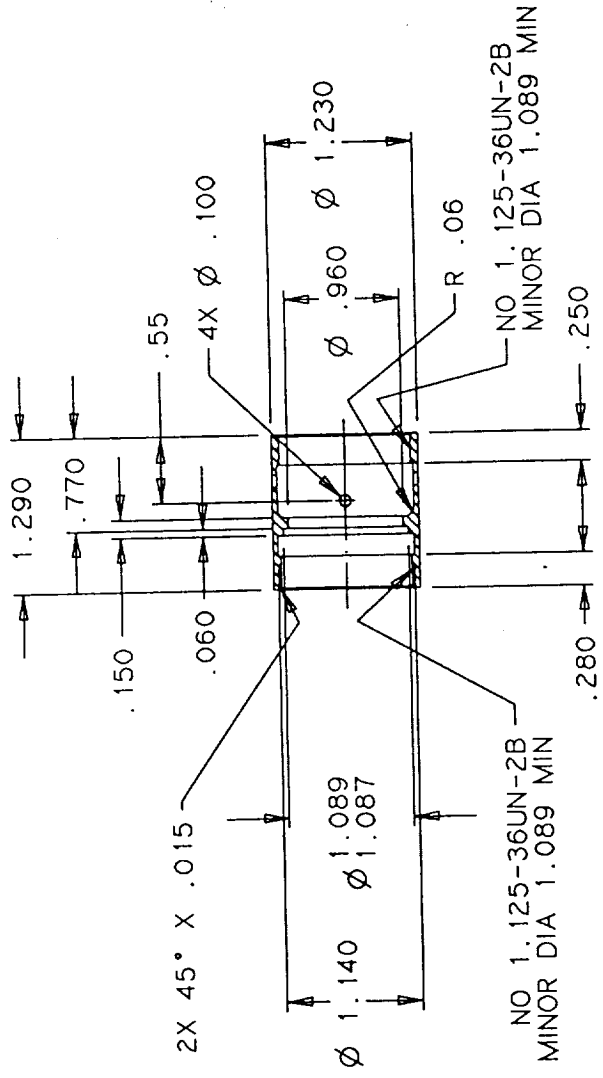
1

REVISIONS

REV	DESCRIPTION	DWN	CHK	APPLY/DATE
A	INITIAL RELEASE PER ECR 92001	KMARF		06/21/FEB92

NOTES:

1. FINISH ALL OVER $\sqrt{32}$
2. REMOVE BURRS AND BREAK SHARP EDGES .01 MAX



UNLESS OTHERWISE SPECIFIED CAPACITOR VALUES ARE IN OHMS RESISTOR VALUES ARE IN OHMS DIMENSIONS ARE IN INCHES TOLERANCE ON		CONTRACT NO.		SatCon Technology Corporation	
DECIMALS	ANGLES	DRAWN	K AVAKIAN	24JAN92	END CAP - LIVE END ACTIVE MEMBER
.XX \pm .01	\pm	CHECKED	R FENN	21FEB92	
.XXX \pm .005		ENGINEER	R FENN	21FEB92	
DO NOT SCALE THIS DRAWING		APPROVED	B JOHNSON	21FEB92	
MATERIAL		APPROVED	R HOCKNEY	21FEB92	
Ti 6AL-4V		SATCON APPROVED		SIZE	FSCM NO.
NEXT ASSY		USED ON		DRAWING NO.	
APPLICATION				1037250	
				SCALE	1/1
				SHEET 1	

4 3 2 1

DWG. NO. 1037251 SH 1

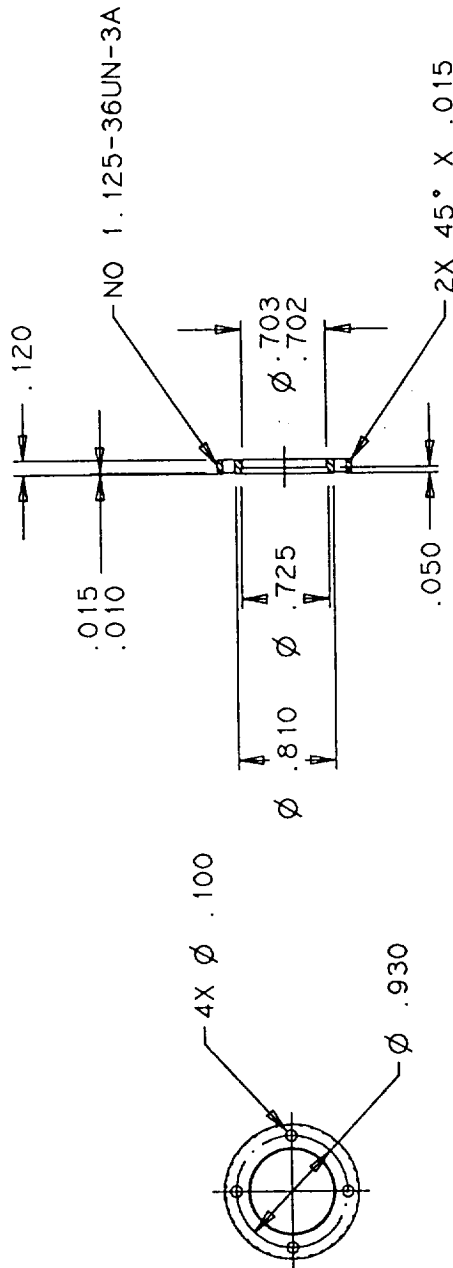
REVISIONS

REV	DESCRIPTION	DWN	CHK	APPVL/DATE
A	INITIAL RELEASE PER ECR 92001	KMARF		RE/21FEB92

NOTES:

1. FINISH ALL OVER $\sqrt{32}$

2. REMOVE BURRS AND BREAK SHARP EDGES .01 MAX



SATCON
Technology Corporation

PRELOAD NUT

			UNLESS OTHERWISE SPECIFIED CAPACITOR VALUES ARE IN OHMS RESISTOR VALUES ARE IN OHMS DIMENSIONS ARE IN INCHES TOLERANCE ON		
			DECIMALS	ANGLES	
			.XX ± .01	± -	
			.XXX ± .005		
			DO NOT SCALE THIS DRAWING		
			MATERIAL		
			Ti 6AL-4V		
</					

SIZE	FSCM NO.	DRAWING NO.	REV
B		1037251	A
SCALE	1/1		SHEET 1

4

3

2

1

FEB 24 1992

4 3 1

DWG. NO.
1037252

SH
1

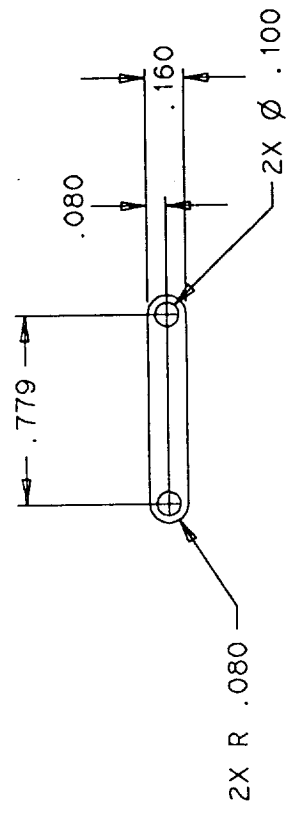
REVISIONS

REV	DESCRIPTION	DWN	CHK	APPLY/DATE
A	INITIAL RELEASE PER ECR 92001	KMARF		RF/21FEB92

NOTES:

1. FINISH ALL OVER $\sqrt{32}$

2. REMOVE BURRS AND BREAK SHARP EDGES .01 MAX



SatCon
Technology Corporation

SENSOR STRAP

UNLESS OTHERWISE SPECIFIED CAPACITOR VALUES ARE IN OHMS RESISTOR VALUES ARE IN OHMS DIMENSIONS ARE IN INCHES TOLERANCE ON	CONTRACT NO.	
	DRAWN	K AVAKIAN 244JAN92
	CHECKED	R FENN 21FEB92
	ENGINEER	R FENN 21FEB92
	APPROVED	B JOHNSON 21FEB92
DO NOT SCALE THIS DRAWING		APPROVED R HOCKNEY 21FEB92
MATERIAL		SATCON APPROVED
NEXT ASSY		USED ON
APPLICATION		
BeCu		
DECIMALS		ANGLES
.XX ± .01		± -
.XXX ± .005		

SIZE	FSCM NO.	DRAWING NO.	REV
B		1037252	A
SCALE 2/1		SHEET 1	

4 3 2 1

FEB 24 1992

4 3 1

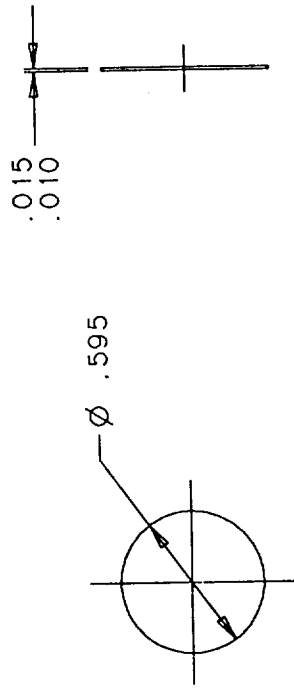
DWG. NO.
1037254

SH
1

REVISIONS				
REV	DESCRIPTION	DWN	CHK	APPVL/DATE
A	INITIAL RELEASE PER ECR 92001	KMA	RF	18/2 1FEB92

NOTES:
1. FINISH ALL OVER $\sqrt{32}$

2. REMOVE BURRS AND BREAK SHARP EDGES .01 MAX
3. MATERIAL: ALUM 1100-0 DEAD SOFT CONDITION



UNLESS OTHERWISE SPECIFIED CAPACITOR VALUES ARE IN RESISTOR VALUES ARE IN OHMS DIMENSIONS ARE IN INCHES TOLERANCE ON		CONTRACT NO.	
DECIMALS		DRAWN	
.XX ± .01		CHECKED R FENNI 21FEB92	
.XXX ± .005		ENGINEER R FENNI 21FEB92	
DO NOT SCALE THIS DRAWING		APPROVED B JOHNSON 21FEB92	
MATERIAL		APPROVED R HOCKNEY 21FEB92	
SEE NOTE 3		SATCON APPROVED	
NEXT ASSY	USED ON	SIZE FSCM NO.	
APPLICATION		B	
4		SCALE 2/1	
3		SHEET 1	

SatCon Technology Corporation	
CRUSH WASHER	
REV	1037254
DRAWING NO.	A

4 3 2 1

DWG. NO.
1037255

SH
1

3

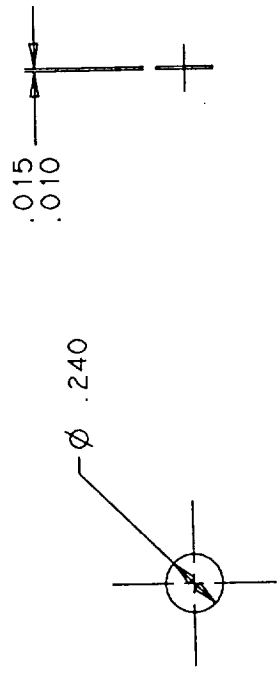
4

REVISIONS				
REV	DESCRIPTION	DWN	CHK	APPVL/DATE
A	INITIAL RELEASE PER ECR 92001	KMARF		RF/21FEB92

NOTES:

32/

1. FINISH ALL OVER
2. REMOVE BURRS AND BREAK SHARP EDGES .01 MAX
3. MATERIAL: SUPPLIED BY SATCON (ALUMINUM SHIM STOCK)



SATCON
Technology Corporation

CRUSH WASHER
TERFENOL

UNLESS OTHERWISE SPECIFIED
CAPACITOR VALUES ARE IN OHMS
RESISTOR VALUES ARE IN OHMS
DIMENSIONS ARE IN INCHES
TOLERANCE ON

DECIMALS ANGLES
.XX ± .01 3°
.XXX ± .005

DO NOT SCALE THIS DRAWING
MATERIAL

SEE NOTE 3

NEXT ASSY USED ON

APPLICATION

CONTRACT NO.	
DRAWN	K AVAKIAN 24JAN92
CHECKED	R FENN 21FEB92
ENGINEER	R FENN 21FEB92
APPROVED	B JOHNSON 21FEB92
APPROVED	R HOCKNEY 21FEB92
SATCON	APPROVED

SIZE	FSCM NO.	DRAWING NO.	REV
B		1037255	A

SCALE	2/1	SHEET	1
-------	-----	-------	---

2

3

4

FEB 24 1992

4

3

DWG. NO.

1037256

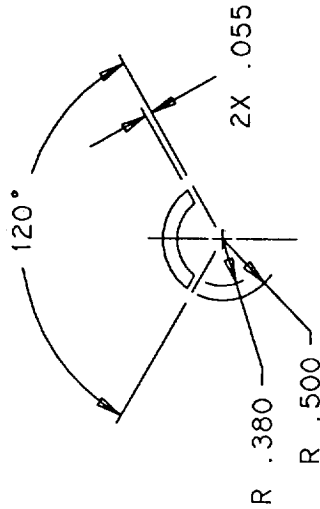
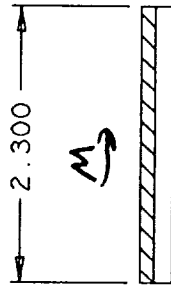
SH

1

1

NOTES:

1. FINISH ALL OVER $\sqrt{32}$
2. REMOVE BURRS AND BREAK SHARP EDGES .01 MAX
3. RUST PROTECT



B

B

A

A

UNLESS OTHERWISE SPECIFIED CAPACITOR VALUES ARE IN PPM RESISTOR VALUES ARE IN OHMS DIMENSIONS ARE IN INCHES TOLERANCE ON		CONTRACT NO.			
		DRAWN	K AVAKIAN		
DECIMALS		CHECKED	R FENN	21 FEB 92	
ANGLES		ENGINEER	R FENN	21 FEB 92	
.XX ± .01		APPROVED B JOHNSON		21 FEB 92	
.XXX ± .005		APPROVED R HOCKNEY		21 FEB 92	
DO NOT SCALE THIS DRAWING		MATERIAL		SIZE FSCM NO. DRAWING NO. REV B 1037256 A	
NEXT ASSY USED ON		Nd Fe35		SCALE 1/1 SHEET 1	
APPLICATION					

4

3

2

1

FEB 24 1992

4 3 1

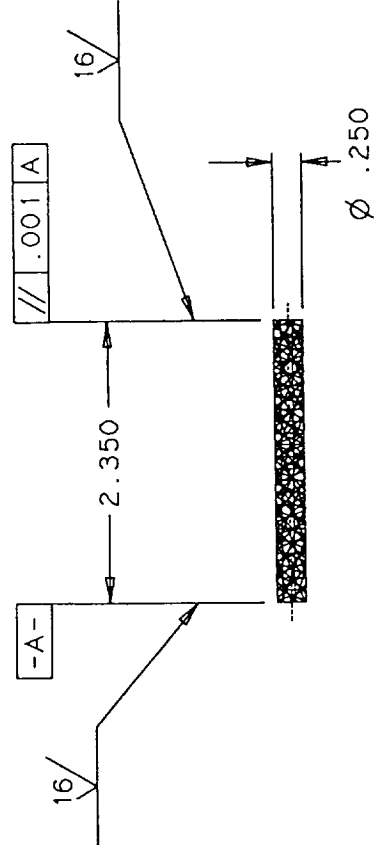
DWG. NO.
1037258

SH
1

REVISIONS			
REV	DESCRIPTION	DMN	CHK
A	INITIAL RELEASE PER ECR 92010	KMARF	RF/18MAY92

NOTES:

1. REMOVE BURRS AND BREAK SHARP EDGES .01 MAX



						UNLESS OTHERWISE SPECIFIED CAPACITOR VALUES ARE IN RESISTOR VALUES ARE IN OHMS DIMENSIONS ARE IN INCHES TOLERANCE ON		CONTRACT NO.				SatCon Technology Corporation			
							DECIMALS	ANGLES	DRAWN	K AVAKIAN	18MAY92	CRYOGENIC TEMPERATURE MAGNETOSTRICTIVE ROD			
							.XX ± .01	± -	CHECKED	R FENN	18MAY92				
							.XXX ± .005		ENGINEER	R FENN	18MAY92				
							DO NOT SCALE THIS DRAWING		APPROVED BY	JOHNSON	18MAY92				
							MATERIAL		APPROVED R	HOCKNEY	18MAY92	SIZE	FSCM NO.	DRAWING NO.	REV
							TERFENOL-D (CRYOGENIC TEMP)		SATCON APPROVED			B		1037258	A
NEXT ASSY															

4 3 2 1

JUL 08 1992

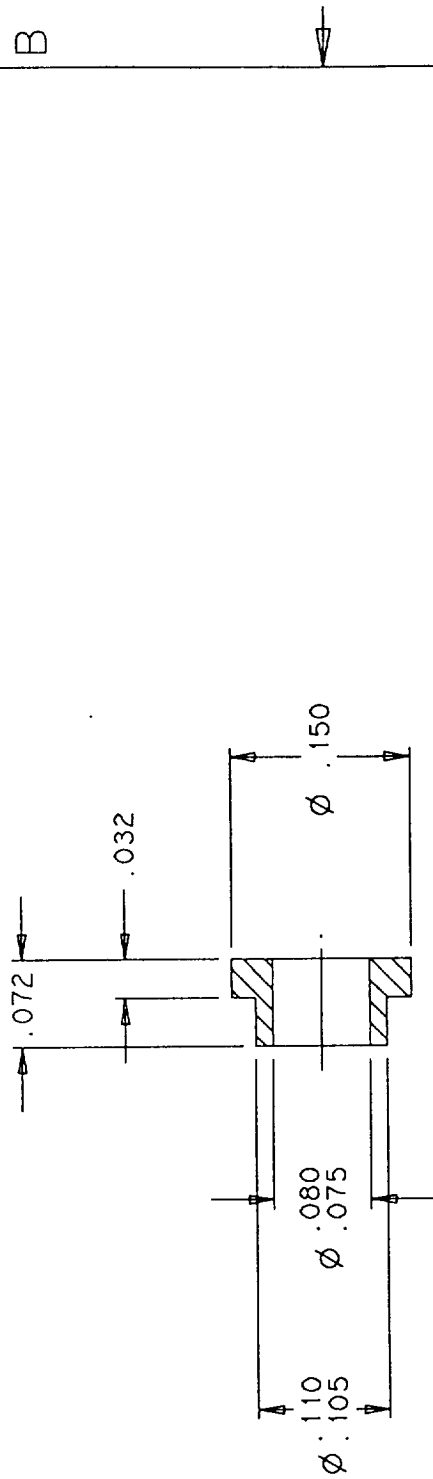
4 | 3 | 1

DWG. NO. 1037259 SH 1

REVISIONS

REV	DESCRIPTION	DWN	CHK	APPVL/DATE
A	INITIAL RELEASE PER ECR 92001	KMA	RF	RF / 2 FEB92

- NOTES:
1. FINISH ALL OVER $\sqrt{32}$
 2. REMOVE BURRS AND BREAK SHARP EDGES .01 MAX



UNLESS OTHERWISE SPECIFIED CAPACITOR VALUES ARE IN INCHES RESISTOR VALUES ARE IN OHMS DIMENSIONS ARE IN INCHES TOLERANCE ON		CONTRACT NO.		SatCon Technology Corporation	
		DRAWN K AVAKIAN 31JAN92		WASHER SHOULDER	
DECIMALS		CHECKED R FENN 21FEB92		SIZE FSCM NO. DRAWING NO. REV	
.XX ± .01		ENGINEER R FENN 21FEB92		B 1037259 A	
.XXX ± .005		APPROVED B JOHNSON 21FEB92		SCALE 10/1 SHEET 1	
DO NOT SCALE THIS DRAWING		APPROVED R HOCKNEY 21FEB92			
MATERIAL		SATCON APPROVED			
ST ST TYPE					
303 OR EQUIV					
(NON-MAGNETIC)					
NEXT ASSY	USED ON				
APPLICATION					

4 | 3 | 2 | 1

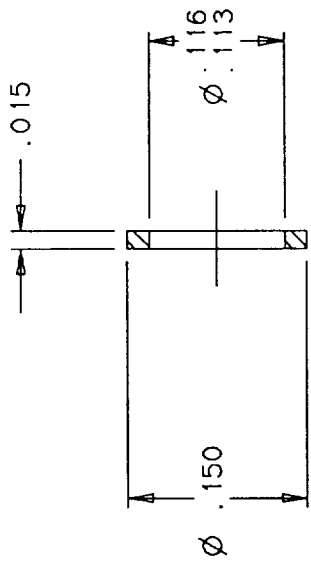
4 3 1

DWG. NO. 1037260 SH 1

REVISIONS				
REV	DESCRIPTION	DWN	CHK	APPLYL/DATE
A	INITIAL RELEASE PER ECR 92001	KMA	RF	RF /2 1FEB92

- NOTES:
1. FINISH ALL OVER $\sqrt{32}$
 2. REMOVE BURRS AND BREAK SHARP EDGES .01 MAX

B B



		UNLESS OTHERWISE SPECIFIED CAPACITOR VALUES ARE IN OHMS RESISTOR VALUES ARE IN OHMS DIMENSIONS ARE IN INCHES TOLERANCE ON	CONTRACT NO.		SatCon Technology Corporation				
			DRAWN	K AVAKIAN				31JAN92	
			CHECKED	R FENN				21FEB92	
			ENGINEER	R FENN				21FEB92	
		DECIMALS	ANGLES		WASHER FLAT				
		.XX ± .01	± -						
		.XXX ± .005							
		DO NOT SCALE THIS DRAWING	APPROVED B JOHNSON					21FEB92	
		MATERIAL	APPROVED R HOCKNEY		21FEB92	SIZE	FSCM NO.	DRAWING NO.	REV
		ST ST TYPE	SATCON APPROVED			B		1037260	A
		303 OR EQUIV							
		(NON-MAGNETIC)							
		NEXT ASSY	USED ON						
		APPLICATION			SCALE	10/1	SHEET		1

4 3 2 1

FER 2 4 1992

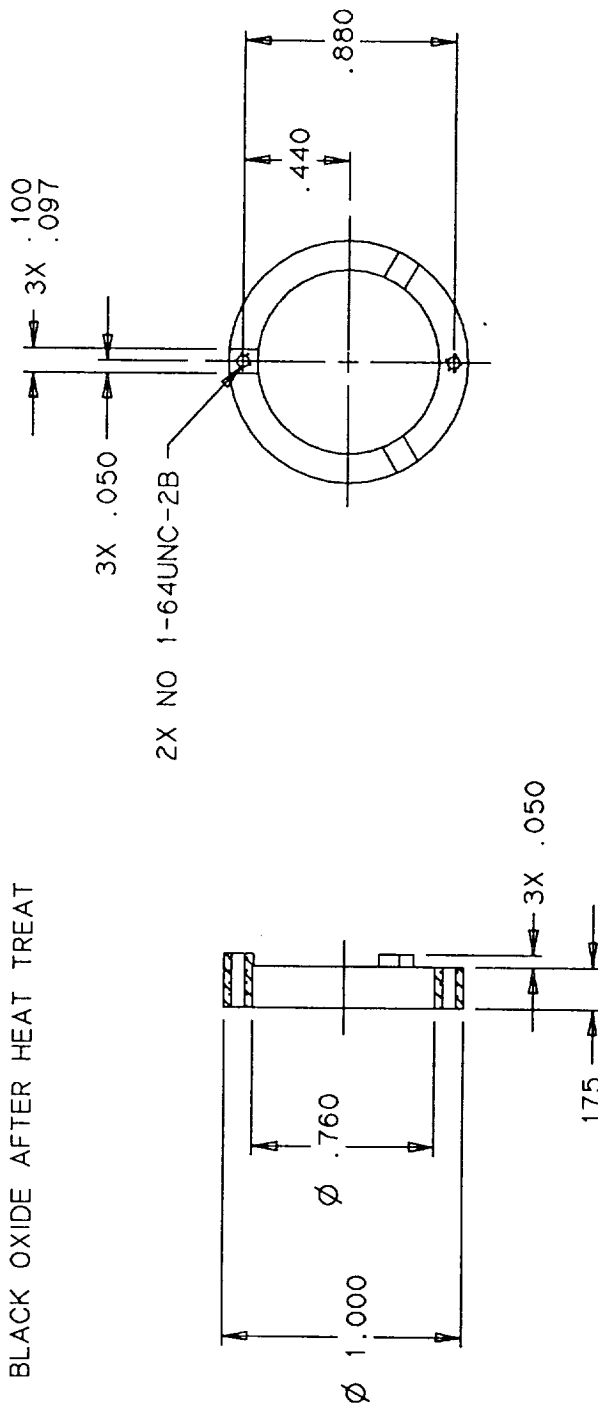
DWG. NO. 1037261 SH 1

REVISIONS

REV	DESCRIPTION	DWN	CHK	APPVL/DATE
A	INITIAL RELEASE PER ECR 92001	KMA	RF	RF/2 1FEB92

NOTES:

1. FINISH ALL OVER $\sqrt{32}$
2. REMOVE BURRS AND BREAK SHARP EDGES .01 MAX
3. HEAT TREAT PER DRAWING NO. 1009-107
4. BLACK OXIDE AFTER HEAT TREAT



UNLESS OTHERWISE SPECIFIED CAPACITOR VALUES ARE IN OHMS RESISTOR VALUES ARE IN OHMS DIMENSIONS ARE IN INCHES TOLERANCE ON		CONTRACT NO.		SatCon Technology Corporation	
DECIMALS	ANGLES	DRAWN	K AVAKIAN	31JAN92	MAGNET SUPPORT UPPER
.XX \pm .01	1 -	CHECKED	R FENNI	21FEB92	
.XXX \pm .005		ENGINEER	R FENNI	21FEB92	
DO NOT SCALE THIS DRAWING		APPROVED	B JOHNSON	21FEB92	
MATERIAL		APPROVED		R HOCKNEY	21FEB92
Si-Fe		SATCON APPROVED			
NEXT ASSY	USED ON	SIZE		FSCM NO.	DRAWING NO.
APPLICATION		B			1037261
		SCALE		2/1	SHEET 1

FEB 24 1992

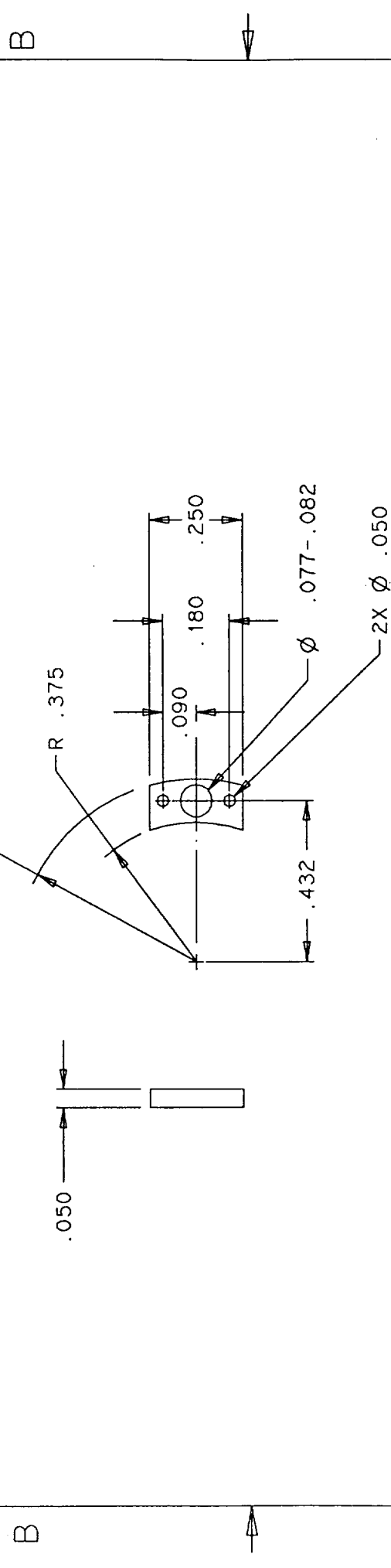
4 3 1

DWG. NO. 1037263 SH 1

REVISIONS				
REV	DESCRIPTION	DWN	CHK	APPVL/DATE
A	INITIAL RELEASE PER ECR 92001	KMARF		RF/2 1FEB92

NOTES:

1. FINISH ALL OVER $\sqrt{32}$
2. REMOVE BURRS AND BREAK SHARP EDGES .01 MAX
3. HEAT TREAT PER DRAWING NO. 1009-107
4. BLACK OXIDE AFTER HEAT TREAT



UNLESS OTHERWISE SPECIFIED RESISTOR VALUES ARE IN OHMS DIMENSIONS ARE IN INCHES TOLERANCE ON		CONTRACT NO. . .		SatCon Technology Corporation	
		DRAWN K AVAKIAN	31JAN92	CLAMP FLEXURE	
DECIMALS	ANGLES	CHECKED R FENNI	21FEB92	SIZE	FSCM NO.
.XX ± .01	± °	ENGINEER R FENNI	21FEB92	B	1037263
.XXX ± .005		APPROVED B JOHNSON	21FEB92	REV	A
DO NOT SCALE THIS DRAWING		APPROVED R HOCKNEY	21FEB92	SCALE 4/1	
MATERIAL		SATCON APPROVED		SHEET 1	
Si-Fe					
NEXT ASSY	USED ON				
APPLICATION					

4 3 2 1

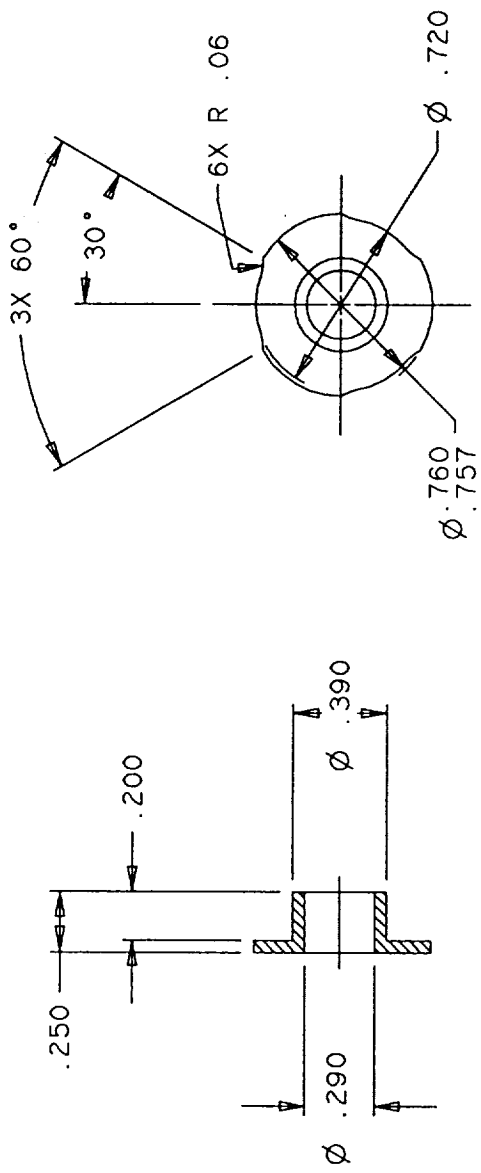
FEB 24 1992

4 3 1

DWG. NO. 1037265 SH 1

NOTES:

1. FINISH ALL OVER $\sqrt[32]{}$
2. REMOVE BURRS AND BREAK SHARP EDGES .01 MAX



UNLESS OTHERWISE SPECIFIED DIMENSIONS ARE IN INCHES TOLERANCES ARE IN INCHES		CONTRACT NO.		SatCon Technology Corporation	
DECIMALS	ANGLES	DRAWN	K AVAKIAN	03FEB92	BOBBIN- UPPER
.XX $\pm .01$	$\pm .5$	CHECKED	R FENN	21FEB92	
.XXX $\pm .005$		ENGINEER	R FENN	21FEB92	
DO NOT SCALE THIS DRAWING		APPROVED	B JOHNSON	21FEB92	
MATERIAL		APPROVED	R HOCKNEY	21FEB92	
G-10		SATCON APPROVED		SIZE	B
NEXT ASSY	USED ON	FSCM NO.		DRAWING NO.	REV
APPLICATION		1037265		1037265	A
3		SCALE 2/1		SHEET 1	

1
FFR 2 4 1992

4 3 1

DWG. NO.
1037266

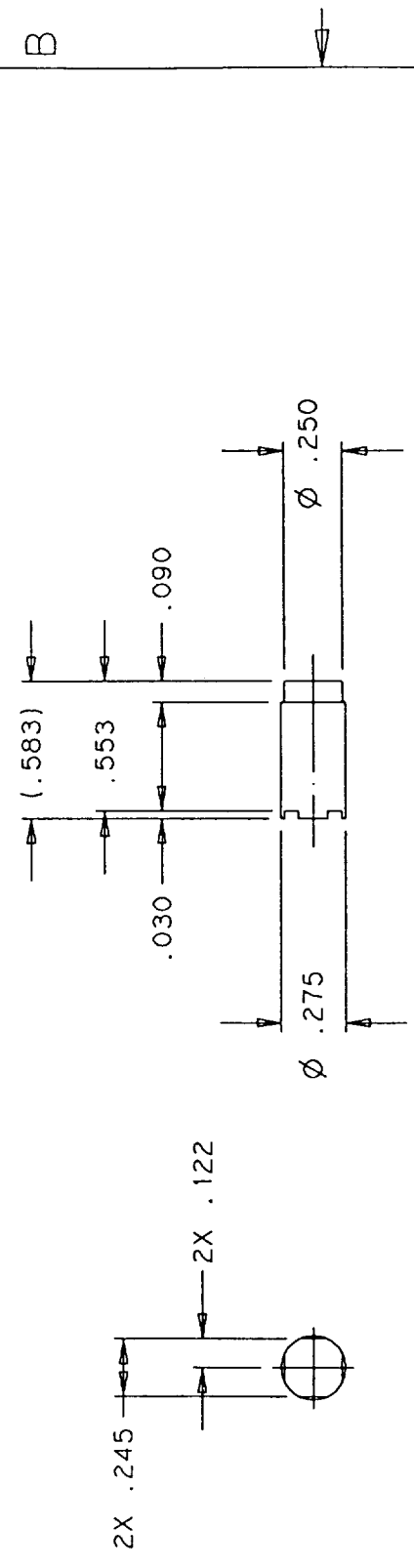
SH
1

REVISIONS

REV	DESCRIPTION	DWN	CHK	APPVL/DATE
-	INITIAL RELEASE PER ECR XXXXX	KMARF		xx/xxxxxx

NOTES:

1. FINISH ALL OVER $\sqrt{32}$
2. REMOVE BURRS AND BREAK SHARP EDGES .01 MAX



SATCON
Technology Corporation

ADAPTER-
TbDY

UNLESS OTHERWISE SPECIFIED CAPACITOR VALUES ARE IN OHMS RESISTOR VALUES ARE IN OHMS DIMENSIONS ARE IN INCHES TOLERANCE ON		CONTRACT NO.	
DRAWN	K AVAKIAN	22JUN92	
CHECKED	R FENNI	22JUN92	
ENGINEER	R FENNI	22JUN92	
APPROVED	B JOHNSON	22JUN92	
APPROVED	R HOCKEY	22JUN92	
SATCON	APPROVED		
DO NOT SCALE THIS DRAWING		MATERIAL	
NEXT ASSY		USED ON	
APPLICATION		SILICON IRON	

SIZE	FSCM NO.	DRAWING NO.	REV
B		1037266	-
SCALE	2/1	SHEET	1

4 3 2 1

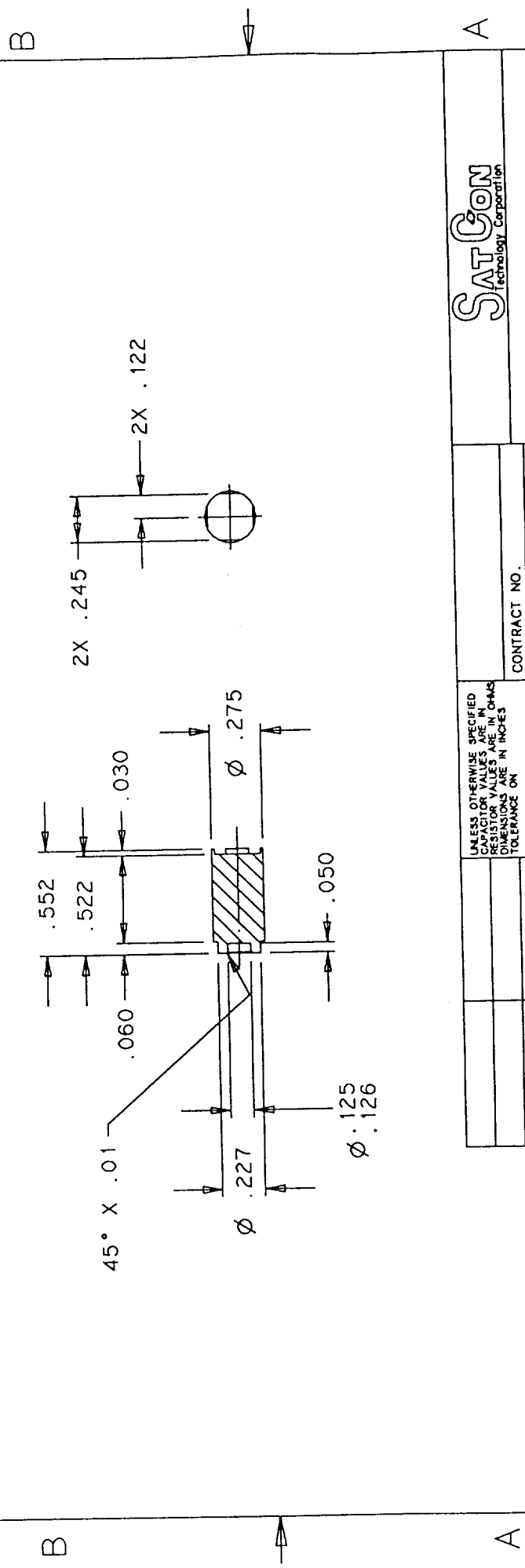
JUL 08 1992

4 3 1

DWG. NO. 1037267 SH 1

REVISIONS			
REV	DESCRIPTION	DWN	CHK
-	INITIAL RELEASE PER ECR XXXXX	KMA	RF
		APPVL/DATE	
		xx/xxxxxx	

- NOTES:
1. FINISH ALL OVER $\sqrt{32}$
 2. REMOVE BURRS AND BREAK SHARP EDGES .01 MAX



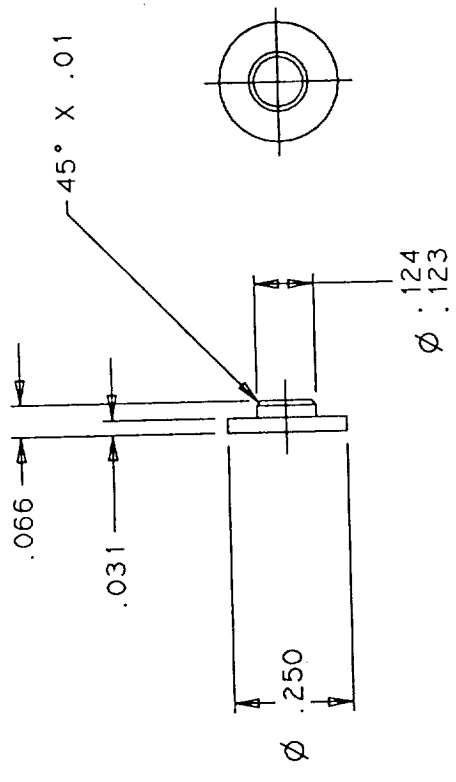
UNLESS OTHERWISE SPECIFIED DIMENSIONS ARE IN INCHES TOLERANCES ARE IN INCHES		CONTRACT NO.	
DECIMALS	ANGLES	DRAWN	K AVAKIAN 22JUN92
.XX ± .01	± .5	CHECKED	R FENNI 22JUN92
.XXX ± .005		ENGINEER	R FENNI 22JUN92
DO NOT SCALE THIS DRAWING		APPROVED	B JOHNSON 22JUN92
MATERIAL		APPROVED	R HOCKNEY 22JUN92
SILICON IRON		SATCON	APPROVED
NEXT ASSY	USED ON		
APPLICATION			

SatCon Technology Corporation	
ADAPTER- G10 SIDE TbDY	
SIZE	FSCM NO.
B	1037267
SCALE	2/1
SHEET	1

4 3 2 1

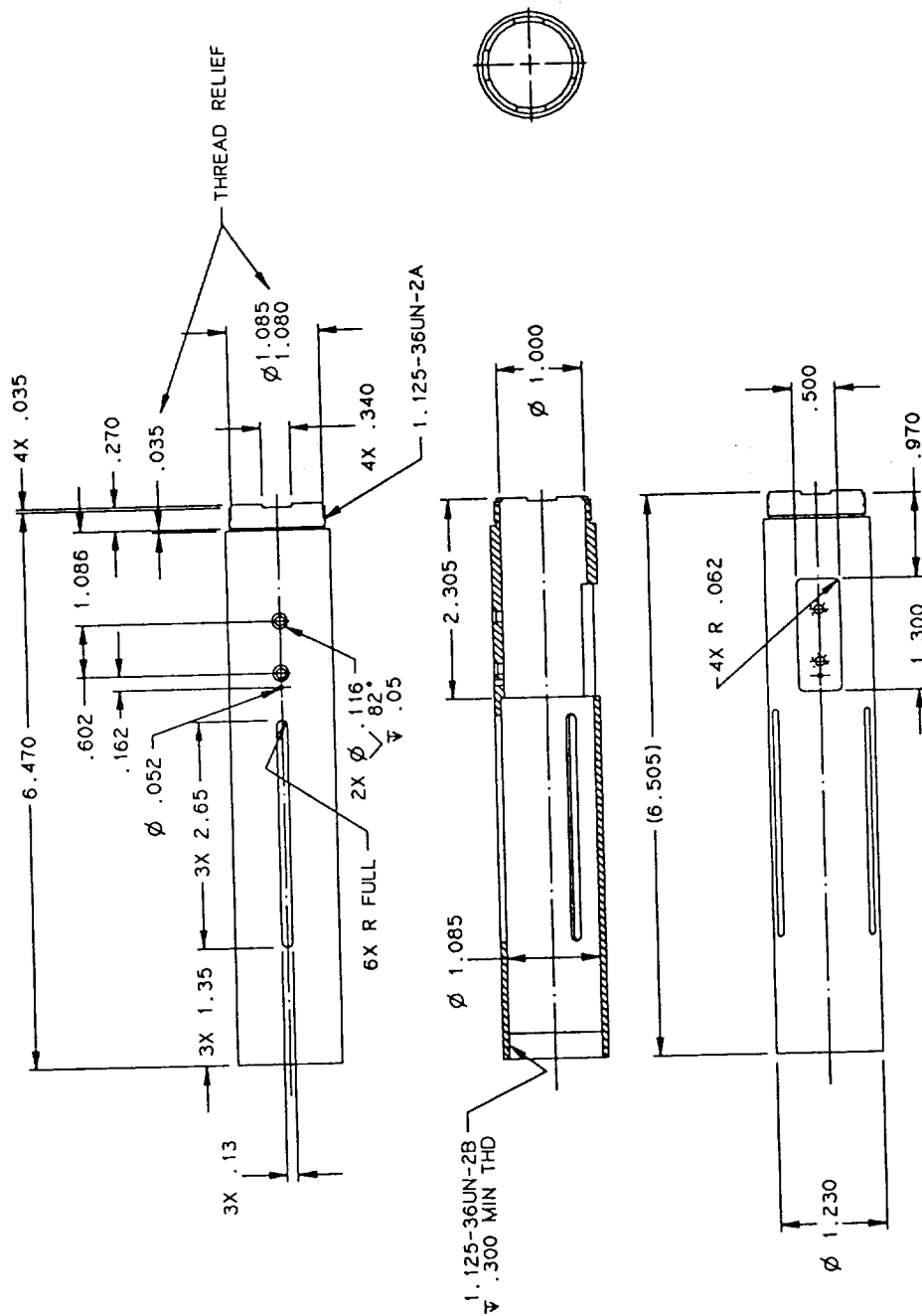
REVISIONS				
REV	DESCRIPTION	DWN	CHK	APPVL/DATE
-	INITIAL RELEASE PER ECR XXXXX	KMARF		xx/xxxxxxx

- NOTES:
1. FINISH ALL OVER $\sqrt[32]{}$
 2. REMOVE BURRS AND BREAK SHARP EDGES .01 MAX

[illegible]

NOTES:

1. FINISH ALL OVER $\sqrt{32}$
2. REMOVE BURRS AND BREAK SHARP EDGES .01 MAX



SATCON HOUSING ACTIVE MEMBER		CONTRACT NO. DRAWN K. AYAKIAN 22JAN92 CHECKED R. FERNI 21FEB92 ENGINEER R. FERNI 21FEB92 APPROVED B. JOHNSON 21FEB92 APPROVED R. HODGNEY 21FEB92 SATCON APPROVED	UNLESS OTHERWISE SPECIFIED DIMENSIONS ARE IN INCHES TOLERANCES ARE IN INCHES DECIMALS ANGLES .XX ± .01 ± .5 .XXX ± .005 DO NOT SCALE THIS DRAWING MATERIAL Ti 6Al-4V	SIZE FSCM NO. DRAWING NO. C 1037351 A SCALE 1/1 SHEET 1
---	--	--	--	--

JUL 08 1992

A horizontal number line with tick marks at 1, 2, 3, and 4. The numbers are written below the line. An arrow points to the tick mark for the number 3.

1. FINISH ALL OVER ✓
2. REMOVE BURRS AND BREAK SHARP EDGES .01 MAX



Technical drawing of a shaft with dimensions: 907, 2X .903, 4X .330, 4X .328, and a hole with dimensions 1.087 and 1.086.

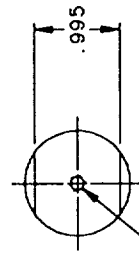
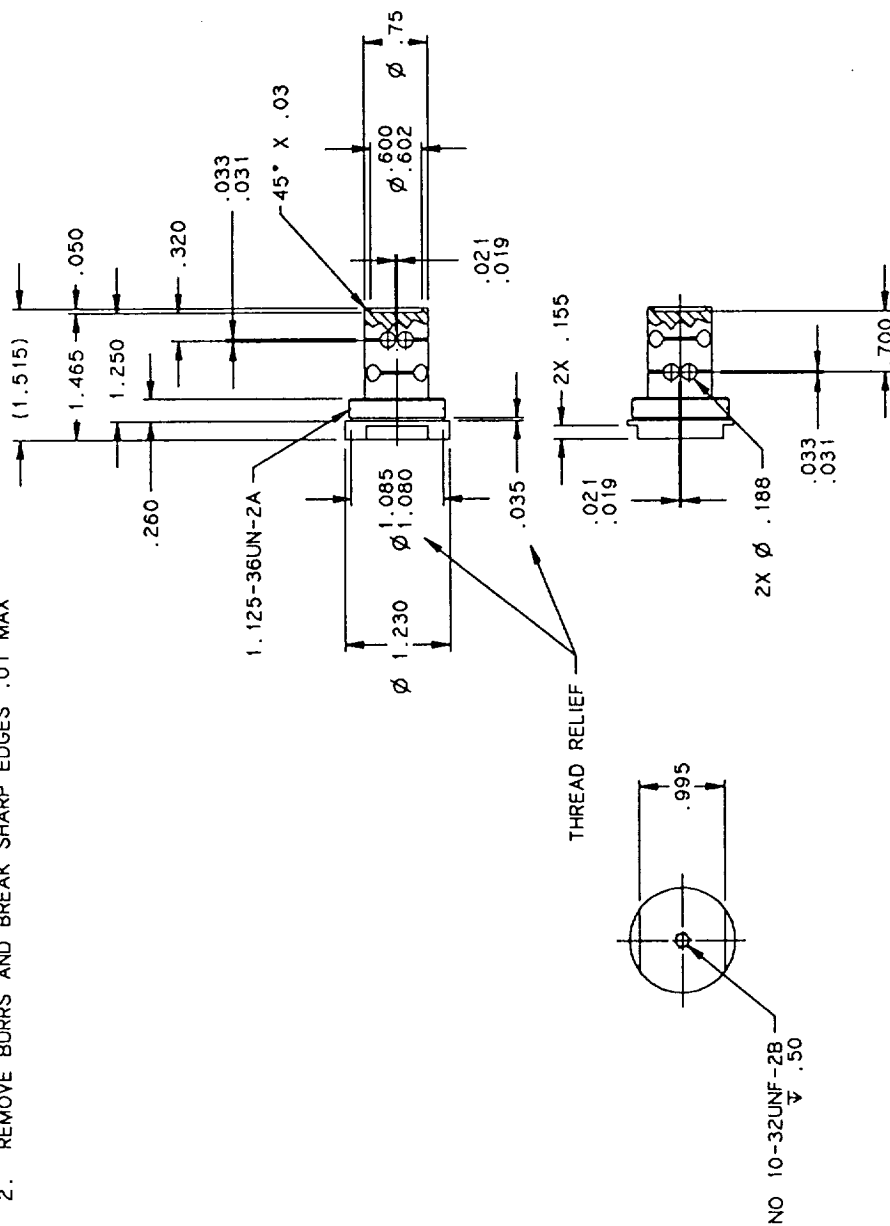
SAT CON

FLEXURE- LONG
ACTIVE MEMBER

	.XXX # .005	APPROVED B JOHNSON DTJUL92	SHEET 1
	DO NOT SCALE THIS DRAWING MATERIAL	REV A	DRAWING NO.
NEXT ASSY	T1 6A1-4V	C	SIZE FSCM NO.
USED ON APPLICATION			SCALE 1/1

NOTES:

1. FINISH ALL OVER $\sqrt{32}$
2. REMOVE BURRS AND BREAK SHARP EDGES .01 MAX



NO 10-32UNF-2B $\sqrt{32}$.50

THREAD RELIEF

DWG. NO. 1037353

SATCON

FLEXURE - SHORT
ACTIVE MEMBER

CONTRACT NO.
DRAWN K AVAKIAN 22JAN92
CHECKED R FENN 21FEB92
ENGINEER R FENN 21FEB92
APPROVED B JOHNSON 21FEB92
APPROVED R MOONEY 21FEB92
SATCON APPROVED

UNLESS OTHERWISE SPECIFIED
DIMENSIONS ARE IN INCHES
TOLERANCES ARE IN INCHES
DECIMALS ANGLES
.XX ± .01 .5
.XXX ± .005
DO NOT SCALE THIS DRAWING
MATERIAL

TI 6Al-4V

APPLICATION

SCALE 1/1 SHEET 1

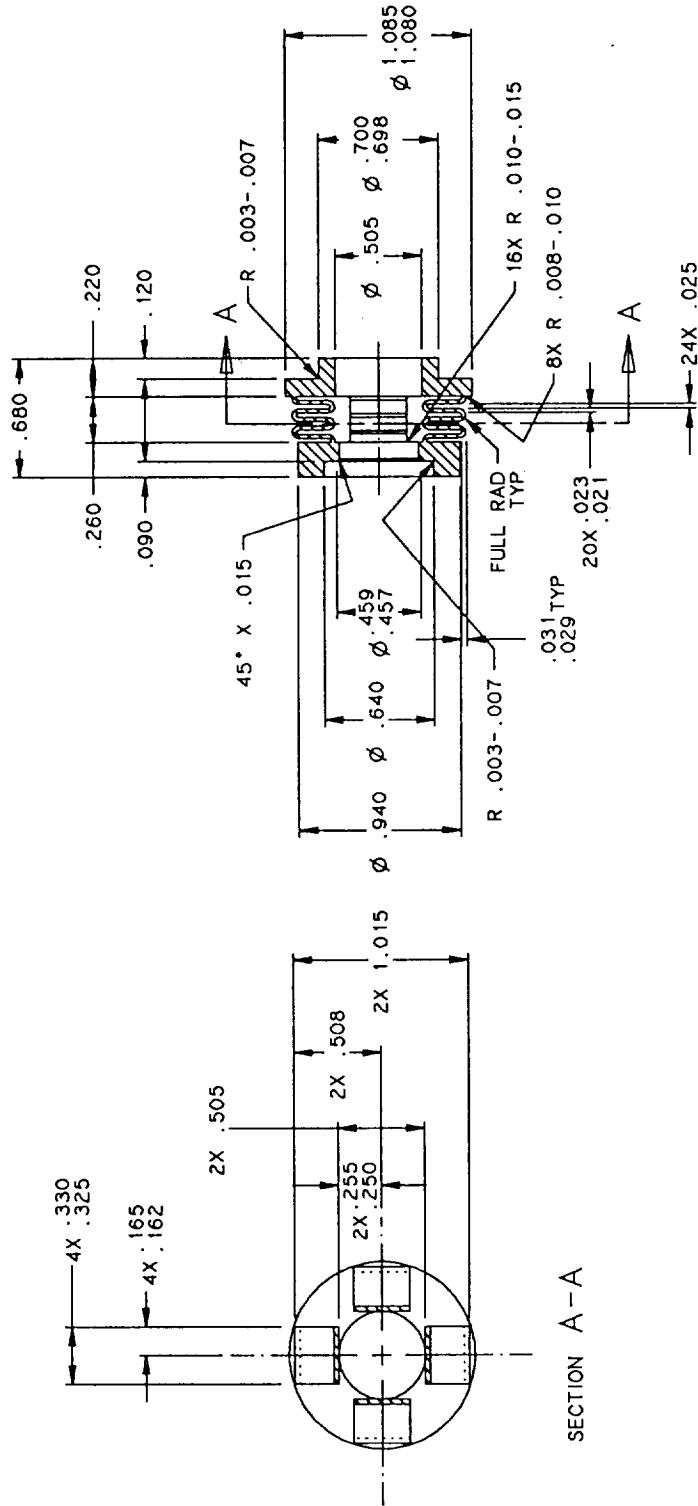
REV A

SIZE FSCM NO. DRAWING NO. 1037353

1 FEB 24 1992

NOTES:

1. FINISH ALL OVER $\sqrt{32}$
2. REMOVE BURRS AND BREAK SHARP EDGES .01 MAX



SECTION A-A

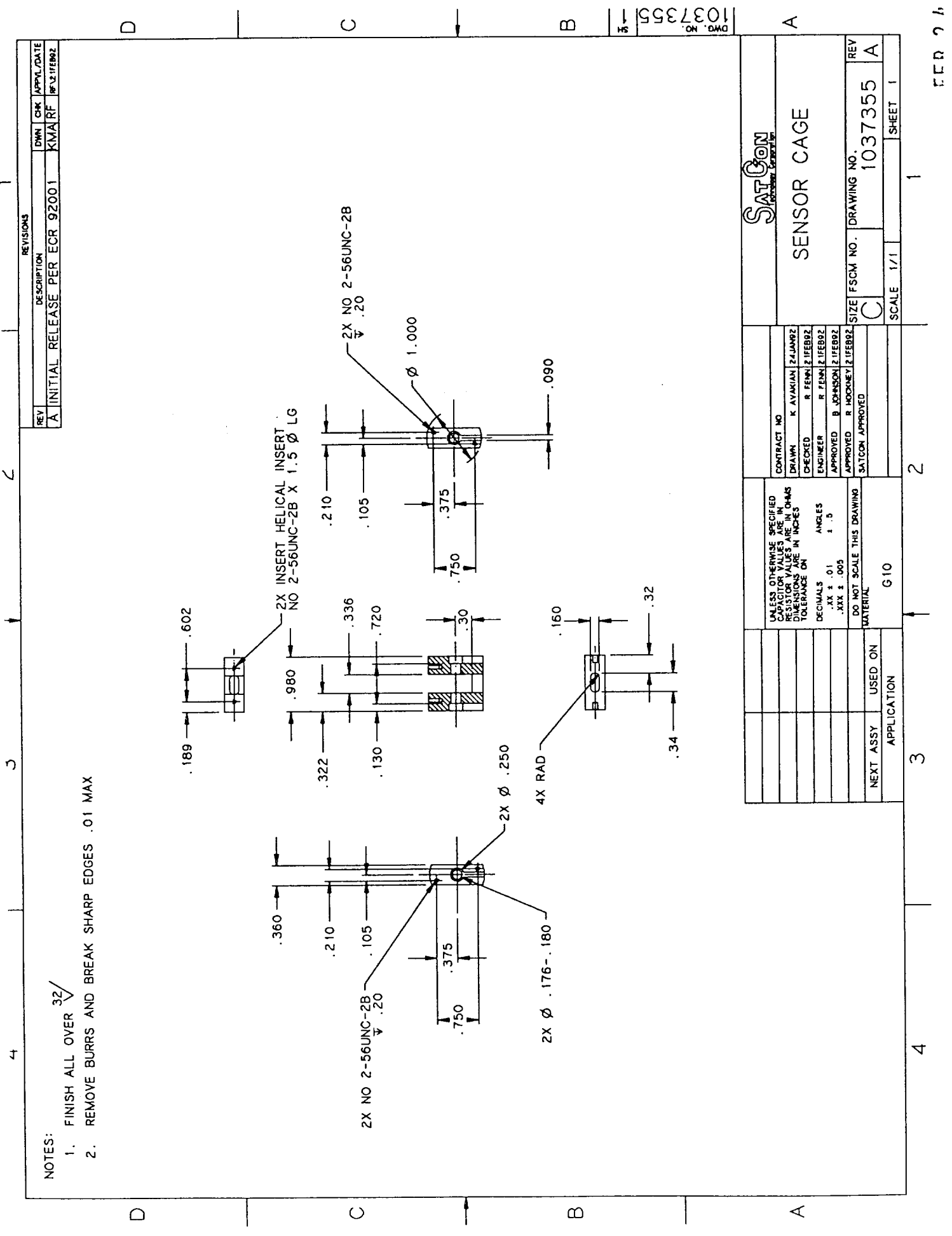
SatCon

PRELOAD
SPRING

CONTRACT NO.	K AVAKIAN 24JAN92
DRAWN	R FENAI 21FEB92
CHECKED	R FENAI 21FEB92
ENGINEER	R FENAI 21FEB92
APPROVED	B JOHNSON 21FEB92
APPROVED	R HOCKNEY 21FEB92
SATCON APPROVED	

SIZE	FSCM NO.	DRAWING NO.	REV
C		1037354	A
SCALE	2/1	SHEET	1

1 FEB 24 1992



NOTES:

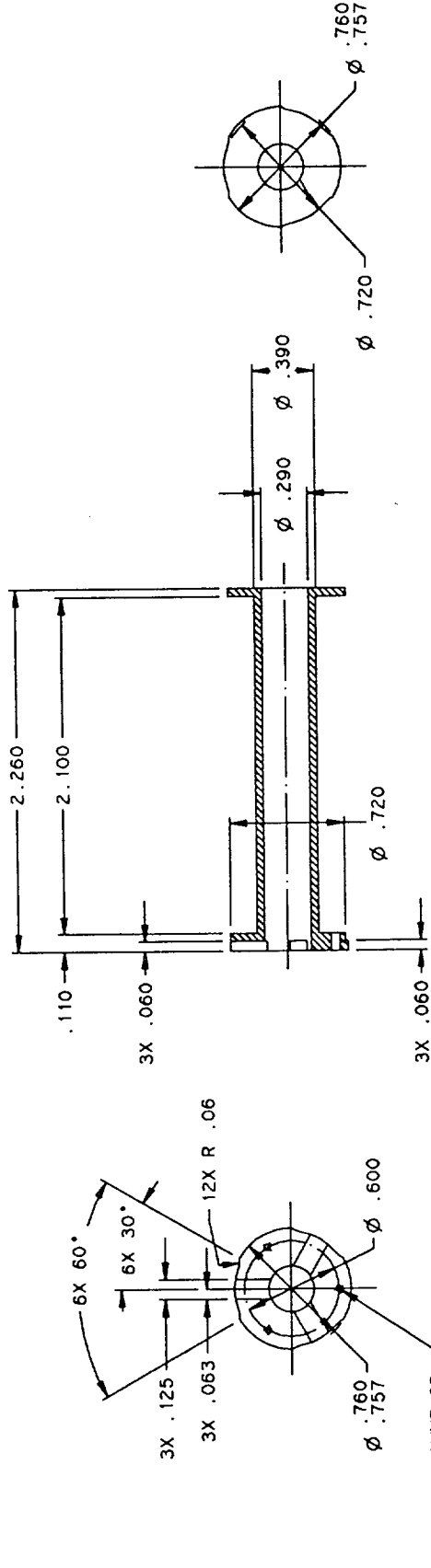
1. FINISH ALL OVER $\sqrt{32}$
2. REMOVE BURRS AND BREAK SHARP EDGES .01 MAX

REVISIONS			
REV	DESCRIPTION	DRAWN	CHK
A	INITIAL RELEASE PER ECR 92001	KVARF	10/12/1992

SatCon		SENSOR CAGE	
CONTRACT NO.		DRAWN: K AYAKIAN 2/2/92	
CHECKED: R FENN 2/12/92		ENGINEER: R FENN 2/12/92	
APPROVED: B JOHNSON 2/12/92		APPROVED: R HOCKNEY 2/12/92	
SATCON APPROVED		SATCON APPROVED	
UNLESS OTHERWISE SPECIFIED DIMENSIONS ARE IN INCHES TOLERANCES ARE IN INCHES		DECIMALS: .01 ANGLES: .5 D	
DO NOT SCALE THIS DRAWING		MATERIAL: G10	
NEXT ASSY		USED ON	
APPLICATION		SCALE: 1/1	
SHEET 1		SHEET 1	

NOTES:

1. FINISH ALL OVER $\sqrt{32}$
2. REMOVE BURRS AND BREAK SHARP EDGES .01 MAX



SATCON

COIL BOBBIN

SIZE FSCM NO. DRAWING NO. 1037356
REV A

SHEET 1

1 FEB 24 1992

CONTRACT NO.

DRAWN K AYANIAN 10 FEB 92

CHECKED R FENN 2 FEB 92

ENGINEER R FENN 2 FEB 92

APPROVED B JOHNSON 2 FEB 92

APPROVED R HOCKEY 2 FEB 92

SATCON APPROVED

UNLESS OTHERWISE SPECIFIED
DIMENSIONS ARE IN INCHES
RESISTOR VALUES ARE IN OHMS
DIMENSIONS ARE IN INCHES
TOLERANCE ON

DECIMALS ANGLES

.XX ± .01 ± .5

.XXX ± .005

DO NOT SCALE THIS DRAWING

MATERIAL

G-10

NEXT ASSY USED ON APPLICATION

3

2

1

4

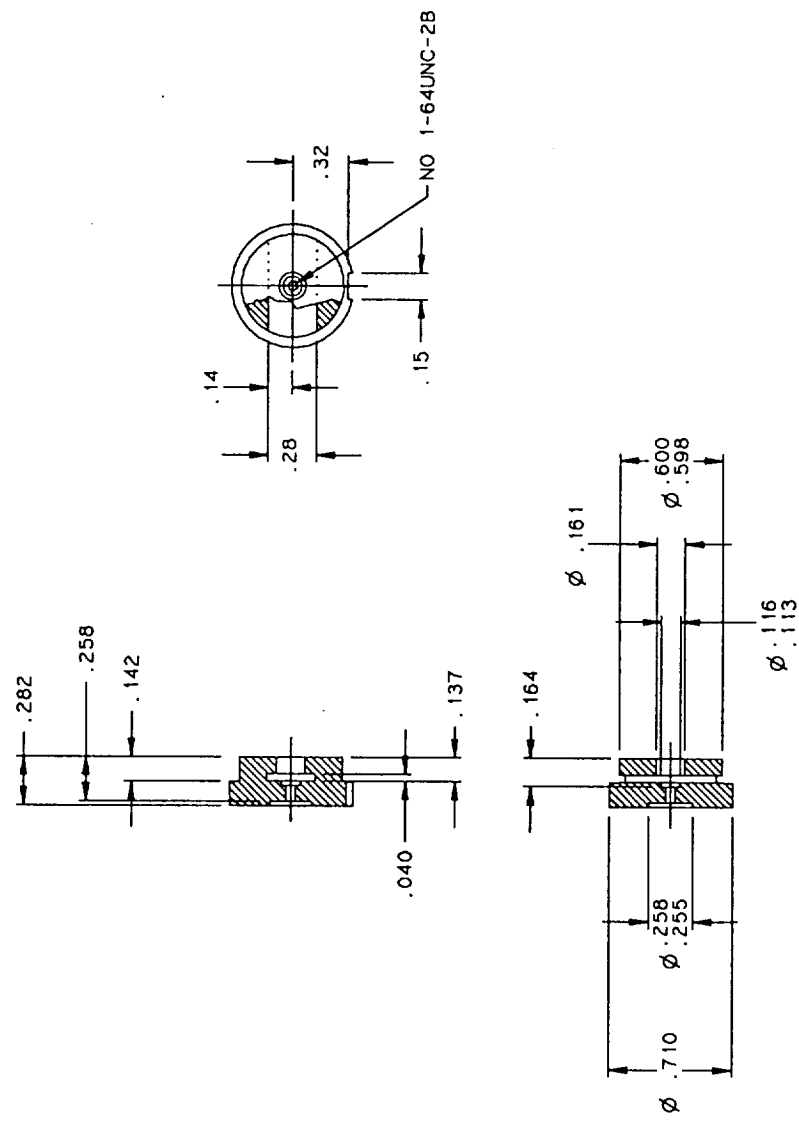
DWG NO. 1037356

HS

4 3 2 1

NOTES:

1. FINISH ALL OVER $\sqrt{32}$
2. REMOVE BURRS AND BREAK SHARP EDGES .01 MAX
3. HEAT TREAT PER DRAWING NO. 1009-107
4. BLACK OXIDE AFTER HEAT TREAT



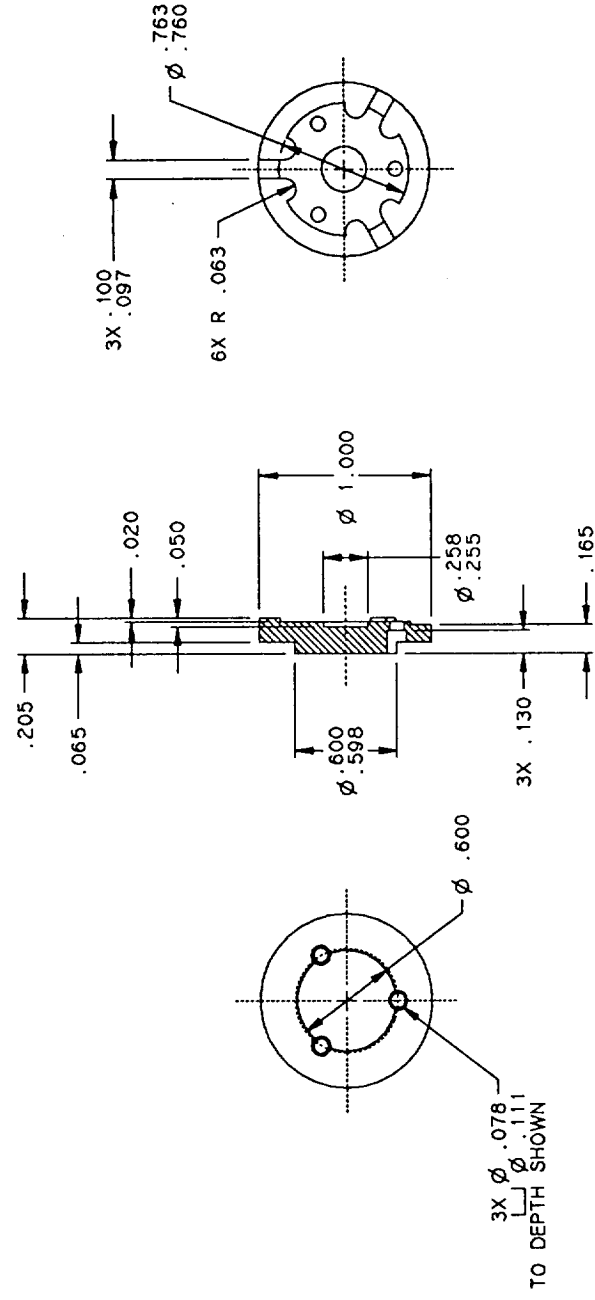
REVISIONS			
REV	DESCRIPTION	DWN	CHK
A	INITIAL RELEASE PER ECR 92001	KMA	RF

SATCON		MOUNT 2 TERFENOL	
CONTRACT NO.	DRAWN	BY	DATE
	K AYAKIAN	31JAN92	
CHECKED	R FENN	21FEB92	
ENGINEER	R FENN	21FEB92	
APPROVED	B JOHNSON	21FEB92	
SATCON APPROVED			
UNLESS OTHERWISE SPECIFIED CAPACITOR VALUES ARE IN OHMS RESISTOR VALUES ARE IN OHMS DIMENSIONS ARE IN INCHES TOLERANCE ON		DECIMALS	ANGLES
		.XX ± .01	± .5
		.XXX ± .005	
DO NOT SCALE THIS DRAWING			
MATERIAL		SI-Fe	
NEXT ASSY	USED ON		
APPLICATION			
SIZE	FSCM NO.	DRAWING NO.	REV
C		1037357	A
SCALE	2/1	SHEET	1

4 3 2 1

NOTES:

1. FINISH ALL OVER $\sqrt{32}$
2. REMOVE BURRS AND BREAK SHARP EDGES .01 MAX
3. HEAT TREAT PER DRAWING NO 1009-107
4. BLACK OXIDE AFTER HEAT TREAT



REVISIONS			
REV	DESCRIPTION	CHK	APPLY DATE
A	INITIAL RELEASE PER ECR 92001	KMA RF	10/21/92

SATCON

MOUNT 1
TERFENOL

CONTRACT NO.	K AVAMIAN 31JAN92
DRAWN	R FENN 21FEB92
CHECKED	R FENN 21FEB92
ENGINEER	R FENN 21FEB92
APPROVED	B JOHNSON 21FEB92
APPROVED	R HOCKEY 21FEB92
SATCON APPROVED	
SIZE	FSCM NO. 1037358
REV	A
SCALE	2/1
SHEET	1

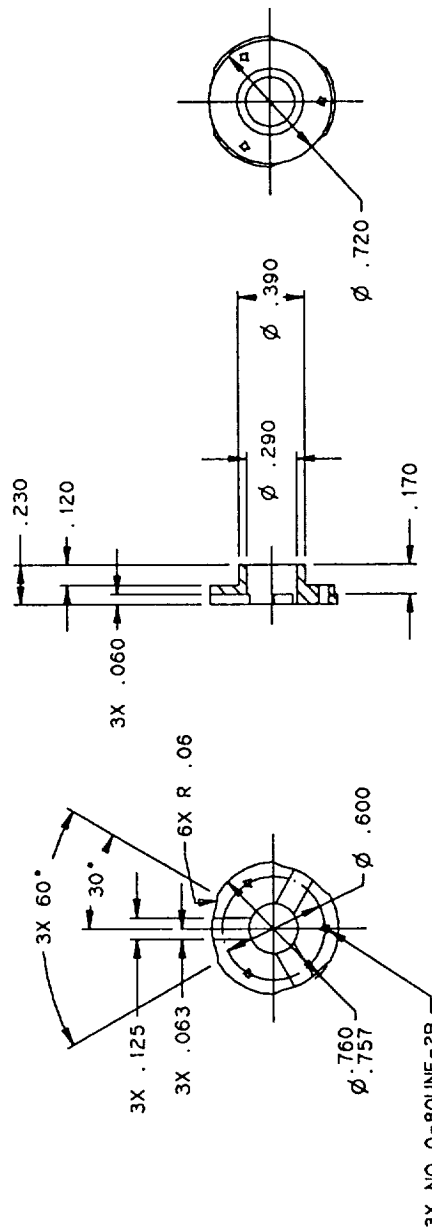
1
FEB 24 1992

NOTES:

1. FINISH ALL OVER

32/✓

1. FINISH ALL OVER $\sqrt{}$
2. REMOVE BURRS AND BREAK SHARP EDGES .01 MAX

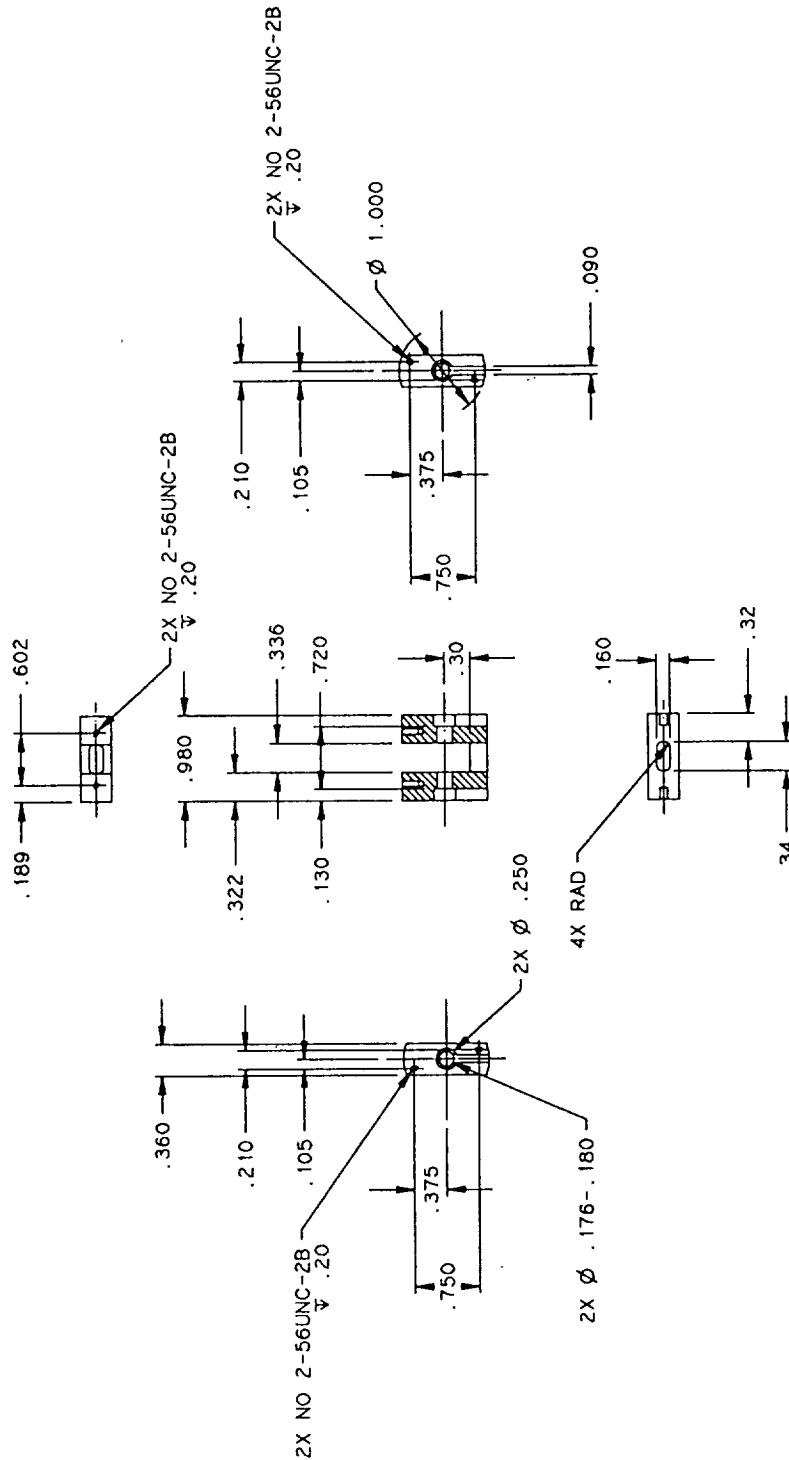
[illegible]

2

FEB 24 1992

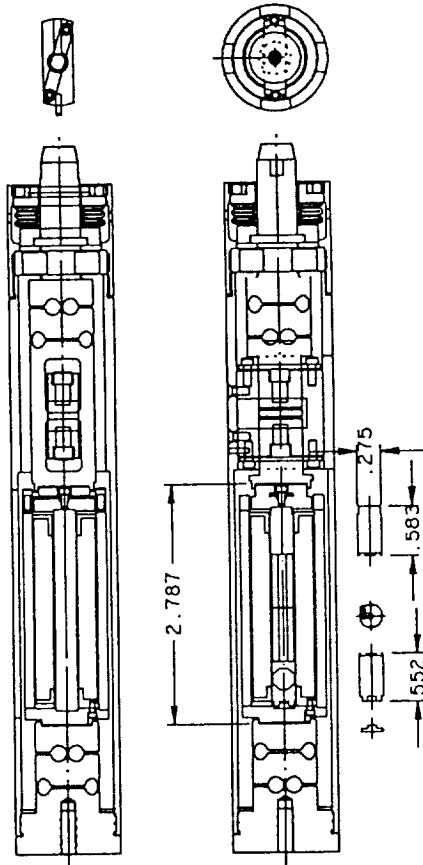
NOTES:

1. FINISH ALL OVER $\sqrt{32}$
2. REMOVE BURRS AND BREAK SHARP EDGES .01 MAX



<p>SATCON Sensors & Controls Corporation</p>		<p>CONTRACT NO.</p>	
<p>UNLESS OTHERWISE SPECIFIED DIMENSIONS ARE IN INCHES TOLERANCES ARE IN INCHES</p>		<p>DRAWN K. AVANIAN 24JAN92 CHECKED R. FENN 21FEB92 ENGINEER R. FENN 21FEB92 APPROVED B. JOHNSON 21FEB92 SATCON APPROVED</p>	
<p>DO NOT SCALE THIS DRAWING</p>		<p>SIZE FSCM NO. DRAWING NO. REV C 1037360 A</p>	
<p>DESCRIPTOR A INITIAL RELEASE PER ECR 92001</p>		<p>SCALE 1/1 SHEET 1</p>	

REVISIONS		
REV	DESCRIPTION	DWN CHK APPL DATE
A	INITIAL RELEASE PER ECR 92001	KMARF RF 2 FEB 92



SATCON

LAYOUT - ACTUATOR TbDy

SIZE	FSCM NO.	DRAWING NO.	REV
C		1037361	-

SCALE 1/1

SHEET 1

CONTRACT NO.

DRAWN	K AYAMIAN	22JAN92
CHECKED	R FENN	2 FEB 92
ENGINEER	R FENN	2 FEB 92
APPROVED	B JOHNSON	2 FEB 92
APPROVED	R MOONEY	2 FEB 92
SATCON APPROVED		

UNLESS OTHERWISE SPECIFIED
DIMENSIONS ARE IN INCHES
TOLERANCES ARE IN INCHES
DECIMALS .01 ANGLES ± .5
DO NOT SCALE THIS DRAWING
MATERIAL

NEXT ASSY	USED ON
	APPLICATION

3

2

1

4

JUL 08 1992

Appendix C - SatCon/JPL Magnetostrictive Active Member Operating Instructions

Recommended Preload -- 12.5 MPa

This preload stress requires a 200 lb_f preload. Preload procedure is similar to other JPL struts -- use fixture to apply external load to preload spring, then snug down preload nut.

Maximum Tested Preload -- 500 lb_f

Terfenol-D Material Compressive Strength -- 700 MPa -- 11,000 lb_f

The other active member mechanical parts, however, are not rated to this level.

Maximum Recommended Current ± 2 Amps

The actuator has been tested thermally at a steady state current level of 2 Amps. Also, actuator becomes non-monotonic below -2 Amps. **Actuator may become damaged if operated for extended periods above 2 amps RMS. Recommend use of 2 Amp slow-blow fuse.**

Assembly into Truss

Use wrench on active member flats to avoid applying torque to internal mechanism.

Gain Constant

Amplitude dependent, approximately 10 microns/amp, see curves below.

Actuator Impedance

$R = 2.25$ ohms

$R/L = 50 - 90$ Hz: depends on preload, current amplitude, etc.

Displacement Sensor Gain -- 24.89 Microns/Volt

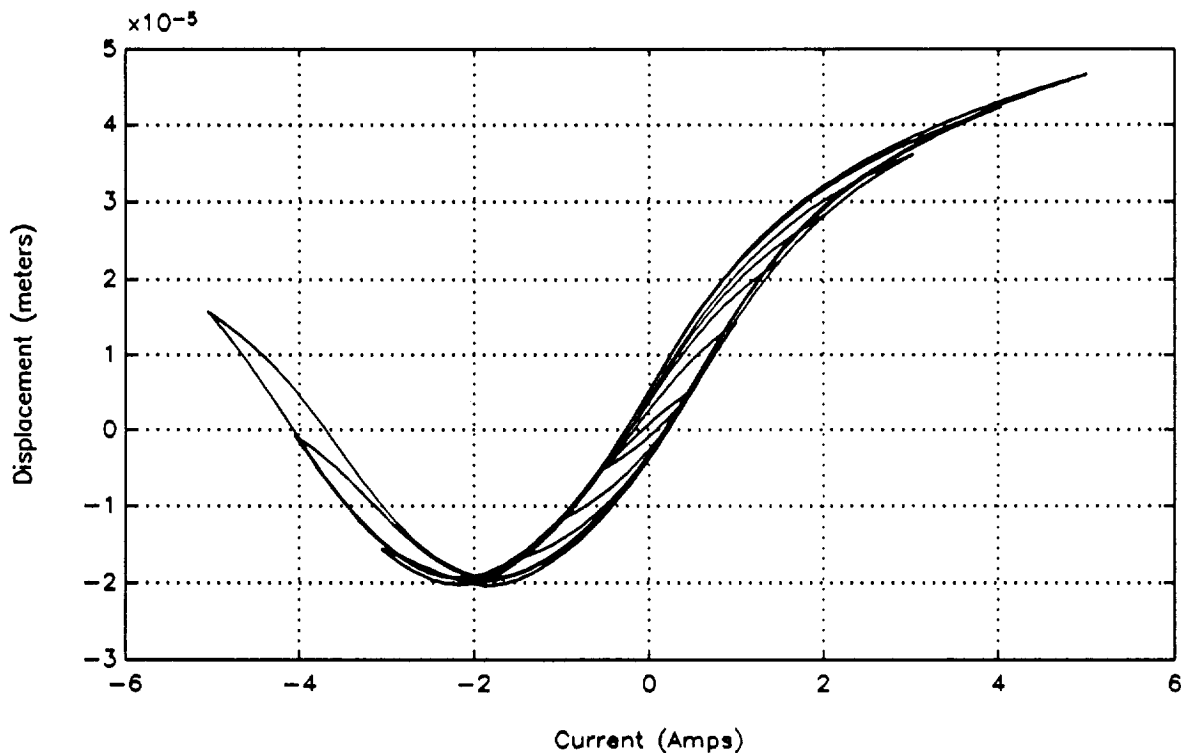


Figure C-1. Actuator displacement vs. current (12.5 MPa preload -- 200 lb_f)

1. Report No.		2. Government Accession No.		3. Recipient's Catalog No.	
4. Title and Subtitle Development of Magnetostrictive Active Members for Control of Space Structures				5. Report Date Aug. 10, 1992	
				6. Performing Organization Code	
7. Author(s) Johnson, Bruce G.; Avakian, Kevin M.; Fenn, Ralph C.; Gaffney, Monique S.; Gerver, Michael J.; Hawkey, Timothy J.; Boudreau, Donald J.				8. Performing Organization Report No. R29-92	
9. Performing Organization Name and Address SatCon Technology Corporation 12 Emily Street Cambridge, MA 02139-4507				10. Work Unit No.	
11. Contract or Grant No. NAS7-1151				13. Type of Report and Period Covered Final Report June 1991 - July 1992	
12. Sponsoring Agency Name and Address NASA Resident Office-JPL 4800 Oak Grove Drive Pasadena, CA 91109				14. Sponsoring Agency Code	
15. Supplementary Notes					
16. Abstract <p>The goal of this Phase II Small Business Innovative Research (SBIR) project was to determine the technical feasibility of developing magnetostrictive active members for use as truss elements in space structures. Active members control elastic vibrations of truss-based space structures and integrate the functions of truss structure element, actively controlled actuator, and sensor. The active members must control structural motion to the sub-micron level and, for many proposed space applications, work at cryogenic temperatures.</p> <p>Under this program both room temperature and cryogenic temperature magnetostrictive active members were designed, fabricated and tested. The results of these performance tests indicated that room temperature magnetostrictive actuators feature higher strain, stiffness and force capability with lower amplifier requirements than similarly sized piezoelectric or electrostrictive active members, at the cost of higher mass. Two different cryogenic temperature magnetostrictive materials were tested at liquid nitrogen temperatures, both with larger strain capability than the room temperature magnetostrictive materials. The cryogenic active member development included the design and fabrication of a cryostat that allows operation of the cryogenic active member in a space structure testbed.</p>					
17. Key Words (Suggested by Author(s)) active strut; magnetostrictive actuators; Terfenol-D; Terbium-Dysprosium			18. Distribution Statement Distribution limited to U.S. Government agencies only; Aug. 10, 1992. Other requests for this document must be referred to NASA-JPL.		
19. Security Classif. (of this report) Unclassified		20. Security Classif. (of this page) Unclassified		21. No. of pages 225	22. Price nsp

